A Thesis for the Degree of Ph.D. in Science

Spin-Chirality Interplay in an XXZ Ladder with Four-Spin Interaction: Duality and Topology

January 2025

Graduate School of Science and Technology
Keio University

FONTAINE, Mateo Olivier Jean-Marie Michel

KEIO UNIVERSITY

Abstract

Center for Physics
School of Fundamental Science and Technology
Graduate School of Science and Technology

Ph.D. in Science

Spin-Chirality Interplay in an XXZ Ladder with Four-Spin Interaction: Duality and Topology

by FONTAINE, Mateo Olivier Jean-Marie Michel

I investigated the ground-state phase diagram of a spin-1/2 XXZ model with chirality-chirality interaction (CCI) on a two-leg ladder, considering both isotropic and weakly anisotropic cases. This model provides a minimal setup to explore the interplay between spin and chirality degrees of freedom and is potentially relevant for understanding the effects of four-spin ring exchange. Additionally, anisotropic interactions enable the emergence of various orders and symmetry-protected topological (SPT) phases on the ladder.

Spin-chirality duality transformations allowed me to relate the regimes of weak and strong CCIs. By applying Abelian bosonization in combination with two types of spin-chirality dualities, I derived a comprehensive phase diagram. Furthermore, I developed a spin-1 hard-core bosons approach to analyze the phase structure around the self-dual line in the presence of strong anisotropy. I have also performed numerical simulations to validate the predicted phase diagrams and to examine the topological and critical properties.

In the isotropic (Heisenberg) model with CCI, the phase diagram consists of the rung singlet (RS) phase, the Haldane phase, dimer phases, and a scalar chiral phase. Within the RS and Haldane phases, I identified eight distinct regions with dominant correlations in terms of spin, dimer, or chirality. In particular, the dominance of staggered and uniform vector chiral (VC) correlations in the RS phase for strong positive and negative CCIs can be interpreted as dual counterparts to the conventional Néel correlation.

The introduction of weak XXZ anisotropy further enriches the phase structure within the region of positive CCI and antiferromagnetic rung interaction. Specifically, Néel and VC orders emerge for easy-axis anisotropy, while two distinct SPT phases emerge for easy-plane anisotropy. For strong anisotropy, a direct Gaussian transition occurs between Néel and VC or between the two SPT phases. Although both SPT phases can be viewed as twisted variants of the Haldane phase, I showed that they, along with the RS phase, can be distinguished by topological indices in the presence of specific symmetries.

In these ways, I demonstrated that the combination of anisotropy and multi-spin interactions generates rich and diverse physics characterized by chirality and topology.

Acknowledgements

The author of this dissertation would like to thank Prof. Shunsuke FURUKAWA, for all his help during these three years, and Prof. Koudai SUGIMOTO for his help during the numerical simulation and stimulating discussions. The author also wants to thank his former institution, the Ecole Normale Supérieure Paris-Saclay for all the financial support and opportunity to study abroad. L'auteur remercie également ses parents et sa famille pour toute l'aide qu'ils lui ont apportée au cours de ses études supérieures. The author thanks Dr. Takuhiro OGINO and Prof. Keisuke TOTSUKA for stimulating discussions. The author would also like to thank Mr. Yuheng SUI and Mr. Mizuki HAMADA for their help in reviewing this dissertation's last version. The author was also supported by Keio "Design the Future" Award for International Students.

Contents

Abstract **iii**

Acknowledgements **v**

1 Introduction **1**
1.1 Topological order 1
1.1.1 Introduction to topological order 1
1.1.2 Symmetry-protected topological phases in one dimension 2
1.2 Spin ladders 3
1.3 SPT phases in spin-$\frac{1}{2}$ ladders 5
1.3.1 Spin-$\frac{1}{2}$ XXZ ladder 5
1.3.2 Spin-$\frac{1}{2}$ ladder with multi-spin interaction 7
1.4 Spin-chirality interplay in a ladder with four-spin ring exchange 10
1.5 Chirality-chirality interaction 12
1.6 Purpose of the dissertation 14
1.7 Outline of the dissertation 15

2 Symmetry and topology in quantum spin systems **17**
2.1 Introduction to quantum spin systems 18
2.2 Long-range order and SSB 20
2.2.1 Definition of long-range order 20
2.2.2 Low-lying state 21
2.2.3 Absence of continuous SSB in one-dimensional systems 22
2.3 Haldane conjecture 23
2.3.1 Introduction 23
Half-odd-integer-spin case case 23
Integer-spin case 24
2.3.2 Discussion on the difference between integer and half-odd-integer spins 24
2.3.3 Haldane phenomena 25
2.4 Affleck-Kennedy-Lieb-Tasaki model 26
Construction of the VBS 27
Properties of the VBS 29
2.5 Symmetry-protected topological phases 31
2.6 Matrix product state 34
2.7 Topological indices 36
2.7.1 Definition of the topological indices 36
2.7.2 SPT phases on spin-$\frac{1}{2}$ ladders 38
2.8 Numerical methods 38
2.8.1 Canonical form of MPS 39

2.8.2 iDMRG algorithm for spin ladder 39
2.8.3 Central charge 40
2.8.4 Generalized transfer matrix method 40
2.9 Conclusions 41

3 Field-theoretical analysis **43**
3.1 Review of the bosonization of spin-$\frac{1}{2}$ chain 44
3.1.1 Effective field theory for a Hubbard chain 44
3.1.2 Bosonization 47
3.2 Heisenberg ladder with CCI 49
3.2.1 Abelian bosonization for weak interchain couplings . . 49
3.2.2 Phase diagram from bosonization: weak interchain regime 50
Analysis of the bosonized Hamiltonian 50
Analysis of the phase structure 51
Analysis of the dominant correlation 53
3.2.3 Spin-chirality dualities 55
3.2.4 Full phase structure 56
Analysis of marginal terms 59
3.3 XXZ ladder with four-spin interaction 59
3.3.1 Phase diagram from bosonization: weak interchain limit 59
3.3.2 Spin-chirality duality 60
3.3.3 Full phase structure 62
3.4 Conclusions 63

4 Effective spin-1 hard-core bosons approach **65**
4.1 Effective spin-1 hard-core bosons approach 65
4.1.1 Mapping to hard-core bosons 65
4.1.2 U(1) symmetry on the self-dual line 66
4.1.3 Easy-axis regime 68
4.1.4 Easy-plane regime 71
4.2 SPT phases in the XXZ-CCI model 73
4.2.1 Simple matrix product states for the SPT phases 73
4.2.2 Projective representation of the symmetry group 74
4.3 Conclusions 75

5 Numerical analyses **77**
5.1 Heisenberg ladder with CCI 77
5.1.1 Phase diagram in the $J_\perp$-K_{ch} plane 77
5.1.2 Ising transitions 79
Haldane-SC transition 79
Plaquette-RS transition 81
5.1.3 $c = 3/2$ transitions 83
5.1.4 Dominant correlation 85
Structure factors 85
Correlation functions 88
5.1.5 Boson density 88
5.2 XXZ-CCI ladder 90
5.2.1 Phase diagram in the Δ-K_{ch} plane 90

5.2.2 Gaussian transitions . . . 91
SC-VC transition . . . 91
c-Haldane*-RS transition . . . 94
5.2.3 Ising transitions . . . 94
VC-RS transition . . . 94
SC-c-Haldane* transition . . . 96
5.2.4 Topological transitions between featureless phases . . . 98
5.2.5 Criticality on the self-dual line . . . 98
5.3 Conclusions . . . 101

6 Conclusions **103**
6.1 Summary . . . 103
Main results . . . 103
Comparison with previous studies . . . 103
Main contributions . . . 104
6.2 Outlook . . . 104
6.2.1 Implications for an XXZ ladder with four-spin ring exchange . . . 104
6.2.2 Dominant correlation in extended ladder model . . . 106
6.2.3 Extending duality transformations for the discovery of exotic phases . . . 106

A Microscopic origins of spin interactions **109**
A.1 Hubbard model and Heisenberg exchange couplings . . . 109
A.2 Origins of dimer-dimer interaction . . . 110
A.3 Origins of chirality-chirality interaction . . . 111

B Some details of the bosonization analysis **113**
B.1 Bosonization of four-spin interactions . . . 113
B.2 Link between the Haldane and Haldane* phases . . . 114

Bibliography **117**

List of Abbreviations

TLL	**T**omonaga-**L**uttinger **L**iquid
WZW	**W**ess-**Z**umino-**W**itten
CCI	**C**hirality-**C**hirality **I**nteraction
DDI	**D**imer-**D**imer **I**nteraction
SPT	**S**ymmetry-**P**rotected **T**opological
iDMRG	**i**nfinite **D**ensity **M**atrix **R**enormalization **G**roup
RS	**R**ung **S**inglet
SD	**S**taggered **D**imer
CD	**C**olumnar **D**imer
SC	**S**calar **C**hiral
VC	**V**ector **C**hiral
SVC	**S**taggered **V**ector **C**hiral
UVC	**U**niform **V**ector **C**hiral
SN	**S**tripe **Néel**
SF	**S**tripe **F**erromagnetic
MPS	**M**atrix **P**roduct **S**tate
SSB	**S**pontaneous **S**ymmetry **B**reaking
AKLT	**A**ffleck-**K**ennedy-**L**ieb-**T**asaki
VBS	**V**alence **B**ond **S**tate
HOI	**H**alf-**O**dd-**I**nteger
MLM	**M**arshall-**L**ieb-**M**attis
DMI	**D**zyaloshinskii–**M**oriya **I**nteraction

To my wife, family, and friends

Chapter 1

Introduction

1.1 Topological order

1.1.1 Introduction to topological order

Ground states are conventionally classified by comparing their symmetries to the symmetry of their Hamiltonian [72, 131]. Local order parameters are typically employed to detect the spontaneous breaking of specific symmetries of a Hamiltonian in its ground state and to identify different phases. However, this paradigm has been challenged in recent years by the discovery of phases with a new type of order that does not fit into this framework, as it is not associated with the breaking of any symmetry. One of the most notable examples is the Haldane phase [82, 83].

These newly recognized orders are referred to as topological orders, and the concerned phase is referred to as a topological phase. The ground state of a topological phase generally exhibits short-range correlations, characteristic of most gapped systems, yet it possesses highly exotic properties. These unique properties include ground-state degeneracy that depends on the structure of the manifold on which the state is defined [269, 270], non-trivial entanglement structures within the ground state [120, 139], the existence of gapless boundary excitations [266, 267], and the presence of bulk excitations with non-trivial statistics [14, 119, 140]. These attributes make topological phases promising candidates for quantum computation [59, 121, 179] and have spurred intense research into their practical realization.

This discovery introduces a new classification paradigm for ground states: two ground states are considered to belong to the same phase if they can be transformed into each other through a finite sequence of local unitary transformations. Within this framework, ground states are broadly categorized into two classes based on their entanglement structure.

The first class is composed of states with long-range entanglement, and one says they possess intrinsic topological order. The long-range entanglement of the ground state within this class cannot be "erased" by local unitary transformations [32]. Consequently, these ground states cannot be continuously connected to trivial states with short-range entanglement. Unlike traditional phase classifications that rely on symmetry, phases with intrinsic topological order do not depend on symmetry for their definition. Examples of systems with intrinsic topological order include quantum Hall systems (integer and fractional) [134, 256], $p + ip$ superconductors [78, 213], string-net models [140], $\mathbb{Z}_2$ spin liquids [165, 214, 268], and chiral spin liquids [108, 271].

The second class is composed of states with short-range entanglement. In the absence of symmetry, all states belonging to this class can potentially be transformed into each other by local unitary transformations. However, if certain symmetries are imposed on the transformation, certain states may never be connected by local unitary transformations and thus should belong to different phases. Ground states belonging to some of such phases possess exotic properties reminiscent of topological order, also known as symmetry-protected topological (SPT) order, and the concerned phase is referred to as SPT phases. Examples of such phases include the Haldane phase in one-dimensional spin chains [82] and topological insulators [19, 61, 109, 110, 169, 212].

It is noteworthy that phases with intrinsic and SPT order are not mutually distinct categories. Two long-range entangled states, belonging to the same phase under intrinsic topological protection, may not be continuously connected by local unitary transformations if additional symmetry constraints are imposed. Topological orders protected by both the presence of long-range entanglement patterns and symmetry constraints are known as symmetry-enriched topological (SET) orders [33].

1.1.2 Symmetry-protected topological phases in one dimension

In one-dimensional systems, strong quantum fluctuations generally "destroy" long-range entanglement structures [156]. Thus, in the absence of symmetry, all ground states in one dimension are connected by local unitary transformations and belong to the same phase. Nevertheless, if some symmetries are imposed, SPT phases can still be defined in one-dimensional systems [30, 31, 77, 187–189, 208, 209, 225].

Historically, the Haldane phase was characterized by degenerate edge states [80, 113, 162] and hidden antiferromagnetic order [114, 116, 198]; the two phenomena rely respectively on the time-reversal and the $D_2 = \mathbb{Z}_2 \times \mathbb{Z}_2$ spin rotation symmetries.[1] However, even in the presence of an external magnetic field that explicitly breaks these symmetries [77], the Haldane phase can still be distinguished from trivial phases by the degeneracy of its entanglement spectrum [208, 209].[2] While degeneracy alone does not distinguish between different SPT phases, it is now understood that this entanglement spectrum degeneracy is protected by system symmetries. This insight has led to the modern classification of topological phases based on topological indices, and the classification of projective representations of symmetry groups [30, 31, 46, 52, 159, 166, 211, 225, 263, 278].

Given a translationally invariant system of dimension d with symmetry group G, the different SPT phases that this system can host are classified according to equivalent projective representations given by the second cohomology group $\mathrm{H}^{\mathrm{d}+1}(G, U(1))$. Projective representations with trivial coefficients are referred to as trivial representations, and the associated phases are likewise classified as trivial.

[1] That is, the group composed of π-rotations of spin around two orthogonal axes.

[2] The inversion symmetry can protect the Haldane phase but it is not directly linked to degenerate edge states or hidden antiferromagnetic order.

1.2 Spin ladders

Spin ladders are one-dimensional quantum spin systems coupled in parallel. In a two-leg spin ladder, spin degrees of freedom are aligned along two lines. In the scope of this dissertation, we only assume short-range interactions between spin-$\frac{1}{2}$'s, which can include two-body interactions between neighboring spins as in Fig 1.1 or more complex multi-spin interactions among spins on a plaquette as in Fig. 1.4. Owing to their rich ground-state properties and the wide range of material systems where they are realized [40, 41, 135, 218, 234], spin-$\frac{1}{2}$ ladder models have been the subject of intensive research over the past three decades. A notorious example of spin ladders includes $Sr_{14-x}Ca_xCu_{24}O_{41}$ [103, 233], at high pressure and a small hole density (doping), these compounds have a superconducting phase. There exist several families of ladders in cuprate materials. Their atomic structure consists of multiple layers of copper and oxygen atoms intercalated with different ions in a 3-dimensional structure. In these materials, the ladders can either be totally independent or weakly coupled with weak inter-ladder ferromagnetic interactions. In a ladder, the copper atoms form the sites of the ladder while oxygen atoms are intercalated between them and do not explicitly appear in our model. Ladders with different numbers of legs have been realized, enabling the study of the crossover between one-dimensional and two-dimensional physics. These materials are also relatively easy to dope by changing their ion content [163, 197]. It is also possible to change their electronic properties by applying pressure. These cuprate families include $Sr_{2n-2}Cu_{2n+2}O_{4n}$ [101, 245], $La_{2-x}Sr_xCuO_{2.5}$ [100], and $A_{14}Cu_{24}O_{41}$ [232]. Spin ladders are not limited to cupprate material and other material like $Pb_{0.55}Cd_{0.45}V_2O_5$ can be considered as spin-$\frac{1}{2}$ ladder [254].

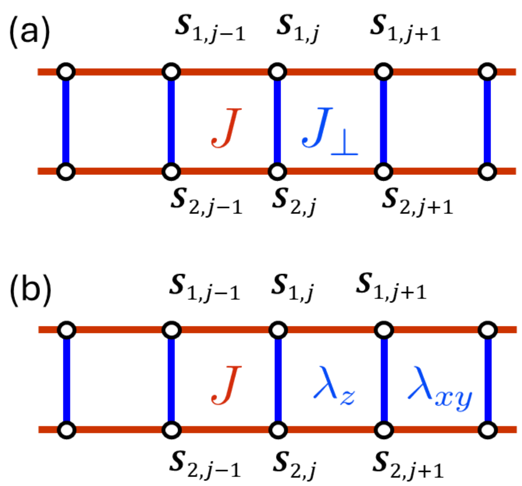

FIGURE 1.1: (a) Spin-$\frac{1}{2}$ Heisenberg ladder described by the Hamiltonian (1.1). (b) Spin-$\frac{1}{2}$ ladder with Heisenberg interaction along the leg and anisotropic interaction along the rung. This model is described by the Hamiltonian (1.4).

Let us consider the spin-$\frac{1}{2}$ Heisenberg ladder, which only contains isotropic and two-spin interactions along the leg (J) and the rung ($J_\perp$):

$$H = J\sum_j \sum_{n=1,2} \boldsymbol{S}_{n,j} \cdot \boldsymbol{S}_{n,j+1} + J_\perp \sum_j \boldsymbol{S}_{1,j} \cdot \boldsymbol{S}_{2,j}. \tag{1.1}$$

More details about the Heisenberg model are provided in Appendix A.1. This Hamiltonian is invariant under numerous symmetries. These include the SO(3) group describing arbitrary global spin rotation (and in particular, the D_2 subgroup), the leg exchange σ, and the time-reversal symmetry $\mathbb{Z}_2^T$. Both SO(3) and σ symmetries are *local* as they can be expressed as the product of unitary transformation acting on each rung.

To describe a state on the spin ladder, it is convenient to introduce the singlet-triplet basis:

$$\left|s^{[j]}\right\rangle := \frac{1}{\sqrt{2}}\left(\left|\uparrow^{[1,j]}\downarrow^{[2,j]}\right\rangle - \left|\downarrow^{[1,j]}\uparrow^{[2,j]}\right\rangle\right), \tag{1.2a}$$

$$\left|t_x^{[j]}\right\rangle := -\frac{1}{\sqrt{2}}\left(\left|\uparrow^{[1,j]}\uparrow^{[2,j]}\right\rangle - \left|\downarrow^{[1,j]}\downarrow^{[2,j]}\right\rangle\right), \tag{1.2b}$$

$$\left|t_y^{[j]}\right\rangle := \frac{i}{\sqrt{2}}\left(\left|\uparrow^{[1,j]}\uparrow^{[2,j]}\right\rangle + \left|\downarrow^{[1,j]}\downarrow^{[2,j]}\right\rangle\right), \tag{1.2c}$$

$$\left|t_z^{[j]}\right\rangle := \frac{1}{\sqrt{2}}\left(\left|\uparrow^{[1,j]}\downarrow^{[2,j]}\right\rangle + \left|\downarrow^{[1,j]}\uparrow^{[2,j]}\right\rangle\right). \tag{1.2d}$$

Throughout this dissertation, spin states will be indicated in this manner with the site or rung indices indicated as superscripts between square brackets. The singlet state $|s\rangle$ has a total magnetic moment $S = 0$ and is invariant under rotation, while $|t_\alpha\rangle$ states have a total magnetic moment $S = 1$.

The phase diagram of this model for antiferromagnetic leg interactions ($J > 0$) is well understood [17, 230, 238, 239, 274], and it is presented in Fig. 1.2 or in Fig. 1.3 along the red double-headed arrow. When the rung interaction is antiferromagnetic ($J_\perp > 0$), the ground state is the rung singlet (RS) phase. This state is given by

$$|\boldsymbol{\phi}_{\mathrm{RS}}\rangle := \bigotimes_j \left|s^{[j]}\right\rangle\ , \tag{1.3}$$

which represents a tensor product of singlet pairs on each rung. Conversely, when the rung interaction is ferromagnetic ($J_\perp < 0$), the ground state of the ladder is known as the Haldane phase [82, 83]. Its wave function can be visualized as an equal-weight superposition of all singlet coverings linking neighboring rungs, with phases tuned such that each rung behaves as a spin-1 degree of freedom. Both phases can be intuitively understood by considering the limit of strong rung interaction. When $J_\perp$ is positive and large, spins on each rung bond into a singlet state with no magnetic moment. These singlets remain nearly independent in the presence of leg interaction. For large negative $J_\perp$, spins on each rung form a triplet state that behaves like a spin-1. Leg interactions create correlations between them, resulting in a phase with properties similar to those of the Haldane phase.

Both the Haldane and RS phases are “featureless” in the sense that they

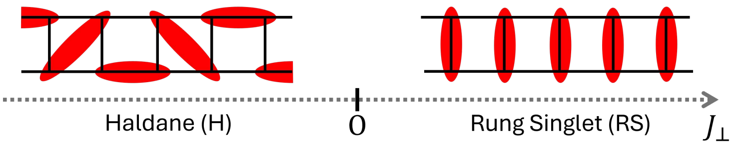

FIGURE 1.2: Schematic ground-state phase diagram of the Heisenberg ladder (1.1) as a function of $J_\perp$ for $J = 1$. Red ovals indicate the singlet state $|s\rangle$ in Eq. (1.2).

have a unique gapped ground state with the same symmetries as the Hamiltonian and cannot be detected by any local order parameter. Similar to the Haldane phase found in spin-1 chains, the Haldane phase in a ladder model is a non-trivial SPT phase [32–34, 77, 227, 272, 279] that cannot be continuously connected to the trivial RS phase in the presence of some symmetry, such as the D_2 symmetry and the time-reversal symmetry [30, 77, 191, 208, 209, 250].

The leg exchange symmetry σ is a symmetry exclusive to the ladder system that does not exist in chain systems. Accordingly, the second cohomology groups of spin ladders are larger than those of spin chains [30, 31, 200, 225]. For example, the classification of projective representations of the symmetry group $\mathbb{Z}_2^3 \times \mathbb{Z}_2^T$ (D_2 rotation, leg exchange σ, and the time-reversal symmetry $\mathbb{Z}_2^T$) is given by $\mathcal{H}^2(\mathbb{Z}_2^3 \times \mathbb{Z}_2^T, U(1)) = \mathbb{Z}_2^7$ which contains 128 elements [276]. Therefore, 128 different topological phases can potentially be realized in a ladder system with the above symmetry. Although the classification of SPT phases based on cohomology groups is extremely valuable, it remains theoretical and does not provide examples of realistic materials that can host these phases. It is thus important to look for examples of "new" SPT phases in concrete models of spin ladders.

1.3 SPT phases in spin-$\frac{1}{2}$ ladders

1.3.1 Spin-$\frac{1}{2}$ XXZ ladder

One approach for the realization of other SPT phases is the introduction of anisotropy in the interactions. This possibility was originally investigated by Z.-X. Liu *et al.* [145]. Consider the spin-$\frac{1}{2}$ ladder defined by the following Hamiltonian:

$$H_{\text{XXZ}} = \sum_j \sum_{n=1,2} J\mathbf{S}_{n,j} \cdot \mathbf{S}_{n,j+1} + \sum_j \left[\frac{1}{2}\lambda_{xy} \left(S^+_{1,j} S^-_{2,j} + S^-_{1,j} S^+_{2,j} \right) + \lambda_z S^z_{1,j} S^z_{2,j} \right]. \tag{1.4}$$

A pictorial representation of this Hamiltonian is given in Fig. 1.1(b), and its ground-state phase diagram is shown in Fig. 1.3. When $|\lambda_z| \gg |\lambda_{xy}|$ the system exhibits classical Néel and stripe Néel (SN) ordering. These two phases spontaneously break the $\mathbb{Z}_2$ symmetry associated with the π rotation

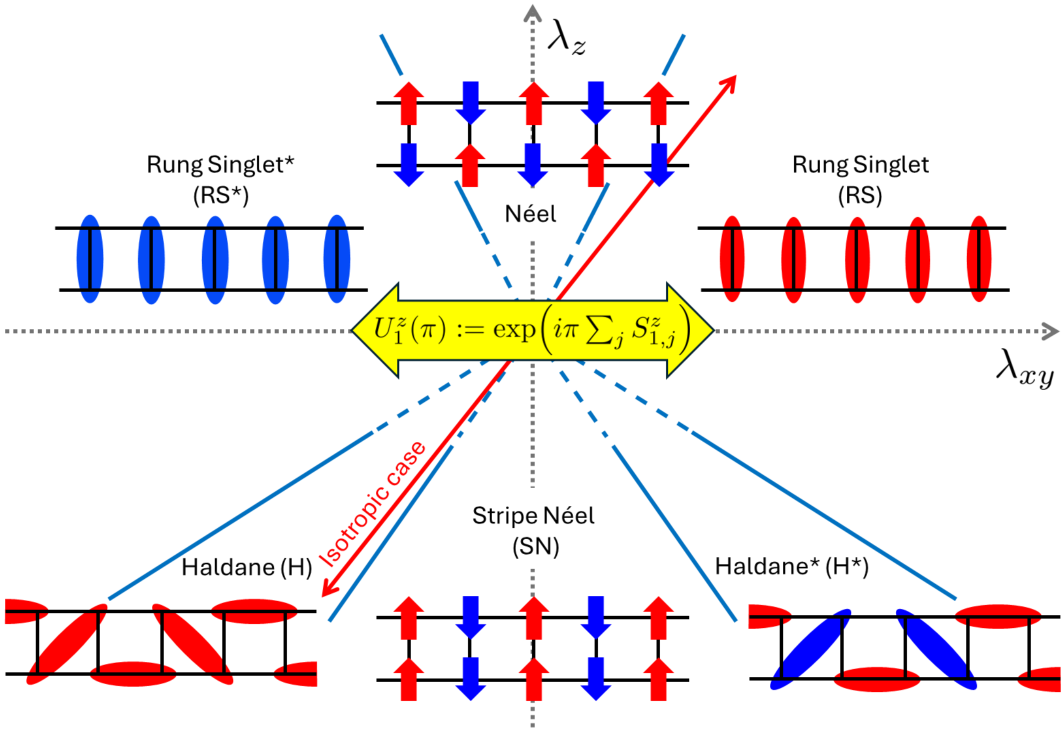

FIGURE 1.3: Schematic ground-state phase diagram of the anisotropic Heisenberg ladder (1.4) in the λ_z-λ_{xy} plane for $J = 1$. Red and blue ovals represent the singlet $|s\rangle$ and triplet $|t_z\rangle$ states in Eq. (1.2), respectively, while red and blue arrows represent the spin-up and spin-down states, respectively. Close to the λ_z-axis, where the easy-axis interaction is dominant, classical Néel or stripe Néel (SN) order appears. Along the double-headed red arrow defined by $\lambda_z = \lambda_{xy}$, the ground-state phase diagram of the isotropic ladder (1.1) in Fig. 1.2 can be observed. The phase boundaries are symmetric about the λ_z-axis. The $U_1^\alpha(\pi)$ unitary transformation defined in Eq. (1.6) with $\alpha = z$ relates the right side to the left side of the phase diagram. In particular, the RS and Haldane phases are mapped respectively to the RS* and Haldane* phases under $U_1^z(\pi)$. See also Fig. 1 in Ref. [145] for numerical results.

of spins about the x-axis and can be detected using the following order operators:

$$\mathcal{O}_{\text{Néel}}(j) := \frac{1}{4}\Big(S^z_{1,j} - S^z_{2,j} - S^z_{1,j+1} + S^z_{2,j+1}\Big), \tag{1.5a}$$

$$\mathcal{O}_{\text{SN}}(j) := \frac{1}{4}\Big(S^z_{1,j} + S^z_{2,j} - S^z_{1,j+1} - S^z_{2,j+1}\Big). \tag{1.5b}$$

For the isotropic model, where $\lambda_z = \lambda_{xy}$, the system can be in either the Haldane phase or the rung singlet phase.

Let $U^\alpha_1(\pi)$ be the local unitary transformation defined by

$$U^\alpha_1(\pi) := \exp\left(i\pi \sum_j S^\alpha_{1,j}\right). \tag{1.6}$$

This transformation corresponds to the π rotation of spins on the first leg around the α-axis. Under this transformation, inter-leg singlet dimers $|s\rangle$ are turned into $|t_\alpha\rangle$ dimers, while intra-leg singlet dimers remain unchanged. In particular, under $U^z_1(\pi)$, the RS and Haldane phases are transformed into the rung singlet* (RS*) and Haldane* phases, respectively. The Haldane and Haldane* phases were referred to as the "t_0" and "t_z" phases in Ref. [145]; we choose the designations "Haldane" and "Haldane*" to refer to these phases, as in Refs. [63, 193, 194]. Likewise, under $U^x_1(\pi)$ or $U^y_1(\pi)$, the t_0 (Haldane) phase is transformed into the t_x or t_y phase.

Like their isotropic counterparts, both the Haldane* and RS* phases are featureless. While the RS* phase is trivial in the SPT sense, the Haldane* phase is non-trivial.[3] The topological nature of the Haldane-like phases can be detected using string order parameters or by examining the degeneracy of the entanglement spectrum. However, these tools do not differentiate between different t_α phases, and therefore a more precise characterization using topological indices is necessary. Experimentally, the t_α phase can be distinguished from the Haldane phase by applying an external magnetic field to the ladder's edges. In the t_α phase, the degeneracy of the spin-$\frac{1}{2}$ edge state can only be split by a field in the α-direction, in contrast to the Haldane phase, where a field in any direction lifts the degeneracy.

Within the model (1.4), the existence of the Haldane* phase depends on strong anisotropy [62, 63, 145, 148], with the in-plane and out-of-plane interactions having opposite signs as shown in Fig. 1.3. Achieving these conditions in real materials may, however, be challenging.

1.3.2 Spin-$\frac{1}{2}$ ladder with multi-spin interaction

Another potential approach for discovering other SPT phases involves extending the Heisenberg ladder to include multi-spin interactions. This direction has been explored by Ogino *et al.* in Ref. [192, 194]. In these studies, the interplay between inter-leg dimer-dimer interactions (DDI) [16, 89, 106, 141, 180, 203, 220, 246] and anisotropy was investigated. DDI models are relevant

[3]The t_x and t_y phases are also non-trivial.

for phonon-mediated interactions [180, 204] and spin-orbital systems [106, 141, 203], and they also share some similarities with ring-exchange models.

The Hamiltonian of an anisotropic spin-$\frac{1}{2}$ ladder with DDI is given by

$$H_{\text{XXZ-DDI}} = J \sum_{n=1}^{2} \sum_{j} \boldsymbol{S}_{n,j} \cdot \boldsymbol{S}_{n,j+1} + J_{\perp} \sum_{j} \left(\boldsymbol{S}_{1,j} \cdot \boldsymbol{S}_{2,j} \right)_{\Delta} + J_{\text{LL}} H_{\text{LL}} \,, \tag{1.7}$$

where

$$\left(\boldsymbol{S}_{n,i} \cdot \boldsymbol{S}_{m,j} \right)_{\Delta} := S^x_{n,i} S^x_{m,j} + S^y_{n,i} S^y_{m,j} + \Delta S^z_{n,i} S^z_{m,j}, \tag{1.8}$$

$$H_{\text{LL}} = \sum_{j} \left(\boldsymbol{S}_{1,j} \cdot \boldsymbol{S}_{1,j+1} \right) \left(\boldsymbol{S}_{2,j} \cdot \boldsymbol{S}_{2,j+1} \right). \tag{1.9}$$

The phase diagram of this model can be investigated for weak interchain couplings ($|J_{\perp}|, |J_{\text{LL}}| \ll J$) [173, 180, 220, 246] by means of a field-theoretical analysis. The expected phase diagram for isotropic rung interaction is shown in Fig. 1.5. The phase diagram is composed of the featureless Haldane and RS phases [17, 230, 238, 239, 274], along with two dimer-ordered phases [27, 28, 89, 92, 180, 192, 194, 215, 220, 246]. The emergence of dimer order can be understood intuitively as follows. In regions dominated by the DDI, dimers spontaneously form along the legs, breaking the translational symmetry. Large positive J_{LL} induces some repulsion among the dimers, leading to a staggered dimer (SD) order. Likewise, large negative J_{LL} induces attraction, leading to a columnar dimer (CD) order. These two dimer orders can be identified using the following order operators:

$$\mathcal{O}_{\text{SD}}(j) := \frac{1}{4} \left(\boldsymbol{S}_{1,j-1} \cdot \boldsymbol{S}_{1,j} - \boldsymbol{S}_{2,j-1} \cdot \boldsymbol{S}_{2,j} - \boldsymbol{S}_{1,j} \cdot \boldsymbol{S}_{1,j+1} + \boldsymbol{S}_{2,j} \cdot \boldsymbol{S}_{2,j+1} \right), \tag{1.10a}$$

$$\mathcal{O}_{\text{CD}}(j) := \frac{1}{4} \left(\boldsymbol{S}_{1,j-1} \cdot \boldsymbol{S}_{1,j} + \boldsymbol{S}_{2,j-1} \cdot \boldsymbol{S}_{2,j} - \boldsymbol{S}_{1,j} \cdot \boldsymbol{S}_{1,j+1} - \boldsymbol{S}_{2,j} \cdot \boldsymbol{S}_{2,j+1} \right). \tag{1.10b}$$

These four phases are separated by two transition lines. One is described by Ising conformal field theory (CFT) with central charge $c = 1/2$ while the other by the $\text{SU}(2)_2$ Wess-Zumino-Witten theory with $c = 3/2$; for the latter, the possibility of a first-order transition is not excluded. Exact diagonalization results are consistent with the $c = 3/2$ scenario for certain parameter ranges [89–91]. In the presence of weak XXZ anisotropy [192, 194], the $c = 3/2$ transition line splits into Gaussian ($c = 1$) and Ising transition lines, as shown in Fig 1.5 (b,c). Between those transition lines, for easy-axis anisotropy, classical Néel or SN order appears depending on the sign of $J_{\perp}$. For easy-plane anisotropy, either the RS* or Haldane* phase appears. Therefore, four-spin interaction can help to stabilize highly anisotropic SPT phases in the vicinity of the isotropic case, opening the gate to possible material realization.[4] This raises an important question: can other multi-spin interactions stabilize additional SPT phases?

[4] The Haldane* phase appearing in the presence of strong anisotropy and the Haldane* phase stabilized by DDI are continuously connected. This will be explained in more detail in Sec. 3.3.1 when discussing the effective field theory or in Appendix B.2

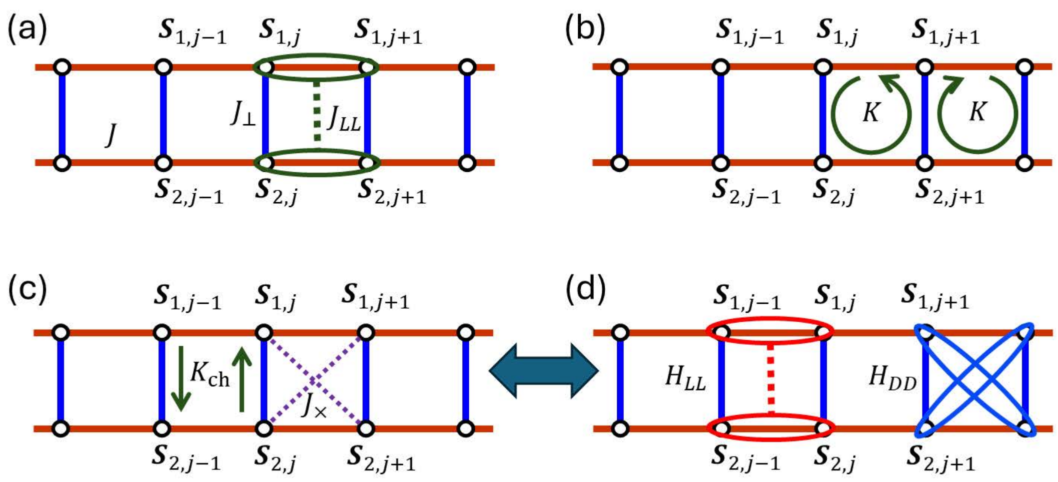

FIGURE 1.4: Spin-$\frac{1}{2}$ ladders with four-spin interactions. (a) The model with the DDI is described by the Hamiltonian (1.7). (b) The model with the four-spin ring exchange interaction is described by the Hamiltonian (1.13). (c) The model with the CCI is described by the Hamiltonian (1.18). Extra diagonal Heisenberg interaction terms ($J_\times$) can be added to this model for the convenience of a theoretical analysis. (d) The CCI can be rewritten as a combination of a leg DDI and a diagonal DDI, as described in Eq. (1.20).

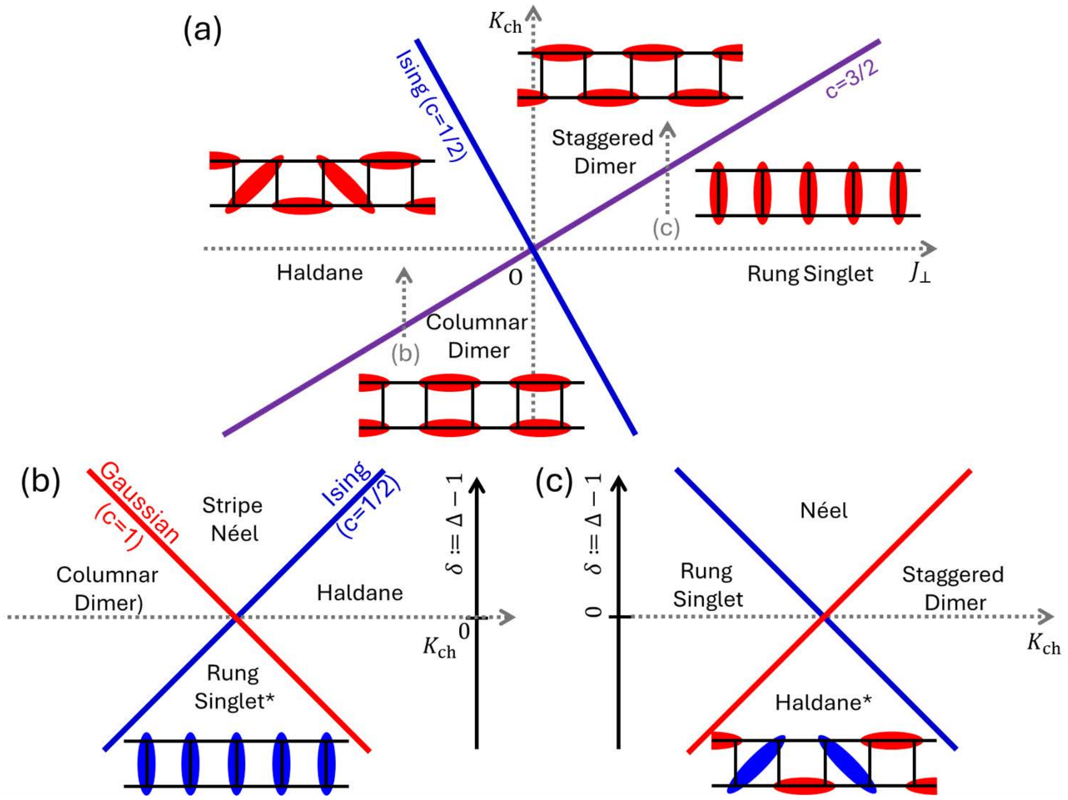

FIGURE 1.5: (a) Schematic ground-state phase diagram of the Heisenberg ladder with DDI in Eq. (1.7), obtained by a field-theoretical analysis for weak interchain couplings [16, 89, 106, 141, 180, 192, 194, 203, 220, 246]. The model with ring exchange interaction in Eq. (1.13) is also expected to have a similar phase structure in this limit. (b,c) Phase diagrams in the presence of anisotropy $\Delta \neq 1$ along the two dashed arrows in (a). Redrawn from Fig. 13 in Ref. [246] and from Figs. 1 and 2 in Ref. [194].

1.4 Spin-chirality interplay in a ladder with four-spin ring exchange

In the context of this Ph.D. thesis, we considered the possibility of using ring-exchange interactions to stabilize other SPT phases. Let us consider a ladder with the four-spin ring exchange defined as follows:

$$\begin{aligned} H_{\text{XXZ-}K} =& J\sum_{n=1}^{2}\sum_{j} \boldsymbol{S}_{n,j}\cdot\boldsymbol{S}_{n,j+1} + J_{\perp}\sum_{j}\left(\boldsymbol{S}_{1,j}\cdot\boldsymbol{S}_{2,j}\right)_{\Delta} \\ &+ K\sum_{j}\Big[P_4(j,j+1)+P_4^{-1}(j,j+1)\Big], \end{aligned} \tag{1.11}$$

where the last term is the ring-exchange term. Under the action of the ring exchange, the spin configuration of a plaquette is transformed as follows (see Fig. 1.4(b) for a pictorial representation):

$$\begin{aligned} &\Big(P_4(j,j+1)+P_4^{-1}(j,j+1)\Big)\begin{vmatrix} \sigma_{1,j}^{[1,j]} & \sigma_{1,j+1}^{[1,j+1]} \\ \sigma_{2,j}^{[2,j]} & \sigma_{2,j+1}^{[2,j+1]} \end{matrix}\Big\rangle \\ &= \begin{vmatrix} \sigma_{1,j+1}^{[1,j]} & \sigma_{2,j+1}^{[1,j+1]} \\ \sigma_{1,j}^{[2,j]} & \sigma_{2,j}^{[2,j+1]} \end{matrix}\Big\rangle + \begin{vmatrix} \sigma_{2,j}^{[1,j]} & \sigma_{1,j}^{[1,j+1]} \\ \sigma_{2,j+1}^{[2,j]} & \sigma_{1,j+1}^{[2,j+1]} \end{matrix}\Big\rangle. \end{aligned} \tag{1.12}$$

The four-spin ring exchange can be rewritten in terms of two-spin and four-spin interactions as

$$\begin{aligned} &P_4(j,j+1)+P_4^{-1}(j,j+1) \\ &:= 4\big(\boldsymbol{S}_{1,j}\times\boldsymbol{S}_{2,j}\big)\cdot\big(\boldsymbol{S}_{1,j+1}\times\boldsymbol{S}_{2,j+1}\big) + P_2(j)P_2(j+1) \\ &\quad+ \big(\boldsymbol{S}_{1,j}+\boldsymbol{S}_{2,j}\big)\cdot\big(\boldsymbol{S}_{1,j+1}+\boldsymbol{S}_{2,j+1}\big), \end{aligned} \tag{1.13}$$

where $P_2(j) := 2\boldsymbol{S}_{1,j}\cdot\boldsymbol{S}_{2,j}+1/2$ is the two-spin exchange on the jth rung.

This interaction emerges in the fourth-order perturbation theory of the Hubbard model, following a similar analysis as in Appendix A.1 [147, 243]. The coupling constant K is then proportional to t^4/U^3. The ring exchange has been studied for its effects on excitation spectra in cuprate layers [35, 37, 147, 221] and ladders [22, 151]. In these cuprate systems, the four-spin exchange coupling is generally estimated to be an order of magnitude weaker than the Heisenberg two-spin exchange couplings, rendering its effects largely perturbative. For example, neutron scattering experiments in Cu_2O_3 ladders reported a ring-exchange interaction value of $K = 0.075J$ [151]. This ratio is consistent with the prediction made with exact diagonalization calculation [164] in Cu_2O_3 ladder. In materials with CuO_2 layers like La_2CuO_4, an optical absorption experiment measured values of around $K = 1.5J$. However, multiple-spin exchanges are thought to play a more prominent role in solid ^{3}He [222] and Wigner crystals [122, 240]. In particular, for the second layer of ^{3}He on graphite, it has been proposed that multi-spin exchanges involving up to six spins are comparable in strength and may drive the spin-liquid behavior observed experimentally [65, 105, 150, 160, 161].

The ground-state phase diagram of a spin-$\frac{1}{2}$ ladder with ring exchange interaction has been extensively studied using powerful field-theoretical methods [25, 76, 157, 173, 253] and numerical approaches [25, 90, 91, 95, 132, 173]. For weak interchain couplings ($|J_\perp|, |K| \ll J$), the phase structure of the ring-exchange model closely resembles that of the DDI model, as illustrated in Fig. 1.5(a). Figure 1.6 presents the ground-state phase diagram of the Heisenberg ladder with ring exchange, defined in Eq. (1.13), for positive $J_\perp$ and K beyond the weak interchain coupling limit. This phase structure can be partly understood via spin-chirality duality $\mathcal{U}$ [76, 81, 95, 97, 137, 138, 168, 253]. Historically, Hikihara *et al.* [95] introduced the spin-chirality duality $\mathcal{U}$, establishing a connection between the weak and strong ring exchange regimes in the phase diagram of the J-$J_\perp$-K ladder with $J, K > 0$. Subsequently, the duality under $\mathcal{U}$ was extended by introducing another duality transformation $\mathcal{U}_\mathrm{s}$ in Ref. [97] to explore the regime where $JK < 0$. Both dualities, $\mathcal{U}$ and $\mathcal{U}_\mathrm{s}$, will be utilized throughout this dissertation. Under these transformations, the antisymmetric combination of spins on each rung, $\boldsymbol{S}_{1,j-1} - \boldsymbol{S}_{2,j-1}$, is mapped to a vector operator on the respective rung, as described by the following equations:

$$\mathcal{U}\left(S^\alpha_{1,j} - S^\alpha_{2,j}\right)\mathcal{U}^\dagger = -2\left(\boldsymbol{S}_{1,j} \times \boldsymbol{S}_{2,j}\right)^\alpha, \tag{1.14a}$$

$$\mathcal{U}_\mathrm{s}\left(S^\alpha_{1,j} - S^\alpha_{2,j}\right)\mathcal{U}_\mathrm{s}^\dagger = -2(-1)^j\left(\boldsymbol{S}_{1,j} \times \boldsymbol{S}_{2,j}\right)^\alpha. \tag{1.14b}$$

The symmetric combination, $\boldsymbol{S}_{1,j-1} - \boldsymbol{S}_{2,j-1}$, remains unchanged. As a result, under $\mathcal{U}$ and $\mathcal{U}_\mathrm{s}$, the Néel order is mapped to the staggered vector chiral (SVC) order and the uniform vector chiral (UVC) order, respectively. The expressions of their order operators are given by

$$\mathcal{O}_\mathrm{SVC}(j) = \frac{1}{2}\left(\boldsymbol{S}_{1,j} \times \boldsymbol{S}_{2,j} - \boldsymbol{S}_{1,j+1} \times \boldsymbol{S}_{2,j+1}\right)^z, \tag{1.15a}$$

$$\mathcal{O}_\mathrm{UVC}(j) = \frac{1}{2}\left(\boldsymbol{S}_{1,j} \times \boldsymbol{S}_{2,j} + \boldsymbol{S}_{1,j+1} \times \boldsymbol{S}_{2,j+1}\right)^z. \tag{1.15b}$$

In Fig. 1.6 the RS phase at small K exhibits dominant Néel correlations, while the RS phase at large K is characterized by dominant SVC correlations. For large $J_\perp$, these two RS phases are connected, as shown later in Fig. 3.3. Similarly, under $\mathcal{U}$ the SD order is mapped to the scalar chiral (SC) order which can be identified by the following order operator:

$$\begin{aligned}\mathcal{O}_\mathrm{SC}(j) := \frac{1}{4}\Big(&\left(\boldsymbol{S}_{1,j-1} + \boldsymbol{S}_{2,j-1}\right)\cdot\left(\boldsymbol{S}_{1,j} \times \boldsymbol{S}_{2,j}\right) + \left(\boldsymbol{S}_{1,j-1} \times \boldsymbol{S}_{2,j-1}\right)\cdot\left(\boldsymbol{S}_{1,j} + \boldsymbol{S}_{2,j}\right)\\ &-\left(\boldsymbol{S}_{1,j} + \boldsymbol{S}_{2,j}\right)\cdot\left(\boldsymbol{S}_{1,j+1} \times \boldsymbol{S}_{2,j+1}\right) - \left(\boldsymbol{S}_{1,j} \times \boldsymbol{S}_{2,j}\right)\cdot\left(\boldsymbol{S}_{1,j+1} + \boldsymbol{S}_{2,j+1}\right)\Big).\end{aligned} \tag{1.16}$$

A field-theoretical analysis around a SU(4) quantum multicritical point[5] [137, 138] reveals that the SD-SC transition at $K = J/2$ falls within the $c = 1$

[5]The ring exchange and the CCI models are the nearest to the SU(4) multicritical point for $\Delta = 1$ and $K_\mathrm{ch}, K = J/2$.

Gaussian universality class. In addition to these findings, VC order

$$\mathcal{V}(i,j) := (\boldsymbol{S}_i \times \boldsymbol{S}_j) , \tag{1.17}$$

has been identified on the square lattice [133, 260], and the possibility of both gapped [39, 160, 161] and gapless [144, 171] quantum spin liquids has been discussed on the triangular lattice.

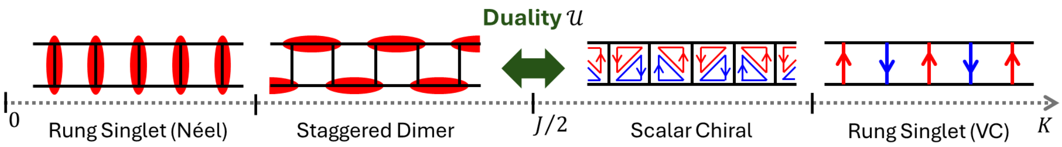

FIGURE 1.6: Schematic phase diagram of the ground state of the Heisenberg ladder with four-spin ring exchange with $J_\perp = J$ as defined in Eq. (1.11). As the exchange interaction K increases, the RS, SD, SC, and RS phases emerge [25, 66, 67, 76, 90, 91, 95, 132, 157, 173, 253]. Phases on either side of the $K = J/2$ point are related by spin-chirality duality. Namely, the SC order is dual to the SD order while the dominant VC correlation in the RS phases for large K is dual to the dominant Néel correlations for small K. See also Fig. 1 in Ref. [132] for numerical results.

While the phase structure in the weak interchain coupling limit is theoretically well understood, analyzing models with strong ring exchange interactions remains challenging, requiring either numerical approaches or perturbative methods around highly symmetric points (like the SU(4) quantum multicritical point). Given that strong four-spin interactions stabilize exotic SC order, introducing anisotropy in the interactions could potentially yield novel SPT phases within this regime. Thus, an analytical understanding of the strong ring exchange limit is essential, and spin-chirality duality offers a promising framework for such an exploration.

1.5 Chirality-chirality interaction

In this dissertation, the interplay between four-spin interaction and XXZ anisotropy in a spin-$\frac{1}{2}$ two-leg ladder will be investigated through a simplification of the ring-exchange model called chirality-chirality interaction (CCI) model, given by

$$H_{\text{XXZ-CCI}} := J \sum_{n=1}^{2} \sum_{j} \boldsymbol{S}_{n,j} \cdot \boldsymbol{S}_{n,j+1} + J_\perp \sum_{j} (\boldsymbol{S}_{1,j} \cdot \boldsymbol{S}_{2,j})_\Delta + K_{\text{ch}} H_{\text{ch}} , \tag{1.18}$$

where

$$H_{\text{ch}} = \sum_{j} 4(\boldsymbol{S}_{1,j} \times \boldsymbol{S}_{2,j}) \cdot (\boldsymbol{S}_{1,j+1} \times \boldsymbol{S}_{2,j+1}). \tag{1.19}$$

Hereafter, we refer to this model as the XXZ-CCI ladder. Unless otherwise specified, J is set to 1 as the energy unit in numerical results. The CCI (1.19) is closely related to the four-spin ring exchange interaction. As seen from its expression given in Eq. (1.13), the ring exchange interaction contains the CCI as its first term. While the four-spin ring exchange naturally has a positive coupling constant $K > 0$ [147, 243], the CCI that arises as a phonon-mediated interaction in multiferroics [69, 195] may have a negative coupling constant $K_{\mathrm{ch}} < 0$. More details about the role of phonon in the emergence of the CCI are provided in Appendix A.3.

The CCI is also closely related to the DDI (1.9) [16, 27, 28, 89, 92, 106, 180, 192, 194, 203, 215, 220, 246]. Indeed the CCI can also be written as

$$H_{\mathrm{ch}} = 4H_{\mathrm{LL}} - 4H_{\mathrm{DD}} \tag{1.20}$$

with

$$H_{\mathrm{LL}} = \sum_j \left(\mathbf{S}_{1,j} \cdot \mathbf{S}_{1,j+1}\right)\left(\mathbf{S}_{2,j} \cdot \mathbf{S}_{2,j+1}\right), \tag{1.21a}$$

$$H_{\mathrm{DD}} = \sum_j \left(\mathbf{S}_{1,j} \cdot \mathbf{S}_{2,j+1}\right)\left(\mathbf{S}_{2,j} \cdot \mathbf{S}_{1,j+1}\right). \tag{1.21b}$$

A pictorial representation is given in Fig. 1.4(c,d). According to field-theoretical analyses for weak interchain couplings [157, 173], the second term $-4H_{\mathrm{DD}}$ only gives a small modification to the effect of the first term $4H_{\mathrm{LL}}$; see Appendix B.1 for more details. Therefore it is expected that in the weak-interchain coupling regime, models with ring exchanges, CCIs, and DDIs are qualitatively the same. Differences only appear in the strong four-spin interaction regime. In this regime, inter-leg DDIs induce a gapless phase [2, 3, 16, 106, 141, 203] in the isotropic case, while the ring exchanges or CCIs are expected to induce gapped phases with chirality-related order or correlation as seen in Fig. 1.6.

The CCI presents several advantages over the ring-exchange model in theoretical investigation. Firstly, as it emphasizes the CCI part of the ring exchange interaction, it helps to stabilize chirality-related phases in numerical simulations. More importantly, the effect of spin-chirality duality is simpler to analyze in the CCI model; this will enable us to use results obtained from effective field theory in the weak interchain regime to gain information on the strong interchain coupling regime.

To highlight the model's duality transformation, it is useful to extend the model (1.18) by adding diagonal exchange couplings (see Fig. 1.4(a)) as

$$H_{\mathrm{ex}} := H_{\mathrm{XXZ\text{-}CCI}} + J_{\times} \sum_j \left(\mathbf{S}_{1,j} \cdot \mathbf{S}_{2,j+1} + \mathbf{S}_{2,j} \cdot \mathbf{S}_{1,j+1}\right). \tag{1.22}$$

Although $J_{\times}$ will be set to 0 at the end of the analysis when drawing ground-state phase diagrams, it aids in the intermediate analysis.

By rewriting the Hamiltonian (1.22) of the J-$J_{\perp}$-$J_{\times}$-K_{ch} ladder as below [137, 253], the effect of the duality transformation can be discussed more easily:

$$H_{\mathrm{ex}} = \frac{J + J_{\times}}{2} H_1 + \frac{J - J_{\times}}{2} H_2 + K_{\mathrm{ch}} H_{\mathrm{ch}} + J_{\perp} \sum_j \mathbf{S}_{1,j} \cdot \mathbf{S}_{2,j}. \tag{1.23}$$

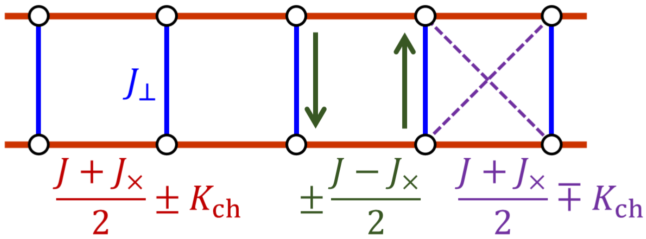

FIGURE 1.7: Models that result from the duality transformation (1.14) of the J-$J_\perp$-$J_\times$-K_{ch} ladder (1.22) in Fig. 1.4(c). The upper and lower signs correspond to the cases of $\mathcal{U}$ and $\mathcal{U}_{\mathrm{s}}$, respectively; see Eqs. (1.23) and (1.25) for the transformation rules. Reproduced from Fig. 5 of Ref. [55]. Copyright 2024 by the Physical Society of Japan.

with

$$H_1 = \sum_j \left(\boldsymbol{S}_{1,j} + \boldsymbol{S}_{2,j}\right) \cdot \left(\boldsymbol{S}_{1,j+1} + \boldsymbol{S}_{2,j+1}\right), \tag{1.24a}$$

$$H_2 = \sum_j \left(\boldsymbol{S}_{1,j} - \boldsymbol{S}_{2,j}\right) \cdot \left(\boldsymbol{S}_{1,j+1} - \boldsymbol{S}_{2,j+1}\right). \tag{1.24b}$$

The duality transformation of the Hamiltonian amounts to the simple exchange of the coupling constants,

$$\frac{J-J_\times}{2} \leftrightarrow \pm K_{\mathrm{ch}}. \tag{1.25}$$

Here $+$ $(-)$ sign corresponds to $\mathcal{U}$ $(\mathcal{U}_{\mathrm{s}})$. The other coupling constants $(J + J_\times)/2$ and $J_\perp$ in Eq. (1.23) remain unchanged by the transformation. The effect of the transformation on the extended model in Eq. (1.22) is summed up in Fig. 1.7.

1.6 Purpose of the dissertation

The objectives of this dissertation are twofold, centering on the exploration of the ground-state phase diagram of an anisotropic spin-$\frac{1}{2}$ XXZ ladder with chirality-chirality interaction.

Firstly, the CCI model is of significant interest for understanding the ground-state phase diagram of the ring-exchange model. We hypothesize that the CCI model is sufficient to capture the physics of the ring-exchange model qualitatively. Its simplified structure allows for an analytical approach beyond the limitations of perturbation theory. Such theoretical analysis will clarify the role of spin-chirality dualities on the phase diagram, potentially offering a rigorous foundation for interpreting previous numerical studies of the ring-exchange model.

Secondly, we propose that anisotropy in the model further enriches the phase structure, especially for strong four-spin interactions, potentially revealing a new SPT phase. This hypothetical SPT phase could arise near the isotropic line, making experimental realization more practical. Additionally, it is intriguing to explore the nature of the system near the self-dual line $K = J/2$, particularly in the presence of strong anisotropy, extending our knowledge beyond the perturbative approach around the SU(4)-symmetric point.

1.7 Outline of the dissertation

Chapter 2 provides background knowledge on quantum spin systems, covering key concepts about the definition of phases. This includes the interplay between long-range order and symmetry breaking related to conventional phases, as well as the concept of SPT phases in one-dimensional systems and their classification. This chapter also introduces matrix product states (MPS) and their application for numerical simulation. In Chapter 3, effective field theory and the spin-chirality duality are employed to examine the phase structure of the CCI model (1.5) in both isotropic and anisotropic cases. As the regime near the self-dual line at $K = J/2$ lies outside the range of validity of the effective field methods, it will be studied in greater depth in Chapter 4. In this chapter, a spin-1 hard-core bosons approach will be employed to explore the phase structure around this region more thoroughly, particularly illuminating the nature of the SPT phases that emerge in the easy-plane anisotropy regime. Methods employed in Chapter 4 also enable the study of a strong easy-axis anisotropy regime in the whole K_{ch}-$J_{\perp}$ plane. Chapter 5 presents numerical simulations to support the theoretical predictions developed in Chapters 3 and 4. Chapter 6 concludes this dissertation by summarizing its main results and outlining potential directions for future research.

Chapter 2

Symmetry and topology in quantum spin systems

In this chapter, some background information about quantum spin systems will be provided. Most of the content included in this chapter is already well-established knowledge and this chapter is greatly inspired by Hal Tasaki's book "Physics and Mathematics of Quantum Many-body Systems" [250]. This chapter aims to highlight the differences between conventional and symmetry-protected topological (SPT) phases. In Sec. 2.1, a more rigorous definition of quantum spin systems is provided. Then, the interplay between long-range order, spontaneous symmetry breaking (SSB), and low-energy level degeneracy will be explored in Sec. 2.2. We will see that SSB of a continuous symmetry cannot occur in one-dimensional systems, which are characterized by disorder.

The properties of quantum spin Heisenberg chains depend crucially on their spin quantum number S, as conjectured by Haldane and explained in Sec. 2.3. Half-odd-integer (HOI) spin chains are gapless and critical, while integer spin chains are gapped and exhibit numerous topological properties, referred to as the Haldane phenomena. While the ground state of the spin-$\frac{1}{2}$ chain can be determined exactly using the Bethe ansatz, there is no exact solution to describe the ground state of the spin-1 chain. To gain an insight into the low-energy physics of the spin-1 Heisenberg chain, we will analyze a closely related model called the Affleck-Kennedy-Lieb-Tasaki (AKLT) model, whose ground state is given exactly by the valence bond state (VBS) wave function. By analyzing the properties of this wave function in Sec. 2.4, we will explain most of the Haldane phenomena. The role of symmetry in the protection of the topological property of the Haldane chain will be explained heuristically in Sec. 2.5.

A more rigorous definition of the SPT phase requires the introduction of the MPS, that will be done in Sec. 2.6. Using the MPS representation, a more general and carefull definition of the SPT phase, based on the topological index, will be provided in Sec. 2.7. The notion of the SPT phase will also be extended to ladder models. Finally, we will show how the MPS representation can be used advantageously to perform numerical calculations in Sec. 2.8.

2.1 Introduction to quantum spin systems

A spin operator S^α is a self-adjoint operator that acts on a Hilbert space $\mathfrak{h}_0$ of dimension $2S+1$. The spin quantum number S is a fixed number that depends on the microscopic physics. It can take only positive integer or HOI values. One can arrange the S^α operators ($\alpha \in \{x,y,z\}$) into a vector to form the $\boldsymbol{S} = (S^x, S^y, S^z)$ operator. The basis states of $\mathfrak{h}_0$ are $|\sigma\rangle$, with $\sigma = -S, -S+1, \cdots, S-1, S$ being their S^z eigenvalues.

Let $\{\boldsymbol{S}_j\}$ be a collection of spin operators, all sharing the same quantum spin number S, and each acting on $\mathfrak{h}_j$, a copy of $\mathfrak{h}_0$, whose basis vectors are $\left|\sigma_j^{[j]}\right\rangle$. Each j is associated with the coordinate of a site on a lattice Λ. For example, sites of a spin chain are labeled by j with $j \in \{1, 2, \cdots, L\}$, and those of a spin ladder by (n, j) with $n \in \{1, 2\}$. The spin operators fulfill the following commutation relation:

$$\left[S_i^\alpha, S_j^\beta\right] = i\delta_{ij} \sum_{\gamma=x,y,z} \epsilon_{\alpha\beta\gamma} S_j^\gamma. \tag{2.1}$$

Where, $\delta_{i,j}$ is the Kronecker delta function and $\epsilon_{\alpha\beta\gamma}$ is the Levi-Civita tensor. The spin operators $\boldsymbol{S}_j$ act on the $(2S+1)^{|\Lambda|}$-dimensional Hilbert space

$$\mathscr{H} := \bigotimes_{j\in\Lambda} \mathfrak{h}_j, \tag{2.2}$$

whose basis is composed of the vectors

$$|\boldsymbol{\sigma}\rangle := \bigotimes_{j\in\Lambda} \left|\sigma_j^{[j]}\right\rangle, \quad \boldsymbol{\sigma} = (\sigma_j)_{j\in\Lambda}. \tag{2.3}$$

Let $\boldsymbol{S}_{\text{tot}} := \sum_{j\in\Lambda} \boldsymbol{S}_j$ be the total spin operator. The global spin rotation around the α-axis by an angle θ is given by

$$U_\alpha(\theta) := e^{-i\theta S^\alpha_{\text{tot}}}. \tag{2.4}$$

In this dissertation, U_α without an argument will represent $U_\alpha(\pi)$.

The total Hilbert space $\mathscr{H}$ can be decomposed according to the eigenvalue of $S^z_{\text{tot}} = \sum_{j\in\Lambda} S^z_j$ as

$$\mathscr{H} = \bigotimes_{M=-|\Lambda|S}^{|\Lambda|S} \mathscr{H}_M\,. \tag{2.5}$$

Here, the eigenvalue of S^z_{tot} for any state in $\mathscr{H}_M$ is M.

The Heisenberg Hamiltonian introduced in Eq. (1.1) can be generalized to arbitrary lattices Λ as

$$H_{\text{Heis}} := \sum_{\{i,j\}\in\mathscr{B}} J\big(\boldsymbol{S}_i \cdot \boldsymbol{S}_j\big)_{\Delta=1}\,, \tag{2.6}$$

where $\mathscr{B}$ is the set of bonds in Λ.

The Hamiltonian in Eq. (2.6) commutes with S^{α}_{tot} for $\alpha \in \{x, y, z\}$, making it invariant under any rotation symmetry. In this case, it is said to be SU(2) invariant.

For simplicity, throughout the rest of the chapter, only bipartite lattices that can be colored using two colors, such that for each $\{i, j\} \in \mathscr{B}$, i and j have different colors, will be considered. By using sites in Λ that are colored the same, two sublattices A and B are formed. It is assumed, for simplicity that $|A| = |B|$.[1] Unless otherwise specified, periodic boundary conditions will be assumed.

For $J < 0$, interactions favor the alignment of spins in the same direction. This is a ferromagnetic interaction. The ground states of this Hamiltonian can be easily obtained. Let us consider the "all-up state", defined as

$$|\boldsymbol{\phi}_{\uparrow}\rangle := \bigotimes_{j\in\Lambda} \left| S^{[j]} \right\rangle . \tag{2.7}$$

This state is a simple tensor product of all the spins pointing in the $+z$ direction. This state minimizes each term of the Heisenberg Hamiltonian in Eq. (2.6) when $J < 0$. In this sense, one says that H_{Heis} is frustration-free. Using the SU(2) invariance of the Hamiltonian, the other ground states $|\boldsymbol{\phi}_M\rangle$ can be obtained by acting with $S^{-}_{\text{tot}} = S^{x}_{\text{tot}} + iS^{y}_{\text{tot}}$ on $|\boldsymbol{\phi}_{\uparrow}\rangle$ up to $2|\Lambda|S$ times. The ground state is therefore $2|\Lambda|S + 1$-fold degenerate, as each $|\boldsymbol{\phi}_M\rangle$ belongs to a different $\mathscr{H}_M$. One says that the system is gapless. By taking a suitable linear combination of the different ground states, it is possible to construct a ground state with the spins pointing in an arbitrary direction. Thus, in a ferromagnet, the symmetry breaking is associated with the existence of infinitely many ground states.

The situation is rather different when $J > 0$. Here, the interaction favors states where spins that belong to different sublattices point in different directions; the interaction is antiferromagnetic. Intuitively, one might expect that the Néel states

$$|\boldsymbol{\phi}_{\text{Néel}}\rangle := \left(\bigotimes_{j\in A} \left| S^{[j]} \right\rangle \right) \otimes \left(\bigotimes_{j\in B} \left| -S^{[j]} \right\rangle \right), \tag{2.8}$$

or any state obtained by a solid rotation of $|\boldsymbol{\phi}_{\text{Néel}}\rangle$, to be the ground state. However, $|\boldsymbol{\phi}_{\text{Néel}}\rangle$ is not even an eigenstate of the Heisenberg model in Eq. (2.6). The situation is more complicated and interesting.

The Marshall-Lieb-Mattis (MLM) theorem [142, 149] states: The ground state $|\boldsymbol{\phi}_{\text{GS}}\rangle$ of the Heisenberg Hamiltonian as given in Eq. (2.6) is (i) unique, (ii) has total spin $S_{\text{tot}} = 0$, and (iii) can be expanded in the standard basis as

$$|\boldsymbol{\phi}_{\text{GS}}\rangle = \sum_{(\sigma|\bar{\sigma}=0)} \left[\prod_{j\in B} (-1)^{\sigma_j - S} c_{\sigma} \right] |\sigma\rangle , \tag{2.9}$$

[1] Some of the theorems given below may apply to more general cases.

where $\bar{\sigma} = \sum_{j\in\Lambda} \sigma_j$ and $c_\sigma > 0$. The two-spin correlation function shows clear signs of antiferromagnetic behavior as

$$\langle \boldsymbol{\phi}_{\text{GS}} | \boldsymbol{S}_i \cdot \boldsymbol{S}_j | \boldsymbol{\phi}_{\text{GS}} \rangle \begin{cases} > 0 & \text{if } i \text{ and } j \text{ belong to the same sublattice,} \\ < 0 & \text{if } i \text{ and } j \text{ belong to different sublattices.} \end{cases} \tag{2.10}$$

Note that the uniqueness of the ground state still holds if there is some anisotropy [153, 184] in the interaction, as given in Eq. (1.8), as long as $\Delta > -1$, in this case, the unique ground state satisfies $S^z_{\text{tot}} = 0$. For isotropic exchange interaction, the theorem still holds even if the coupling constant $J_{i,j} = J_{j,i} > 0$ depends on i, j. Unfortunately, the MLM theorem does not provide much more information concerning the nature of the ground state and the low-energy spectra. As we shall observe, there are fundamental differences in the low-energy spectrum depending on S in quantum spin chains and on the dimensionality d of the system.

Finally, before closing this section, the time-reversal symmetry and Kramers degeneracy [130] will be introduced. The time-reversal map of a quantum spin system is defined as

$$U_{\text{TR}} := U_y \hat{K}, \tag{2.11}$$

with $\hat{K}$ being the complex conjugation map. Under U_{TR}, a general state $|\boldsymbol{\phi}\rangle = \sum_\sigma c_\sigma |\boldsymbol{\sigma}\rangle$ transforms as

$$U_{\text{TR}} |\boldsymbol{\phi}\rangle = \sum_\sigma c^*_\sigma |-\boldsymbol{\sigma}\rangle, \tag{2.12}$$

where $-\boldsymbol{\sigma}$ is the spin configuration obtained by inverting the sign of the spin on each site. Let $|\boldsymbol{\phi}\rangle$ be a state defined on a lattice such that $|\Lambda|2S$ is an odd number (e.g., for a single spin-$\frac{1}{2}$). It can be shown that

$$\langle \boldsymbol{\phi} | U_{\text{TR}} | \boldsymbol{\phi} \rangle = 0. \tag{2.13}$$

This implies that the eigenstates are at least doubly degenerate. This is called Kramers degeneracy.

2.2 Long-range order and SSB

In the Landau-Ginzburg-Wilson paradigm, phases of matter can be characterized by local order parameters and classified according to the symmetry of the ground state. Most phases can be classified under this paradigm. The spontaneous breaking of a symmetry of the Hamiltonian by its ground state (SSB) is a fascinating subject with deep implications for the low-energy properties of the system.

2.2.1 Definition of long-range order

In the remainder of this section, Λ_L will denote the d-dimensional hypercubic lattices. These are composed of a set of points j with coordinates $(j_1, j_2, \cdots, j_d)$, with $j_i \in \mathbb{Z}$, $-\frac{L}{2} < j_i \leq \frac{L}{2}$, and a set of bonds

$\mathscr{B}_L = \{\{i,j\} | i,j \in \Lambda_L, |i-j| = 1\}$. One has $|\Lambda_L| = L^d$, and Λ_L is a bipartite lattice that can be decomposed as $\Lambda_L = A \cup B$ with

$$A := \{(j_1, j_2, \cdots, j_d) \in \Lambda_L | \sum_{i=1}^{d} j_i \text{ is even}\}, \tag{2.14a}$$

$$B := \{(j_1, j_2, \cdots, j_d) \in \Lambda_L | \sum_{i=1}^{d} j_i \text{ is odd}\}. \tag{2.14b}$$

One also introduces the sign factor defined as

$$(-1)^j := \begin{cases} 1 & j \in A, \\ -1 & j \in B, \end{cases} \tag{2.15}$$

and the symmetry-breaking order operator as

$$\mathscr{O}_L^{\alpha} := \sum_{j \in \Lambda_L} (-1)^j S_j^{\alpha}. \tag{2.16}$$

This order operator is designed to detect the breakdown of the SU(2) symmetry and the appearance of Néel order. Similar order operators can be defined to detect the breakdown of other symmetries, such as the translation symmetry, as seen in Eqs. (1.5), (1.10), and (1.16).

For $d \geq 2$ and any S, there exists a positive constant q_0 (which depends only on d and S) such that

$$\langle \boldsymbol{\phi}_{\mathrm{GS}} | \left(\frac{\mathscr{O}_L^{\alpha}}{L^d} \right)^2 | \boldsymbol{\phi}_{\mathrm{GS}} \rangle \geq q_0, \tag{2.17}$$

as L goes to infinity. This is the definition of the long-range order. This theorem has been proven exactly [44, 115, 181], except for the case $d = 2$, $S = \frac{1}{2}$, for which no proof exists, but strong numerical evidence supports the existence of long-range ordering [224, 248]. The existence of strictly positive q_0 is a stronger condition than the inequality (2.10), as the inequality (2.10) does not rule out the possibility that the correlation goes to 0 as $|i-j|$ goes to infinity.

2.2.2 Low-lying state

There is an apparent paradox in the existence of long-range order as defined in Eq. (2.17) and the uniqueness of the ground state predicted by the MLM theorem. The uniqueness implies the SU(2)-invariance of the ground state. Therefore, from a symmetry argument, the expectation value of the order operator is null, i.e,

$$\langle \boldsymbol{\phi}_{\mathrm{GS}} | \frac{\mathscr{O}_L^{\alpha}}{L^d} | \boldsymbol{\phi}_{\mathrm{GS}} \rangle = 0, \tag{2.18}$$

which is the absence of SSB. An unusual feature also appears if one calculates the fluctuation of the density of $\mathscr{O}_L^\alpha$ which is given by

$$\lim_{L\to\infty}\sqrt{\langle\boldsymbol{\phi}_{\mathrm{GS}}|\left(\frac{\mathscr{O}_L^\alpha}{L^d}\right)^2|\boldsymbol{\phi}_{\mathrm{GS}}\rangle-\left(\langle\boldsymbol{\phi}_{\mathrm{GS}}|\frac{\mathscr{O}_L^\alpha}{L^d}|\boldsymbol{\phi}_{\mathrm{GS}}\rangle\right)^2}\geq\sqrt{q_0}. \tag{2.19}$$

This inequality shows that $\mathscr{O}_L^\alpha$ violates the law of large numbers[2], indicating that the exact ground state is pathological and not physical.

This inconsistency can be resolved if one considers the existence of $2C_1L^{\frac{1}{2}}$ low-lying, orthogonal states [12, 13, 102, 127, 128, 242, 249]. The existence of these low-energy states relies on the presence of continuous symmetry of the Hamiltonian. Each of these states lies in a different $\mathscr{H}_M$ with $|M|\leq C_1L^{\frac{1}{2}}$. This implies the existence of $2C_1L^{\frac{1}{2}}$ energy eigenstates $|\boldsymbol{\phi}_M\rangle\in\mathscr{H}_M$ whose energies satisfy

$$E_{\mathrm{GS}}<E_{\mathrm{M}}\leq E_{\mathrm{GS}}+C_2\frac{M^2}{L^d}, \tag{2.20}$$

with $C_{1,2}$ being two constants independent of M and L. By taking a suitable linear combination of these low-lying energy eigenstates, it is possible to construct a "physical ground state" that exhibits SSB in any direction and thus fulfills the law of large numbers.

Before closing this section, it is important to note that the existence of infinitely many low-lying levels is only relevant for the SSB of a continuous symmetry. Therefore, the spontaneous breaking of a discrete symmetry, like the translation symmetry or D_2 symmetry, can occur in gapped systems where a finite number of low-lying states exist, but an energy gap above them does not vanish in the thermodynamic limit. Throughout this dissertation, we will still use the word "gapped" to describe situations where an energy gap exists above unique or (nearly) degenerate ground states, with a degeneracy that does not depend on the system size.

2.2.3 Absence of continuous SSB in one-dimensional systems

For one-dimensional systems with continuous symmetry, the Mermin-Wagner theorem directly implies the absence of long-range order even at zero temperature due to the divergence of quantum fluctuations [156].

As an example, consider a Heisenberg chain with SU(2) symmetry. The emergence of Néel order would imply the spontaneous breaking of this symmetry. To trigger this symmetry breaking, one can introduce a fictitious external staggered magnetic field. The system is then described by the following Hamiltonian:

$$\hat{H}_h=\sum_{j=1}^{L}\boldsymbol{S}_j\cdot\boldsymbol{S}_{j+1}-(-1)^jhS_j^z. \tag{2.21}$$

[2] The density of any bulk quantity such as $\frac{\mathscr{O}_L^\alpha}{L^d}$ should have a definite value in the thermodynamic limit.

It has been proven by Shastry [229] that for any value of S, the ground state of the above Hamiltonian satisfies the following relation:

$$\lim_{h\to\infty}\lim_{L\to\infty}\langle\boldsymbol{\phi}_{\mathrm{GS},h}|\frac{\mathscr{O}^z_L}{L}|\boldsymbol{\phi}_{\mathrm{GS},h}\rangle = 0, \tag{2.22}$$

where $|\boldsymbol{\phi}_{\mathrm{GS},h}\rangle$ is the ground state of the Heisenberg model under the fictitious staggered magnetic field, defined in Eq. (2.21). The absence of spontaneous symmetry breaking (SSB) strongly suggests that long-range order cannot emerge in a one-dimensional system in the same favorable condition. By combining Eq. (2.22) with the MLM theorem and the Kaplan–Horsch–von der Linden theorem [242], the absence of magnetic long-range order in one-dimensional antiferromagnetic Heisenberg models can be rigorously proven. This highlights the distinctive nature of the low-energy spectrum of one-dimensional systems, which is characterized by disorder [156, 167, 206, 229], in sharp contrast to the behavior observed in higher-dimensional systems.

2.3 Haldane conjecture

2.3.1 Introduction

In 1983, Haldane published two papers [82, 83] that argued that the low-energy properties of a one-dimensional Heisenberg chain should depend on S.

Half-odd-integer-spin case case

All Heisenberg chains with HOI spin have essentially the same low-energy properties as the spin-$\frac{1}{2}$ chain. The ground state of the latter can be determined exactly using the "Bethe ansatz" method [20], and from this solution and other methods such as bosonization [71, 73]), the following properties concerning the low-energy spectrum and the ground state are believed to be true [129, 241, 244].

HOI.1 The ground state is unique (for finite and infinite chains). The case of a finite chain corresponds to the MLM theorem.

HOI.2 There exists no energy gap above the ground state. Note that the gapless excitations are not Nambu–Goldstone bosons, which are excitation modes relative to ground states with SSB, while spontaneous breaking of continuous symmetry should not occur in one-dimensional systems [74, 178, 261].

HOI.3 The ground state correlation function decays slowly, with an asymptotic behavior given by

$$\langle\boldsymbol{\phi}_{\mathrm{GS}}|\boldsymbol{S}_i\cdot\boldsymbol{S}_j|\boldsymbol{\phi}_{\mathrm{GS}}\rangle \approx (-1)^{i-j}\frac{\sqrt{\log|i-j|}}{|i-j|}, \tag{2.23}$$

for $1 \ll |i-j| \ll L$.

These facts suggest that HOI-spin chains are critical [51, 60, 85, 223] and can be described by an effective massless field theory. [3]

Integer-spin case

Similarly, all Heisenberg chains with integer spin should exhibit essentially the same low-energy properties as the spin-1 chain.

I.1 The ground state is unique (for finite and infinite chains).

I.2 There exists an energy gap above the ground state. This means that there exists a constant $\Delta E(S)$ independent of L such that there is one state with energy $E \leq E_{\mathrm{GS}} + \Delta E(S)$. Here, the gap behaves as $\Delta E(S) \approx 2Se^{-\pi S}$ for $S \gg 1$ [1, 4, 5, 82]. This is consistent with the fact that in the large-S limit, the system should behave like a classical system with degenerate ground states. The presence of a gap in a system with a continuous symmetry implies the absence of SSB, as SSB requires the presence of low-lying states.

I.3 The ground state correlation function decays exponentially as

$$\langle \boldsymbol{\phi}_{\mathrm{GS}} | \boldsymbol{S}_i \cdot \boldsymbol{S}_j | \boldsymbol{\phi}_{\mathrm{GS}} \rangle \approx (-1)^{i-j} \frac{\exp[-\frac{|i-j|}{\xi}]}{|i-j|^{\frac{1}{2}}}, \tag{2.24}$$

where ξ is the correlation length.

These facts suggest that the effective field theory of integer-spin chains should be massive. The Haldane conjecture for integer spin has been confirmed experimentally [21, 182, 202] and numerically [23, 75, 237].

2.3.2 Discussion on the difference between integer and half-odd-integer spins

In this section, several arguments will be given to explain that there should be a fundamental difference between the integer- and HOI-spin systems.

In Sec. 2.1, Kramers degeneracy has already been mentioned. However, Kramers degeneracy only appears in finite systems with an odd number of sites and the argument does not apply to infinite chains.

Another strong argument in favor of a difference is the Lieb-Schultz-Mattis theorem [6, 143, 252]. The proof of this theorem is famous and quite enlightening. Suppose that a Hamiltonian and its ground state $|\boldsymbol{\phi}_{\mathrm{GS}}\rangle$ are invariant under the U(1) rotation around the z-axis and the translation symmetry, and that $|\boldsymbol{\phi}_{\mathrm{GS}}\rangle \in \mathscr{H}_0$. That is, under a translation by one lattice site, one has $\hat{T}\,|\boldsymbol{\phi}_{\mathrm{GS}}\rangle = e^{i\alpha}\,|\boldsymbol{\phi}_{\mathrm{GS}}\rangle$, where $\hat{T}$ is the standard translation unitary operator, and $|\boldsymbol{\phi}_{\mathrm{GS}}\rangle$ is the ground state of a spin-S chain of length L with periodic boundary conditions $(L + j \equiv j)$. Under the rotation around the z-axis defined in Eq. (2.4), the ground state transforms as

$$U_z(\theta)\,|\boldsymbol{\phi}_{\mathrm{GS}}\rangle = |\boldsymbol{\phi}_{\mathrm{GS}}\rangle\,. \tag{2.25}$$

[3] See the bosonization of a spin-$\frac{1}{2}$ ladder in the Sec. 3.1.

Here, the fact that $|\phi_{\text{GS}}\rangle$ belongs to $\mathscr{H}_0$ has been used.

Now, let us introduce the "twist" operator

$$\hat{U}_{\text{LSM}} := \exp\left(-i\sum_j \theta_j S_j^z\right), \tag{2.26}$$

with $\theta_j = \frac{2\pi j}{L}$. This operator introduces a gradual modification of the ground state across the chain. Since the ground state is invariant under a global rotation ($\theta_j = \theta$), it is expected that the state $|\phi_{\text{LSM}}\rangle \equiv \hat{U}_{\text{LSM}}|\phi_{\text{GS}}\rangle$ is close in energy to the ground state $|\phi_{\text{GS}}\rangle$. Suppose that the Hamiltonian is in the form

$$\hat{H} = \sum_{j=1}^{L} \hat{h}_j, \tag{2.27}$$

where $\hat{h}_j$ is a local Hamiltonian that acts on a finite number of sites, is bounded by a constant h_0, and is invariant under $U_z(\theta)$.[4] Then, there exists a constant C, independent of L, such that [252]

$$\langle\phi_{\text{LSM}}|H|\phi_{\text{LSM}}\rangle - E_{\text{GS}} \leq \frac{C}{L}. \tag{2.28}$$

Thus $|\phi_{\text{LSM}}\rangle$ is a low-energy state. However, $|\phi_{\text{LSM}}\rangle$ may be nothing more than $|\phi_{\text{GS}}\rangle$. This possibility can be ruled out by calculating the inner product $\langle\phi_{\text{GS}}|\phi_{\text{LSM}}\rangle$ as

$$\begin{aligned}
\langle\phi_{\text{GS}}|\phi_{\text{LSM}}\rangle &= \langle\phi_{\text{GS}}|\hat{U}_{\text{LSM}}|\phi_{\text{GS}}\rangle, && (2.29a)\\
&= \langle\phi_{\text{GS}}|\hat{T}^\dagger\hat{U}_{\text{LSM}}\hat{T}|\phi_{\text{GS}}\rangle, && (2.29b)\\
&= \langle\phi_{\text{GS}}|e^{i2\pi S_L^z}\hat{U}_{\text{LSM}}e^{-i\frac{2\pi}{L}S_{\text{tot}}^z}|\phi_{\text{GS}}\rangle, && (2.29c)\\
&= (-1)^{2S}\langle\phi_{\text{GS}}|\phi_{\text{LSM}}\rangle, && (2.29d)
\end{aligned}$$

where we used $e^{-i2\pi S_L^z}|\phi_{\text{GS}}\rangle = (-1)^{2S}|\phi_{\text{GS}}\rangle$. For HOI S, the above equality indicates that $|\phi_{\text{LSM}}\rangle$ is orthogonal to $|\phi_{\text{GS}}\rangle$, which implies the existence of a low-lying eigenstate.[5] For integer spin, one cannot prove that $|\phi_{\text{LSM}}\rangle$ is different from $|\phi_{\text{GS}}\rangle$. In fact, if the existence of a gap is assumed, then $\langle\phi_{\text{LSM}}|\phi_{\text{GS}}\rangle \to 1$ when $L \to \infty$ can be proven.

Finally, two of the most famous arguments in favor of Haldane's conjecture are the path integral formulation of the spin chain and the effective field theory in terms of a nonlinear sigma model. In the latter, a gapped spectrum is predicted for integer-spin chains while the presence of a topological term complicates the analysis for HOI-spin chains [1, 4, 5, 57, 82–84].

2.3.3 Haldane phenomena

The ground state of the spin-1 chain exhibits exotic properties collectively known as the Haldane phenomena, which are characteristic of topological

[4]This is the case in the Heisenberg Hamiltonian in Eq. (2.6).

[5]$|\phi_{\text{LSM}}\rangle$ is not necessarily the ground state, but the fact that there are two orthogonal states with low-energy, imply that there are necessarily two eigenstates with low energy.

phases in one-dimensional systems.

H.1 While there is no long-range order in the ground state of the Heisenberg chain, non-local correlations exist between spins, known as hidden antiferromagnetism. These correlations can be detected using non-local order parameters [183, 251]. More details on this topic will be presented in the next section.

H.2 The ground state is unique in a system with periodic boundary conditions but becomes nearly degenerate in systems with open boundary conditions [113].

H.3 Low-energy states with effective spin-$\frac{1}{2}$ degrees of freedom at the edges emerge in open Heisenberg chains. These edge states induce a near four-fold degeneracy.

Historically, these phenomena were understood as manifestations of the breaking of a hidden $\mathbb{Z}_2 \times \mathbb{Z}_2$ symmetry [114, 116]. Let U_{KT} be the Kennedy-Tasaki non-local unitary transformation given by[198]

$$U_{\mathrm{KT}} := \prod_{i<j} \exp\left[i\pi S_i^z S_j^x\right]. \tag{2.30}$$

Under this transformation, the Heisenberg Hamiltonian in Eq. (2.6) is transformed into

$$U_{\mathrm{KT}} H U_{\mathrm{KT}}^{\dagger} = \sum_{j=1}^{L} \left\{ -S_j^x S_{j+1}^x - \Delta S_j^z S_{j+1}^z + S_j^y \exp\left[i\pi(S_j^z + S_{j+1}^x)\right] S_{j+1}^y \right\}. \tag{2.31}$$

This transformed Hamiltonian has short-range interactions and is invariant under the $\mathbb{Z}_2 \times \mathbb{Z}_2$ symmetry. The ground state of this Hamiltonian is expected to exhibit ferromagnetic order in either the z or x direction, resulting in four-fold degenerate ground states as $L \to \infty$. Under the U_{KT} transformation, ferromagnetic long-range order in the α direction is mapped to non-local string order in the same direction.[6] However, the hidden $\mathbb{Z}_2 \times \mathbb{Z}_2$ symmetry-breaking picture cannot explain several phenomena, such as the degeneracy of the ground state for systems with integer S larger or equal to 2 [198] or the robustness of the Haldane phase to external magnetic fields [77]. In modern understanding, the Haldane phase is recognized as a non-trivial SPT phase under the $\mathbb{Z}_2 \times \mathbb{Z}_2$ symmetry, the time-reversal symmetry, or the bond-centered inversion symmetry [77, 208, 209] as we shall explain in detail in Sec. 2.5.

2.4 Affleck-Kennedy-Lieb-Tasaki model

In the absence of an exact expression for the ground state of the spin-1 Heisenberg chain, its properties are difficult to predict. To proceed, we will

[6] $U_{\mathrm{KT}} S_i^\alpha S_j^\alpha U_{\mathrm{KT}}^\dagger = S_i^\alpha \exp[i\pi \sum_{k=i+1}^{j-1} S_k^\alpha] S_j^\alpha$

analyze a closely related model. In 1987, Affleck, Kennedy, Lieb, and Tasaki introduced the following spin-1 chain now known as the AKLT model:

$$H_{\text{AKLT}} := \sum_{j=1}^{L} \left\{ \boldsymbol{S}_j \cdot \boldsymbol{S}_{j+1} + \frac{1}{3} (\boldsymbol{S}_j \cdot \boldsymbol{S}_{j+1})^2 \right\}, \tag{2.32}$$

where the factor $\frac{1}{3}$ is finely tuned such that the model is equivalent to

$$H_{\text{AKLT}} = \sum_{j=1}^{L} \left\{ 2\hat{P}_2[\boldsymbol{S}_j + \boldsymbol{S}_{j+1}] - \frac{2}{3} \right\}, \tag{2.33}$$

with $\hat{P}_2[\boldsymbol{S}_j + \boldsymbol{S}_{j+1}]$ being a projection onto the subspace of total spin-2. The ground state and low-energy spectrum of the AKLT model share numerous similarities with those of the antiferromagnetic spin-1 Heisenberg chain [7, 8]. It is now well established that the ground states of both models belong to the same phase, as one can continuously modify the AKLT model into the Heisenberg model without explicitly breaking any symmetry of these two models or closing the gap above the ground state [125, 273].

The ground state of the AKLT model has been determined exactly and is called the valence bond solid (VBS) state. In this section, the VBS state $|\boldsymbol{\phi}_{\text{VBS}}\rangle$ will be constructed step-by-step and some of its most important properties will be explained. If not specified otherwise, periodic boundary conditions will be considered.

Construction of the VBS

The symmetrization operator $\mathscr{S}$ acts on the tensor product of two spins $\left|\sigma_L^{[L]}\right\rangle \left|\sigma_R^{[R]}\right\rangle$ as

$$\mathscr{S} \left|\sigma_L^{[L]}\right\rangle \left|\sigma_R^{[R]}\right\rangle := \frac{1}{2} \left\{ \left|\sigma_L^{[L]}\right\rangle \left|\sigma_R^{[R]}\right\rangle + \left|\sigma_R^{[L]}\right\rangle \left|\sigma_L^{[R]}\right\rangle \right\}. \tag{2.34}$$

The resulting state behaves like a spin-1 under rotation, namely

$$\mathscr{S} \left|\uparrow^{[L]}\right\rangle \left|\uparrow^{[R]}\right\rangle = |+\rangle\,, \tag{2.35a}$$

$$\mathscr{S} \left|\uparrow^{[L]}\right\rangle \left|\downarrow^{[R]}\right\rangle = \mathscr{S} \left|\downarrow^{[L]}\right\rangle \left|\uparrow^{[R]}\right\rangle = \frac{1}{\sqrt{2}} |0\rangle\,, \tag{2.35b}$$

$$\mathscr{S} \left|\downarrow^{[L]}\right\rangle \left|\downarrow^{[R]}\right\rangle = |-\rangle\,. \tag{2.35c}$$

The first step to construct the ground state of Eq. (2.32) is to decompose each site j of the lattice into two sites j, L and j, R and to associate a spin-$\frac{1}{2}$ to each of these sites as shown in Fig. 2.1. Based on elementary considerations about the coupling of angular momenta, the following operator identity can be proved:

$$(\boldsymbol{S}_j + \boldsymbol{S}_{j+1}) \left(\bigotimes_{j=1}^{L} \mathscr{S}_j \right) = \left(\bigotimes_{j=1}^{L} \mathscr{S}_j \right) (\boldsymbol{S}_{j,L} + \boldsymbol{S}_{j,R} + \boldsymbol{S}_{j+1,L} + \boldsymbol{S}_{j+1,R}). \tag{2.36}$$

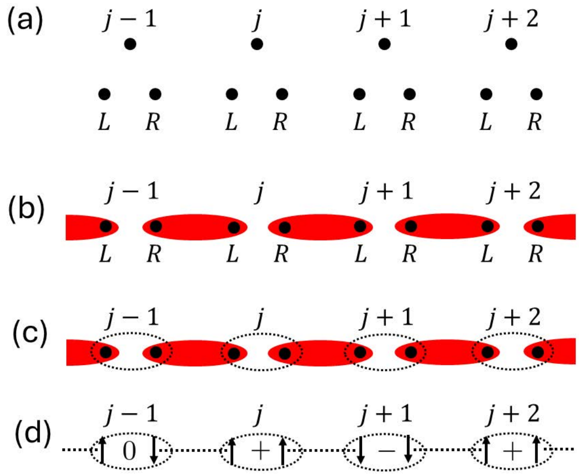

FIGURE 2.1: Schematic explanation of the construction of the VBS state. (a) Each spin-1 at sites j is separated into two spin-$\frac{1}{2}$'s at sites j, L and j, R. (b) Between j, R and $j+1, L$, singlet pairs are formed as represented by red ovals. (c) The symmetrization operators $\mathscr{S}_j$ represented by dashed ovals are applied on each site j, turning the two spin-$\frac{1}{2}$'s back to the original spin-1. (d) Representation of a typical state that appears in the decomposition of the VBS state in the basis of Eq. (2.3). The presence of hidden antiferromagnetic order is clearly seen as there are no configurations that contain consecutive $++$ or $--$, even separated by an arbitrary number of 0's. Redrawn from Figs. 7.1, 7.2, and 7.3 in Ref. [250].

Then using these $2L$ spin-$\frac{1}{2}$ degrees of freedom, one can construct the $\left|\boldsymbol{\phi}_{\text{pre-VBS}}\right\rangle$ state by forming singlet pairs between spins on the j, R and $j+1, L$ sites, as shown in Fig. 2.1(b):

$$\left|\boldsymbol{\phi}_{\text{pre-VBS}}\right\rangle := \bigotimes_{j=1}^{L} \frac{1}{\sqrt{2}} \left\{ \left|\uparrow^{[j,R]}\right\rangle \left|\downarrow^{[j+1,L]}\right\rangle - \left|\downarrow^{[j,R]}\right\rangle \left|\uparrow^{[j+1,L]}\right\rangle \right\}. \tag{2.37}$$

This state is a simple tensor product, and sites that do not belong to the same singlet pair are uncorrelated. The VBS $|\boldsymbol{\phi}_{\text{VBS}}\rangle$ is constructed by applying the symmetrization operator $\mathscr{S}_j$ of Eq. (2.34) on each site j as shown in Fig. 2.1(c):

$$|\boldsymbol{\phi}_{\text{VBS}}\rangle := \left(\bigotimes_{j=1}^{L} \mathscr{S}_j \right) \left|\boldsymbol{\phi}_{\text{pre-VBS}}\right\rangle. \tag{2.38}$$

This is the exact ground state of the AKLT model (2.32) as it minimizes each term of the AKLT Hamiltonian as

$$\hat{P}_2\left[\boldsymbol{S}_j+\boldsymbol{S}_{j+1}\right]|\boldsymbol{\phi}_{\text{VBS}}\rangle = \hat{P}_2\left[\boldsymbol{S}_j+\boldsymbol{S}_{j+1}\right]\left(\bigotimes_{j=1}^{L}\mathscr{S}_j\right)|\boldsymbol{\phi}_{\text{pre-VBS}}\rangle \tag{2.39a}$$

$$= \left(\bigotimes_{j=1}^{L}\mathscr{S}_j\right)\hat{P}_2\left[\boldsymbol{S}_{j,L}+\boldsymbol{S}_{j,R}+\boldsymbol{S}_{j+1,L}+\boldsymbol{S}_{j+1,R}\right]|\boldsymbol{\phi}_{\text{pre-VBS}}\rangle \tag{2.39b}$$

$$= 0. \tag{2.39c}$$

Indeed, since spins on sites j, R and $j+1, L$ form a singlet pair with angular momentum 0, the maximum angular momentum that can be formed using spins on sites j and $j+1$ is 1.

Proving that the $|\boldsymbol{\phi}_{\text{VBS}}\rangle$ is the unique ground state of the AKLT model and that there is a gap above it is more involved and will not be done in this dissertation [49, 50, 124, 174, 186]. Several works on the robustness of the energy gap against external perturbations have been done [116, 158, 277].

Properties of the VBS

The $|\boldsymbol{\phi}_{\text{VBS}}\rangle$ state shares numerous similarities with the ground state of the spin-1 antiferromagnetic Heisenberg chain. The spin correlation function decays exponentially as

$$\lim_{L\to\infty}\frac{\langle\boldsymbol{\phi}_{\text{VBS}}|\boldsymbol{S}_j\cdot\boldsymbol{S}_{j+r}|\boldsymbol{\phi}_{\text{VBS}}\rangle}{\langle\boldsymbol{\phi}_{\text{VBS}}|\boldsymbol{\phi}_{\text{VBS}}\rangle} = 4\left(-\frac{1}{3}\right)^r. \tag{2.40}$$

Like $|\boldsymbol{\phi}_{\text{GS}}\rangle$, the $|\boldsymbol{\phi}_{\text{VBS}}\rangle$ exhibits hidden antiferromagnetic order. Let $\left|\alpha_j^{[j]}\right\rangle$ be the state defined as

$$\left|1^{[j]}\right\rangle := \frac{1}{\sqrt{2}}\left|\uparrow^{[j,R]}\right\rangle\otimes\left|\downarrow^{[j+1,L]}\right\rangle, \tag{2.41a}$$

$$\left|2^{[j]}\right\rangle := -\frac{1}{\sqrt{2}}\left|\downarrow^{[j,R]}\right\rangle\otimes\left|\uparrow^{[j+1,L]}\right\rangle. \tag{2.41b}$$

In the following, α_j will be referred to as the bond indices. Using these states, $\left|\boldsymbol{\phi}_{\text{pre-VBS}}\right\rangle$ can be rewritten as

$$\left|\boldsymbol{\phi}_{\text{pre-VBS}}\right\rangle = \sum_{\boldsymbol{\alpha}}\bigotimes_{j=1}^{L}\left|\alpha_j^{[j]}\right\rangle. \tag{2.42}$$

Here, the sum over $\boldsymbol{\alpha}$ is a sum over all the configurations of α_j. After applying the symmetrization operator $\mathscr{S}_j$ on the site j, one can associate a spin configuration $\boldsymbol{\sigma}$ to each bond configuration $\boldsymbol{\alpha}$ using the rule given in Table 2.1.

Then it is clear that a configuration with two consecutive $++$ or $--$ signs, even separated by an arbitrary number of 0s, cannot appear, as shown in Fig.

$\alpha_j\ \alpha_{j+1}$	σ_j	factor for j
$2\cdots\uparrow\uparrow\cdots 1$	1	$-\frac{1}{\sqrt{2}}\times 1$
$1\cdots\downarrow\downarrow\cdots 2$	-1	$\frac{1}{\sqrt{2}}\times 1$
$1\cdots\downarrow\uparrow\cdots 1$	0	$\frac{1}{\sqrt{2}}\times\frac{1}{\sqrt{2}}$
$2\cdots\uparrow\downarrow\cdots 2$	0	$-\frac{1}{\sqrt{2}}\times\frac{1}{\sqrt{2}}$

TABLE 2.1: Link between α_j and σ_j. The value of the physical degree of freedom σ_j is fixed by the value of the bond degrees of freedom α_j and α_{j+1}. The coefficient in the last column corresponds to the element $A^{\sigma_j}_{\alpha_j\alpha_{j+1}}$ of the expression of $|\boldsymbol{\phi}_{\mathrm{VBS}}\rangle$ as a MPS.

2.1(d). Thus, the $|\boldsymbol{\phi}_{\mathrm{VBS}}\rangle$ exhibits hidden antiferromagnetic order. The presence of hidden antiferromagnetic order can be detected using string correlation functions introduced by den Nijs and Rommelse [183]:

$$\mathscr{S}^{\alpha}_{i,j}(\boldsymbol{\phi}) := \frac{\langle\boldsymbol{\phi}|S^{\alpha}_i \exp[i\pi\sum_{k=i+1}^{j-1} S^{\alpha}_k] S^{\alpha}_j|\boldsymbol{\phi}\rangle}{\langle\boldsymbol{\phi}|\boldsymbol{\phi}\rangle}, \tag{2.43}$$

with $0<i<j<L$. The operator $\exp[i\pi\sum_{k=i+1}^{j-1} S^{\alpha}_k]$ in Eq. (2.43) is equivalent to $(-1)^{(\text{number of }\pm\text{ signs between } i \text{ and } j)}$. In a system with hidden antiferromagnetic order, the string order parameter defined as

$$\mathscr{O}^{(\alpha)}_{\mathrm{string}}(\boldsymbol{\phi}) := \lim_{j-i\to\infty}\lim_{L\to\infty}\mathscr{S}^{\alpha}_{i,j}(\boldsymbol{\phi}), \tag{2.44}$$

is expected to take a finite value. For the VBS, we obtain

$$\mathscr{O}^{(x,y,z)}_{\mathrm{string}}(\boldsymbol{\phi}_{\mathrm{VBS}}) = \frac{4}{9}. \tag{2.45}$$

From this point, open boundary conditions will be considered. The VBS states on open chains are defined as

$$\left|\boldsymbol{\phi}^{\sigma_1,\sigma_L}_{\mathrm{VBS}}\right\rangle := \left(\bigotimes_{j=1}^{L}\mathscr{S}_j\right)\left|\boldsymbol{\phi}^{\sigma_1,\sigma_L}_{\text{pre-VBS}}\right\rangle, \tag{2.46a}$$

$$\left|\boldsymbol{\phi}^{\sigma_1,\sigma_L}_{\text{pre-VBS}}\right\rangle := \left|\sigma^{[1,L]}_1\right\rangle\left[\sum_{\boldsymbol{\alpha}}\bigotimes_{j=1}^{L-1}\left|\alpha^{[j]}_j\right\rangle\right]\left|\sigma^{[L,R]}_L\right\rangle\quad(\sigma_1,\sigma_L=\uparrow,\downarrow). \tag{2.46b}$$

By calculating the local magnetization along the z-axis, we observe the existence of an effective spin-$\frac{1}{2}$ state localized on each edge of the system as

$$\left\langle\boldsymbol{\phi}^{\sigma_1,\sigma_L}_{\mathrm{VBS}}\middle|S^z_j\middle|\boldsymbol{\phi}^{\sigma_1,\sigma_L}_{\mathrm{VBS}}\right\rangle \approx \mp\frac{2}{3}\left(-\frac{1}{3}\right)^j\ (j\ll L)\,, \tag{2.47a}$$

$$\sum_{j=1}^{L/2}\left\langle\boldsymbol{\phi}^{\sigma_1,\sigma_L}_{\mathrm{VBS}}\middle|S^z_j\middle|\boldsymbol{\phi}^{\sigma_1,\sigma_L}_{\mathrm{VBS}}\right\rangle \approx \pm\frac{1}{2}\,. \tag{2.47b}$$

Here, the $+$ $(-)$ sign refers to the case $\sigma_1 = \uparrow$ $(\downarrow)$. Similar relations hold for the other side. An effective spin-$\frac{1}{2}$ degree of freedom localized on the edge of an open chain appears when changing the boundary condition [80, 162]. The degeneracy of the nearly isolated spin-$\frac{1}{2}$ degree of freedom on each edge is protected by Kramers degeneracy. The only time-reversal-symmetric perturbations capable of splitting the degeneracy must act on both edge spins and thus through the bulk, and therefore is unlikely to occur.

The low-energy spectrum of the spin-1 antiferromagnetic Heisenberg chain with open boundary conditions is similar to that of the AKLT model. For the Heisenberg chain, the MLM theorem (2.9) implies that the unique ground state has $\boldsymbol{S}_{\text{tot}} = 0$. Just above the ground state, there are three low-lying energy eigenstates with $\boldsymbol{S}_{\text{tot}} = 1$, whose energies converge to E_{GS} as $L \to \infty$. In fact, the existence of low-lying energy states is also linked to hidden symmetry breaking. Let us introduce the string order operator as

$$\hat{\mathscr{O}}^{(\alpha)}_{\text{string}} := \sum_{j=1}^{L} S_j^{\alpha} \exp\left[i\pi \sum_{i=1}^{j-1} S_i^{\alpha}\right]. \tag{2.48}$$

In the presence of hidden antiferromagnetic order, the expectation value of $\left(\hat{\mathscr{O}}^{(\alpha)}_{\text{string}}\right)^2$ takes a finite value, as seen from the equality below:

$$\left(\hat{\mathscr{O}}^{(\alpha)}_{\text{string}}\right)^2 = \sum_{j=1}^{L} (S_j^{\alpha})^2 - 2 \sum_{1 \le i < j \le L} S_i^{\alpha} \exp\left[i\pi \sum_{k=i+1}^{j-1} S_k^{\alpha}\right] S_j^{\alpha}, \tag{2.49}$$

where the last term is nothing but Eq. (2.43). One can construct three low-lying orthogonal states by acting with $\hat{\mathscr{O}}^{(\alpha)}_{\text{string}}$ on the ground state. One concludes that the degeneracy of the ground state for both the AKLT and Heisenberg Hamiltonians depends on the manifold on which they are defined, and this degeneracy is linked to the existence of edge modes in open boundary conditions.

2.5 Symmetry-protected topological phases

As discussed in Sec. 1.1.2, ground states of one-dimensional systems exhibit short-range entanglement and should be continuously connected by local unitary transformations if no symmetry restrictions are imposed [30, 31, 187–189, 225]. For example, consider the Hamiltonian H_D defined as

$$H_D := D \sum_{j=1}^{L} \left(S_j^z\right)^2, \tag{2.50}$$

where $D > 0$ is the single-ion anisotropy parameter. The ground state $|\boldsymbol{\phi}_0\rangle$ of this Hamiltonian is unique and gapped. This state is trivial, as it is a simple tensor product as

$$|\boldsymbol{\phi}_0\rangle := \bigotimes_{j=1}^{L} \left|0^{[j]}\right\rangle. \tag{2.51}$$

While both $|\boldsymbol{\phi}_0\rangle$ and the ground state of the antiferromagnetic Heisenberg Hamiltonian $|\boldsymbol{\phi}_{\mathrm{GS}}\rangle$ are gapped and have the same symmetry as their respective Hamiltonian, these two states have drastically different properties and should belong to different phases. For example, the string order parameter can distinguish between these two phases [88, 176].

The following symmetries can prevent $|\boldsymbol{\phi}_0\rangle$ and $|\boldsymbol{\phi}_{\mathrm{VBS}}\rangle$ from being continuously connected.

S.1 $\mathbb{Z}_2 \times \mathbb{Z}_2$ symmetry. This symmetry plays a role in the hidden symmetry breaking, as discussed earlier.

S.2 Time-reversal symmetry. The degeneracy of the ground state is linked to the presence of spin-$\frac{1}{2}$ degrees of freedom at the edges of the chain. This edge-state degeneracy is protected by Kramers degeneracy.

S.3 Bond inversion symmetry. This symmetry corresponds to invariance under site inversion $j \to L - j$.

The role of symmetry in protecting the SPT phase is most clearly understood through the lens of entanglement entropy (EE) [208, 209]. Consider the Schmidt decomposition of the ground state $|\boldsymbol{\phi}_{\mathrm{GS}}\rangle$ for an infinite system:

$$|\boldsymbol{\phi}_{\mathrm{GS}}\rangle = \sum_{\alpha} \lambda_\alpha \, |\boldsymbol{\phi}_\alpha\rangle_L \otimes |\boldsymbol{\phi}_\alpha\rangle_R \,, \tag{2.52}$$

where the coefficients λ_α satisfy $\sum_\alpha \lambda_\alpha^2 = 1$. Here, $|\boldsymbol{\phi}_\alpha\rangle_R$ and $|\boldsymbol{\phi}_\alpha\rangle_L$ are orthogonal effective states defined on semi-infinite chains.[7]

While the summation over α typically extends to infinity, for a gapped ground state with short-range entanglement, an accurate approximation can be achieved by retaining only the χ largest λ_α values [86]. The entanglement entropy, which measures how strongly one half of the system is entangled with the other half, can be calculated using the Schmidt decomposition as

$$S := -\sum_{\alpha=1}^{\chi} \lambda_\alpha^2 \ln \lambda_\alpha^2. \tag{2.53}$$

For example, the Schmidt decomposition of $|\boldsymbol{\phi}_{\mathrm{VBS}}\rangle$ obtained by splitting the singlet pair between sites 0 and 1 is given by

$$|\boldsymbol{\phi}_{\mathrm{VBS}}\rangle = \frac{1}{\sqrt{2}} \left\{ |\boldsymbol{\phi}_\uparrow\rangle_L \otimes |\boldsymbol{\phi}_\downarrow\rangle_R - |\boldsymbol{\phi}_\downarrow\rangle_L \otimes |\boldsymbol{\phi}_\uparrow\rangle_R \right\}. \tag{2.54}$$

[7] This definition is not mathematically rigorous but serves as a heuristic argument.

Here, $\chi = 2$ and $\lambda_{1,2} = \frac{1}{\sqrt{2}}$. Both $|\boldsymbol{\phi}_\alpha\rangle_R$ and $|\boldsymbol{\phi}_\alpha\rangle_L$ can be regarded as effective states with spin-$\frac{1}{2}$ degrees of freedom, defined as

$$|\boldsymbol{\phi}_\sigma\rangle_R = \left(\bigotimes_{j=1}^{\infty} \mathscr{S}_j\right)\left[\left|\sigma^{[1,L]}\right\rangle \otimes \sum_{\boldsymbol{\alpha}} \bigotimes_{i=1}^{\infty} \left|\alpha_i^{[i]}\right\rangle\right], \tag{2.55a}$$

$$|\boldsymbol{\phi}_\sigma\rangle_L = \left(\bigotimes_{j=-\infty}^{0} \mathscr{S}_j\right)\left[\left|\sigma^{[0,R]}\right\rangle \otimes \sum_{\boldsymbol{\alpha}} \bigotimes_{i=-\infty}^{-1} \left|\alpha_i^{[i]}\right\rangle\right]. \tag{2.55b}$$

Due to Kramers degeneracy, there must be an even number of states associated with each distinct value of λ. Thus, for the VBS, the EE satisfies $S \geq \ln 2$. This nonzero entanglement entropy, which cannot be removed by any local unitary transformation respecting the symmetry of the system, protects the Haldane phase from local perturbations.

This observation can be generalized to other symmetries by introducing topological indices. These indices represent invariants that remain constant within a given phase, distinguishing between different SPT phases. For example, the topological index associated with time-reversal symmetry $\mathcal{O}_{\mathrm{TR}} = \pm 1$ can be calculated as follows. Let U_{TR} be the time-reversal map acting on $|\boldsymbol{\phi}_\alpha\rangle_R$. From the time-reversal invariance of $|\boldsymbol{\phi}_{\mathrm{VBS}}\rangle$, one has

$$U_{\mathrm{TR}}^2 |\boldsymbol{\phi}_\alpha\rangle_R = \mathcal{O}_{\mathrm{TR}} |\boldsymbol{\phi}_\alpha\rangle_R . \tag{2.56}$$

Since $|\boldsymbol{\phi}_\alpha\rangle_R$ behaves like a spin-$\frac{1}{2}$, $\mathcal{O}_{\mathrm{TR}} = -1$. Similarly, let $\mathcal{O}_{xy} = \pm 1$ be another index related to the $\mathbb{Z}_2 \times \mathbb{Z}_2$ symmetry. For the VBS state, one has $U_x U_z |\boldsymbol{\phi}_\alpha\rangle_R = \mathcal{O}_{xz} U_z U_x |\boldsymbol{\phi}_\alpha\rangle_R$ with $\mathcal{O}_{xy} = -1$. Likewise, another topological index can be defined for the bond inversion symmetry.

The discussion above, while insightful, is based on the informal concept of effective edge states, which introduces several complications. A significant issue arises because for an open chain, each half-chain has two edges. Consequently, the states $|\boldsymbol{\phi}_\alpha\rangle_R$ and $|\boldsymbol{\phi}_\alpha\rangle_L$ behave as states with an effective integer spin. Under this assumption, all topological indices would be trivially equal 1, which does not capture the true nature of the topological phase. Thus, a more formal definition of these topological indices must be developed. Such formalism can be constructed by using MPS, providing a more rigorous framework for describing the entanglement structure and topological properties of the system.

In addition to topological indices, alternative methods have been proposed for identifying non-trivial SPT phases. One such method involves the Berry phase for quantum spin chains, which has been explored in early studies such as those by Hatsugai *et al.* [87, 88] and Hirano *et al.* [98, 99]. These approaches are closely related to techniques involving topological indices. For further information about non-local order parameters, you may refer to the works of Haegeman *et al.* [79] and Pollmann *et al.* [207]. Additionally, Shiozaki *et al.* [231] discuss the topological field theory perspective.

2.6 Matrix product state

The expression of $|\boldsymbol{\phi}_{\mathrm{VBS}}\rangle$ in the $|\boldsymbol{\sigma}\rangle$ basis can be conveniently obtained using the MPS formalism [47, 49, 50, 123, 259]. In this framework, the $c_{\boldsymbol{\sigma}}$ coefficient in the expansion of any state can be written as a product of matrices

$$c_{\boldsymbol{\sigma}} = \sum_{\boldsymbol{\alpha}} A^{\sigma_1}_{\alpha_1,\alpha_2} A^{\sigma_2}_{\alpha_2,\alpha_3} \cdots A^{\sigma_L}_{\alpha_L,\alpha_1} \tag{2.57a}$$

$$= \boldsymbol{Tr}[\boldsymbol{A}^{\sigma_1} \boldsymbol{A}^{\sigma_2} \cdots \boldsymbol{A}^{\sigma_L}]. \tag{2.57b}$$

Here, the α_j indices are vectors of dimension χ. $|\boldsymbol{\phi}_{\mathrm{VBS}}\rangle$ can be represented using a bond dimension $\chi = 2$ and the following matrix:

$$\boldsymbol{A}^{+} = \begin{pmatrix} 0 & 0 \\ -\frac{1}{\sqrt{2}} & 0 \end{pmatrix}, \ \boldsymbol{A}^{0} = \begin{pmatrix} \frac{1}{2} & 0 \\ 0 & -\frac{1}{2} \end{pmatrix}, \ \boldsymbol{A}^{-} = \begin{pmatrix} 0 & \frac{1}{\sqrt{2}} \\ 0 & 0 \end{pmatrix}. \tag{2.58}$$

The MPS representation has a graphical representation shown in Fig. 2.2(a) that enables performing calculations in a very intuitive way.

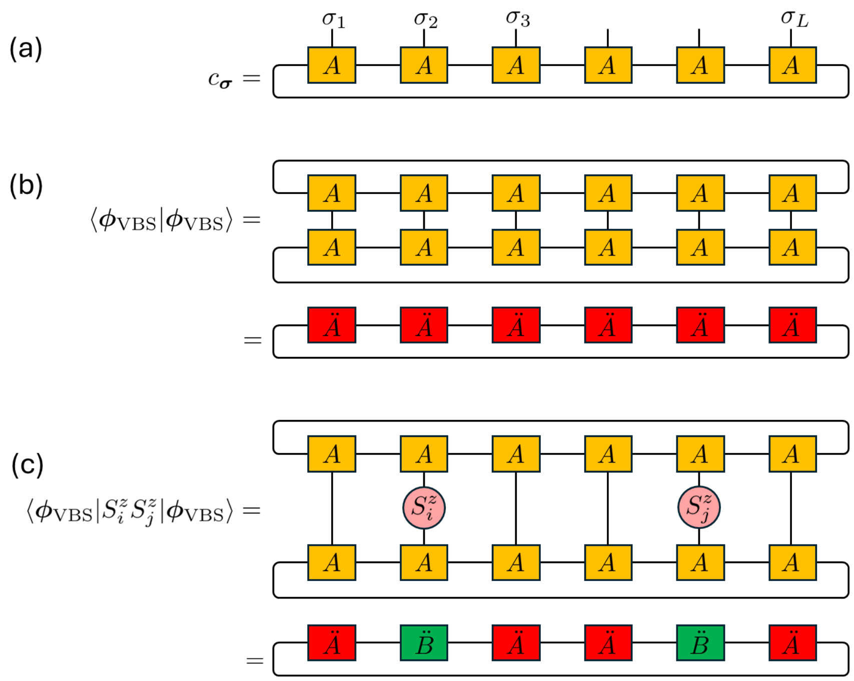

FIGURE 2.2: (a) Schematic representation of an MPS with periodic boundary conditions. Horizontal lines represent the bond indices, the loop is to be understood as the periodic boundary condition. Vertical lines represent the physical degree of freedom. (b) Calculation of the norm of the VBS, $\langle\boldsymbol{\phi}_{\mathrm{VBS}}|\boldsymbol{\phi}_{\mathrm{VBS}}\rangle$ as in Eq. (2.62), using the transfer matrix method. (c) Calculation of unnormalized spin correlation function $\langle\boldsymbol{\phi}_{\mathrm{VBS}}|S^z_i S^z_j|\boldsymbol{\phi}_{\mathrm{VBS}}\rangle$ as in Eq. (2.62). Redrawn from Figs. 7.2.15, 7.2.18, 7.2.21, and 7.2.27 in Ref. [250].

As a simple example, the norm of the VBS, $\langle\boldsymbol{\phi}_{\mathrm{VBS}}|\boldsymbol{\phi}_{\mathrm{VBS}}\rangle$ is calculated as follows. Let $\ddot{A}$ be the transfer matrix whose elements are given by

$$\ddot{A}_{\alpha,\beta;\alpha',\beta'} := \sum_{\sigma=+1,0,-1} \left(A^{\sigma}_{\alpha,\alpha'}\right)^{*} A^{\sigma}_{\beta,\beta'} \, . \tag{2.59}$$

Using $\ddot{A}$, $\langle \boldsymbol{\phi}_{\mathrm{VBS}} | \boldsymbol{\phi}_{\mathrm{VBS}} \rangle$ can be calculated as shown in Fig. 2.2(b):

$$\langle \boldsymbol{\phi}_{\mathrm{VBS}} | \boldsymbol{\phi}_{\mathrm{VBS}} \rangle = \sum_{\sigma} \sum_{\boldsymbol{\alpha},\boldsymbol{\beta}} \left(A^{\sigma_1}_{\alpha_1,\alpha_2} \cdots A^{\sigma_L}_{\alpha_L,\alpha_1} \right)^* A^{\sigma_1}_{\beta_1,\beta_2} \cdots A^{\sigma_L}_{\beta_L,\beta_1} \tag{2.60a}$$

$$= \boldsymbol{Tr}[\ddot{\boldsymbol{A}}^L] \tag{2.60b}$$

$$= \left(\frac{3}{4}\right)^L + 3\left(-\frac{1}{4}\right)^L. \tag{2.60c}$$

Likewise, the spin correlation function can be calculated easily by introducing the following matrix

$$\ddot{B}_{\alpha,\beta;\alpha',\beta'} := \sum_{\sigma=+,0,-} \left(A^{\sigma}_{\alpha,\alpha'} \right)^* \sigma A^{\sigma}_{\beta,\beta'}. \tag{2.61}$$

Then, the unnormalized spin-spin correlation function is given by

$$\langle \boldsymbol{\phi}_{\mathrm{VBS}} | S^z_i S^z_j | \boldsymbol{\phi}_{\mathrm{VBS}} \rangle = \boldsymbol{Tr}[\ddot{\boldsymbol{B}} \ddot{\boldsymbol{A}}^{j-i-1} \ddot{\boldsymbol{B}} \ddot{\boldsymbol{A}}^{L-j+i-1}] \tag{2.62a}$$

$$= \left(-\frac{1}{4}\right)^{j-i} \left(\frac{3}{4}\right)^{L-j+i-1} + \left(-\frac{1}{4}\right)^{L-j+i} \left(\frac{3}{4}\right)^{j+i-1}, \tag{2.62b}$$

as shown in Fig. 2.2(c).

MPS can also represent a state defined on a system with open boundary conditions by replacing $\boldsymbol{A}^{\sigma_1}$ and $\boldsymbol{A}^{\sigma_L}$ with a row vector $\boldsymbol{l}$ and a column vector $\boldsymbol{r}$ of dimension χ, respectively, as

$$\sum_{\sigma} \boldsymbol{l}^{\sigma_1} \boldsymbol{A}^{\sigma_2} \cdots \boldsymbol{A}^{\sigma_{L-1}} \boldsymbol{r}^{\sigma_L} \left| \boldsymbol{\sigma} \right\rangle. \tag{2.63}$$

Before closing this section, it is important to highlight some key properties of the MPS. Similarly to $|\boldsymbol{\phi}_{\mathrm{VBS}}\rangle$, which can be represented exactly by an MPS, it has been shown that a unique ground state accompanied by a finite energy gap can always be efficiently approximated by a MPS (see, e.g., Ref. [21]). In fact, the set of MPSs is known to be weak-$*$ dense in the set of all translation-invariant states of a quantum spin chain [48, 64]. This means that the expectation value of any local observable in an arbitrary translation-invariant state can be approximated with the desired precision by a MPS with a sufficiently large bond dimension χ [80]. This makes MPSs particularly interesting for numerical simulation. Indeed, while the Hilbert space of a spin-S chain of length L contains $(2S+1)^L$ linearly independent states, the number of parameters in a MPS is just $L \times (2S+1) \times \chi^2$, which represents a considerable reduction in the number of parameters needed to investigate large systems.

Quite generally, MPSs with short-range correlations can be chosen to be injective.[8] An injective MPS is a collection of matrices $\boldsymbol{A}^{\sigma}$ that satisfies

$$\sum_{\sigma} \boldsymbol{A}^{\sigma} (\boldsymbol{A}^{\sigma})^{\dagger} = \epsilon_1 \boldsymbol{I}, \tag{2.64}$$

[8] A counter-example can be the Schrödinger-cat-like state $|\boldsymbol{\phi}_{\mathrm{CAT}}\rangle = |\boldsymbol{\phi}_{\uparrow}\rangle + |\boldsymbol{\phi}_{\downarrow}\rangle$.

with $\epsilon_1 > 0$, and one of the following properties:[9]

i There exists l_0 such that the set of matrices $\boldsymbol{A}^{\sigma_1}\boldsymbol{A}^{\sigma_2}\cdots\boldsymbol{A}^{\sigma_{l_0}}$, with all possible $\sigma_1, \sigma_2, \cdots, \sigma_{l_0}$, spans the whole space of $\chi \times \chi$ matrices.

ii ϵ_1 is a nondegenerate eigenvalue of the transfer matrix $\ddot{\boldsymbol{A}}$, and any other eigenvalue ϵ_j satisfies $|\epsilon_j| < \epsilon_1$.

Suppose that a state has two different injective MPS representations with the same bond dimension χ, as

$$\sum_{\boldsymbol{\sigma}} \boldsymbol{Tr}[\boldsymbol{A}^{\sigma_1}\boldsymbol{A}^{\sigma_2}\cdots\boldsymbol{A}^{\sigma_L}]\,|\boldsymbol{\sigma}\rangle = \sum_{\boldsymbol{\sigma}} \boldsymbol{Tr}[\boldsymbol{B}^{\sigma_1}\boldsymbol{B}^{\sigma_2}\cdots\boldsymbol{B}^{\sigma_L}]\,|\boldsymbol{\sigma}\rangle\,. \tag{2.65}$$

Then there is a unique (up to a phase) unitary matrix U such that, for all σ,

$$B^{\sigma} = U^{\dagger}A^{\sigma}U. \tag{2.66}$$

2.7 Topological indices

2.7.1 Definition of the topological indices

The notion of topological indices can be made more rigorous by working in the MPS framework [208, 209].[10] Let $|\boldsymbol{\Phi}\rangle$ be a general MPS that is invariant under a symmetry group G. Let g be an element of G. The action of g on $\mathscr{H}$ is represented by the unitary operator $\Sigma^g = \bigotimes_j \Sigma_j^g$, with Σ_j^g acting on $\mathfrak{h}_j$. Under this symmetry operation, $|\boldsymbol{\phi}\rangle$ is transformed as

$$\Sigma^g\,|\boldsymbol{\phi}\rangle = \sum_{\boldsymbol{\sigma}} \boldsymbol{Tr}\left[\tilde{\boldsymbol{A}}^{\sigma_1}\tilde{\boldsymbol{A}}^{\sigma_2}\cdots\tilde{\boldsymbol{A}}^{\sigma_L}\right]|\boldsymbol{\sigma}\rangle = e^{iL\theta_g}\,|\boldsymbol{\phi}\rangle \tag{2.67}$$

with

$$\tilde{\boldsymbol{A}}^{\sigma_j} := \sum_{\sigma'_j=-S}^{S} \left\langle \sigma_j^{[j]} \middle| \Sigma_j^g \middle| \sigma_j'^{[j]} \right\rangle \boldsymbol{A}^{\sigma'_j}\,. \tag{2.68}$$

Since $\Sigma^g\,|\boldsymbol{\phi}\rangle = e^{iL\theta_g}\,|\boldsymbol{\phi}\rangle$ can be represented by two injective and translationally invariant MPSs $\boldsymbol{A}^{\sigma}$ and $\tilde{\boldsymbol{A}}^{\sigma}$, these two MPSs are related by

$$\tilde{\boldsymbol{A}}^{\sigma} = e^{i\theta_g}U_g^{\dagger}\boldsymbol{A}^{\sigma}U_g, \tag{2.69}$$

for all σ, with U_g a $\chi \times \chi$ unitary matrix independent of σ, as shown in Fig. 2.3(c).

Thus, a symmetric MPS $\boldsymbol{A}$ must fulfill the following equation

$$\sum_{\sigma'} \Sigma^g_{\sigma\sigma'}\boldsymbol{A}^{\sigma'} = e^{i\theta_g}U_g^{\dagger}\boldsymbol{A}^{\sigma}U_g, \tag{2.70}$$

with $\Sigma^g_{\sigma\sigma'} = \left\langle \sigma_j^{[j]} \middle| \Sigma_j^g \middle| \sigma_j'^{[j]} \right\rangle$.

[9]The two properties can be proved to be equivalent.

[10]See Refs. [152, 190, 191, 198, 252] for other rigorous works that do not rely on the MPS formalism.

By using repetitively Eq. (2.70) for g and h or gh, the following relation can be obtained

$$W := U_g U_h U_{gh}^{\dagger}, \tag{2.71a}$$
$$[W, \boldsymbol{A}^{\sigma}] = 0, \tag{2.71b}$$

for all σ. By using repeatedly Eq. (2.71b) and the injectivity of $\boldsymbol{A}$, one obtains

$$W = e^{i\mathcal{O}_{g,h}} \boldsymbol{I}. \tag{2.72}$$

If for all g and h, $\mathcal{O}_{g,h}$ is null, then the U_g matrices form a genuine representation of G. Generally $\mathcal{O}_{g,h}$ is not null. Let $U'_g = e^{i\psi_g} U_g$ with $\psi_g \in \mathbb{R}$ be another representation. If the two representations fulfill the following equation

$$\mathcal{O}'_{g,h} = \mathcal{O}_{g,h} + \psi_{gh} - \psi_h - \psi_g \pmod{2\pi} \text{ for any } g, h \in G, \tag{2.73}$$

they are said to be equivalent. In particular, all representations where $\mathcal{O}_{g,h}$ is decomposable as $\psi_{gh} - \psi_h - \psi_g$ with some ψ_g are trivial, and in this case $|\boldsymbol{\phi}\rangle$ belongs to the trivial phase. The search for non-trivial projective representations and their classification can be done by calculating the second group cohomology $\mathrm{H}^2(G, U(1))$ [30, 31, 52, 225].

In dimensions higher than one, the most complete classification is the one given by Chen, Gu, Liu, and Wen [33, 34], who argued that SPT phases in d-dimensional quantum spin systems are classified in terms of the group cohomology $\mathrm{H}^{\mathrm{d+1}}(G, U(1))$ of the symmetry group G [46, 113, 159, 166, 211, 263, 278]. However, contrary to one dimension, there is no guarantee that a gapped ground state can be accurately approximated by a tensor product state, which is a higher-dimensional generalization of a MPS. Consequently, the classification of SPT phases is still an open problem.

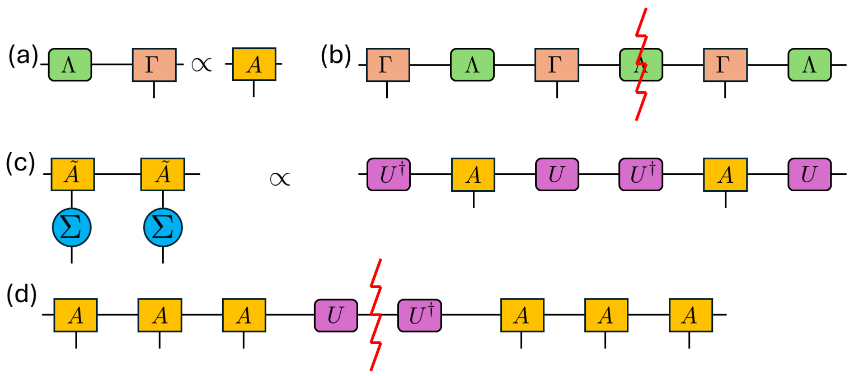

FIGURE 2.3: (a,b) Schematic representation of the canonical form of a MPS. (a) The left-orthogonalized matrix $A^s = \Lambda\Gamma^s$. (b) Representation of the Schmidt decomposition. The matrix $\Lambda = \mathrm{diag}(\lambda_1, \cdots, \lambda_\chi)$ contains the coefficient of the Schmidt decomposition. (c) The action of the symmetry Σ on the physical index and its representation U on the virtual (bond) index. (d) The action of the symmetry on states defined on the half-infinite chain. Redrawn from Figs. 1 and 2 in Ref. [207].

The calculation of topological indices related to time-reversal symmetry and bond inversion symmetry can be performed similarly, with small modifications. In particular, the time-reversal symmetry which is an anti-unitary transformation has the associated topological index that is defined by

$$U_{\mathrm{TR}} U_{\mathrm{TR}}^{*} = \mathcal{O}_{\mathrm{TR}} \boldsymbol{I}, \tag{2.74}$$

where $\mathcal{O}_{\mathrm{TR}} = \pm 1$ [208, 250], and I is the identity matrix. Here, the U_{TR} matrix is determined by solving the following equation:

$$\sum_{\sigma'} \Sigma^{y}_{\sigma\sigma'} \boldsymbol{A}^{*\sigma'} = e^{i\theta_{\mathrm{TR}}} U_{\mathrm{TR}}^{\dagger} \boldsymbol{A}^{\sigma} U_{\mathrm{TR}}. \tag{2.75}$$

This dissertation does not use the topological index associated with the bond inversion symmetry [208].

2.7.2 SPT phases on spin-$\frac{1}{2}$ ladders

The construction of the VBS in Sec. 2.4 makes the parallel between the SPT phase in the spin-1 chain and the spin-$\frac{1}{2}$ ladder evident. The MPS representation of the Haldane state on the ladder can be obtained from the MPS representation of the Haldane chain by identifying the sites j, L and j, R of the spin chain in Eq. (2.37) with the site $1, j$ and $2, j$ in the spin ladder. Namely:

$$\boldsymbol{A}^{t_+} = \boldsymbol{A}^{+},\ \boldsymbol{A}^{t_z} = \boldsymbol{A}^{0},\ \boldsymbol{A}^{t_-} = \boldsymbol{A}^{-},\ \boldsymbol{A}^{s} = 0. \tag{2.76}$$

In addition to the D_2 spin rotation ($\Sigma_j^{x,y} := \exp\left[i\pi(S_{1,j}^{x,y} + S_{2,j}^{x,y})\right]$) and the time-reversal symmetry ($\Sigma^y \hat{K}$) present in the spin-1 chain, the spin-$\frac{1}{2}$ ladder possesses the leg-exchange symmetry:

$$\Sigma_j^{\sigma} := \sum_{\alpha,\beta=\uparrow,\downarrow} \left|\alpha^{[1,j]}\beta^{[2,j]}\right\rangle \left\langle \beta^{[1,j]}\alpha^{[2,j]}\right| . \tag{2.77}$$

This symmetry, unique to ladder systems, suggests that the classification of SPT phase for ladder systems might be richer than that for chain systems.

2.8 Numerical methods

In the previous sections, the concept of a MPS was introduced. A MPS can accurately represent a non-degenerate ground state with a short correlation length. The significant reduction in parameters enables highly efficient numerical calculations of ground states of one-dimensional systems. Commonly used numerical methods that employ MPS representations include time-evolving block decimation (TEBD) [196, 259] and the density matrix renormalization group (DMRG) for both finite (fDMRG) and infinite (iDMRG) systems [154, 155]. In this dissertation, numerical simulations of infinite systems are performed using the iDMRG algorithm, implemented with the C++ library ITensor [53, 54]. The iDMRG algorithm is a numerical method that iteratively optimizes a translationally invariant MPS to approximate the ground state of an infinite system. The accuracy of this approximation depends on the bond dimension χ. After completing the iterative process, the algorithm returns the approximate ground state in the canonical form of a MPS.

2.8.1 Canonical form of MPS

The translationally invariant MPS in a canonical form is expressed as

$$|\boldsymbol{\phi}_{\mathrm{CAN}}\rangle := \sum_{\sigma}[\cdots\Lambda\Gamma^{\sigma_i}\Lambda\Gamma^{\sigma_j}\Lambda\Gamma^{\sigma_t}\cdots]\,|\boldsymbol{\sigma}\rangle\,, \tag{2.78}$$

where Γ^{σ_j} is a $\chi\times\chi$ matrix and $\Lambda = \mathrm{diag}(\lambda_1,\cdots,\lambda_\chi)$ is a diagonal matrix comprised of Schmidt coefficients λ_α, as shown in Fig. 2.3(b). The canonical form of a MPS exhibits interesting properties that facilitate the calculation of some physical quantities. Using both Γ^σ and Λ, one can construct the left- (and right-) orthogonalized matrices $A^\sigma = \Lambda\Gamma^\sigma$ ($B^\sigma = \Gamma^\sigma\Lambda$) which satisfy the following orthogonalization conditions

$$\boldsymbol{I} = \sum_{\sigma}(\boldsymbol{A}^{\sigma})^{\dagger}\boldsymbol{A}^{\sigma}, \tag{2.79a}$$

$$\boldsymbol{I} = \sum_{\sigma}\boldsymbol{B}^{\sigma}(\boldsymbol{B}^{\sigma})^{\dagger}. \tag{2.79b}$$

as shown in Fig. 2.3(a). The transfer matrix can be written in terms of the B matrix as

$$T_{\alpha,\beta;\alpha',\beta'} = \sum_{\sigma}\left(\Gamma^{\sigma}_{\alpha,\alpha'}\right)^{*}\Gamma^{\sigma}_{\beta,\beta'}\Lambda_{\alpha'}\Lambda_{\beta'} \tag{2.80a}$$

$$= \sum_{\sigma}(B^{\sigma}_{\alpha,\alpha'})^{*}B^{\sigma'}_{\beta,\beta'}\,. \tag{2.80b}$$

The largest correlation length, which quantifies the slowest possible decaying rate of correlations, is determined by the second largest eigenvalue ϵ_2, and is given by

$$\xi(\chi) = \frac{-n}{\ln|\epsilon_2(\chi)|}, \tag{2.81}$$

where n is a factor that depends on the number of legs and the size of the unit cell. This correlation length corresponds to the asymptotic decay of correlations at large distances. However, at shorter distances, non-trivial corrections may arise due to contributions from other eigenvalues of the transfer matrix. These corrections must be taken into account for a more accurate description of the correlations. Quite generally, continuous phase transitions are associated with divergences of the correlation length ξ. In iDMRG calculations, owing to finite χ, a genuine divergence of ξ does not occur. One rather observes a peak in ξ that grows with an increase in χ at the transition.

2.8.2 iDMRG algorithm for spin ladder

The iDMRG algorithm can also be used to investigate spin ladder systems by enumerating the lattice sites in a zig-zag pattern, as shown in Fig. 2.4. Such methods can also be used to investigate higher-dimensional systems.

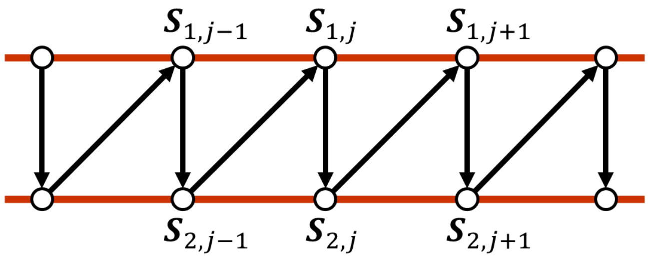

FIGURE 2.4: Order of enumeration of the lattice sites for the iDMRG calculation.

However, depending on the enumeration patterns, interactions that are local in the original Hamiltonian can become non-local. The iDMRG results presented in this dissertation were all obtained from calculations using a four-site unit cell, except for the calculation of the topological indices, which were calculated using a two-site unit cell.

2.8.3 Central charge

When the critical point can be described by a conformal field theory (CFT), the canonical form can help to calculate the central charge c of the CFT. The central charge is a key parameter in CFT, as it intuitively corresponds to the number of gapless modes, it governs many universal properties of the system. According to CFT, the relationship between the half-chain EE S defined in Eq. (2.53) and the correlation length ξ defined in Eq.(2.81) is given by [24, 210]

$$S = \frac{c}{6} \ln \xi + S_0, \tag{2.82}$$

where S_0 a constant. By fitting the EE S defined in Eq. (2.53) with the local maximum of ξ calculated at different χ, S_0 and c can be determined. This method will be extensively employed in this dissertation to characterize and analyze the different transitions in the system.

2.8.4 Generalized transfer matrix method

As the iDMRG method returns the ground state in the MPS representation, the calculation of topological indices can be done conveniently. The expression of a projective representation of the symmetry group can be obtained via the relation (2.70). However, this expression is not practical for numerical calculation, and one would rather use the generalized transfer matrix as [194, 205, 207]

$$T^{\Sigma^g}_{\alpha,\beta;\alpha',\beta'} := \sum_{\sigma} \left(\Gamma^{\sigma}_{\beta,\beta'}\right)^* \left(\sum_{\sigma'} \Sigma^g_{\sigma,\sigma'} \tilde{\Gamma}^{\sigma'}_{\alpha,\alpha'}\right) \Lambda_{\alpha'} \Lambda_{\beta'}. \tag{2.83}$$

Here $\tilde{\Gamma} = \Gamma$ except for Σ^{TR}, where $\tilde{\Gamma} = \Gamma^*$. Let $\boldsymbol{X}$ be the $\chi \times \chi$ dimensional eigenvector of $\boldsymbol{T}^{\Sigma^g}$ with the largest eigenvalue

$$T^{\Sigma^g}_{\alpha,\beta;\alpha',\beta'} (X_g)_{\alpha',\beta'} = \mu^g (X_g)_{\alpha,\beta}. \tag{2.84}$$

If the ground state is invariant under Σ^g, the largest eigenvalue satisfies $|\mu^g| = 1$. In this case, $\boldsymbol{X}$ and U are related by

$$(U_g)_{\alpha,\beta} = (X_g)^*_{\beta,\alpha}. \tag{2.85}$$

Similarly, the relations in Eqs. (2.72) or (2.74) are not practical for numerical calculation. Instead, it is convenient to define the topological indices as [15, 207, 235]

$$\mathcal{O}_{xy} := \frac{1}{\chi}\boldsymbol{Tr}(U_x U_y U_x^\dagger U_y^\dagger), \tag{2.86a}$$

$$\mathcal{O}_{x\sigma} := \frac{1}{\chi}\boldsymbol{Tr}(U_x U_\sigma U_x^\dagger U_\sigma^\dagger), \tag{2.86b}$$

$$\mathcal{O}_{\mathrm{TR}} := \frac{1}{\chi}\boldsymbol{Tr}(U_{\mathrm{TR}} U_{\mathrm{TR}}^*), \tag{2.86c}$$

provided that the ground state is invariant under those symmetries.

2.9 Conclusions

In this chapter, some fundamental aspects of quantum spin systems have been presented, focusing on the relevance of symmetries in the definition of phases. In Sec. 2.1, the definition of a quantum spin system has been made more rigorous. It has been shown that the ground state of the simple Heisenberg model can be highly non-trivial for antiferromagnetic interaction. In Sec. 2.2, conventional phases of matter are discussed. The notion of long-range order has been introduced and we showed that, in a physical ground state with long-range order, spontaneous breaking of some symmetries of the Hamiltonian is expected in order to respect the law of large numbers. When the broken symmetry is continuous, one should observe the presence of infinitely many low-lying energy eigenstates. While SSB is expected to occur in a system of dimensions larger or equal to two, strong quantum fluctuations in a one-dimensional system prevent long-range correlation and the breaking of continuous symmetry.

In Sec. 2.3, it was argued that the nature of the ground state in the Heisenberg chain should depend on S. In particular, for odd integer spin, the ground state should be gapped and possess non-trivial topological propriety. In Sec. 2.4, a model closely related to the spin-1 Heisenberg chain, the AKLT model, has been introduced. This model is exactly solvable, and its ground state $|\boldsymbol{\phi}_{\mathrm{VBS}}\rangle$ captures the essence of the properties of the Haldane state. While the properties of the Haldane phase used to be explained through the mechanism of hidden symmetry breaking, the Haldane phase is now understood as a SPT phase characterized by topological indices. A heuristic derivation of these indices and their role in the protection of the phases is presented in Sec. 2.5.

A first step toward a more rigorous definition of topological indices is the introduction of the MPS formalism as presented in Sec. 2.6. This framework enables simpler and more efficient calculations both analytically and numerically. In Sec. 2.7, MPSs are used to discuss topological indices and the classification of the projective representation of the symmetry group of the Hamiltonian. Finally, in Sec. 2.8, numerical methods based on the MPS representation are described. In particular, it is shown how physical quantities or topological indices can be obtained using the iDMRG algorithm.

Chapter 3

Field-theoretical analysis

In this chapter, the ground-state phase diagrams of the spin-$\frac{1}{2}$ XXZ ladder with CCI will be explored in detail using an effective field method called bosonization [71, 73], and spin-chirality dualities. The bosonization is a very powerful method used to analyze one-dimensional systems. It allows the low-energy sector of certain fermionic models at specific points to be connected to corresponding bosonic models, which are typically easier to analyze. For this dissertation, we consider the special point where the two legs of the ladder are independent and treat all inter-leg interactions as perturbations:

$$|J_{\perp}|, |J_{\times}|, 2|K_{\mathrm{ch}}| \ll J. \tag{3.1}$$

Such an approach has been used in a variety of ladder models [27, 28, 62, 63, 68–70, 96, 118, 173, 175, 180, 192–194, 215, 220, 230, 238, 239, 246, 257]. Other approaches are possible, such as an effective field theory around the SU(4)-symmetric point [137, 138]. Bosonization results obtained in the perturbative regime as in Sec. 3.2.1 are not applicable to the strong CCI regime. To study the latter regime, the two types of dualities are employed to map the bosonization results to other parameter regimes, including both positive and negative strong K_{ch} interactions.

This chapter will be split into three main sections: In the first section, 3.1, a review of the bosonization and its application to a spin-$\frac{1}{2}$ chain will be provided. This review is inspired by Gogolin's book [73]. In Sec. 3.1.1 an effective field theory that describes the Heisenberg chain in terms of fermionic currents will be developed. Then, in Sec. 3.1.2, this effective field theory will be mapped to a bosonic model. The bosonized expressions of some operators will also be provided in this section.

In Sec. 3.2, the SU(2)-symmetric version of the Hamiltonian in Eq. (1.22) with arbitrary signs of $J_{\perp}$ and K_{ch} interactions will be investigated to establish the global phase structure. This section starts with the derivation of the bosonized expression of the CCI model for weak interchain coupling in Sec. 3.2.1. In Sec. 3.2.2, the bosonized version of the Hamiltonian will be analyzed, deriving the expression of the different transition and crossover lines. As the SU(2) symmetry of the Hamiltonian is explicitly lost during the Abelian bosonization. The results obtained in this section can be used directly for the study of the anisotropic model. The effect of the spin-chirality duality transformations on this phase diagram will be explained in Sec. 3.2.3. And in Sec. 3.2.4, the full phase diagram in the K_{ch}-$J_{\perp}$ plane will be presented. This phase diagram will contain many ordered phases but no "new" SPT phase so an extended version of the model will be investigated in the third section of this chapter.

In Sec. 3.3, $J_\perp$ and K_{ch} interactions will be restricted to positive values, and XXZ anisotropy in the interaction along the rung ($J_\perp$) will be considered. This interaction explicitly breaks the SU(2) symmetry of the Hamiltonian in Eq. (1.22) down to the $\mathrm{U}(1) \times \mathbb{Z}_2$ symmetry, splitting some transition lines into two and enabling the emergence of new ordered and SPT phases. The same strategies as in Sec. 3.2 will be employed to establish a theoretical phase diagram in the Δ-K_{ch} plane for fixed $J_\perp$ which is shown in Fig. 3.5.

3.1 Review of the bosonization of spin-$\frac{1}{2}$ chain

In this section, we review the bosonization method. As explained in Appendix A.1, the Heisenberg chain corresponds to the low-energy effective Hamiltonian that describes a half-filled Hubbard chain with strong Coulomb interaction. To derive the bosonized expression for the Heisenberg chain, we first obtain a continuous field description of the Hubbard chain in Sec. 3.1.1. While deriving this description, we preserve the SU(2) symmetry by expressing the model exclusively in terms of fermionic currents. The effective Hamiltonian takes the Sugawara form, perturbed by marginal terms. These fermionic currents represent both the spin and charge sectors of the theory. The charge sector is gapped and can be disregarded when analyzing the low-energy properties of the model. The spin sector corresponds to the continuous field description of the Heisenberg Hamiltonian. In Sec. 3.1.2, this Hamiltonian will be mapped to a Gaussian model by re-expressing the original fermionic operators in terms of scalar fields.

3.1.1 Effective field theory for a Hubbard chain

The bosonization of a spin-1/2 Heisenberg chain will be derived from the low-energy effective theory of the Hubbard model given by

$$H = -t \sum_j \sum_{\alpha=\uparrow,\downarrow} \left(c^\dagger_{j,\alpha} c_{j+1,\alpha} + h.c. \right) + U \sum_j n_{j\uparrow} n_{j\downarrow}. \tag{3.2}$$

This Hamiltonian can be rewritten as the sum of the kinetic (H_0) and the interaction (H_{int}) part. At first, we suppose that the interactions is sufficiently weak so that we can treat it as a perturbation; we then assume that the same field theory qualitatively holds for larger interactions, in order to obtain the field theory for a Heisenberg chain.

To obtain the field-theoretical expression of this Hamiltonian, it is convenient to separate the fermionic operator into its left and right components as follows:

$$c_\alpha(x) = e^{ik_{\text{F}}x} R_\alpha + e^{-ik_{\text{F}}x} L_\alpha. \tag{3.3}$$

Here, $k_{\text{F}} = \frac{\pi}{2a}$ is the Fermi point, and a is the lattice spacing. Using this decomposition, the continuous limit of the kinetic part is given by

$$H_0 = -iv_{\text{F}} \int \mathrm{d}x \sum_\alpha \left(R^\dagger_\alpha \partial_x R_\alpha - L^\dagger_\alpha \partial_x L_\alpha \right), \tag{3.4}$$

with $v_{\rm F} = 2ta$ being the Fermi velocity.

The H_0 term can be rewritten in the form of the Sugawara Hamiltonian by introducing two types of left and right fermionic currents as

$$\bar{J} = \sum_{\alpha,\beta} R^{\dagger}_{\alpha,\beta} R_{\alpha,\beta} \; J = \sum_{\alpha,\beta} L^{\dagger}_{\alpha,\beta} L_{\alpha,\beta}, \tag{3.5a}$$

$$\bar{\boldsymbol{J}}^a = \frac{1}{2}\sum_{\alpha,\beta} R^{\dagger}_{\alpha}\sigma^a_{\alpha\beta} R_{\beta}, \;\; \boldsymbol{J}^a = \frac{1}{2}\sum_{\alpha,\beta} L^{\dagger}_{\alpha}\sigma^a_{\alpha\beta} L_{\beta}. \tag{3.5b}$$

Here, J and $\bar{J}$ are currents associated with the U(1) symmetry and $\boldsymbol{J}$, $\bar{\boldsymbol{J}}$ are associated with the SU(2) symmetry. In its Sugawara form, the Hamiltonian is written in terms of the fermionic currents as

$$H_0 = \frac{\pi v_{\rm F}}{2}\int {\rm d}x(: JJ : + : \bar{J}\bar{J} :) + \frac{2\pi v_{\rm F}}{3}\int {\rm d}x(: \boldsymbol{J}\cdot\boldsymbol{J} : + : \bar{\boldsymbol{J}}\cdot\bar{\boldsymbol{J}} :), \tag{3.6}$$

where ":" denotes the normal ordering of operators.

Let us now consider the interaction part of the Hamiltonian,

$$H_{\rm int} = \frac{1}{2}\int {\rm d}x{\rm d}x' \sum_{\alpha,\beta,\alpha',\beta'} c_{\alpha}(x)^{\dagger} c_{\beta}(x')^{\dagger} Q_{\alpha\beta\alpha'\beta'}(x-x') c_{\beta'}(x') c_{\alpha'}(x). \tag{3.7}$$

Here, $Q_{\alpha\beta\alpha'\beta'}(x-x')$ determines the type of interaction. For onsite Coulomb interaction, one has

$$Q_{\alpha\beta\alpha'\beta'}(x-x') = U_1(x-x')\delta_{\alpha\alpha'}\delta_{\beta\beta'} - U_2(x-x')\delta_{\alpha\beta'}\delta_{\beta\alpha'}, \tag{3.8}$$

with $U_1(x) = 2U_2(x) = \frac{2}{3}U\delta(x)$. The interaction part can also be expressed in terms of the fermionic currents. Let us consider the most general situation for a moment and suppose that the system is not half-filled and ignore scattering processes that do not conserve the total momentum. Using the decomposition in Eq. (3.3) and the following identities

$$\sum_{\alpha,\beta} R^{\dagger}_{\alpha} L_{\alpha} L^{\dagger}_{\beta} R_{\beta} = -\frac{1}{2} J\bar{J} - 2\boldsymbol{J}\cdot\bar{\boldsymbol{J}}, \tag{3.9a}$$

$$\lim_{x\to x'}\sum_{\alpha,\beta} R^{\dagger}_{\alpha}(x) R_{\beta}(x) R^{\dagger}_{\beta}(x') R_{\alpha}(x') = \frac{1}{2}\bar{J}\bar{J} + 2\bar{\boldsymbol{J}}\cdot\bar{\boldsymbol{J}}, \tag{3.9b}$$

$$\lim_{x\to x'}\sum_{\alpha,\beta} L^{\dagger}_{\alpha}(x) L_{\beta}(x) L^{\dagger}_{\beta}(x') L_{\alpha}(x') = \frac{1}{2} JJ + 2\boldsymbol{J}\cdot\boldsymbol{J}, \tag{3.9c}$$

the interaction part can be rewritten as

$$H_{\rm int} = \int {\rm d}x\Big[g_4(J^2 + \bar{J}^2) + g_c J\bar{J} + g'_4(\boldsymbol{J}\cdot\boldsymbol{J} + \bar{\boldsymbol{J}}\cdot\bar{\boldsymbol{J}}) + g_s \boldsymbol{J}\cdot\bar{\boldsymbol{J}}\Big], \tag{3.10}$$

with the coupling constants given by

$$g_4 = \frac{U}{4}, \;\; g'_4 = -\frac{U}{3}, \;\; g_s = -2U, \;\; g_c = \frac{U}{2}. \tag{3.11}$$

Thus, the Hamiltonian can be fully expressed in terms of currents. Remarkably, the charge and spin currents remain decoupled, allowing the Hamiltonian to be written as the sum of a charge part H_c (depending on J) and a spin part H_s (depending on $\boldsymbol{J}$). This is the well-known spin-charge separation in the Hubbard chain. The spin part is given by

$$H_s = \frac{2\pi v_s}{3} \int \mathrm{d}x (: \boldsymbol{J} \cdot \boldsymbol{J} + \bar{\boldsymbol{J}} \cdot \bar{\boldsymbol{J}} :) + g_s \int \mathrm{d}x \boldsymbol{J} \cdot \bar{\boldsymbol{J}}, \tag{3.12}$$

with

$$v_s = v_\mathrm{F} + \frac{2g_4}{\pi}. \tag{3.13}$$

For the half-filled Hubbard chain, Umklapp processes that change the total momentum by $4k_\mathrm{F} = \frac{2\pi}{a}$ cannot be ignored; indeed, on a lattice, total momentum is only conserved up to a reciprocal vector. These processes correspond to

$$g_u \sum_{\alpha,\beta} \left(R^\dagger_\alpha L_\alpha R^\dagger_\beta L_\beta + h.c. \right), \tag{3.14}$$

with $g_c = g_u$ for Coulomb interaction. In the presence of Umklapp processes, the charge part of the Hamiltonian can be rewritten using the pseudospin vector currents $\boldsymbol{I}$. These currents are obtained from the usual spin current $\boldsymbol{J}$ by a particle-hole transformation, $c_{j\downarrow} \to (-1)^j c^\dagger_{j\downarrow}$. The pseudospin currents are defined as

$$\bar{I}^z = \sum_\alpha : R^\dagger_\alpha R_\alpha := \frac{1}{2} \bar{J}, \;\; \bar{I}^+ = R^\dagger_\uparrow R^\dagger_\downarrow, \;\; \bar{I}^- = \left(\bar{I}^+\right)^\dagger. \tag{3.15}$$

Using these definitions, the charge Hamiltonian H_c takes the form

$$H_c = \frac{2\pi v_c}{3} \int \mathrm{d}x (: \boldsymbol{I} \cdot \boldsymbol{I} + \bar{\boldsymbol{I}} \cdot \bar{\boldsymbol{I}} :) + \int \mathrm{d}x \left[4g_c I^z \bar{I}^z + 2g_u \left(I^+ \bar{I}^- + I^- \bar{I}^+ \right) \right], \tag{3.16}$$

where

$$v_c = v_\mathrm{F} + \frac{3g_4'}{\pi}. \tag{3.17}$$

Both the spin and charge sectors share a similar form and include backscattering terms $\boldsymbol{J} \cdot \bar{\boldsymbol{J}}$ and $\boldsymbol{I} \cdot \bar{\boldsymbol{I}}$. Since the currents obey the $\mathrm{SU}_1(2)$ Kac-Moody algebra, the renormalization group (RG) equation for the coupling constants of the backscattering terms can be obtained as

$$\frac{\mathrm{d}g}{\mathrm{d}l} = \frac{1}{2\pi} g^2, \tag{3.18}$$

with l being the logarithmic RG scale. For $g = g_s < 0$, the backscattering term in the spin sector is irrelevant and vanishes under RG. Consequently, the spin part of the Hamiltonian remains gapless, consistent with Haldane's prediction. On the other hand, for $g = g_c = g_u > 0$, these coupling constants grow under RG, driving the system to strong coupling. At strong coupling, charge excitations become gapped, and the charge sector can be ignored in the analysis of the low-energy physics. This is equivalent to the Mott transition discussed in Appendix A.1. Remarkably, in one-dimensional systems, the Mott transition occurs for any finite value of the Coulomb interaction, in contrast to higher dimensions, where a minimum threshold of Coulomb interaction is required to induce the Mott transition.

In the present derivation, it has been assumed that the interaction part is small enough to be treated as a perturbation. Consequently, the relations in Eq. (3.11) cannot be trusted for large Coulomb interactions. However, the structure of the Hamiltonian, written as products of currents, is dictated by the symmetry of the theory and remains valid even for larger Coulomb interactions. Using the Bethe ansatz solution [58, 112], it is possible to determine the values of some parameters in the theory. For instance, as $U/t \to \infty$, the spin velocity v_s approaches $\frac{\pi J a}{2}$

3.1.2 Bosonization

The manifestly SU(2) invariant form of the spin Hamiltonian in Eq. (3.12) is convenient, for example, in deriving the RG equation (3.18) while keeping this symmetry. However, in discussing physical operators, it is useful to break this manifest invariance and employ Abelian bosonization. In bosonization, the left and right components of the fermionic field using continuous scalar fields as

$$L_\alpha(x) \approx \frac{1}{\sqrt{2\pi a}} \exp\left(-i2\sqrt{\pi}\varphi_{L\alpha}(x)\right), \tag{3.19a}$$

$$R_\alpha(x) \approx \frac{1}{\sqrt{2\pi a}} \exp\left(+i2\sqrt{\pi}\varphi_{R\alpha}(x)\right). \tag{3.19b}$$

From these fields, it is possible to construct a scalar field and its dual counterpart for each spin component as

$$\Phi_\alpha = \varphi_{R\alpha} + \varphi_{L\alpha}, \;\; \Theta_\alpha = -\varphi_{R\alpha} + \varphi_{L\alpha}. \tag{3.20}$$

The charge and spin sectors of the theory can now be described in terms of symmetric and antisymmetric combinations of these fields:

$$\phi_c = \frac{\Phi_\uparrow + \Phi_\downarrow}{\sqrt{2}}, \;\; \phi_s = \frac{\Phi_\uparrow - \Phi_\downarrow}{\sqrt{2}}, \tag{3.21a}$$

$$\theta_c = \frac{\Theta_\uparrow + \Theta_\downarrow}{\sqrt{2}}, \;\; \theta_s = \frac{\Theta_\uparrow - \Theta_\downarrow}{\sqrt{2}}. \tag{3.21b}$$

Using the fact that

$$\frac{1}{3}(\boldsymbol{J} \cdot \boldsymbol{J} + \bar{\boldsymbol{J}} \cdot \bar{\boldsymbol{J}}) = J^z J^z + \bar{J}^z \bar{J}^z, \tag{3.22a}$$

$$J^z = \frac{1}{2\sqrt{2\pi}} \partial_x (\phi_s + \theta_s), \tag{3.22b}$$

$$\bar{J}^z = \frac{1}{2\sqrt{2\pi}} \partial_x (\phi_s - \theta_s). \tag{3.22c}$$

the kinetic part of the spin Hamiltonian can be bosonized as

$$H_s = \int \mathrm{d}x \frac{v}{2}\Big[(\partial_x\phi_s)^2 + (\partial_x\theta_s)^2\Big]. \tag{3.23}$$

This equality holds because the currents of the Gaussian Hamiltonian obey the same algebra as the currents J and $\bar{J}$.

Likewise, Eq. (3.19) can be used to obtain the bosonized expression of the spin operator $\boldsymbol{S}_j \to a\boldsymbol{S}(x)$. To this end, we first express it as

$$\boldsymbol{S}(x) = \frac{1}{2}\sum_{\alpha,\beta} c^\dagger_\alpha(x)\boldsymbol{\sigma}_{\alpha\beta}c_\beta(x) = \boldsymbol{J}(x) + \bar{\boldsymbol{J}}(x) + (-1)^j\boldsymbol{n}(x), \tag{3.24}$$

where the staggered part $\boldsymbol{n}$ is given by

$$\boldsymbol{n}(x) = \sum_{\alpha,\beta}\left(R^\dagger_\alpha(x)\frac{\boldsymbol{\sigma}_{\alpha\beta}}{2}L_\beta(x) + L^\dagger_\alpha(x)\frac{\boldsymbol{\sigma}_{\alpha\beta}}{2}R_\beta(x)\right), \tag{3.25}$$

and $\boldsymbol{\sigma}$ is given by $(\sigma^x, \sigma^y, \sigma^z)$ is the vector comprised of the different Pauli matrices. The uniform part of the spin operator, $\boldsymbol{J}$ and $\bar{\boldsymbol{J}}$, can be bosonized using only the spin fields

$$J^+ = R^\dagger_\uparrow R_\downarrow = \frac{1}{2\pi a}\exp\left(-i\sqrt{2\pi}(\phi_s - \theta_s)\right), \tag{3.26a}$$

$$\bar{J}^+ = L^\dagger_\uparrow L_\downarrow = \frac{1}{2\pi a}\exp\left(i\sqrt{2\pi}(\phi_s + \theta_s)\right), \tag{3.26b}$$

and J^z, $\bar{J}^z$ given in Eq. (3.22). The bosonized version of the staggered part depends on the charge and spin fields as

$$n^z = -\frac{1}{\pi a}\cos\left(\sqrt{2\pi}\phi_c\right)\sin\left(\sqrt{2\pi}\phi_s\right), \tag{3.27a}$$

$$n^\pm = \frac{1}{\pi a}\cos\left(\sqrt{2\pi}\phi_c\right)\exp\left(\pm i\sqrt{2\pi}\theta_s\right). \tag{3.27b}$$

As the charge excitations are gapped, the ϕ_c field is locked around a certain value. Accordingly, the term $\cos\left(\sqrt{2\pi}\phi_c\right)$ can be replaced by its expectation value in Eq. (3.27). As a consequence, the spin operator is expressed entirely using only ϕ_s and θ_s. To make the link with the notation used in [192–194, 246], we shall rescale those fields as

$$\phi_s \to \sqrt{2}\phi + \sqrt{\pi}, \tag{3.28a}$$

$$\theta_s \to \frac{\theta}{\sqrt{2}}. \tag{3.28b}$$

Grouping all together, one can derive the expression of the spin and dimer operators on the nth chain of the ladder in terms of the bosonic field ϕ_n and

θ_n as

$$S^z_{n,j} = \frac{a}{\sqrt{\pi}}\partial_x\phi_n + (-1)^j a_1 \cos\left(2\sqrt{\pi}\phi_n\right) + \cdots, \tag{3.29a}$$

$$S^+_{n,j} = e^{i\sqrt{\pi}\theta_n}\Big[b_0(-1)^j + b_1\cos\left(2\sqrt{\pi}\phi_n\right) + \cdots\Big], \tag{3.29b}$$

$$S^\alpha_{n,j}S^\beta_{n,j+1} = (-1)^j\delta_{\alpha\beta}d_\alpha\sin\left(2\sqrt{\pi}\phi_n\right) + \cdots, \tag{3.29c}$$

where $S^\pm_{n,j} := S^x_{n,j} \pm iS^y_{n,j}$, a is the lattice constant, and a_1, b_0, b_1, and d_α ($\alpha = x, y, z$) are non-universal coefficients [93, 94, 146, 246]. For SU(2)-symmetric models, these coefficients satisfy $a_1 = b_0 =: \bar{a}$ and $d_x = d_y = d_z := \bar{d}$. The Hamiltonian for the nth chain is given by

$$H = \int \mathrm{d}x \frac{v}{2}\left[\frac{1}{K}(\partial_x\phi_n)^2 + K(\partial_x\theta_n)^2\right] \tag{3.30}$$

with K=1/2. Here, the marginal term has been dropped.

3.2 Heisenberg ladder with CCI

3.2.1 Abelian bosonization for weak interchain couplings

Now, let $|J_\perp|$, $|J_\times|$, $2|K_{\mathrm{ch}}| \ll J$ be non-null, and treat the interchain interactions as perturbations. In this regime, using the rules of bosonization given in Eq. (3.29), one can obtain a low-energy effective field Hamiltonian of the XXZ-CCI ladder as

$$\begin{aligned} H^{\mathrm{eff}}_{\mathrm{ex}} = &\int \mathrm{d}x \sum_{\nu=\pm}\frac{v_\nu}{2}\left[\frac{1}{K_\nu}(\partial_x\phi_\nu)^2 + K_\nu(\partial_x\theta_\nu)^2\right] \\ &+ g_+\cos\left(2\sqrt{2\pi}\phi_+\right) + g_-\cos\left(2\sqrt{2\pi}\phi_-\right) \\ &+ \tilde{g}_-\cos\left(\sqrt{2\pi}\theta_-\right) - \gamma_1\cos\left(2\sqrt{2\pi}\phi_+\right)\cos\left(\sqrt{2\pi}\theta_-\right) \\ &+ \gamma_{\mathrm{bs}}\cos\left(2\sqrt{2\pi}\phi_+\right)\cos\left(2\sqrt{2\pi}\phi_-\right) + \ldots, \end{aligned} \tag{3.31}$$

where

$$\phi_\pm := \frac{1}{\sqrt{2}}(\phi_1 \pm \phi_2), \quad \theta_\pm := \frac{1}{\sqrt{2}}(\theta_1 \pm \theta_2), \tag{3.32}$$

and ellipses indicate terms that have higher scaling dimensions.

The bare coupling constants are given by

$$g_\pm = \frac{1}{2a}\Big[a_1^2(J_\perp\Delta - 2J_\times) \mp 4K_{\mathrm{ch}}(9d^2 - 3d'^2)\Big], \tag{3.33a}$$

$$\tilde{g}_- = \frac{b_0^2}{a}(J_\perp - 2J_\times), \tag{3.33b}$$

$$\gamma_1 = \frac{b_1^2}{2a}(J_\perp + 2J_\times - CK_{\mathrm{ch}}), \tag{3.33c}$$

where $3d := \sum_\alpha d_\alpha$, $3d'^2 := \sum_\alpha d_\alpha^2$, and $\gamma_{\rm bs}$ is generated from the backscattering in each chain and the CCI. Here, $C > 0$ is defined in Appendix B.1. For an SU(2)-symmetric model, the expressions of the coupling constants $g_\pm$ take simpler forms:

$$g_\pm = \frac{1}{2a}\Big[\bar{a}^2(J_\perp - 2J_\times) \mp 24\bar{d}^2 K_{\rm ch}\Big]. \tag{3.34}$$

The terms $g_\pm$ and $\tilde{g}_-$ have scaling dimensions $2K_\pm$ and $(2K_-)^{-1}$, respectively. Assuming that the value of $K_\pm$ remains close to those of isolated spin-$\frac{1}{2}$ chain, the $g_\pm$ and $\tilde{g}_-$ terms both have scaling dimensions 1, making them strongly relevant. Although interchain coupling effects could modify the values of $K_\pm$, for the purpose of this dissertation, such changes will be considered negligible. Therefore, the value of the parameter given in Eqs. (3.28) will be used, namely $K_\pm = \frac{1}{2}$. On the contrary, the γ_1 and $\gamma_{\rm bs}$ terms have scaling dimensions of 2 in this regime and are only marginal.

3.2.2 Phase diagram from bosonization: weak interchain regime

In this section, the bosonized expression of the Hamiltonian (3.31) will be used to analyze the ground-state phase structure of the CCI model given in Eq. (1.18). The competition between the different cosine terms in Eq. (3.31) tends to pin the scalar field at different positions depending on the relative strength or sign of the coupling constants. These changes in the pinning position are associated with phase transitions, which will be analyzed in the first part. Subsequently, we will see that some of the phases identified earlier can be characterized using order parameters, whose bosonized expressions depend on the pinning values of the scalar fields. Finally, in phases that cannot be characterized by order parameters (featureless phases), the dominant correlations will be analyzed using both a heuristic argument from Abelian bosonization and a more rigorous argument derived from the mapping of the Hamiltonian to free massive Majorana fermions.

Analysis of the bosonized Hamiltonian

In the first instance, the marginal γ_1 and $\gamma_{\rm bs}$ terms will be neglected while establishing the phase diagram in Fig. 3.1(a); their effect will be discussed later when comparing this tentative phase diagram to the numerical simulation results.

In the effective Hamiltonian, the $\pm$ channels are decoupled and can be analyzed independently, as in Refs. [192–194, 246]. The $+$ channel is described by a sine-Gordon model. The strongly relevant g_+ term tends to lock the ϕ_+ field at a position that depends on the sign of g_+. A $c = 1$ Gaussian transition will occur at

$$g_+ = 0. \tag{3.35}$$

The $-$ channel is described by a dual-field double sine-Gordon Hamiltonian [136]. Both g_- and $\tilde{g}_-$ terms are strongly relevant and tend to lock either the ϕ_- or θ_- field. Since the two fields do not commute, the g_- and $\tilde{g}_-$

terms compete with each other, and the term with the larger coupling constant dominates. Namely, if $|g_-| \gtrsim |\tilde{g}_-|$ ($|g_-| \lesssim |\tilde{g}_-|$), the ϕ_- (θ_-) field is locked, and a $c = 1/2$ Ising transition occurs at [136, 230]

$$|g_-| \approx |\tilde{g}_-|. \tag{3.36}$$

By replacing $g_\pm$ and $\tilde{g}_-$ in Eqs. (3.35) and (3.36) with their expressions in Eqs. (3.34) and (3.33b), one can derive the expressions of the Gaussian and Ising transition lines.

Along the purple line in Fig. 3.1, defined by

$$K_{\mathrm{ch}} = \gamma(J_\perp - 2J_\times) \neq 0, \tag{3.37}$$

Gaussian and Ising transitions occur simultaneously. Here the proportionality constant γ is estimated to be

$$\gamma = \frac{\bar{a}^2}{4(9d^2 - 3d'^2)} \approx 0.75, \tag{3.38}$$

where the numerical values of $\bar{a}$, d, and d' are those of a Heisenberg chain at a certain scale [246]. This simultaneous occurrence of the transitions in the two channels is due to the SU(2) symmetry of the model. At this transition, the system can be described by a $SU(2)_2$ Wess-Zumino-Witten (WZW) theory with a central charge $c = 3/2$ [25, 27, 28, 76, 89–92, 173, 180, 215, 220, 255].

Along the blue line in Fig. 3.1, defined by

$$K_{\mathrm{ch}} = -3\gamma(J_\perp - 2J_\times) \neq 0, \tag{3.39}$$

another Ising transition occurs in the $-$ channel while the $+$ channel remains gapped.

Analysis of the phase structure

The phase diagram in the weak coupling regime is very similar to the phase diagram of the DDI model, which is given in Fig. 1.5(a). Two transition lines separate the phase diagram in the K_{ch}-$J_\perp$ plane into four regions, depending on the signs and magnitudes of $J_\perp - 2J_\times$ or K_{ch}.

In regions dominated by the CCI, the SD or CD orders appear for positive or negative K_{ch}, respectively. The heuristic argument made in Sec. 1.3.2 can be formalized by calculating the bosonized expression of the SD and CD order operators:

$$\mathcal{O}_{\mathrm{SD}}(j) = -(-1)^j(3d)\cos\left(\sqrt{2\pi}\phi_+\right)\sin\left(\sqrt{2\pi}\phi_-\right), \tag{3.40a}$$

$$\mathcal{O}_{\mathrm{CD}}(j) = -(-1)^j(3d)\sin\left(\sqrt{2\pi}\phi_+\right)\cos\left(\sqrt{2\pi}\phi_-\right). \tag{3.40b}$$

In the regions with large $|K_{\mathrm{ch}}|$, the $\phi_\pm$ fields are pinned at specific values. For $K_{\mathrm{ch}} > 0$, the fields are pinned at $2\sqrt{2\pi}(\phi_+, \phi_-) = (0, \pm\pi)$, leading to a finite value of the SD order parameter. From its bosonized expression (3.40a), one finds $\langle \mathcal{O}_{\mathrm{SD}}(j) \rangle = \pm(-1)^j c_{\mathrm{SD}}$, where c_{SD} is a constant independent of j.

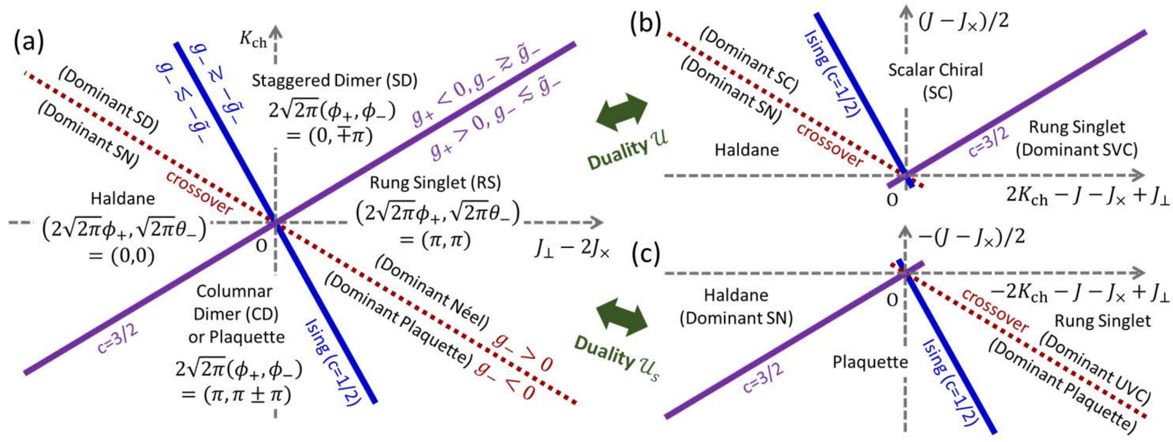

FIGURE 3.1: Schematic ground-state phase diagrams of the J-$J_\perp$-$J_\times$-$K_{\rm ch}$ ladder (1.22), predicted by the Abelian bosonization and the two types of dualities. (a) Case of weak interchain couplings (3.1). Each phase in (a) is characterized by the locking positions of bosonic fields, as described in Refs. [192, 194, 246]. (b,c) Dual counterparts to (a) obtained by the transformations $\mathcal{U}$ and $\mathcal{U}_{\rm s}$, respectively, in Eqs. (3.48); see Eq. (1.25) for the transformation of the coupling constants. These phase diagrams are valid under the condition (3.54). The transition and crossover lines in (a) are given by Eqs. (3.37), (3.39), and (3.43) while those in (b,c) are given by Eqs. (3.55), (3.56), and (3.57). Reproduced from Fig. 4 of Ref. [55]. Copyright 2024 by the Physical Society of Japan.

Similarly, for $K_{\rm ch} < 0$, the fields are pinned at $2\sqrt{2\pi}(\phi_+, \phi_-) = (\pi, \pi \pm \pi)$. In this case, the CD order parameter acquires a finite value.

The CD order parameter may not fully capture the characteristics of the concerned phase for some reason. As shown in Fig. 3.3, this phase is expected to extend into regions with significantly large negative values of $J_\perp$. There strong ferromagnetic interactions along the rungs favor a state where spins on each rung are symmetrized. Additionally, the CD order parameter is not invariant under the transformation $\mathcal{U}_{\rm s}$, even though this transformation does not alter the broken symmetry of the phase.

To resolve these issues, we introduce the plaquette order operator

$$\begin{aligned}\mathcal{O}_{\rm plaq}(j) = \frac{1}{4}&\left(\boldsymbol{S}_{1,j-1} + \boldsymbol{S}_{2,j-1}\right) \cdot \left(\boldsymbol{S}_{1,j} + \boldsymbol{S}_{2,j}\right) \\ &- \left(\boldsymbol{S}_{1,j} + \cdot \boldsymbol{S}_{2,j}\right) \cdot \left(\boldsymbol{S}_{1,j+1} + \boldsymbol{S}_{2,j+1}\right),\end{aligned} \tag{3.41}$$

which provides a more suitable characterization of the concerned phase. Indeed, the introduction of a diagonal dimer operator, explicitly symmetrizes the roles of the spins on each end of a rung, as illustrated in Fig. 1.4(e). Furthermore, since it depends only on the total spin on each rung $\left(\boldsymbol{S}_{1,j} + \boldsymbol{S}_{2,j}\right)$, it is clearly invariant under $\mathcal{U}_{\rm s}$.

In regions dominated by $|J_\perp - 2J_\times|$, the Hamiltonian (1.22) can be well approximated by the Heisenberg ladder model in Eq. (1.1). The RS and Haldane phases are naturally expected in this regime, as discussed in Sec. 1.2 and illustrated in Fig. 1.3.

Analysis of the dominant correlation

Both the RS and Haldane phases are featureless in the sense that they do not break any symmetry of the Hamiltonian and their respective ground state is unique and separated from excitations by an energy gap. These phases, however, can be further separated into different regions, according to their dominant short-range correlations. Near the $K_{\text{ch}} = 0$ line, strong Néel or SN correlations are expected in the RS and Haldane phases, respectively. The corresponding order operators, given in Eq. (1.5), can be bosonized as

$$\mathcal{O}_{\text{Néel}}(j) = -(-1)^j a_1 \sin\left(\sqrt{2\pi}\phi_+\right) \sin\left(\sqrt{2\pi}\phi_-\right), \tag{3.42a}$$

$$\mathcal{O}_{\text{SN}}(j) = (-1)^j a_1 \cos\left(\sqrt{2\pi}\phi_+\right) \cos\left(\sqrt{2\pi}\phi_-\right). \tag{3.42b}$$

As shown by the locking positions of the fields (summarized in Fig. 3.1(a)), within the RS phase, the $\sin\left(\sqrt{2\pi}\phi_+\right)$ component of the CD and Néel order operators in Eqs. (3.40b) and (3.42a) acquires a finite average. On the other hand, due to the locking of θ_-, the ϕ_- field fluctuates significantly inside the RS phase. Consequently, the $\cos\left(\sqrt{2\pi}\phi_-\right)$ and $\sin\left(\sqrt{2\pi}\phi_-\right)$ components of the CD and Néel order operators have vanishing averages. Despite such fluctuations, when $g_- < 0$, the g_- term in Eq. (3.31) favors states around $\sqrt{2\pi}\phi_- = 0$ or π over short distances, leading to a short-range CD correlation. Likewise, $g_- > 0$ leads to short-range Néel correlation. A similar crossover is observed in the Haldane phase. While the $\cos\left(\sqrt{2\pi}\phi_+\right)$ component of the SD and SN order operators in Eqs. (3.40a) and (3.42b) acquires a finite average, the ϕ_- field fluctuates significantly over long distances. Accordingly, SD short-range correlations dominate for $g_- > 0$, while SN short-range correlations are expected for $g_- < 0$. At $g_- = 0$, i.e.,

$$K_{\text{ch}} = -\gamma(J_\perp - 2J_\times) \neq 0, \tag{3.43}$$

a crossover occurs between the two regions, as indicated by the red dotted line in Fig. 3.1(a).

The arguments presented above can be made more rigorous through the fermionization framework, as developed in Refs. [27, 28, 73, 76, 173, 180, 215, 220, 230]. Using this formalism, the two-component TLLs at $K = 1/2$, perturbed by the strongly relevant $g_\pm$ and $\tilde{g}$ terms in Eq. (3.31), can be mapped to four-component free massive Majorana fields (i.e., noncritical two-dimensional Ising models) with masses given by

$$\begin{aligned} m_{\text{t}} &= \pi a g_+ = \pi a(\tilde{g}_- - g_-) \\ &= 12\pi \bar{d}^2[\gamma(J_\perp - 2J_\times) - K_{\text{ch}}], \end{aligned} \tag{3.44a}$$

$$\begin{aligned} m_{\text{s}} &= -\pi a(\tilde{g}_- + g_-) \\ &= -12\pi \bar{d}^2[3\gamma(J_\perp - 2J_\times) + K_{\text{ch}}]. \end{aligned} \tag{3.44b}$$

The masses of the triplet m_{t} and the singlet m_{s} correspond respectively to the distance to the $c = 3/2$ and $c = 1/2$ transitions given in Eqs. (3.37) and (3.39). Depending on the signs of $m_{\text{t,s}}$, each Ising model can be in an ordered

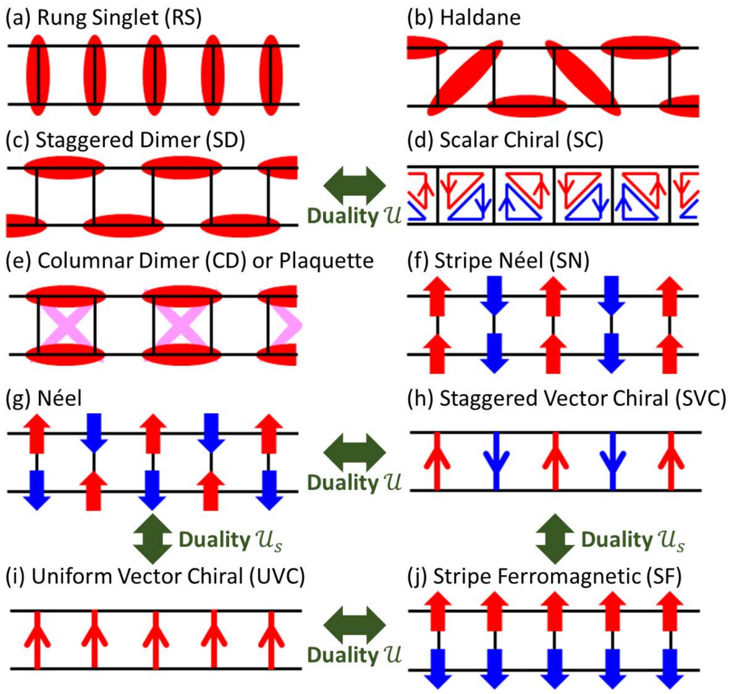

FIGURE 3.2: Ground states of the ladder models in Fig. 1.4. (a,b) Featureless states. The Haldane state is a superposition of various singlet-covering states. (c,d,e) Non-magnetic ordered states. In the SC state, each directed triangle indicates a positive scalar chirality of three spins along it. The CD state, which is predicted by bosonization for weak interchain couplings, is expected to evolve gradually into a plaquette state for large negative $J_\perp$, where two spins on each rung get symmetrized as indicated by the pink diagonal bonds. (f,g,h,i,j) Possible short-range spin and VC correlations in the RS [(g,h,i,j)] and Haldane [(f)] states. These panels should be understood as typical snapshots, and they may turn into genuine long-range orders in the presence of easy-axis anisotropy. In (f,g,j), each arrow indicates a magnetic moment along a certain axis. In (h,i), each directed bond indicates a positive vector chirality along it. See Eqs. (1.10), (3.41), (1.5), (3.52), and (1.16) for the operators that characterize these orders and correlations. All the states and the correlations in this figure appear in the phase diagram of the J-$J_\perp$-K_{ch} ladder (1.18) with $J > 0$ in Fig. 3.3, except for (j) the SF correlation which appears for $J < 0$. The duality transformations $\mathcal{U}$ and $\mathcal{U}_{\mathrm{s}}$ in Eq. (3.48) relate some of the orders and the correlations, as indicated by green two-headed arrows. Reproduced from Fig. 2 of Ref. [55]. Copyright 2024 by the Physical Society of Japan.

or disordered phase. These phases can be detected by non-local products of the Majorana operator. Namely, the σ_α and μ_α with $\alpha \in \{1,2,3\}$ are the order and disorder fields of the "triplet" Ising models, and σ and μ are the corresponding fields for the "singlet" Ising model. By retracing our steps back, the spin (3.42) and the dimer (3.40) operators in the original model can be expressed in terms of the order and disorder operators.

$$\mathcal{O}_{\mathrm{SD}}(j) \sim (-1)^j \sigma_1\sigma_2\sigma_3\mu, \tag{3.45a}$$
$$\mathcal{O}_{\mathrm{CD}}(j) \sim (-1)^j \mu_1\mu_2\mu_3\sigma, \tag{3.45b}$$
$$\mathcal{O}_{\text{Néel}}(j) \sim (-1)^j \mu_1\mu_2\sigma_3\mu, \tag{3.45c}$$
$$\mathcal{O}_{\mathrm{SN}}(j) \sim (-1)^j \sigma_1\sigma_2\mu_3\sigma. \tag{3.45d}$$

In the RS phase, the mass term m_{t} is positive while m_{s} is negative, therefore disorder operators associated with the triplet (singlet) channels have the non-zero average $\langle\mu_\alpha\rangle \neq 0$ ($\langle\mu\rangle \neq 0$). Conversely, the order operators σ_α and σ take null average values, and their correlation functions decay as follows:

$$\langle\sigma_\alpha(0)\sigma_\alpha(r)\rangle \sim K_0\left(\frac{m_{\mathrm{t}}r}{v}\right)\ (\alpha = 1,2,3), \tag{3.46a}$$
$$\langle\sigma(0)\sigma(r)\rangle \sim K_0\left(\frac{|m_{\mathrm{s}}|r}{v}\right), \tag{3.46b}$$

where the velocity is denoted by v. Here, $K_0(\cdot)$ refers to the MacDonald function, whose behavior at long distances can be approximated by

$$K_0(r) \approx \sqrt{\frac{\pi}{2r}}e^{-r}\ \ (r \gg 1). \tag{3.47}$$

Thus, within the RS phase, Néel and CD correlations decay at rates dictated by their order fields, as given by Eqs. (3.46a) and (3.46b), respectively. If $m_{\mathrm{t}} < |m_s|$, ($m_{\mathrm{t}} > |m_s|$) Néel (CD) correlation is dominant, as it decays slower than the CD (Néel) correlation. Likewise, in the Haldane phase, where $m_{\mathrm{t}} < 0$ and $m_{\mathrm{s}} > 0$, similar reasoning can be applied by interchanging the roles of the order and disorder fields. If $|m_{\mathrm{t}}| < m_s$ ($|m_{\mathrm{t}}| > m_s$), the SN (SD) correlation dominates, which decays primarily according to the correlation of μ_3 (μ) . In both the RS and Haldane phases, when $m_{\mathrm{t}} = -m_{\mathrm{s}}$, a crossover occurs in the dominant short-range correlation [27]. This criterion matches that outlined in Eq. (3.43), derived through Abelian bosonization.

3.2.3 Spin-chirality dualities

As hinted in the introduction (Sec. 1.4), both spin-chirality dualities can be used to relate the phase diagram in the strong CCI regime to the phase diagram in the weak CCI regime. In this section, this relation will be made more explicit by examining how the different order parameters transform under both spin-chirality dualities.

The two spin-chirality dualities [76, 81, 95, 97, 137, 138, 168, 253] defined in Eq. (1.14) can be described by the unitary transformations

$$\mathcal{U} := \mathcal{U}\left(\frac{\pi}{2}\right),\ \mathcal{U}_{\mathrm{s}} := \mathcal{U}_{\mathrm{s}}\left(\frac{\pi}{2}\right), \tag{3.48}$$

where

$$\mathcal{U}(\theta) = \exp\left(i\theta\sum_j n_j^{\mathrm{B}}\right), \tag{3.49a}$$

$$\mathcal{U}_{\mathrm{s}}(\theta) = \exp\left[i\theta\sum_j (-1)^j n_j^{\mathrm{B}}\right] \quad (\theta \in \mathbb{R}), \tag{3.49b}$$

with $n_j^{\mathrm{B}} := \boldsymbol{S}_{1,j}\cdot\boldsymbol{S}_{2,j} + 3/4$ being the projection operator onto the triplet states on the jth rung (i.e., the local occupation number of a triplon). Under these unitary transformations, antisymmetric spin combination $\boldsymbol{S}_{1,j} - \boldsymbol{S}_{2,j}$ and vector chirality $\boldsymbol{S}_{1,j}\times\boldsymbol{S}_{2,j}$ are exchanged as

$$e^{\pm i\frac{\pi}{2}n_j^{\mathrm{B}}}\left(S_{1,j}^{\alpha} - S_{2,j}^{\alpha}\right)e^{\mp i\frac{\pi}{2}n_j^{\mathrm{B}}} = \mp 2\left(\boldsymbol{S}_{1,j}\times\boldsymbol{S}_{2,j}\right)^{\alpha}, \tag{3.50}$$

while the uniform spin component $\boldsymbol{S}_{1,j} + \boldsymbol{S}_{2,j}$ is invariant.

Under $\mathcal{U}$ and $\mathcal{U}_{\mathrm{s}}$, the Néel operator (1.5a) is mapped to the staggered and uniform vector chiral (UVC) operators as

$$\mathcal{U}\mathcal{O}_{\text{Néel}}(j)\mathcal{U}^{\dagger} = -\mathcal{O}_{\mathrm{SVC}}(j), \tag{3.51a}$$

$$(-1)^j\mathcal{U}_{\mathrm{s}}\mathcal{O}_{\text{Néel}}(j)\mathcal{U}_{\mathrm{s}}^{\dagger} = -\mathcal{O}_{\mathrm{UVC}}(j), \tag{3.51b}$$

with

$$\mathcal{O}_{\mathrm{SVC}}(j) = \frac{1}{2}\left(\boldsymbol{S}_{1,j}\times\boldsymbol{S}_{2,j} - \boldsymbol{S}_{1,j+1}\times\boldsymbol{S}_{2,j+1}\right)^{z}, \tag{3.52a}$$

$$\mathcal{O}_{\mathrm{UVC}}(j) = \frac{1}{2}\left(\boldsymbol{S}_{1,j}\times\boldsymbol{S}_{2,j} + \boldsymbol{S}_{1,j+1}\times\boldsymbol{S}_{2,j+1}\right)^{z}. \tag{3.52b}$$

Likewise, the SD order parameter (1.10a) is mapped to the SC order parameter defined by Eq. (1.16) under the $\mathcal{U}$ duality transformation:

$$\mathcal{U}\mathcal{O}_{\mathrm{SD}}(j)\mathcal{U}^{\dagger} = -\mathcal{O}_{\mathrm{SC}}(j). \tag{3.53}$$

By comparison, the plaquette and SN operators, which depend uniquely on the symmetric spin combination $\boldsymbol{S}_{1,j} + \boldsymbol{S}_{2,j}$ as seen in Eqs. (3.41) and (1.5b), remain unchanged under $\mathcal{U}$ or $\mathcal{U}_{\mathrm{s}}$. Figure 3.2 presents a pictorial representation of all the different orders and correlations expected to appear in our model, along with their relations under $\mathcal{U}$ and $\mathcal{U}_{\mathrm{s}}$.

3.2.4 Full phase structure

Spin-chirality dualities can be used to extend the phase diagram in Fig. 3.1(a), via transformation rules outlined in the preceding section and in Sec. 1.4 in the introduction. Under $\mathcal{U}$ in Eq. (3.48), the upper half of Fig. 3.1(a) is mapped

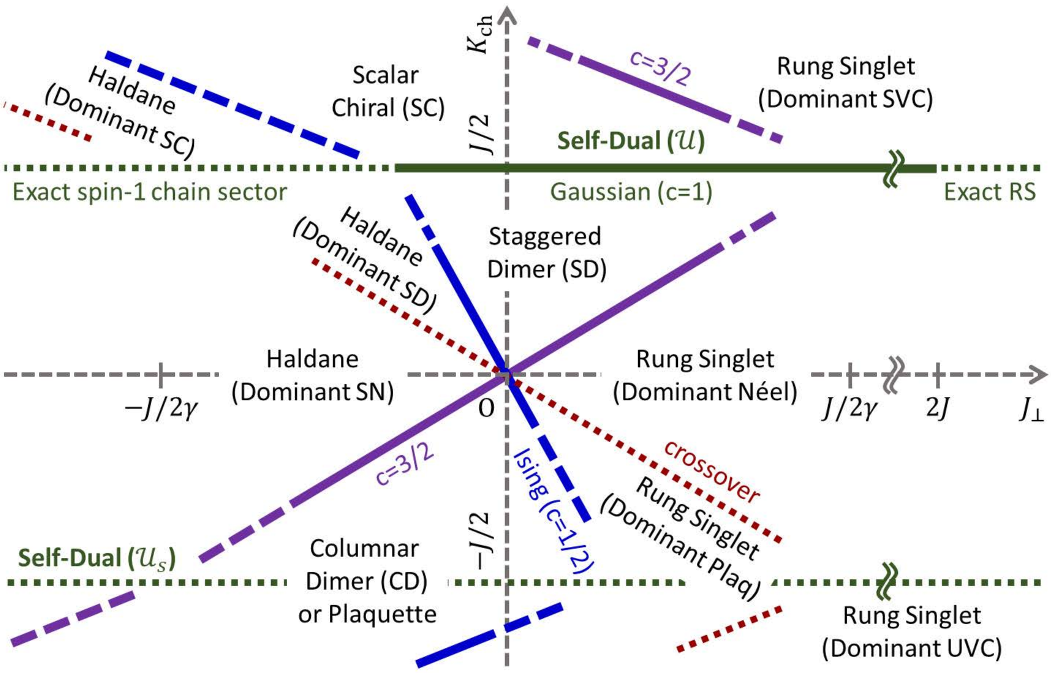

FIGURE 3.3: Schematic ground-state phase diagram of the J-$J_{\perp}$-K_{ch} ladder (1.18) with $J > 0$, predicted by the Abelian bosonization and the duality. This diagram is obtained by combining Figs. 3.1(a,b,c) and setting $J_{\times} = 0$. The model is self-dual under $\mathcal{U}$ or $\mathcal{U}_{\mathrm{s}}$ in Eq. (3.48) at $K_{\mathrm{ch}} = J/2$ and $K_{\mathrm{ch}} = -J/2$, respectively. Along the self-dual line at $K_{\mathrm{ch}} = J/2$, the system has the U(1) symmetry under Eq. (4.7), and the triplon density n^{B} is exactly conserved. Along this line, triplons are fully depleted ($n^{\mathrm{B}} = 0$) for $J_{\perp} > 2J$, leading to the exact RS ground state [76, 126, 173]; triplons are fully filled ($n^{\mathrm{B}} = 1$) for $J_{\perp} \lesssim -0.6J$, and the ground state resides in the exact spin-1 chain sector [81]. The SD-SC transition occurs on this self-dual line when triplons are partially filled ($0 < n^{\mathrm{B}} < 1$); this belongs to the $c = 1$ Gaussian universality class, according to a field-theoretical analysis around an SU(4) quantum multicritical point [137, 138]. Reproduced from Fig. 3 of Ref. [55]. Copyright 2024 by the Physical Society of Japan.

to Fig. 3.1(b). The Néel and SD correlations and orders are mapped respectively to the SVC and SC ones, while the SN correlation remains unchanged. Likewise, under $\mathcal{U}_s$, the lower half of Fig. 3.1(a) is mapped to Fig. 3.1(c). The Néel correlation is mapped to the UVC correlation, while the plaquette order and correlation remain unchanged. In Figs. 3.1(b,c), the condition for weak interchain coupling in Eq. (3.1) is modified according to the transformation rule of Eq. (1.25) as

$$|J_\perp|, \left|\frac{J+J_\times}{2} \mp K_{\text{ch}}\right|, |J-J_\times| \ll \frac{J+J_\times}{2} \pm K_{\text{ch}} \,. \tag{3.54}$$

Similarly, transition and crossover lines in Eqs. (3.37), (3.39), and (3.43) in Fig. 3.1(a) are transformed into those in Figs. 3.1(b,c) according to Eq. (1.25). The $c = 3/2$ RS-SC and Haldane-plaquette transitions occur at

$$\pm K_{\text{ch}} = \left(\frac{1}{2} \pm \frac{1}{4\gamma}\right) J - \frac{J_\perp}{2} + \left(\frac{1}{2} \mp \frac{1}{4\gamma}\right) J_\times \,, \tag{3.55}$$

the $c = 1/2$ Haldane-SC and RS-plaquette transitions occur at

$$\pm K_{\text{ch}} = \left(\frac{1}{2} \mp \frac{1}{12\gamma}\right) J - \frac{J_\perp}{2} + \left(\frac{1}{2} \pm \frac{1}{12\gamma}\right) J_\times \,, \tag{3.56}$$

and crossover in dominant correlations occurs at

$$\pm K_{\text{ch}} = \left(\frac{1}{2} \mp \frac{1}{4\gamma}\right) J - \frac{J_\perp}{2} + \left(\frac{1}{2} \pm \frac{1}{4\gamma}\right) J_\times \,. \tag{3.57}$$

Here, the upper and lower signs correspond to the cases of Figs. 3.1(b) and (c), respectively.

Below, we assume that the phase structures in Fig. 3.1 continue qualitatively even when the conditions (3.1) and (3.54) are nearly saturated. The phase diagram in Fig. 3.3 can then be obtained by combining Figs. 3.1(a,b,c) and setting $J_\times = 0$. This assumption is justified *a posteriori* through an overall agreement with the phase diagram obtained numerically in Fig. 5.1. In Fig. 5.1, the Ising transition calculated from iDMRG is located entirely in the $J_\perp < 0$ region. This discrepancy between numerical simulation and analytical prediction can be attributed to the marginal γ_1 and γ_{bs} terms in the effective Hamiltonian (3.31), which have been neglected so far.

In the $J_\perp$-K_{ch} plane, the regions of the phase diagram situated inside and outside the two self-dual lines are not direct images of each other. Indeed, consider a point with the following parameters:

$$(J, J_\perp, J_\times, K_{\text{ch}}) = (1, x, 0, y). \tag{3.58}$$

Under the duality transformations, and a rescaling such that $J = 1$, this point is mapped to

$$(J, J_\perp, J_\times, K_{\text{ch}}) = (1, \frac{2x}{1 \pm 2y}, \frac{1 \mp 2y}{1 \pm 2y}, \frac{\pm 1}{1 \pm 2y}). \tag{3.59}$$

One sees that the diagonal term is non-null after the transformations. This highlights the importance of introducing the diagonal terms during the theoretical analysis.

Analysis of marginal terms

The $\gamma_{\rm bs}$ term, originating from backscattering interactions, is negative in the limit of the decoupled chain. The CCI gives an additional contribution $C'K_{\rm ch}$ with $C' > 0$ (see Appendix B.1) to $\gamma_{\rm bs}$, making the coupling constant of the $\gamma_{\rm bs}$ term strongly negative in the region where $K_{\rm ch} < 0$ and $J_\perp - 2J_\times > 0$. As seen from its expression in Eq. (3.33c), the γ_1 coupling constant is positive in this region. Therefore in this region, where $\left\langle \cos\left(2\sqrt{2\pi}\phi_+\right)\right\rangle < 0$, the γ_1 term, with the $\cos\left(\sqrt{2\pi}\theta_-\right)$ component, tends to favor the RS phase. In addition, the $\gamma_{\rm bs}$ term, with the $\cos\left(2\sqrt{2\pi}\phi_-\right)$ component, disfavors the plaquette phase. The combined effect of these two terms tends to stabilize the RS phase over the plaquette phase in this region, thus explaining the numerical results.

As discussed in Appendix B.1, only the term $-4H_{\rm DD}$ in the CCI (Eq. (1.20)) contributes to γ_1. This contribution is absent in the inter-leg DDI model studied in Refs. [27, 28, 89, 92, 180, 192, 194, 215, 220, 246]. In these models, the effect of the γ_1 term on the plaquette-RS boundary is expected to be weaker, and this qualitative difference might explain why the plaquette-RS boundary is located entirely on the $J_\perp > 0$ side in numerical results for DDI model [28, 92, 220].

A more detailed study of the marginal perturbations would require analyzing the renormalization group flow equations, as in Ref. [157], which is beyond the scope of this dissertation.

3.3 XXZ ladder with four-spin interaction

3.3.1 Phase diagram from bosonization: weak interchain limit

The ground-state phase diagram of the J-$J_\perp$-$K_{\rm ch}$ ladder (1.18) was investigated in the previous section using both effective field theory and duality transformations. It was established that the phase diagram is separated into different phases by a $c = 3/2$ transition and an Ising transition. Notably, the $c = 3/2$ transition line is associated with the simultaneous occurrence of Gaussian and Ising transitions in the SU(2)-symmetric model. In the phase diagram of the isotropic model, no SPT phase other than the Haldane phase appears. We anticipate that introducing anisotropy in the interactions might split the $c = 3/2$ transition line into two transitions, potentially leading to the emergence of new phases in between. Indeed, in a ladder model with DDI studied in Ref. [194], the introduction of easy-axis anisotropy in the rung and leg interactions stabilized the Neel order, while easy-plane anisotropy stabilized a SPT phase called Haldane*.

In this section, the effect of anisotropy on the ground-state phase diagram will be analyzed in more detail. Particular attention will be given to the region with $J_\perp$ and K_{ch} positives, where the phase structure is especially rich. In contrast, in the region with $K_{\mathrm{ch}} < 0$, the $\mathcal{U}_{\mathrm{s}}$ self-dual line is not associated with any phase transition. For instance, the SN and RS* phases, which emerge in the presence of anisotropy for $K_{\mathrm{ch}} < 0$, as shown in Fig. 1.5(b), or the plaquette phase remain invariant under $\mathcal{U}_{\mathrm{s}}$. Therefore, this analysis will focus on regions with positive $J_\perp$ and K_{ch} interactions. Using the same approach as in the previous section, the effect of anisotropy on the phase diagram of the J-$J_\perp$-K_{ch} ladder (1.18) will first be discussed in the weak coupling regime while ignoring marginal terms.[1]

To determine the Gaussian transition line, the expression for g_+ in Eq. (3.35) is replaced with its explicit form from Eq. (3.33a), yielding

$$K_{\mathrm{ch}} = \gamma(J_\perp - 2J_\times + J_\perp\delta), \tag{3.60a}$$

where $\delta := \Delta - 1$. Similarly, by substituting Eqs. (3.33a) and (3.33b) into Eq. (3.36), the Ising transition boundary is given by

$$K_{\mathrm{ch}} = \gamma(J_\perp - 2J_\times - J_\perp\delta). \tag{3.60b}$$

These two transition lines, the Gaussian in red and the Ising in blue, are depicted schematically in Fig. 3.4(b). Both lines intersect at the isotropic point $\delta = 0$, where the coupling constants satisfy $J_4 = \gamma(J_\perp - 2J_\times)$. This point corresponds to the $c = 3/2$ transition, as described by Eq. (3.55).

The Ising and Gaussian transitions divide the phase diagram into four different regions. Along the isotropic line, RS and SD phases emerge with increasing K_{ch} as illustrated in Fig. 3.4(a). The introduction of finite δ can stabilize highly anisotropic phases, such as the Néel and Haldane* phases, near the SU(2)-symmetric line. Indeed, for easy-axis anisotropy, both the $\sin\left(\sqrt{2\pi}\phi_+\right)$ and $\sin\left(\sqrt{2\pi}\phi_-\right)$ components of the Néel order operator, given in Eq. (3.42a), acquire finite value. Meanwhile, for easy-plane anisotropy, it can be verified that all order operators defined so far have a null average value, suggesting that the Haldane* phase is featureless. In the weak coupling regime, the phase diagram of the CCI model closely resembles that of the DDI model in Eq. (1.7), reported in Ref. [192, 194] (see Fig. 1.5).

When K_{ch} decreases, the upper boundary of the Haldane* phase shifts to lower Δ. Eventually, when $K_{\mathrm{ch}} = 0$, this boundary reaches negative Δ, as seen in Fig. 1.3. More details are provided in Appendix B.2.

3.3.2 Spin-chirality duality

Using the $\mathcal{U}$ duality transformation, the phase diagrams in Figs. 3.4(a,b) can be mapped to a regime of high K_{ch}, similar to the approach in Sec. 3.2.3. Under the $\mathcal{U}$ duality, the $c = 3/2$ transition line in the isotropic case (Fig. 3.4(a)) is mapped to the corresponding line in Fig. 3.4(c). The effect of anisotropy

[1] This approximation provides good agreement with numerical results, as demonstrated in Fig. 5.9.

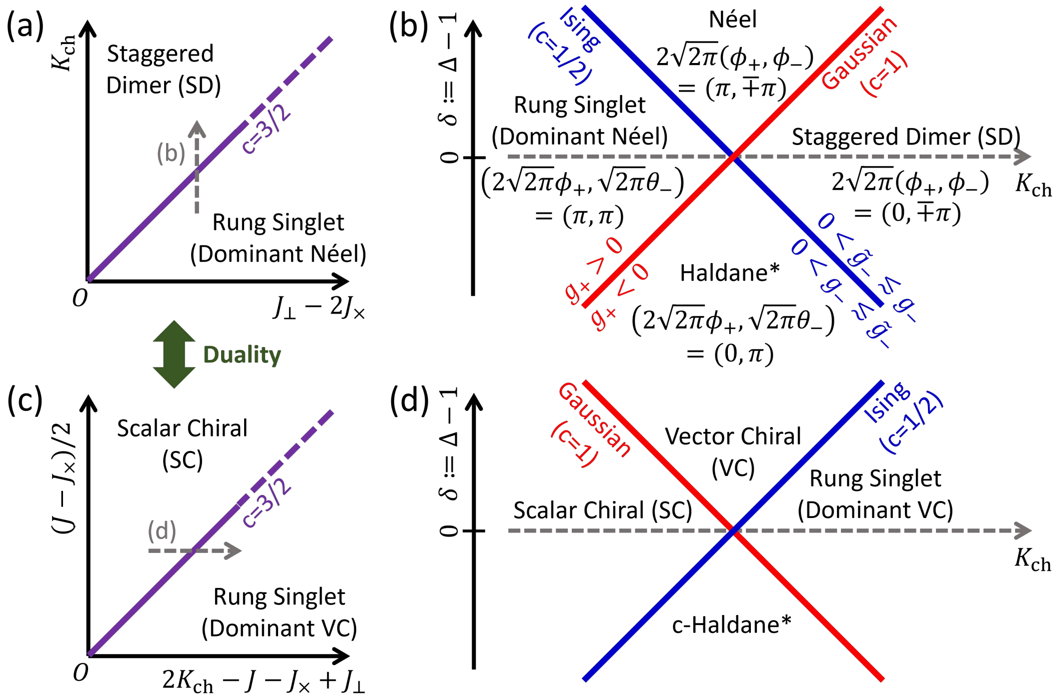

FIGURE 3.4: Schematic ground-state phase diagrams of the extended XXZ-CCI ladder H_{ex} (1.22) predicted by the Abelian bosonization and the duality. (a) Isotropic model ($\Delta = 1$) with weak interchain couplings (3.1). (c) Dual counterpart of (a), obtained through the transformation (1.25). See also the first quadrant of Fig. 3.1(a,b). (b,d) Anisotropic model ($\Delta \neq 1$) along the dashed lines in (a,c). Each phase in (b) is characterized by the locking positions of bosonic fields. The transition lines in (b,d) are given by Eqs. (3.60) and (3.61), respectively; those in (a,c) are obtained by setting $\delta = 0$ in these equations. Reproduced from Fig. 3 of Ref. [56]. Copyright 2024 by the American Physical Society.

on the phase diagram along the two gray dashed arrows in Figs. 3.4(a,c) is shown in Figs. 3.4(b,d) .

The Gaussian and Ising transitions, defined respectively in Eqs. (3.60a) and (3.60b) and shown in Fig. 3.4(b), can be mapped to the transitions in Fig. 3.4(d) via the relation (1.25). More precisely, the Gaussian transition line, drawn in red in Fig. 3.4(d), is given by

$$K_{\mathrm{ch}} = \frac{J + J_\times - J_\perp}{2} + \frac{J - J_\times}{4\gamma} - \frac{J_\perp \delta}{2}, \tag{3.61a}$$

and the Ising transition line, drawn in blue, is given by

$$K_{\mathrm{ch}} = \frac{J + J_\times - J_\perp}{2} + \frac{J - J_\times}{4\gamma} + \frac{J_\perp \delta}{2}. \tag{3.61b}$$

Likewise, the weak coupling condition (3.1), where these transition lines can be trusted, transforms according to the relation (1.25), and becomes

$$J_\perp, \left| \frac{J + J_\times}{2} - K_{\mathrm{ch}} \right|, J - J_\times \ll \frac{J + J_\times}{2} + K_{\mathrm{ch}}. \tag{3.62}$$

The Néel ordered phase and the Haldane* phase, appearing between the Ising and Gaussian transition lines in Fig. 3.4(b), are respectively mapped to the VC ordered phase and the c-Haldane* phase in Fig. 3.4(d). Gaussian transitions occurring for $\delta > 0$ are interesting examples of continuous transitions between two ordered phases that break different symmetries. Based on its duality to the Néel-SD transition, the SC-VC transition gives a novel example of deconfined quantum critical points [228] in one dimension [107, 172, 192, 219].

As far as the author knows, the c-Haldane* phase represents a novel instance of an SPT phase under the symmetries of $D_2 \times \sigma$ and time-reversal. We will explore the nature of the Haldane* and c-Haldane* phases, including their topological characterization, in greater detail in Secs. 4.2 and 5.2.4.

3.3.3 Full phase structure

As explained in Sec. 3.3.3, the first quadrant of the phase diagram in Fig. 3.3 can be obtained by combining Fig. 3.4(a,c) and setting $J_\times = 0$. Similarly, by combining Fig. 3.4(b,d), the phase diagram in the K_{ch}-Δ plane can be obtained, as shown in Fig. 3.5. It is assumed that the effective field predictions made using bosonization in the weak-coupling regime remain valid even when Eqs. (3.1) and (3.62) are nearly saturated.[2] In Sec. 5.2.1, the phase diagram determined by numerical simulation (Fig. 5.1) is found to be in qualitative agreement with the theoretical phase diagram in Fig. 3.5.

[2]It is frequent for predictions made using bosonization in weak-coupling regime to qualitatively hold beyond their validity ranges; see, e.g., Refs. [96, 220].

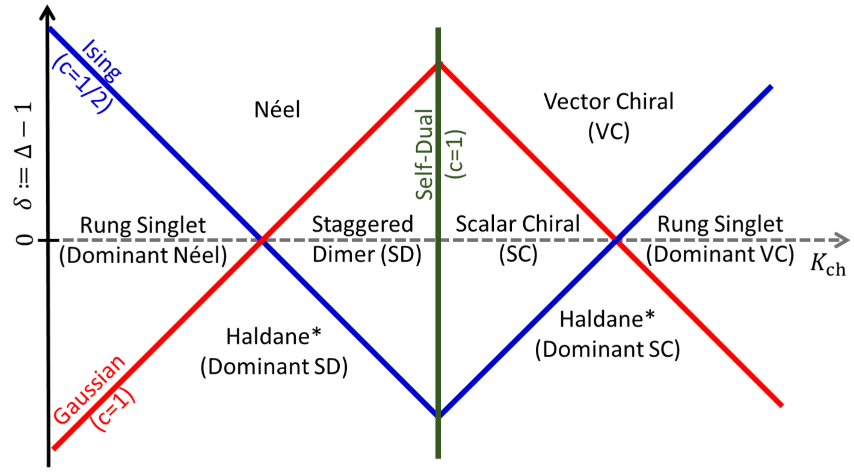

FIGURE 3.5: Schematic ground-state phase diagrams of the extended XXZ-CCI ladder (1.22), obtained by combining Fig. 3.4(b,d). The self-dual line at $K_{ch} = J/2$ corresponds to a Gaussian transition with central charge $c = 1$. The existence of a direct transition between the Néel and VC phase is discussed in Sec. 4.1.3 while the Haldane*-c-Haldane* transition is discussed in Sec. 4.1.4.

3.4 Conclusions

In this chapter, effective field methods and the two types of dualities were used to investigate the ground-state phase diagram of the XXZ-CCI ladder (1.18). In the weak interchain limit (3.1) for isotropic interaction, the phase diagram in the K_{ch}-$J_\perp$ plane consists of four different phases. Boundaries between those phases consist of $c = 3/2$ and Ising transitions. According to the signs and relative magnitudes of K_{ch} or $J_\perp$, the system is either in the featureless RS or Haldane phases or in the ordered SD or plaquette phases. In the featureless phases, a crossover between regions with different correlations in terms of spin or dimer occurs. By using both the $\mathcal{U}$ and $\mathcal{U}_s$ dualities, the $K_{ch} > 0$ and $K_{ch} < 0$ parts of the phase diagram can be mapped to other regions. This enables the extension of the phase diagram to larger values of $|K_{ch}|$ as indicated in Eq. (3.54). Phases obtained by the duality transformations are characterized by the presence of chiral order or correlations.

In Sec 3.3, the effect of anisotropy on the phase structure was analyzed in the $K_{ch}, J_\perp > 0$ region. Finite XXZ anisotropy can split the $c = 3/2$ transitions into Gaussian and Ising transitions. For easy-axis anisotropy, the Néel order and its dual under $\mathcal{U}$, i.e., the VC order, appear between the Gaussian and Ising transitions. For easy-plane, the Haldane* phase and its dual, i.e., the c-Haldane* phase, appear between the transitions. Near the self-dual lines, the condition of weak interchain coupling is saturated and the effective field analysis performed in this chapter can no longer give reliable results. Some effective field methods predicted the existence of a $c = 1$ SD-SC transition near a SU(4)-symmetric point on a self-dual line [137, 138]. However, apart from this special case, the phase structure around the $\mathcal{U}$ self-dual line remains unclear. In particular, regions with strong anisotropy around the self-dual line are beyond the scope of the analysis done in this chapter, requiring an alternative approach presented in the next chapter.

Chapter 4

Effective spin-1 hard-core bosons approach

The ground-state phase diagram of the XXZ-CCI ladder (1.18) in weak- and strong-K_{ch} regimes was investigated in the previous chapter using bosonization and dualities. However, the $\mathcal{U}$ self-dual line, located at $K_{\mathrm{ch}} = J/2$, lies outside both regimes, leaving the precise phase structure around this line unclear. Field-theoretical analysis around the $\mathrm{SU}(4)$ quantum multicritical point predicts a direct transition between the SD and SC phases, belonging to the Gaussian universality class, on the self-dual line of the isotropic model [137, 138]. However, the nature of this transition in the presence of anisotropy remains unknown. In addition, the Haldane* and c-Haldane* phases, predicted in the previous chapter, are yet to be analyzed. To investigate the effect of strong anisotropy on the phase diagram, we extend an effective spin-1 hard-core bosons approach, previously introduced in Refs. [137, 253], to the XXZ-CCI ladder (1.18). In Sec. 4.1, the spin-$\frac{1}{2}$ ladder in Eq. (1.18) is mapped to hard-core bosons hopping on a one-dimensional lattice, leading to the effective Hamiltonian (4.4). This Hamiltonian simplifies significantly in the presence of strong XXZ anisotropy. These simplifications enable analytical treatment of the system for strong easy-axis anisotropy in Sec. 4.1.3 and strong easy-plane anisotropy in Sec. 4.1.4. Among the conclusions of this analysis, the Haldane* and c-Haldane* phases emerge as twisted variants of the conventional Haldane phase, suggesting that they possess distinct topological properties. To confirm this, the topological indices of the Haldane and c-Haldane phases are calculated for representative wave functions in Sec. 4.2.

4.1 Effective spin-1 hard-core bosons approach

4.1.1 Mapping to hard-core bosons

The spin-$\frac{1}{2}$ ladder can be mapped to a system of spin-1 hard-core bosons by introducing three distinct species of bosons on the jth rung. The creation operators for these bosons are defined as

$$b^{\dagger}_{j,\alpha} := \left| t^{[j]}_{\alpha} \right\rangle \left\langle s^{[j]} \right| \quad (\alpha = x, y, z), \tag{4.1}$$

where the triplet states $\left|t_\alpha^{[j]}\right\rangle$ are given in Eq. (1.2). The total number of bosons on the jth rung is given by the operator

$$n_j^{\mathrm{B}} := \sum_\alpha b_{j,\alpha}^\dagger b_{j,\alpha} = \sum_\alpha \left|t_\alpha^{[j]}\right\rangle \left\langle t_\alpha^{[j]}\right|. \tag{4.2}$$

This operator acts as a projector onto the triplet sector of the rung. The singlet state, corresponding to the eigenvalue 0 of n_j^{B}, represents the vacuum of the boson, whereas the triplet states (eigenvalue 1) indicate the presence of a boson. In terms of the original spin operators, the boson creation operators can be expressed as a combination of the antisymmetric spin combination and the vector chirality

$$b_{j,\alpha}^\dagger = \frac{1}{2}(\boldsymbol{S}_{1,j} - \boldsymbol{S}_{2,j})^\alpha + i(\boldsymbol{S}_{1,j} \times \boldsymbol{S}_{2,j})^\alpha. \tag{4.3}$$

Using this mapping, the Hamiltonian (1.18) of the XXZ-CCI ladder can be expressed in terms of hard-core bosons as

$$\begin{aligned} H = {} & t \sum_{j,\alpha} \left(b_{j,\alpha}^\dagger b_{j+1,\alpha} + b_{j+1,\alpha}^\dagger b_{j,\alpha} \right) \\ & + u \sum_{j,\alpha} \left(b_{j,\alpha}^\dagger b_{j+1,\alpha}^\dagger + b_{j+1,\alpha} b_{j,\alpha} \right) + J_{\mathrm{bl}} \sum_j \boldsymbol{T}_j \cdot \boldsymbol{T}_{j+1} \\ & + J_\perp \sum_j \left[n_j^{\mathrm{B}} - \frac{3}{4} + \frac{\delta}{2} \left(b_{j,x}^\dagger b_{j,x} + b_{j,y}^\dagger b_{j,y} - \frac{1}{2} \right) \right] + \text{const.}, \end{aligned} \tag{4.4}$$

where the coefficients t, u, J_{bl} are given by

$$t = \frac{J}{2} + K_{\mathrm{ch}}, \quad u = \frac{J}{2} - K_{\mathrm{ch}}, \quad J_{\mathrm{bl}} = \frac{J}{2}. \tag{4.5}$$

Here, $\boldsymbol{T}_j$ represents the spin of the hard-core boson on the jth rung, which is defined as

$$T_j^\alpha := -i \sum_{\beta,\gamma} \epsilon_{\alpha\beta\gamma} b_{j,\beta}^\dagger b_{j,\gamma}. \tag{4.6}$$

4.1.2 U(1) symmetry on the self-dual line

The unitary transformation $\mathcal{U}$ in Eq. (1.14) can be expressed in the bosonic basis as

$$\mathcal{U}(\theta) = \exp\left(i\theta \sum_j n_j^{\mathrm{B}} \right) \quad (\theta \in \mathbb{R}), \tag{4.7}$$

which acts as a gauge transformation on the bosons, i.e.,

$$\mathcal{U}(\theta) b_{j,\alpha}^\dagger \mathcal{U}^\dagger(\theta) = e^{i\theta} b_{j,\alpha}^\dagger. \tag{4.8}$$

By combining Eq. (4.8) with Eq. (4.3) and setting $\theta = \pi/2$, the spin-chirality duality in Eq. (3.50) can be recovered. Hence, $\mathcal{U} = \mathcal{U}(\pi/2)$. Under $\mathcal{U}(\pi/2)$, the u-term in Eq. (4.4) flips its sign ($u \to -u$) while the other coupling constants remain unchanged. Hence, the u-term explicitly breaks the $\mathrm{U}(1)$ gauge symmetry associated with the transformation in Eq. (4.7). On the self-dual line ($u = 0$), the global $\mathrm{U}(1)$ gauge symmetry is restored. The self-dual model is equivalent to spin-1 bosonic atoms loaded into an optical lattice [42, 104, 111, 236].

One the $\mathcal{U}$-self-dual line only, the $\mathrm{U}(1)$ gauge symmetry (4.8) of the model allows us to apply the Lieb-Schultz-Mattis-type theorem [143, 199, 250] to obtain information about the low-energy spectrum. We introduce the number of bosons per rung as

$$n^{\mathrm{B}} := \frac{1}{L}\sum_{j=1}^{L} n_j^{\mathrm{B}}, \tag{4.9}$$

where L is the ladder length, i.e., the total number of rungs. According to the theorem, for non-integer values of n^{B} (i.e., $0 < n^{\mathrm{B}} < 1$), there must exist some low-lying energy states (gapless excitations) or degenerate ground states in the thermodynamic limit. For integer values of n^{B}, the theorem does not rule out the existence of a unique bulk ground state below an excitation gap.

To understand how the Lieb-Schultz-Mattis-type theorem is related to the global U(1) symmetry of the self-dual model, one needs to modify the proof given in Sec. 2.3.2. The twist operator (2.26) associated with the $\mathrm{U}(1)$ gauge symmetry (4.8) is now

$$\hat{U}_{\mathrm{LSM}} = \exp\left(-i\sum_j \theta_j n_j^{\mathrm{B}}\right). \tag{4.10}$$

Following the same steps, the state $\hat{U}_{\mathrm{LSM}}\,|\boldsymbol{\phi}_{\mathrm{GS}}\rangle$ is a low-lying energy state whose inner product with $|\boldsymbol{\phi}_{\mathrm{GS}}\rangle$ is given by

$$\begin{aligned}
\langle \boldsymbol{\phi}_{\mathrm{GS}}|\boldsymbol{\phi}_{\mathrm{LSM}}\rangle &= \langle \boldsymbol{\phi}_{\mathrm{GS}}|\hat{U}_{\mathrm{LSM}}|\boldsymbol{\phi}_{\mathrm{GS}}\rangle && \text{(4.11a)}\\
&= \langle \boldsymbol{\phi}_{\mathrm{GS}}|\hat{T}^{\dagger}\hat{U}_{\mathrm{LSM}}\hat{T}|\boldsymbol{\phi}_{\mathrm{GS}}\rangle && \text{(4.11b)}\\
&= \langle \boldsymbol{\phi}_{\mathrm{GS}}|e^{i2\pi n_L^{\mathrm{B}}}\hat{U}_{\mathrm{LSM}}e^{-i2\pi n^{\mathrm{B}}}|\boldsymbol{\phi}_{\mathrm{GS}}\rangle && \text{(4.11c)}\\
&= e^{-i2\pi n^{\mathrm{B}}}\,\langle \boldsymbol{\phi}_{\mathrm{GS}}|\boldsymbol{\phi}_{\mathrm{LSM}}\rangle\,. && \text{(4.11d)}
\end{aligned}$$

Here, the fact that n_L^{B} is a projector and only has integer eigenvalues has been used to go from the third to the fourth lines. Then, if $0 < n^{\mathrm{B}} < 1$, (4.11) imply that $\langle \boldsymbol{\phi}_{\mathrm{GS}}|\boldsymbol{\phi}_{\mathrm{LSM}}\rangle = 0$. Together with Eq. (2.28), this implies the existence of at least one energy eigenstate whose energy converges to E_{GS} as L goes to infinity. Therefore the system is gapless when $0 < n^{\mathrm{B}} < 1$.

By examining the single-boson excitation spectrum [126, 173], one can determine the boundary of the RS ground state, i.e., the boson vacuum in the self-dual model. For a single-boson problem, boson-boson interactions (J_{bl} term in the Hamiltonian (4.4)) are null, and the dispersion relations $\epsilon_\alpha(k)$ for the α-boson ($\alpha = x, y, z$) in Eq. (4.1) can be obtained exactly as

$$\epsilon_{x,y}(k) = 2J\cos k + J_{\perp}\left(1 + \frac{\delta}{2}\right), \tag{4.12a}$$

$$\epsilon_{z}(k) = 2J\cos k + J_{\perp}, \tag{4.12b}$$

where k is the wave number.

When the minimum of $\epsilon_{x,y}(\pi)$ or $\epsilon_z(\pi)$ of the dispersion relations becomes zero, the ground state is destabilized. This analysis leads to the range of the exact RS state in Fig. 4.1.

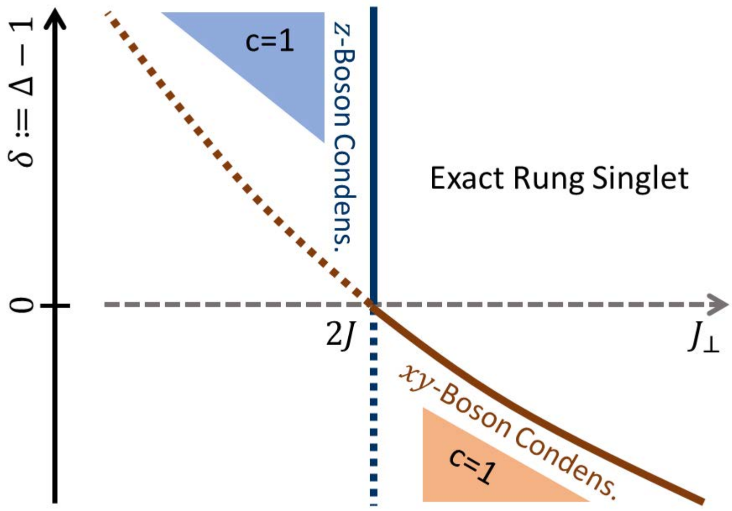

FIGURE 4.1: Ground-state phase diagram of the XXZ-CCI ladder (1.18) on the self-dual line $K_{\mathrm{ch}} = J/2$, obtained from the spinor hard-core bosons Hamiltonian (4.4) with $u = 0$. For $J_\perp > 2J\max(1, (1+\delta/2)^{-1})$, where all of Eq. (4.12) are gapped, the ground state is the boson vacuum, i.e., the exact RS state [126, 173]. This ground state is destabilized when the minimum of $\epsilon_{x,y}(k)$ or $\epsilon_z(k)$ in Eq. (4.12) becomes zero, i.e., the xy- or z-bosons condense. The shaded $c = 1$ region for easy-axis anisotropy ($\delta > 0$) corresponds to the Néel-VC transition in Fig. 4.3. The shaded $c = 1$ region for easy-plane anisotropy ($\delta < 0$) corresponds to the Haldane*-c-Haldane* transition. The region of the exact RS corresponds to a crossover line in the RS phase across which the dominant correlation changes from Néel- to VC-type, as shown in Figs. 3.3 and 4.3. Reproduced from Fig. 4 of Ref. [56]. Copyright 2024 by the American Physical Society.

4.1.3 Easy-axis regime

In this section, the easy-axis regime ($\delta > 0$) will be investigated. As seen in the dispersion relations (4.12), the energy difference between the xy and z-boson is $J_\perp\delta/2$. Therefore, when $J_\perp\delta \gg J, K_{\mathrm{ch}}$, the xy-bosons can safely be neglected when analyzing the low-energy properties of the bosonic Hamiltonian (4.4). Using the z-bosons creation and annihilation operators, a

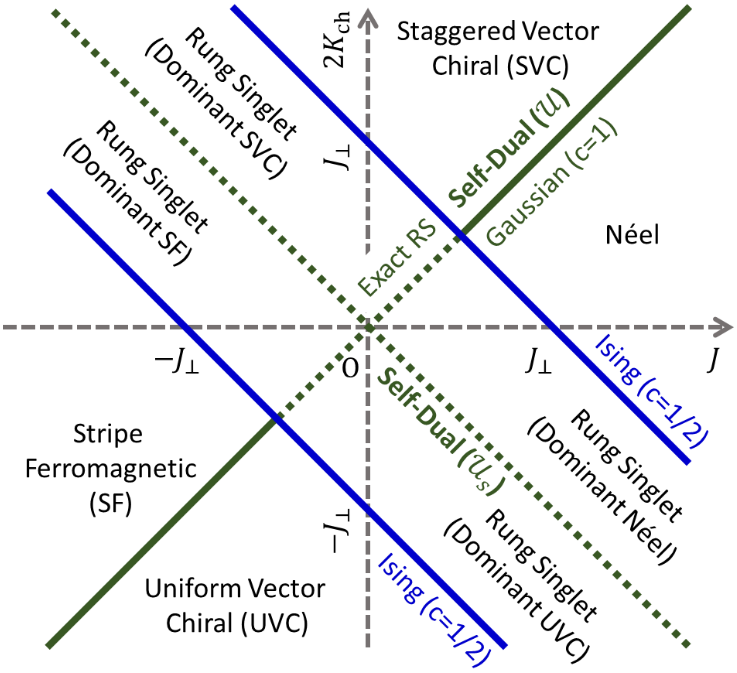

FIGURE 4.2: Ground-state phase diagram of the XXZ-CCI ladder defined in Eqs. (1.18) with $J_\perp > 0$ in the easy-axis regime, shown in the J-$2K_{\rm ch}$ plane. This is based on the effective XY Hamiltonian (4.14), which is exactly solvable. The four types of orders are shown in Fig. 3.2(g,h,i,j). Ising transitions with the central charge $c = 1/2$ occur along the blue lines between the RS and ordered phases. The model is self-dual under $\mathcal{U}$ or $\mathcal{U}_{\rm s}$ at $K_{\rm ch} = J/2$ and $K_{\rm ch} = -J/2$, respectively (green lines). Along the $\mathcal{U}$-self-dual line with $|J| < J_\perp/2$, the ground state is given by the exact RS state. Reproduced from Fig. A.1 of Ref. [55]. Copyright 2024 by the Physical Society of Japan.

pseudospin-$\frac{1}{2}$ operator can be created as

$$\mathcal{S}_j^x = \frac{1}{2}\left(b_{j,z}^\dagger + b_{j,z}\right), \tag{4.13a}$$

$$\mathcal{S}_j^y = \frac{1}{2i}\left(b_{j,z}^\dagger - b_{j,z}\right), \tag{4.13b}$$

$$\mathcal{S}_j^z = b_{j,z}^\dagger b_{j,z} - \frac{1}{2}. \tag{4.13c}$$

In terms of the pseudospin operator, the Hamiltonian in Eq. (4.4) can be rewritten as the Hamiltonian of the XY chain in a magnetic field:

$$H = \sum_j \left(2J\mathcal{S}_j^x\mathcal{S}_{j+1}^x + 4K_{\rm ch}\mathcal{S}_j^y\mathcal{S}_{j+1}^y\right) + J_\perp \sum_j \mathcal{S}_j^z + \text{const.} \tag{4.14}$$

The effective Hamiltonian (4.14) is invariant under a π rotation around the z-axis. It is exactly solvable, and its ground-state phase diagram is well-known [18, 43].

When $J_\perp < |J + 2K_{\rm ch}|$, the pseudospin model in Eq. (4.14) exhibits different ordered phases according to the signs and relative magnitudes of J and $2K_{\rm ch}$. When $|J| > 2|K_{\rm ch}|$, the model spontaneously breaks the $\mathcal{S}_j^x \leftrightarrow -\mathcal{S}_j^x$

invariance, and (anti)ferromagnetic order along the x axis occurs for negative (positive) J. Similarly, when $2|K_{\rm ch}| > |J|$, the $\mathcal{S}_j^y \leftrightarrow -\mathcal{S}_j^y$ invariance is spontaneously broken, and (anti)ferromagnetic order along the y axis occurs for negative (positive) $K_{\rm ch}$. Going back to the original description of the model in terms of spin operators ($\mathcal{S}_j^x = (S_{1,j}^z - S_{2,j}^z)/2$ and $\mathcal{S}_j^y = (\boldsymbol{S}_{1,j} \times \boldsymbol{S}_{2,j})^z$), these phases can be interpreted as SF, Néel, UVC, and SVC phases [see Figs. 3.2(g,h,i,j)].

When $J_\perp > |J + 2K_{\rm ch}|$, the pseudospins are mainly polarized in the $-z$ direction. The pseudospin model (4.14) is in a "paramagnetic phase", and no spontaneous symmetry breaking occurs. This corresponds to the RS phase of the ladder model. Depending on which of J and $2K_{\rm ch}$ is dominant and which sign the dominant one has, dominant SF, Néel, UVC, or SVC correlations develop inside the RS phase. This analysis leads to the phase diagram in Fig. 4.2. The crossover between dominant SVC and SF correlations in Fig. 4.2 has also been found in the J-$J_\perp$-K ladder defined in Eq. (1.11) [Fig. 1.4(b)] with $J = J_\perp < 0$ and $K > 0$ [132, 253].

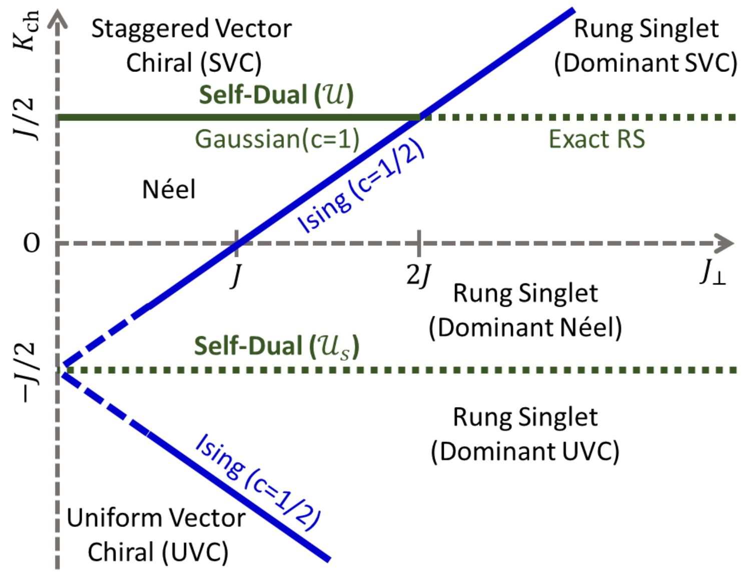

FIGURE 4.3: Ground-state phase diagram of the XXZ-CCI ladder with $J, J_\perp > 0$ in the easy-axis regime, shown in the $J_\perp$-$K_{\rm ch}$ plane. This is converted from the right half of Fig. 4.2. Reproduced from Fig. A. 2 of Ref. [55]. Copyright 2024 by the Physical Society of Japan.

The phase diagram in the $J_\perp$-$K_{\rm ch}$ plane in Fig. 4.3 can be obtained from Fig. 4.2 with the restriction $J > 0$. By comparing the phase diagram for strong easy-axis anisotropy in Fig. 4.3 with the phase diagram obtained in the previous section for the isotropic model, we observe that Néel and VC ordered phases appear in place of dimer and scalar chiral ordered phases. In the RS phase, while the region with dominant Néel and VC orders extend to a strongly anisotropic region, the region with dominant plaquette correlation is not predicted in the hard-core bosons approaches.

4.1.4 Easy-plane regime

In the easy-plane regime, when $-J_\perp\delta \gg J, K_{\rm ch}$, z-bosons can be neglected when analyzing the Hamiltonian (4.4). Using the remaining xy-boson operators, one can form two new bosonic operators as

$$b^\dagger_{j,\pm} = \frac{1}{\sqrt{2}}\left(\mp b^\dagger_{j,x} - i b^\dagger_{j,y}\right). \tag{4.15}$$

In terms of states of the spin ladder, these operators correspond, respectively, to the creation of the states $\left|t_+^{[j]}\right\rangle = \left|\uparrow^{[1,j]}\uparrow^{[2,j]}\right\rangle$ and $\left|t_-^{[j]}\right\rangle = \left|\downarrow^{[1,j]}\downarrow^{[2,j]}\right\rangle$ on the jth rung. Namely, $b^\dagger_{j,+} = \left|t_+^{[j]}\right\rangle\left\langle s^{[j]}\right|$ and $b^\dagger_{j,-} = \left|t_-^{[j]}\right\rangle\left\langle s^{[j]}\right|$. After removing the z-bosons, the Hamiltonian (4.4) can be expressed in terms of the new bosonic operators as

$$\begin{aligned} H = {} & t\sum_{\nu=\pm}\sum_j\left(b^\dagger_{j,\nu}b_{j+1,\nu} + b^\dagger_{j+1,\nu}b_{j,\nu}\right) \\ & - u\sum_{\nu=\pm}\sum_j\left(b^\dagger_{j,\nu}b^\dagger_{j+1,-\nu} + b_{j+1,-\nu}b_{j,\nu}\right) \\ & + J_{\rm bl}\sum_j T^z_j T^z_{j+1} + D\sum_{\nu=\pm}\sum_j b^\dagger_{j,\nu}b_{j,\nu} + \text{const.}, \end{aligned} \tag{4.16}$$

where $D = J_\perp(1+\delta/2)$ and $T^z_j = \sum_{\nu=\pm}\nu b^\dagger_{j,\nu}b_{j,\nu}$.

While t, u, and $J_{\rm bl}$ are mutually dependent parameters, as seen in Eq. (4.5), they will be treated as independent parameters during the analysis of the properties of the effective Hamiltonian (4.16). For $u = 0$, Eq. (4.16) can be viewed as a model of two-component hard-core bosons on a lattice. Here, t and $-D$ can be interpreted respectively as the hopping amplitude and the chemical potential.

Under a statistical transformation [247], this model becomes equivalent to the infinite-U limit of the fermionic Hubbard chain. For the convenience of our analysis, we relax infinite U to a large but finite intercomponent repulsion $0 < U < \infty$ in the following. When $D < 2t$, the finite-U model is in the two-component TLL phase described by dual pairs of bosonic fields (ϕ_c, θ_c) and (ϕ_s, θ_s) in the charge and spin sectors, respectively [71, 73]. Then, the u and $J_{\rm bl}$ terms, which play roles of a pairing term and state-dependent density-density interactions, respectively, can be treated as perturbations. Accordingly, the Hamiltonian (4.16) can be bosonized as follows

$$\begin{aligned} H^{\rm eff} = {} & \int \mathrm{d}x \sum_{\eta=c,s}\frac{v_\eta}{2}\left[\frac{1}{K_\eta}\left(\partial_x\phi_\eta\right)^2 + K_\eta\left(\partial_x\theta_\eta\right)^2\right] \\ & + g_s\cos\left(2\sqrt{2\pi}\phi_s\right) + \tilde{g}_c\cos\left(\sqrt{2\pi}\theta_c\right) + \ldots, \end{aligned} \tag{4.17}$$

with v_c and K_c (v_s and K_s) being the velocity and the TLL parameter in the charge (spin) sector. Ellipses indicate terms with higher scaling dimensions that can be neglected in a first approximation.

The spin and charge sectors are separated and can be analyzed independently. At finite U, for $u = J_{\rm bl} = 0$, the TLL parameter $K_s = 1$ and the g_s

term with the scaling dimension $2K_s$ is marginally irrelevant. In the infinite U limit, finite $J_{\mathrm{bl}} > 0$ makes the g_s term relevant via a modification of the value K_s. In this case, the spin sector becomes gapped. On the other hand, in the infinite U limit, $K_c \to 1/2$ and $v_s \to 0$ [71]. The charge sector of the theory is equivalent to the sine-Gordon Hamiltonian with strongly relevant $\tilde{g}_c$ term (scaling dimension $(2K_c)^{-1}$). As $\tilde{g}_c \propto u$, finite u immediately opens a gap, while the system is gapless on the self-dual line with $u = 0$. In this way, we have distinct gapped phases depending on the sign of $u = \frac{J}{2} - K_{\mathrm{ch}}$, and a $c = 1$ Gaussian transition occurs between them at $u = 0$.

To investigate the nature of gapped phases for $\frac{J}{2} > K_{\mathrm{ch}}$ and $\frac{J}{2} < K_{\mathrm{ch}}$, it is convenient to rewrite the Hamiltonian (4.16) as the sum of two pseudo spin-1 XXZ chains by introducing two types of pseudo-spin-1 operators in Eqs. (4.18) and (4.20). As shown in the following, the Haldane* and c-Haldane* phases will then emerge as the ground states of this Hamiltonian in the $\frac{J}{2} > K_{\mathrm{ch}}$ and $\frac{J}{2} < K_{\mathrm{ch}}$ regimes, respectively.

Let the pseudo spin-1 operator $\boldsymbol{L}_j$ on each rung j be defined as

$$L_j^+ = \sqrt{2}\left(b_{j,+}^\dagger - b_{j,-}\right), \tag{4.18a}$$

$$L_j^z = b_{j,+}^\dagger b_{j,+} - b_{j,-}^\dagger b_{j,-}. \tag{4.18b}$$

This operator can be regarded as a spin-1 operator acting on the state basis

$$\left|t_+^{[j]}\right\rangle, \left|s^{[j]}\right\rangle, -\left|t_-^{[j]}\right\rangle. \tag{4.19}$$

These states are derived from the usual spin-triplet states via the unitary transformation $(-i)^L U_1^z(\pi)$; see Eq. (1.6).

Similarly, the $\tilde{\boldsymbol{L}}$ pseudo spin-1 operator is defined by

$$\tilde{\boldsymbol{L}}_j = e^{i\frac{\pi}{2}n_j^{\mathrm{B}}} \boldsymbol{L}_j e^{-i\frac{\pi}{2}n_j^{\mathrm{B}}}, \tag{4.20}$$

where $e^{i\frac{\pi}{2}n_j^{\mathrm{B}}}$ is the single-rung part of transformation $\mathcal{U}(\pi/2)$, as defined in Eq. (4.7). $\tilde{\boldsymbol{L}}$ behaves like a pseudo spin-1 when acting on the basis

$$-\left|t_+^{[j]}\right\rangle, i\left|s^{[j]}\right\rangle, \left|t_-^{[j]}\right\rangle. \tag{4.21}$$

These states are obtained from Eq. (4.19) by applying the transformation $i^L \mathcal{U}(\pi/2)$. Notably, L_j^z is invariant under the $i^L \mathcal{U}(\pi/2)$ transformation, so $\tilde{L}_j^z = L_j^z$.

Using both $\boldsymbol{L}_j$ and $\tilde{\boldsymbol{L}}_j$, the Hamiltonian in Eq. (4.16) can be rewritten as a spin-1 chain Hamiltonian as

$$\begin{aligned} H = \frac{J}{2} \sum_j \left(L_j^x L_{j+1}^x + L_j^y L_{j+1}^y\right) + K_{\mathrm{ch}} \sum_j \left(\tilde{L}_j^x \tilde{L}_{j+1}^x + \tilde{L}_j^y \tilde{L}_{j+1}^y\right) \\ + J_{\mathrm{bl}} \sum_j L_j^z L_{j+1}^z + D \sum_j \left(L_j^z\right)^2 + \text{const.} \ . \end{aligned} \tag{4.22}$$

It is more convenient to keep treating $J/2$, K_{ch}, and J_{bl} as independent parameters for analyzing the properties of Hamiltonian (4.22). When $K_{\text{ch}} = 0$, Eq. (4.22) simplifies to the spin-1 XXZ chain with single-ion anisotropy, expressed in terms of the $\boldsymbol{L}_j$ spins. The phase diagram of this Hamiltonian is well known [29, 183, 226]. When the single-ion anisotropy term dominates, the system is in the large-D phase where the ground state is approximated by the product of the $L_j^z = 0$ states. This corresponds to the RS phase of the ladder model.

When the XXZ interaction dominates, the system is in the Haldane state in the basis of Eq. (4.19), which corresponds to the Haldane* state discussed in Refs. [63, 145, 193, 194]. Similarly, when $\frac{J}{2} = 0$, the Hamiltonian in Eq. (4.22) reduces to the spin-1 XXZ chain with single-ion anisotropy in terms of the $\tilde{\boldsymbol{L}}_j$ spins. The Haldane state in the basis of Eq. (4.21) basis corresponds to the c-Haldane* state, which is the dual counterpart of the Haldane* state.

When both $\frac{J}{2}$ and K_{ch} are finite, the Haldane* and c-Haldane* phases compete with each other. It is reasonable to expect that each phase extends up to the self-dual line, where a $c = 1$ Gaussian transition occurs between them. Consequently, the gapped phases identified for $\frac{J}{2} > K_{\text{ch}}$ and $\frac{J}{2} < K_{\text{ch}}$ in the field-theoretical analysis correspond to the Haldane* and c-Haldane* phases, respectively.

Contrary to the Haldane* phase, the Haldane phase is invariant under both spin-chirality duality. Indeed, $e^{\pm i\frac{\pi}{2}n_j^{\text{B}}} = \pm i\boldsymbol{I}$ when acting on any triplet state. As seen from its representation in Eq. (4.24), the representative state of the Haldane phase contains only triplet states. Therefore it is invariant (up to a global phase factor) under both duality transformations.

4.2 SPT phases in the XXZ-CCI model

4.2.1 Simple matrix product states for the SPT phases

In the previous section, an effective model for strong easy-plane anisotropy, Eq. (4.22), was derived. The ground state of this model for $\frac{J}{2} > K_{\text{ch}}$ $\left(\frac{J}{2} < K_{\text{ch}}\right)$, belongs to the Haldane* (c-Haldane*) phases, which can be seen as a Haldane phase expressed in the basis (4.19) ((4.21)), rather than in the standard basis in term of triplet states given in Eq. (1.2). Consequently, it is reasonable to expect that both the Haldane* and c-Haldane* are non-trivial SPT phases. One way to unambiguously confirm this is to calculate topological indices directly. As explained in Sec. 2.7, this is done efficiently within the MPS framework.

For convenience, the MPS representation given in Eq. (2.57) will be modified to

$$|\boldsymbol{\phi}\rangle = \boldsymbol{Tr}\left[\boldsymbol{A}^{[1]}\boldsymbol{A}^{[2]}\dots\boldsymbol{A}^{[L]}\right], \tag{4.23}$$

for a periodic system, where the state of each rung is included in the definition of the matrix. The $\boldsymbol{A}^{[j]}$ matrices are related to those in Eq. (2.78) via $\boldsymbol{A}^{[j]} := \sum_{\sigma_j} \Lambda\Gamma^{\sigma_j}\left|\sigma_j^{[j]}\right\rangle$. Using this notation, the MPS representation of the

State	$e^{i\theta_x}$	U_x	$e^{i\theta_y}$	U_y	$e^{i\theta_\sigma}$	U_σ	$e^{i\theta_{\mathrm{TR}}}$	U_{TR}
H	$+1$	$i\sigma^x$	$+1$	$i\sigma^y$	$+1$	I	$+1$	$i\sigma^y$
H*	-1	$i\sigma^x$	-1	$i\sigma^y$	-1	$i\sigma^z$	-1	$i\sigma^y$
cH*	-1	$i\sigma^x$	-1	$i\sigma^y$	-1	$i\sigma^z$	$+1$	$i\sigma^x$

TABLE 4.1: The phase factors $e^{i\theta_\Sigma}$ and the 2×2 matrices U_Σ in Eqs. (2.70) and (2.75) for the spin rotations Σ^x and Σ^y, the leg exchange Σ^σ, and time-reversal $\Sigma^{\mathrm{TR}} = \Sigma^y \hat{K}$ in the representative Haldane, Haldane*, and c-Haldane* states described by Eqs. (4.24), (4.25), and (4.26).

ground state of the AKLT model [7, 8, 123, 250] on a ladder is given by

$$A_{\mathrm{H}}^{[j]} = \frac{1}{2}\left(\left|t_x^{[j]}\right\rangle \sigma^x + \left|t_y^{[j]}\right\rangle \sigma^y + \left|t_z^{[j]}\right\rangle \sigma^z\right). \tag{4.24}$$

Here the $\{\sigma^x, \sigma^y, \sigma^z\}$ matrices are the Pauli matrices. The subscript "H" denotes the Haldane phase. Likewise, MPS representations of states in the Haldane* (H*) and c-Haldane* (cH*) phases are given by

$$A_{\mathrm{H}^*}^{[j]} = \frac{1}{2}\left(i\left|t_y^{[j]}\right\rangle \sigma^x - i\left|t_x^{[j]}\right\rangle \sigma^y + \left|s^{[j]}\right\rangle \sigma^z\right), \tag{4.25}$$

$$A_{\mathrm{cH}^*}^{[j]} = \frac{1}{2}\left(-i\left|t_y^{[j]}\right\rangle \sigma^x + i\left|t_x^{[j]}\right\rangle \sigma^y + i\left|s^{[j]}\right\rangle \sigma^z\right). \tag{4.26}$$

Notably, while A_{H} and A_{H^*} are real in the basis $\left|\alpha^{[1,j]}\beta^{[2,j]}\right\rangle$, $(\alpha, \beta = \uparrow, \downarrow)$; A_{cH^*} is complex in this same basis. This distinction suggests that these phases might exhibit different behaviors under the time-reversal symmetry.

4.2.2 Projective representation of the symmetry group

Using the MPS representations A_{H}, A_{H^*}, and A_{cH^*} above, as well as the Eqs. (2.70) and (2.75), the phase factors $e^{i\theta_\Sigma}$ and the matrices U_Σ associated with various symmetries can be determined. The results are summarized in Table 4.1. Previous studies on the classification of featureless phases on a two-leg spin ladder with the $D_2 \times \sigma$ and translational symmetries have already predicted the existence of Haldane and Haldane* phases. These phases are referred to as t_0 and t_z phases, respectively, in Ref. [145]. Using the relation (2.86), topological indices characterizing the Haldane, Haldane*, and c-Haldane* can be extracted from the Table 4.1. In particular, the index associated with time-reversal symmetry $\mathcal{O}_{\mathrm{TR}}$ takes the value -1 in the Haldane and Haldane* states while it is equal to $+1$ in the c-Haldane* state. Thus the topological nature of c-Haldane* is not protected by time-reversal symmetry, unlike the Haldane and Haldane* phases.

It is also interesting to observe how the Haldane* phase is transformed under $\mathcal{U}_{\mathrm{s}}$ duality. Since $\mathcal{U}_{\mathrm{s}}$ acts in a staggered manner, it is necessary to change the basis and consider transformations acting on two consecutive sites to recover translational symmetry. Under this change of basis, the MPS representation of a state in the Haldane* phase is transformed as

$$\breve{A}_{\mathrm{H}^*}^{[j]} = A_{\mathrm{H}^*}^{[2j]} A_{\mathrm{H}^*}^{[2j+1]}. \tag{4.27}$$

On the right-hand side, one must take the product of the matrices and the tensor product of the states.

Under the action of a symmetry σ, $\breve{A}^{[j]}_{\mathrm{H}^*}$ still satisfies Eq. (2.70) with U_σ defined in Table 4.1. However, the coefficients $e^{i\theta_\sigma}$ must be equal to 1, as they are squared due to the doubling of the unit cell. By direct calculation, one can show that

$$\begin{aligned}
&4e^{i\frac{\pi}{2}\left(n^{\mathrm{B}}_{2j}-n^{\mathrm{B}}_{2j+1}\right)}\breve{A}^{[j]}_{\mathrm{H}^*} = \\
&-\boldsymbol{I}\left|t_y^{[2j]}\right\rangle\otimes\left|t_y^{[2j+1]}\right\rangle+i\sigma_z\left|t_y^{[2j]}\right\rangle\otimes\left|t_x^{[2j+1]}\right\rangle+i\sigma_y\left|t_y^{[2j]}\right\rangle\otimes\left|s^{[2j+1]}\right\rangle \\
&-i\sigma_z\left|t_x^{[2j]}\right\rangle\otimes\left|t_y^{[2j+1]}\right\rangle-\boldsymbol{I}\left|t_x^{[2j]}\right\rangle\otimes\left|t_x^{[2j+1]}\right\rangle+i\sigma_x\left|t_x^{[2j]}\right\rangle\otimes\left|s^{[2j+1]}\right\rangle \\
&+i\sigma_y\left|s^{[2j]}\right\rangle\otimes\left|t_y^{[2j+1]}\right\rangle+i\sigma_x\left|s^{[2j]}\right\rangle\otimes\left|t_x^{[2j+1]}\right\rangle+\boldsymbol{I}\left|s^{[2j]}\right\rangle\otimes\left|s^{[2j+1]}\right\rangle .
\end{aligned} \tag{4.28}$$

Under any symmetry σ, both $\breve{A}^{[j]}_{\mathrm{cH}^*}$ and the state defined above transform according to the same U_σ matrices defined in Table 4.1 (with $e^{i\theta_\sigma}$ set to 1). Thus, the Haldane* phase is transformed into the c-Haldane* phase under $\mathcal{U}$ and $\mathcal{U}_{\mathrm{S}}$.

As discussed in Sec. 2.4, string order parameters were originally used to characterize the Haldane phases of spin-S chains with S = odd [116, 183, 198]. Similar types of string order parameters have since been developed to detect the topological properties of ladder models [117, 118, 175, 185, 230, 262]. For instance, in Ref. [194], the RS-Haldane* transition in the DDI-ladder was analyzed using such string order parameters. However, in the context of the present model, this kind of string order parameters can only distinguish the trivial RS phase from the three Haldane-like phases but fail to differentiate between the latter three. Therefore, the classification of gapped, featureless phases based on topological indices associated with $D_2 \times \sigma \times \mathbb{Z}_2^T$ symmetry (2.86) is more precise. For instance, while the index $\mathcal{O}_{xy}$ gives the same amount of information as string order parameters, and cannot distinguish between Haldane* and c-Haldane* phases, the index $\mathcal{O}_{\mathrm{TR}}$ can differentiate between the latter two. In cases when the MPS representation of the ground state is unavailable, such as in numerical Monte Carlo simulations, exact diagonalization studies, or experimental setups, generalizations of nonlocal order parameters to symmetry groups beyond $D_2 = \mathbb{Z}_2 \times \mathbb{Z}_2$ become necessary. These extensions, as explored in Refs. [205, 207], have proven effective in identifying topological orders in various contexts. Recently, different generalizations of string order parameters have been proposed to characterize a range of phases in extended Kitaev ladder models [9, 26, 201, 235].

4.3 Conclusions

In this chapter, a mapping to spin-1 hard-core bosons has been developed to analyze the ground-state phase diagram of the XXZ-CCI ladder (1.18) in the presence of strong anisotropy. Thanks to several simplifications occurring on the self-dual line or in the presence of strong easy-axis anisotropy, a theoretical analysis of the model was possible in these regimes. In particular, this analysis extended our understanding of the nature of the self-dual line beyond the surroundings of the $\mathrm{SU}(4)$ quantum multicritical point [137, 138].

The spin-1 hard-core bosons approach recovered that, in the presence of strong easy-axis anisotropy, orders that explicitly break the $\mathbb{Z}_2$ symmetry associated with π-rotation around the x axis emerge. These orders are the Néel, SF, SVC, and UVC as shown in Figs. 4.2 and 4.3. We predict that a direct transition between the Néel and SVC phases should occur on the self-dual line in the presence of strong easy-axis anisotropy. Likewise, in the presence of strong easy-plane anisotropy, a direct transition between the Haldane* and c-Haldane* phases is expected to occur. As both Haldane-like phases are featureless, this transition is not associated with the onset of the growth of any local order parameter, making it a topological phase transition. The calculation of topological indices associated with $D_2 \times \sigma \times \mathbb{Z}_2^T$ symmetry enables one to distinguish the Haldane* phase from the c-Haldane* phase. Specifically, both phases are protected by D_2 and σ symmetries, whereas only the Haldane* phase is protected by time-reversal symmetry.

Furthermore, from the hard-core bosons analysis, it is expected that both the RS–VC and Haldane*-c-Haldane* transitions belong to the Gaussian universality class. As the SD-SC transition on the isotropic line belongs to the Gaussian universality class [137, 138], it is reasonable to expect that the entire self-dual line belongs to the Gaussian universality class.

Chapter 5

Numerical analyses

In this chapter, several numerical methods will be employed to establish the ground-state phase diagram of the XXZ-CCI ladder (1.18). The first part of this Chapter (Sec. 5.1), will be devoted to the confirmation of the phase diagram of the isotropic model (1.18) given in Fig. 3.3. In Secs. 5.1.2 and 5.1.3, the Ising and $c = 3/2$ transitions will be investigated in detail. The crossovers between regions dominated by different correlations will be looked into in Sec. 5.1.4. Except for Sec. 5.1.5 where the critical properties of the self-dual line are analyzed, most of the theoretical background is covered in Sec. 3.2. The second part (Sec. 5.2) will be devoted to the confirmation of the phase diagram of the anisotropic model (1.18) given in Fig. 3.5. This part will be based on the material covered in Sec. 3.3. In Secs. 5.2.2 and 5.2.3, the Gaussian and Ising transitions will be investigated. The topological indices characterizing the Haldane* and c-Haldane* phases will be confirmed using numerical simulation in Sec. 5.2.4. The nature of the self-dual line will be discussed in Sec. 5.2.5.

5.1 Heisenberg ladder with CCI

5.1.1 Phase diagram in the $J_\perp$-$K_{\rm ch}$ plane

In this section, the numerical analysis of the ground-state phase diagram for the Heisenberg-CCI ladder (Eq. (1.18) with $\Delta = 1$) is carried out, focusing on the $J_\perp$-$K_{\rm ch}$ parameter space and fixing J to 1. The resulting phase diagram (Fig. 5.1) generally aligns with the schematic phase diagram (Fig. 3.3) predicted by Abelian bosonization and duality considerations. However, there are some deviations, particularly in the position of the plaquette-RS transition line (depicted in blue for $K_{\rm ch} < 0$). In Fig. 5.1, this transition line appears entirely on the $J_\perp < 0$ side and does not curve near the $\mathcal{U}_{\rm s}$ self-dual line, unlike in Fig. 3.3. These discrepancies can potentially be attributed to the omission of marginal terms as discussed in Sec. 3.2.4 or to the fact that the $\mathcal{U}_{\rm s}$ self-dual line is beyond the perturbative field theory regime.

In Fig. 5.1, the Ising transition and crossover lines were determined using iDMRG calculations. However, for the $c = 3/2$ transitions, we encountered convergence difficulties in iDMRG; a similar situation was encountered in Ref. [192]. Specifically, for iDMRG with a finite bond dimension χ, the $c = 3/2$ transition splits into two separate transitions, between which a spontaneous magnetic or VC order emerges. Such a spontaneous breaking of the SU(2) symmetry is not allowed in the ground state of 1D systems as explained in Sec. 2.2.3 (unless the uniform magnetic susceptibility diverges [167]). As χ increases, the extent of these artificially induced ordered phases diminishes, yet it does not completely vanish, making it challenging to pinpoint the exact transition points. To address this, we examine the $c = 3/2$ transitions using exact diagonalization of the polarization amplitude, as explained later in Sec. 5.1.3.

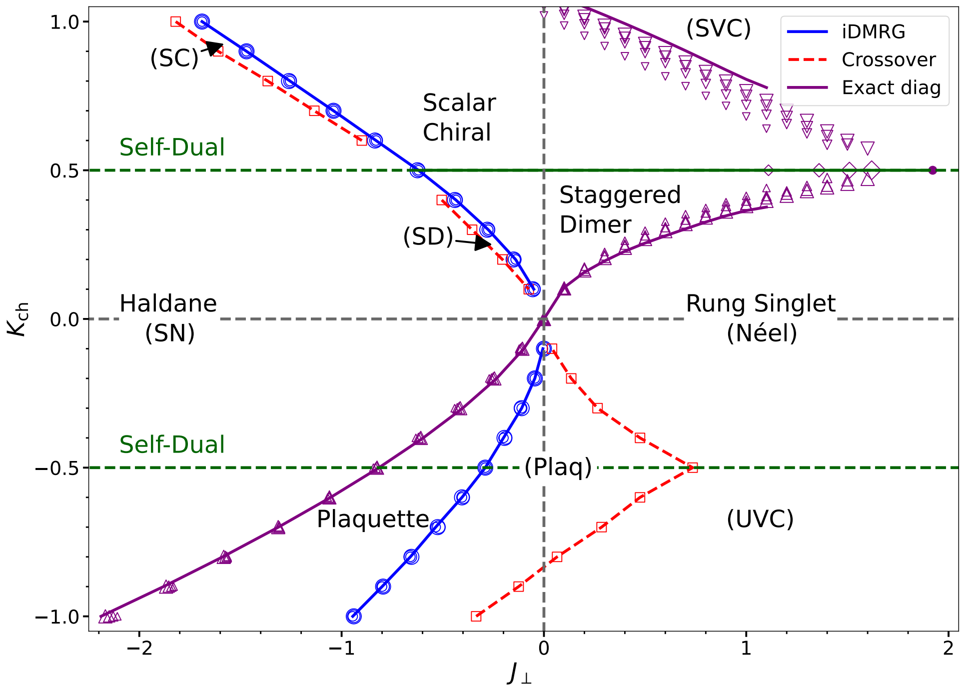

FIGURE 5.1: Ground-state phase diagram of the Heisenberg-CCI ladder (Eq. (1.18) with $\Delta = 1$]), obtained numerically. Ising transition points (blue circles) are determined by iDMRG from the (local) maxima of the correlation length. Small, medium, and large circles correspond to the bond dimensions $\chi = 128, 192$, and 256, respectively, and large circles are interpolated by blue solid lines as a guide for the eye. Purple triangles and diamonds indicate the sign change of the polarization amplitude $z_{\rm rung}$ in Eq. (5.2) calculated by exact diagonalization. For $K_{\rm ch} \neq 0$ and $J/2$, these points are expected to correspond to the $c = 3/2$ transitions in Fig. 3.3. Symbols with increasing marker sizes correspond to the ladder lengths $L = 8$, 10, 12, and 14. For $K_{\rm ch} \geq 0$, up- and down-pointing triangles indicate, respectively, points at which $z_{\rm rung}$ becomes negative and positive with increasing $K_{\rm ch}$. For $K_{\rm ch} = J/2$ and for $K_{\rm ch} < 0$, the sign change of $z_{\rm rung}$ is investigated along the $J_\perp$ axis, and the zeros of $z_{\rm rung}$ are shown by diamonds and up-pointing triangles, respectively. For $J_\perp \leq 1.0$, where the L-dependence of the points is relatively smooth, extrapolation of the transition points to the infinite-size limit is conducted, and the results are interpolated by purple solid lines. Red squares interpolated by dashed lines indicate changes in dominant correlation inside the RS and Haldane phases. These points are determined by iDMRG with $\chi = 128$ as described in Sec. 5.1.4. The types of dominant correlation are indicated in parentheses. Reproduced from Fig. 6 of Ref. [55]. Copyright 2024 by the Physical Society of Japan.

5.1.2 Ising transitions

The Ising transitions can be determined numerically by calculating the correlation length using iDMRG. To this end, eigenvalues of the transfer matrix were used as explained in Sec. 2.8.1. As seen in Figs. 5.2 and 5.4, the Ising transitions are associated with divergences in the correlation length. Locations of the (local) maximum correlation length calculated with a finite bond dimension are indicated in blue circles on the phase diagram in Fig. 5.1. Estimated transition points for bond dimensions $\chi = 128$, 192, and 256 are almost overlapping. Therefore in plotting the phase diagram in Fig. 5.1, it is sufficient to interpolate estimates calculated with $\chi = 256$ as indicated by blue solid lines, to obtain a reasonably accurate transition line.

For the sake of conciseness, only the Haldane-SC and plaquette-RS Ising transitions located respectively beyond the $\mathcal{U}$ and $\mathcal{U}_s$ self-dual line will be discussed in this dissertation. These transitions are exclusive to our model (1.22) while the Haldane-SD and plaquette-RS transitions in the weak interchain coupling regime were already analyzed in related ladder models with an inter-leg DDI (1.22) [28, 92, 220].

Near the transition, convergence issues arose, leading to an underestimation of the extent of the symmetry-broken phase. To address this, we initiated the optimization process from points deep within either the symmetric or symmetry-broken phase. Corresponding results are represented respectively by blue or red markers in Figs. 5.2 and 5.4. Subsequently, for each set of values of K_{ch}, $J_\perp$, and χ, we retained only the point with the lowest energy.

Haldane-SC transition

As discussed from a field-theoretical point of view in Sec. 3.2.3, the Haldane-SC transition is expected to belong to the Ising universality class. It is related to the Haldane-SD transition via the $\mathcal{U}$ transformation. We analyze this transition, at $K_{\text{ch}} = 0.8$ as a representative case, by inspecting the correlation length, the SC order parameter, and its 8th power in Fig. 5.2(a,b,c), respectively. Comparing Fig. 5.2(a,b), the onset of the growth of the SC order parameter is concomitant with the maximum of the correlation length ξ, giving two methods for detecting the phase transition. In addition, the maximum of ξ increases with the bond dimension, supporting a continuous transition.

The most straightforward way to verify the nature of the Haldane-SC transition is to calculate the central charge using the method explained in Sec. 2.8.1. Figure 5.3(a) presents the relationship between S and ξ computed via iDMRG at the Haldane-SC transition. The data closely follow the scaling form (2.82), and the central charge value, $c = 0.523(7)$ [1] obtained from the fit aligns well with $c = 1/2$ predicted for Ising universality class.

Another method consists of plotting the order parameter to the 8th power. Indeed for the Ising universality class, the order parameter is expected to grow as

$$\langle \mathcal{O}(J_\perp) \rangle \propto |J_\perp - J_{\perp,c}|^\beta \tag{5.1}$$

in the SC phase near the transition. Here $J_{\perp,c}$ corresponds to the critical value of $J_\perp$ and $\beta = 1/8$ to the critical exponent of the order parameter.

[1] The number in parentheses represents the standard error in the last digit(s).

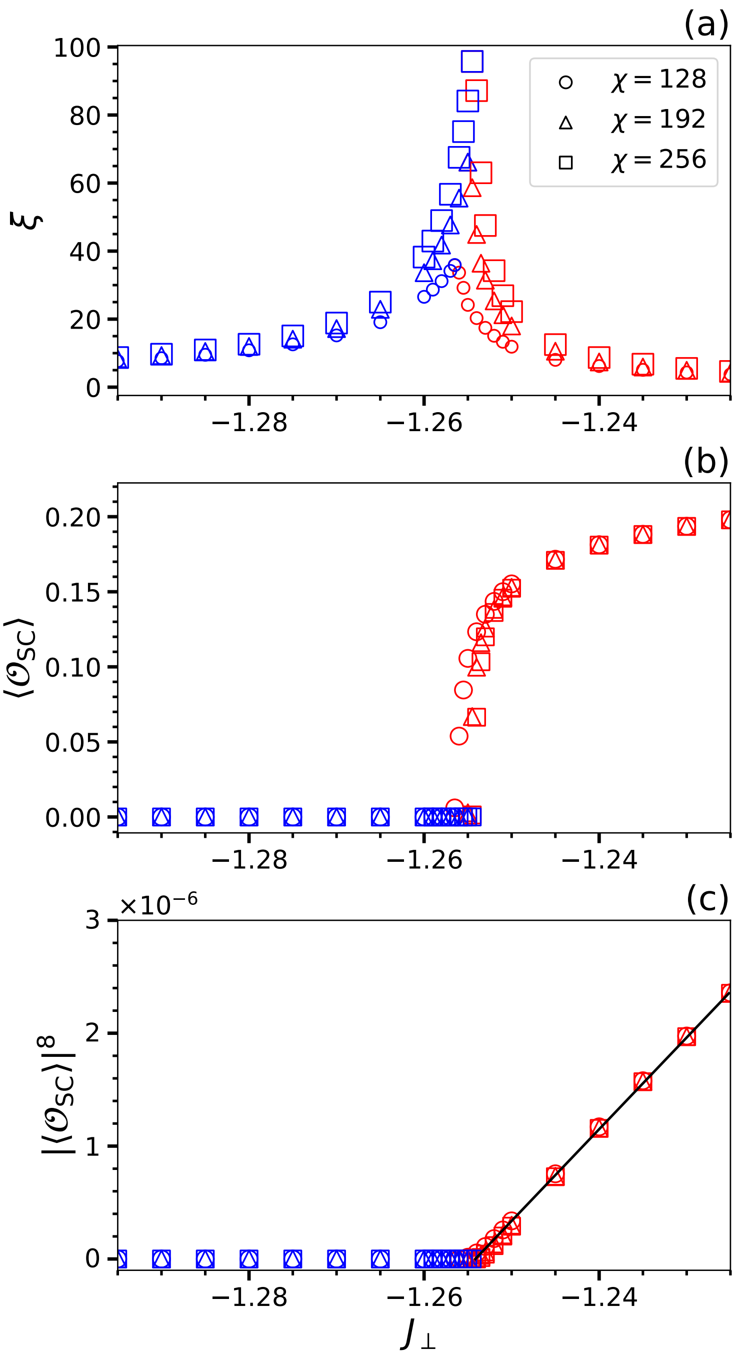

FIGURE 5.2: (a) Correlation length ξ, (b) the SC order parameter $\langle \mathcal{O}_{\mathrm{SC}} \rangle$ in Eq. (1.16), and (c) $\langle \mathcal{O}_{\mathrm{SC}} \rangle^8$, calculated by iDMRG across the Haldane-SC transition at $K_{\mathrm{ch}} = 0.8$. Blue (red) symbols indicate data calculated using an initial point deep in the Haldane (SC) phase. Three different symbol shapes correspond to different bond dimensions χ, as indicated in the legends. In (a), a maximum of ξ occurs at $J_{\perp,c} \approx -1.2565, -1.2550$, and -1.2545 for $\chi = 128$, 192, and 256, respectively. In (c), the solid black line is the linear fitting done in the range not too close to the transition where the χ-dependence of $\langle \mathcal{O}_{\mathrm{SC}} \rangle$ is almost impreceptible. The intercept with the horizontal axis gives $J_{\perp,c} \approx -1.2541$. Reproduced from Fig. 7 of Ref. [55]. Copyright 2024 by the Physical Society of Japan.

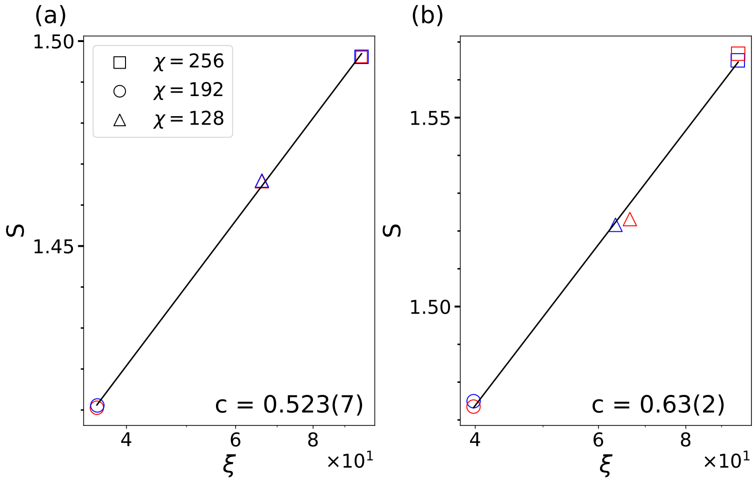

FIGURE 5.3: Half-chain EE S versus the correlation length ξ, calculated by iDMRG at (a) the Haldane-SC transition at $K_{\mathrm{ch}} = 0.8$ in Fig. 5.2 and (b) the plaquette-RS transition at $K_{\mathrm{ch}} = -0.8$ in Fig. 5.4. For each bond dimension χ, the point with the highest correlation length in each phase is plotted. The same symbols and colors as in Figs. 5.2 and 5.4 are used. A logarithmic scale is used for the horizontal axis. Solid lines show the fitting with Eq. (2.82), from which the central charge c is estimated as shown in each panel. Here, the number in parentheses in estimated c shows an error in the last digit that is associated with the linear fitting. In (b), the anomalous point has been neglected during the fitting. The results are in good agreement with the Ising universality class with $c = 1/2$. Reproduced from Fig. 8 of Ref. [55]. Copyright 2024 by the Physical Society of Japan.

As seen in Fig. 5.2(c) near the transition, the finite χ prevents the genuine divergence of the correlation length, and Eq. (5.1) fails. Sufficiently far away from the transition, in a region where $\langle \mathcal{O}_{\mathrm{SC}} \rangle$ is almost independent of χ, $\langle \mathcal{O}_{\mathrm{SC}} \rangle^8$ is well approximated by a linear function, giving another support for the transition to belong to the Ising universality class.

Plaquette-RS transition

The plaquette-RS transition is also expected to belong to the Ising universality class. As both plaquette and RS phases are invariant under $\mathcal{U}_{\mathrm{s}}$, this transition is expected to occur on both sides of the $\mathcal{U}_{\mathrm{s}}$ self-dual line. In this dissertation, the transition will be analyzed in Fig. 5.4 at $K_{\mathrm{ch}} = -0.8$ as a representative case.

The correlation length ξ depicted in Fig. 5.4(a) exhibits a peak that grows with the bond dimension χ. This peak is associated with the onset of the plaquette order parameter (3.41) growth, as indicated by the red symbols in Fig. 5.4(b). In Fig. 5.4(b), the CD order parameter (1.10b) for $\chi = 256$ is also shown in black for reference. The plaquette and CD order parameters display similar behavior as both begin to increase at the same $J_\perp$ in Fig. 5.4(b). Therefore, the plaquette order parameter (3.41), which remains invariant under $\mathcal{U}_{\mathrm{s}}$, will be used to characterize the phase. In Fig. 5.4(c), a linear fit of $\langle \mathcal{O}_{\mathrm{plaq}} \rangle^8$ is applied for each χ. While $\langle \mathcal{O}_{\mathrm{plaq}} \rangle^8$ deviates from the fit close to the transition to an extent that depends on χ, the linear fitting is quite accurate away from it, supporting the possibility of an Ising universality class.

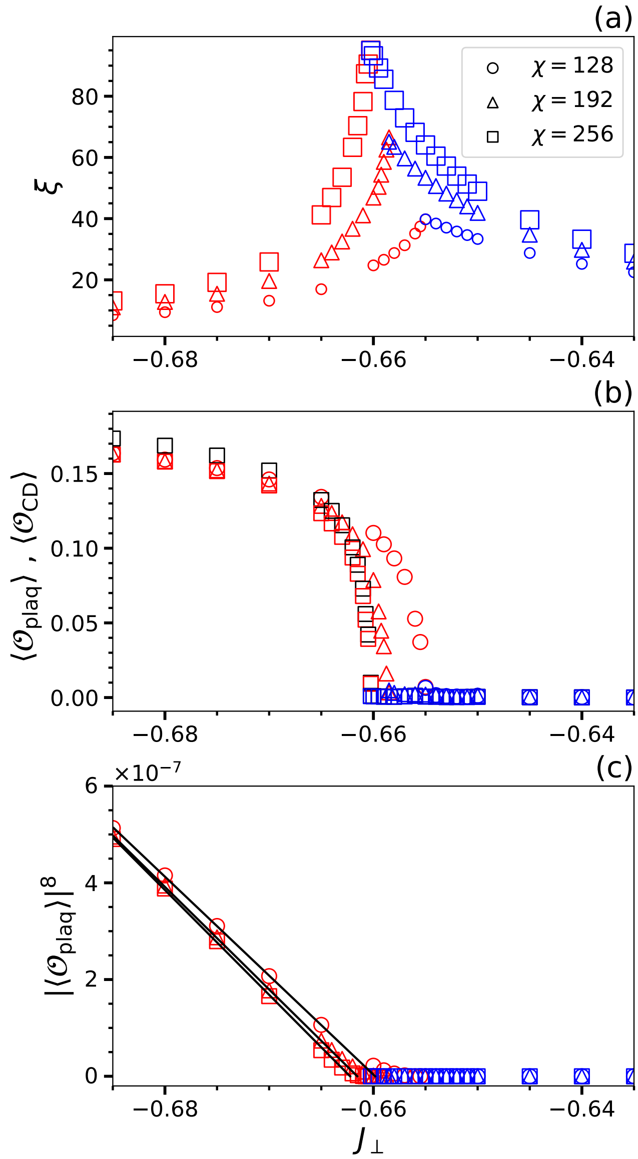

FIGURE 5.4: (a) Correlation length ξ, (b) the plaquette order parameter $\langle\mathcal{O}_{\text{plaq}}\rangle$ in Eq. (3.41) (red and blue) and the CD order parameter $\langle\mathcal{O}_{\text{CD}}\rangle$ in Eq. (1.10b) (black), (c) $\langle\mathcal{O}_{\text{plaq}}\rangle^8$, calculated by iDMRG across the plaquette-RS transtion at $K_{\text{ch}} = -0.8$. Red (blue) symbols indicate data points calculated using an initial point in the plaquette (RS) phase. In (a), a maximum of ξ occurs at $J_{\perp,c} \approx -0.65500(25)$, $-0.65850(25)$, and $-0.66025(25)$ for $\chi = 128$, 192, and 256, respectively. In (b), the CD order parameter is plotted only for $\chi = 256$ for reference. In (c), the solid lines show the linear fitting done not to close to the transition for each χ. The intercept with the horizontal axis gives $J_\perp \approx -0.6598$, -0.6615, and -0.6622 for $\chi = 128$, 192, and 256, respectively. Reproduced from Fig. 9 of Ref. [55]. Copyright 2024 by the Physical Society of Japan.

Transition points inferred from the intercept of the linear fit are provided in the caption of Fig. 5.4. However, since the linear fit in Fig. 5.4(c) may be influenced by the chosen fitting region, we found this method introduces some arbitrariness. Consequently, the simpler estimates obtained from the maximum of ξ for the largest χ has been used in the phase diagram of Fig. 5.1. The calculated value of the central charge, $c = 0.63(2)$ (see Fig. 5.14(b)) is in good agreement with the anticipated value for the Ising universality class.

5.1.3 $c = 3/2$ transitions

The $c = 3/2$ transition line indicated in purple in the phase diagram in Fig. 5.1 is based on the calculation of the polarization amplitude z_{rung} [10, 11, 70, 175–177, 216, 217, 252]. This calculation was performed using the Python package QuSpin [264, 265] on ladders of lengths $L = 8$, 10, 12, and 14. On a two-legged ladder, z_{rung} is defined as [96, 132]

$$z_{\text{rung}} := \left\langle \exp\left(i\frac{2\pi}{L} \sum_{n=1}^{2} \sum_{j=1}^{L} j S^z_{n,j} \right) \right\rangle. \tag{5.2}$$

This corresponds to the value of the Lieb-Schultz-Mattis twist operator [143, 199]. This twist operator related to the rotation around the z-axis is different from the one given in Eq. (2.26) which is associated with the continuous version of the spin-chirality transformation (3.48). As seen from its bosonized expression [70, 175, 177]

$$z_{\text{rung}} \propto -\left\langle \cos\left(2\sqrt{2\pi}\phi_+\right) \right\rangle, \tag{5.3}$$

the sign of z_{rung} depends on the locking position of $2\sqrt{2\pi}\phi_+$. Therefore its zeros are associated with the $c = 3/2$ transition shown in Fig. 3.1(a). The polarization amplitude is invariant under duality transformations $\mathcal{U}$ and $\mathcal{U}_s$ and can also be used to investigate the dual counterpart of the $c = 3/2$ transition shown in Fig. 3.1(b,c).

In Fig. 5.5, z_{rung} is plotted as a function of K_{ch} with $J_\perp$ set to 0.5 as a representative case. The zeros in Fig. 5.5(a) correspond to the finite-size estimates of the RS-SD and SC-RS transition points which are reported respectively in upward and downward triangles on Fig. 5.1. Away from the $\mathcal{U}$-self-dual line ($J_\perp \lesssim 1.2$), transition points for finite systems are well fitted by a linear function of L^{-2}, as seen in Fig. 5.5(b). The transition points in an infinite system can be estimated from this fitting. They are represented by the solid purple lines in Fig. 5.1. For larger $J_\perp$, closer to the self-dual line, the L^{-2}-fitting is not reliable. Therefore we choose not to indicate the extrapolation to infinity for those points in Fig. 5.1.

Notably, the polarization amplitude z_{rung} cannot be used to investigate the SD-SC transition. According to the spin-chirality duality (3.53) and the field-theoretical analysis around an SU(4) quantum multicritical point [137, 138], it should be located on the self-dual line $K_{\text{ch}} = 1/2$. According to the hard-core bosons picture in Sec. 4.1.2, the SD-SC transition should extend up

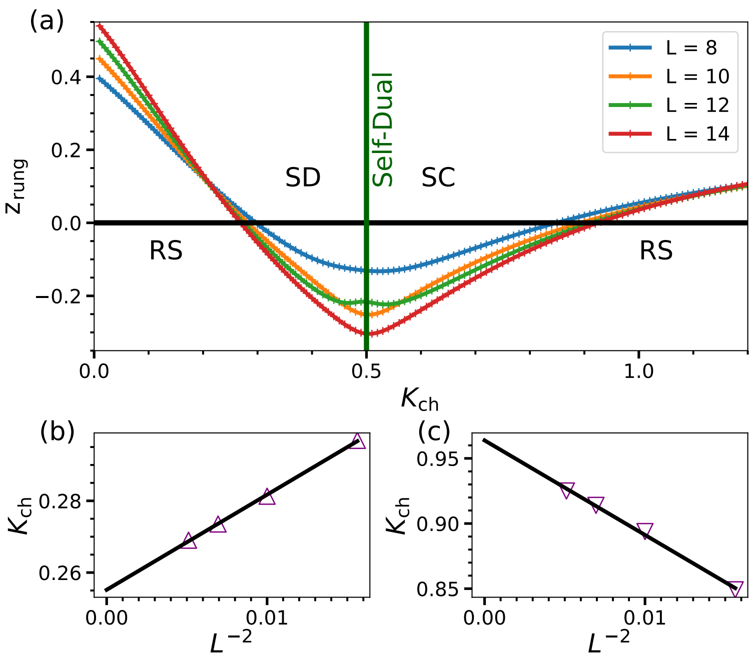

FIGURE 5.5: (a) Polarization amplitude z_{rung} in Eq. (5.2) as a function of K_{ch}, obtained by exact diagonalization for the case of $J_{\perp} = 0.5$ in Fig. 5.1. Results for different ladder lengths L are shown by different colors. The sign changes of z_{rung} give finite-size estimates of the RS-SD and SC-RS transitions. (b,c) Extrapolation of the RS-SD (b) and SC-RS (c) transition points, based on a linear function of L^{-2} [176]. The transition point in the infinite-size limit is given by the intercept. Reproduced from Fig. 7 of Ref. [56]. Copyright 2024 by the American Physical Society.

to $J_\perp < 2$. This is coherent with the estimated transition point toward the RS phase indicated in diamonds symbols in Fig. 5.1.

5.1.4 Dominant correlation

In this section, structure factors and correlation functions are examined to investigate the dominant correlation. As seen in the field-theoretical analysis in Sec. 3.2.2, despite being featureless and not spontaneously breaking any symmetry, the RS and Haldane phases can still be characterized by their dominant correlation.

Structure factors

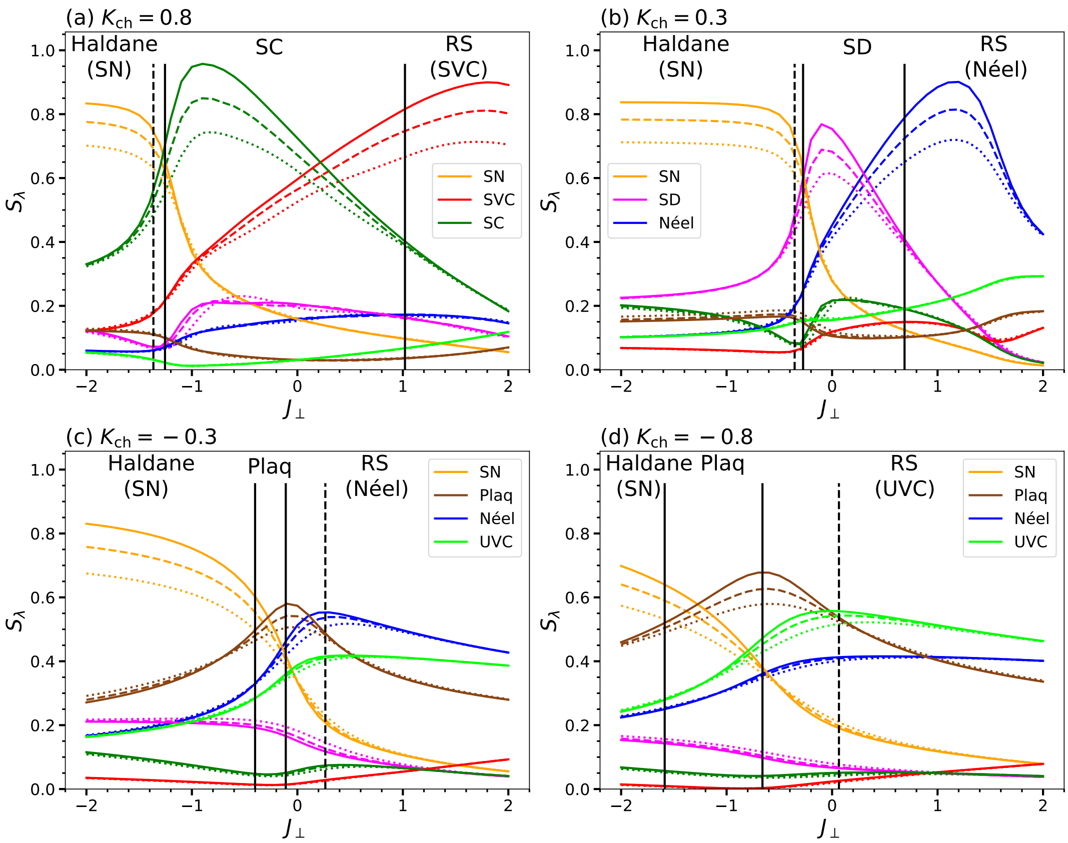

FIGURE 5.6: Structure factors in Eqs. (5.4) and (5.5) calculated by exact diagonalization at (a,d) $K_{ch} = \pm 0.8$ and (b,c) $K_{ch} = \pm 0.3$. Data for the ladder lengths $L = 8$, 10, and 12 are shown by dotted, dashed, and solid lines, respectively. Vertical solid lines indicate the $c = 3/2$ and Ising transition points determined in Secs. 5.1.3 and 5.1.2. Vertical dashed lines indicate the crossover points determined as in Fig. 5.7. On the top of each figure, we indicate the names of the phases and the expected dominant correlations in parenthesis. Dominant correlations in the region between the crossover and transition lines are the same as the ones in the symmetry-broken phase. Reproduced from Fig. 10 of Ref. [55]. Copyright 2024 by the Physical Society of Japan.

Before calculating the correlation function, it is helpful to first examine the structure factors to identify the most dominant correlation in each region. Let the staggered structure factor be defined by

$$S_\lambda = \frac{1}{L}\left\langle \left[\sum_j (-1)^j \mathcal{O}_\lambda(j) \right]^2 \right\rangle, \tag{5.4}$$

for $\lambda =$ Néel, SN, SD, plaq, SC, and SVC, as well as the UVC structure factor

$$S_{\mathrm{UVC}} = \frac{1}{L}\left\langle \left[\sum_j \mathcal{O}_{\mathrm{UVC}}(j) \right]^2 \right\rangle. \tag{5.5}$$

In Fig. 5.6(a,b,c,d), the structure factors calculated by exact diagonalization of a periodic ladder of length $L \in \{8, 12, 14\}$ are plotted for $K_{\mathrm{ch}} \in \{0.8, 0.3, -0.3, -0.8\}$ respectively. Valuable insights into the phases can be obtained by examining the limit $L \to \infty$ of the structure factors. In general, for phases with long-range order, the structure factor scales proportionally with L as seen in Eq. (2.17), whereas for phases with short-range order, the structure factor converges to a constant value.

For this dissertation, the structure factor will solely be used to identify the development of different correlations in the phase diagram. Quantitative information like the distinction between long- or short-range orders or precise localization of crossover lines will be done using iDMRG results.

For $K_{\mathrm{ch}} = -0.3$ in Fig. 5.6(c), the SN, plaquette, and Néel structure factors become dominant in this order as $J_\perp$ increases. Notably, the plaquette structure factor remains large even beyond the plaquette-RS transition point at $J_\perp = -0.110(5)$. The shift in dominant correlations from plaquette to Néel appears to occur *within* the RS phase, aligning with the field-theoretical prediction shown in Fig. 3.3. In the case of $K_{\mathrm{ch}} = -0.8$, presented in Fig. 5.6(d), the behavior can be interpreted as the $\mathcal{U}_{\mathrm{s}}$-dual counterpart of Fig. 5.6(c). Instead of the Néel structure factor, the UVC structure factor becomes dominant in the rightmost region of Fig. 5.6(d). Notably, the Néel and UVC structure factors are expected to coincide along the $\mathcal{U}_{\mathrm{s}}$-self-dual line at $K_{\mathrm{ch}} = -1/2$.

For $K_{\mathrm{ch}} = 0.3$ in Fig. 5.6(b), the SN, SD, and Néel structure factors become dominant in this order as $J_\perp$ increases. As the crossover from SN to SD dominant correlation appears to occur very close to the Haldane-SD transition point at $J_\perp = -0.660(5)$, and it is not entirely clear whether this transition occurs *within* the Haldane phase, as predicted in Figs. 3.3 and 3.1(a) or not. To determine this in a conclusive manner a more detailed analysis will be carried out in the subsequent section. The result for $K_{\mathrm{ch}} = 0.8$ in Fig. 5.6(a) can be interpreted as the $\mathcal{U}$-dual counterpart to Fig. 5.6(b). Instead of the SD and Néel correlations seen in Fig. 5.6(b), the SC and SVC correlations become dominant in Fig. 5.6(c). The SD and SC, or Néel and SVC structure factors, should coincide along the $\mathcal{U}$-self-dual line at $K_{\mathrm{ch}} = 1/2$. It is also worth noting that in the exact RS state for $K_{\mathrm{ch}} = 1/2$ and $J_\perp > 2$ (as shown in Fig. 3.3), all local correlation functions, such as those in Eqs. (5.6) and (5.7), vanish unless the two operators overlap.

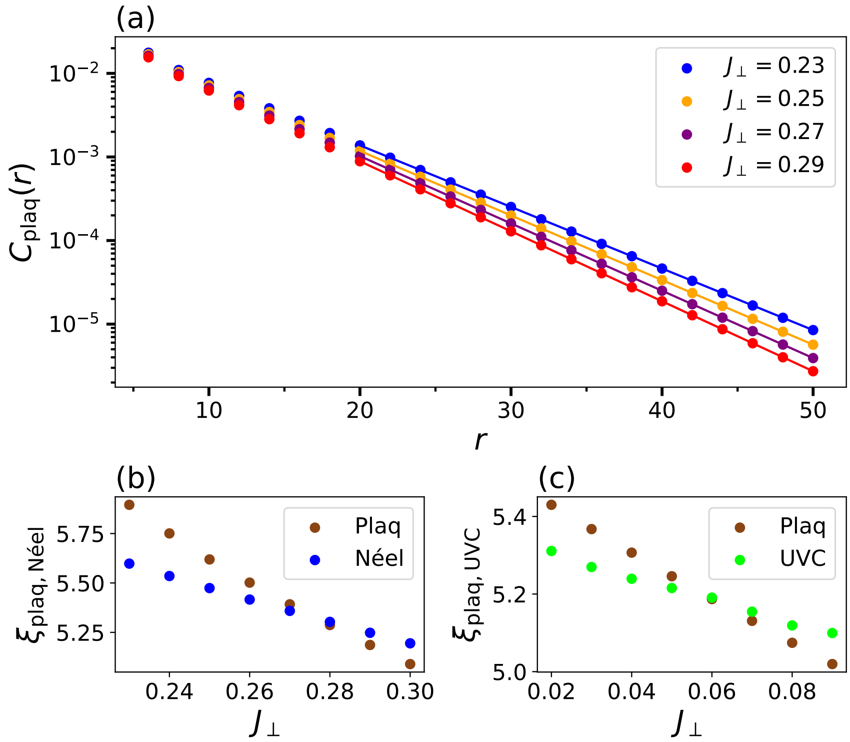

FIGURE 5.7: (a) Plaquette correlation function $C_{\mathrm{plaq}}(r)$ in Eqs. (5.6) (in logarithmic scale) calculated by iDMRG with $\chi = 128$ for fixed $K_{\mathrm{ch}} = -0.3$ and for different values of $J_\perp$ shown in the legend. Lines show the fitting with the exponential form $A \exp\left(-r/\xi_{\mathrm{plaq}}\right)$ for $20 \leq r \leq 50$, from which the correlation length ξ_{plaq} can be extracted. (b) Correlation lengths extracted from the plaquette and Néel correlation functions at $K_{\mathrm{ch}} = -0.3$. (c) Correlation lengths from the plaquette and UVC correlation functions at $K_{\mathrm{ch}} = -0.8$. The crossover points inside the RS phase are estimated to be $J_\perp \approx 0.28$ and 0.06 in (b) and (c), respectively. Reproduced from Fig. 11 of Ref. [55]. Copyright 2024 by the Physical Society of Japan.

Correlation functions

In the previous section, the dominant correlation inside the Haldane and RS phases has been discussed through the structure factors. However, numerical result on such a small system makes difficult the precise localization of crossover lines. In this section, through a careful examination of the correlation function, the crossover line predicted in Fig. 3.3 will be precisely determined.

Let the staggered correlation functions be defined by

$$C_\lambda(r) = (-1)^r \langle \mathcal{O}_\lambda(0)\mathcal{O}_\lambda(r)\rangle , \tag{5.6}$$

where λ stands for Néel, SN, SD, plaq, SC, and SVC, as well as the UVC correlation function

$$C_{\mathrm{UVC}}(r) = \langle \mathcal{O}_{\mathrm{UVC}}(0)\mathcal{O}_{\mathrm{UVC}}(r)\rangle . \tag{5.7}$$

As a representative case, the plaquette correlation function C_{plaq}(r) inside the RS phase at $K_{\mathrm{ch}} = -0.3$ is shown in Fig. 5.7(a). When r is large enough, the C_{plaq}(r) function, plotted using a logarithmic scale, can be approximated by a linear function. The correlation length associated with the Néel ($\xi_{\text{Néel}}$) and plaquette (ξ_{plaq}) order operators, calculated from similar fitting, are plotted as a function of $J_\perp$ at $K_{\mathrm{ch}} = -0.3$ in Fig. 5.7(b). These correlation lengths should be respectively identified with v/m_{t} and $v/|m_{\mathrm{s}}|$, as seen in Eq. (3.46). The crossover between regions with dominant Néel and plaquette correlations is estimated from the crossing to occur at $J_\perp \approx 0.28$. Likewise, the plaquette-UVC crossover point inside the RS phase at $K_{\mathrm{ch}} = -0.8$ can be estimated from the crossing in Fig. 5.7(c) to be $J_\perp \approx 0.06$. The crossover points plotted in red squares in Fig. 5.1 have been determined by a similar procedure.

A similar analysis has been carried out for the SN-SD and SN-SC crossovers for $K_{\mathrm{ch}} > 0$. The presence of the Ising transition close to the crossover makes the representation of the correlation function less readable so we chose to not represent it. Still, the crossover unambiguously occurs inside the Haldane phase. On the $\mathcal{U}$-self-dual line, due to convergence issues the analysis of the correlation function was not possible.

5.1.5 Boson density

In this short section, the gapless nature of the $\mathcal{U}$-self-dual line will be discussed, based on the calculation of the expectation value of the boson density n^B in Eq. (4.9) introduced in Sec. 4.1.

The boson density is calculated by exact diagonalization for ladder lengths up to $L = 14$ and plotted in Fig. 5.8. As seen in Sec. 4.1.2, the continuous version of the duality transformation can be interpreted as a $U(1)$ gauge transformation of the Hamiltonian written in terms of hard-core bosons (4.4). On the self-dual line ($K_{\mathrm{ch}} = 1/2$), the Hamiltonian (1.18) is gauge invariant and the boson number is a good quantum number. For the isotropic model ($\delta = 0$), the $J_\perp$ term acts as a chemical potential changing the expectation value of n^{B}. The ground state expectation value of n^B increases with decreasing $J_\perp$. In a ladder of length L, the boson density changes in a steplike manner with discontinuity equal to $1/L$. The boson density curve behaves similarly to the magnetization curve in spin systems with the spin-rotational U(1) symmetry. As predicted in Fig. 4.1, when $J_\perp > 2$, bosonic excitation is gapped and we have $n^{\mathrm{B}} = 0$; in terms of the original model, this corresponds to the RS phase [126, 173]. Oppositely, $J_\perp \lesssim -0.6$, all rungs are occupied by a boson ($n^{\mathrm{B}} = 1$), and the system behaves as a chain of spin-1 interacting through the J_{bl} term in Eq. (4.4); accordingly, the system is in the Haldane phase. Between these two extreme cases, for $-0.6 \lesssim J_\perp < 2$, the boson density n^{B} takes a non-integer value between 0 and 1. According to the Lieb-Schultz-Mattis-type theorem in Sec. 4.1, the system must show degenerate ground states or gapless excitations in the thermodynamic limit in this region.

In addition, no robust plateau-like features [2] are observed in $n^{\mathrm{B}}(\neq 0, 1)$. As such features are usually associated with energy gaps, one expects the SD-SC transition to have gapless excitations for $-0.6 \lesssim J_\perp < 2$. This suggests that the SD-SC transition that occurs on the self-dual line is continuous. Note that the upper bound is consistent with the value calculated from the twist operator in Fig. 5.1. Away from the self-dual line, the gauge invariance is explicitly broken. Therefore, the boson density is no longer a good quantum number and the n^B curve behaves more smoothly. Still, near the self-dual line, the discontinuity of the boson density causes finite-size effects in other quantities, explaining the difficulty in extrapolating the transition points determined by the polarization amplitude for $J_\perp \geq 1.2$ in Fig. 5.1.

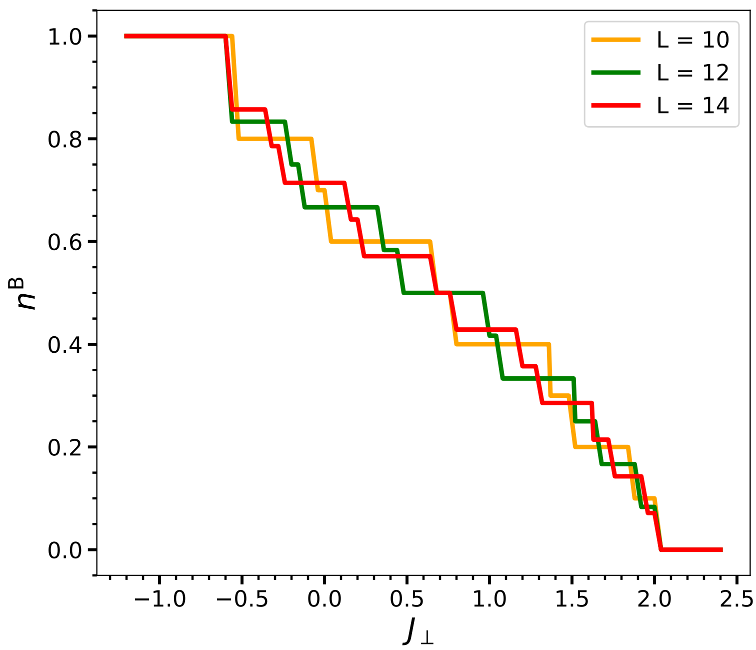

FIGURE 5.8: The ground-state value of the boson density n^B in Eq. (4.9), calculated by exact diagonalization along the self-dual line $K_{\mathrm{ch}} = 1/2$ in Fig. 5.1. Results for different ladder lengths L are shown by different colors. Reproduced from Fig. 8 of Ref. [56]. Copyright 2024 by the American Physical Society.

[2]Other than the small steps that decreases with increasing L.

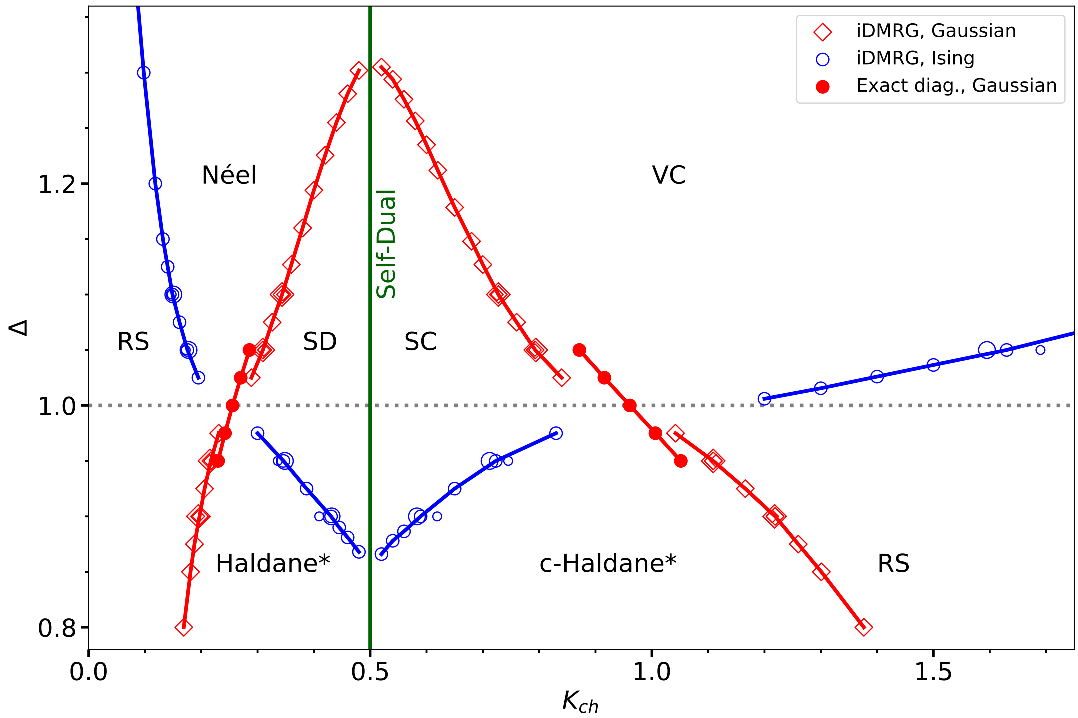

FIGURE 5.9: Ground-state phase diagram of the XXZ-CCI ladder (1.18) with $J = 1$ and $J_\perp = 0.5$, obtained numerically. Red and blue empty symbols indicate Gaussian and Ising transition points, respectively, that are determined by iDMRG from the (local) maxima of the correlation length. Medium-size empty symbols connected by solid lines show the data for the bond dimension $\chi = 192$, which gives semi-quantitative phase boundaries. In some cases, the data for $\chi = 128$ and $\chi = 256$ are also presented with small and large empty symbols, respectively, to illustrate the χ-dependence of the results. Near the isotropic case $\Delta = 1$, where iDMRG tends to converge worse, we performed an exact diagonalization analysis of the polarization amplitude z_{rung}, as shown in Fig. 5.5. A sign change of z_{rung} corresponds to a Gaussian transition in the symmetric channel. Red filled symbols connected by solid lines show exact diagonalization results from extrapolating to the infinite-size limit. Reproduced from Fig. 9 of Ref. [56]. Copyright 2024 by the American Physical Society.

5.2 XXZ-CCI ladder

5.2.1 Phase diagram in the Δ-K_{ch} plane

In this second part, the effect of anisotropy on the ground-state phase diagram will be investigated numerically. We will restrict ourselves to the case of $J_\perp = 0.5$ and $K_{\mathrm{ch}} > 0$ while investigating the phase diagram in the K_{ch}-Δ plane presented in Fig. 5.9.

Empty symbols in Fig. 5.9 indicate the Ising (blue) and Gaussian (red) transitions, which were determined from the local maxima of the correlation length calculated using iDMRG, similarly to Sec. 5.1.2. The effect of finite χ has been investigated for $\Delta \in \{0.9, 0.95, 1.05, 1.10\}$. For these Δ's, transition points calculated with $\chi = 128$, 192, and 256 are indicated with symbols of increasing size. While the estimated Gaussian transition points are almost χ-independent, the estimated Ising transition points slightly depend on χ.

For the rest of the phase diagram, both transitions were investigated using $\chi = 192$, and the estimated transition points are interpolated with solid lines in Fig. 5.9, which are sufficient for a semiquantitative phase diagram.

Near the isotropic case with $\Delta = 1$, some difficulties arose in iDMRG. First, due to the proximity of the two phase transitions, the analysis of maxima of the correlation length was challenging. A more profound issue was that we did not observe a direct RS-SD or SC-RS transition at $\Delta = 1$. Instead, we observed the presence of Néel (VC) order between the RS and SD (SC) phases. With increasing χ, the extent of these symmetry-broken regions diminishes and it is natural to suspect that their presence is a mere finite-χ effect.[3] To overcome these difficulties, near the self-dual line, the Gaussian transition line was determined from the zeros of the polarization amplitude as done in Fig. 5.5 in Sec. 5.1.3. The transition points extrapolated to the infinite-size limit are shown by red filled circles in Fig. 5.9. Remarkably, despite the limited system sizes used for ED, the two methods agree quantitatively well in the regimes slightly away from $\Delta = 1$, and minor differences could be attributed to the lack of a proper infinite-size extrapolation.

Overall, the phase diagram in Fig. 5.9 aligns with the prediction of Abelian bosonization and the duality developed in Sec. 3.3.3. On each side of the self-dual line, the Ising and Gaussian transition lines cross near the isotropic line, as depicted in Fig. 3.4(b,d). The self-dual line is precisely located at $K_{\mathrm{ch}} = 1/2$ for all values of anisotropy. For sufficiently strong easy-axis (easy-plane) anisotropy, a direct Néel-VC (Haldane*-c-Haldane*) transition occurs on the self-dual line in agreement with the hard-core bosons picture in Sec. 4.1. A SD-SC transition occurs on the self-dual line around the isotropic line, which is consistent with Refs. [137, 138].

As the exact diagonalization analysis near the isotropic line has already been covered in Sec. 5.1.3, the remaining of this chapter will be devoted to the analysis of the iDMRG calculation. The crossing of the Ising and Gaussian transition lines on the left side ($K_{\mathrm{ch}} < 1/2$) has already been investigated in a similar model with an inter-leg DDI [192, 194] and will not be discussed further in this chapter.

5.2.2 Gaussian transitions

SC-VC transition

The SC-VC transition is the dual counterpart of the SD-Néel transition. As argued in Secs. 3.3.1 and 3.3.2, this transition is expected to belong to the Gaussian universality class. To verify this fact, the case $\Delta = 1.05$ will be analyzed as a representative case. Convergence issues similar to those encountered in Sec. 5.1 occurred near the transition. As the two ordered phases compete with each other, precise localization of the transition point is difficult. Therefore, similarly to the previous section, two different initial conditions (represented in blue or red) were used for the calculation. At the transition, the correlation length ξ plotted in Fig. 5.10(a) forms a peak whose size increases with χ, suggesting that the SC-VC transition is continuous. The value at which the maximum occurs depends weakly on χ. Therefore, the transition point

[3] Similar behavior was also discussed in Appendix B of Ref. [192].

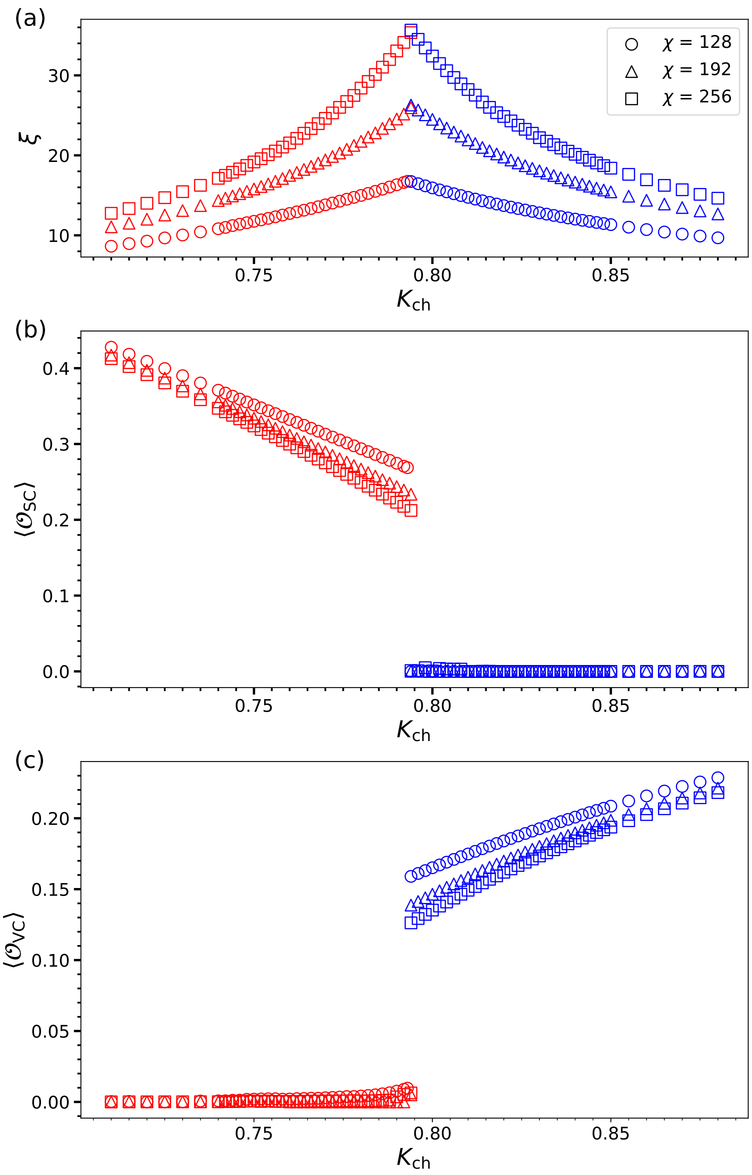

FIGURE 5.10: (a) Correlation length ξ in Eq. (2.81) and (b,c) the SC and VC order parameters in Eqs. (1.16) and (1.16) respectively, calculated by iDMRG across the SC-VC Gaussian transition at $\Delta = 1.05$ in Fig. 5.9. Red (blue) symbols indicate data points calculated using an initial point in the SC (VC) phase. Three different symbol shapes correspond to different χ, as indicated in the legends. The maximum of ξ in (a) is independent of χ within the parameter sampling of our calculation; we thus obtain a reasonable estimate $K_{ch,c} = 0.794(2)$ of the transition point. Reproduced from Fig. 10 of Ref. [56]. Copyright 2024 by the American Physical Society.

estimated from $\chi = 192$ ($K_{\mathrm{ch,c}} = 0.794(2)$) has been used when drawing the phase diagram in Fig. 5.9 without performing any extrapolation as a function of χ.

The SC and VC phases are both characterized by an order parameter that takes a non-zero value exclusively inside the corresponding phase, as seen in Fig. 5.10(b,c). As one approaches the transition, the order parameter exhibits a discontinuity that diminishes with the bond dimension. This is in contradiction with the behavior expected for a Gaussian transition.

$$\langle \mathcal{O}_{\mathrm{SC,VC}} \rangle \sim |K_{\mathrm{ch}} - K_{\mathrm{ch,c}}|^{\beta}, \tag{5.8}$$

where $\beta = K_+/(4 - 4K_+)$ and K_+ is the TLL parameter. This discrepancy could be attributed to finite-χ effects, which can be mitigated by an appropriate extrapolation of the order parameter as a function of χ. For the purpose of this dissertation, such an extrapolation will not be carried out. See Ref. [192] for a detailed discussion on the critical behavior of the correlation length and order parameters at the Néel-SD transition (the $\mathcal{U}$ dual to the SC-VC transition).

As we did in Sec. 5.1.2, the nature of the transition will be analyzed by calculating the central charge using Eq. (2.82). The fitting of the half-chain EE S as a function of the correlation length ξ is shown in Fig. 5.11(a). The central charge calculated from Eq. (2.82) is $c = 1.06(4)$, which aligns with the central charge $c = 1$ anticipated for the Gaussian universality class.

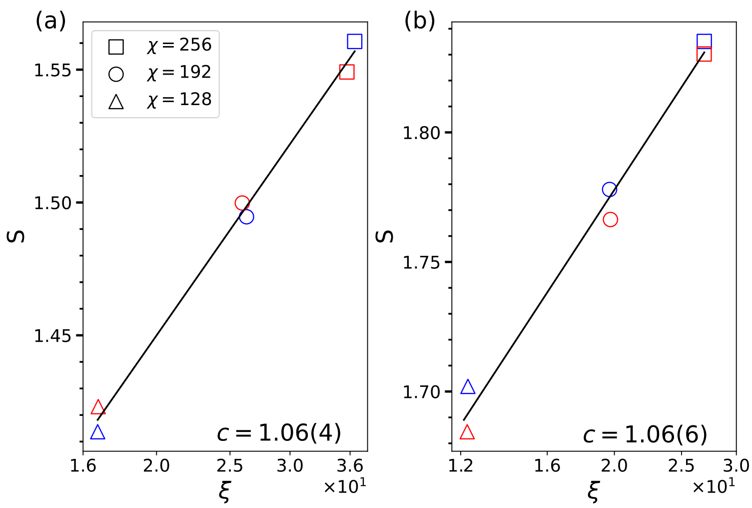

FIGURE 5.11: Half-chain EE S in Eq. (2.53) versus the correlation length ξ in Eq. (2.81), calculated by iDMRG at (a) the SC-VC transition at $\Delta = 1.05$ in Fig. 5.10 and (b) the c-Haldane*-RS transition at $\Delta = 0.95$ in Fig. 5.12. For each bond dimension χ, the point with the highest correlation length in each phase is plotted. The same symbols and colors as in Figs. 5.10 and 5.12 are used. A logarithmic scale is used for the horizontal axis. Solid lines show the fitting with Eq. (2.82), from which the central charge c is estimated as shown in each panel. Here, the number in parentheses in estimated c shows an error in the last digit that is associated with the linear fitting. The results are in good agreement with the Gaussian universality class with $c = 1$. Reproduced from Fig. 11 of Ref. [56]. Copyright 2024 by the American Physical Society.

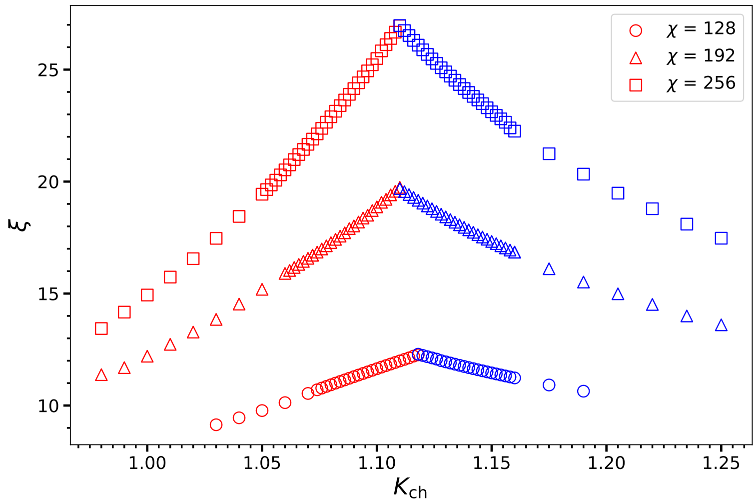

FIGURE 5.12: Correlation length ξ in Eq. (2.81), calculated by iDMRG across the c-Haldane*-RS transition at $\Delta = 0.95$ in Fig. 5.9. Red (blue) symbols indicate data points calculated using an initial point in the c-Haldane* (RS) phase. The peak position of ξ depends little on χ; in particular, the peak positions for $\chi = 192$ and 256 are precisely the same within the parameter sampling of our calculation, giving a reasonable estimate $K_{\mathrm{ch,c}} = 1.110(2)$ of the transition point. Reproduced from Fig. 15 of Ref. [56]. Copyright 2024 by the American Physical Society.

c-Haldane*-RS transition

The c-Haldane*-RS transition is an example of a topological phase transition between two featureless phases. This transition is dual to the Haldane*-RS transition. From the effective field theoretical study in Secs. 3.3.1 and 3.3.2, this transition is expected to belong to the Gaussian universality class. The correlation length ξ is plotted for the representative case $\Delta = 0.95$ in Fig. 5.12(b). The maximum of the correlation length increases with the bond dimension χ, indicating a continuous transition. Given the weak dependence of the estimated transition point on χ, the estimate calculated with $\chi = 192$ ($K_{\mathrm{ch,c}} = 1.110(2)$) was used while establishing the phase diagram.

The central charge calculated from the fit in Fig. 5.11 is 1.06(6), giving support for a Gaussian transition.

5.2.3 Ising transitions

VC-RS transition

The VC-RS transition is the $\mathcal{U}$ dual to the Néel-RS transition. As argued in Secs. 3.3.1 and 3.3.2, this transition is expected to belong to the Ising universality class. Similarly to the investigation of the Ising transition done in Sec. 5.1.2, the nature of the transition will be determined by analyzing the central charge and the scaling behavior of the VC order parameter at the transition for the representative case $\Delta = 1.05$.

As seen in Fig. 5.13(a), the maximum of the correlation length increases with χ, indicating a continuous transition. The peak of the correlation length is associated with the onset of the VC order parameter in Fig. 5.13(b). This

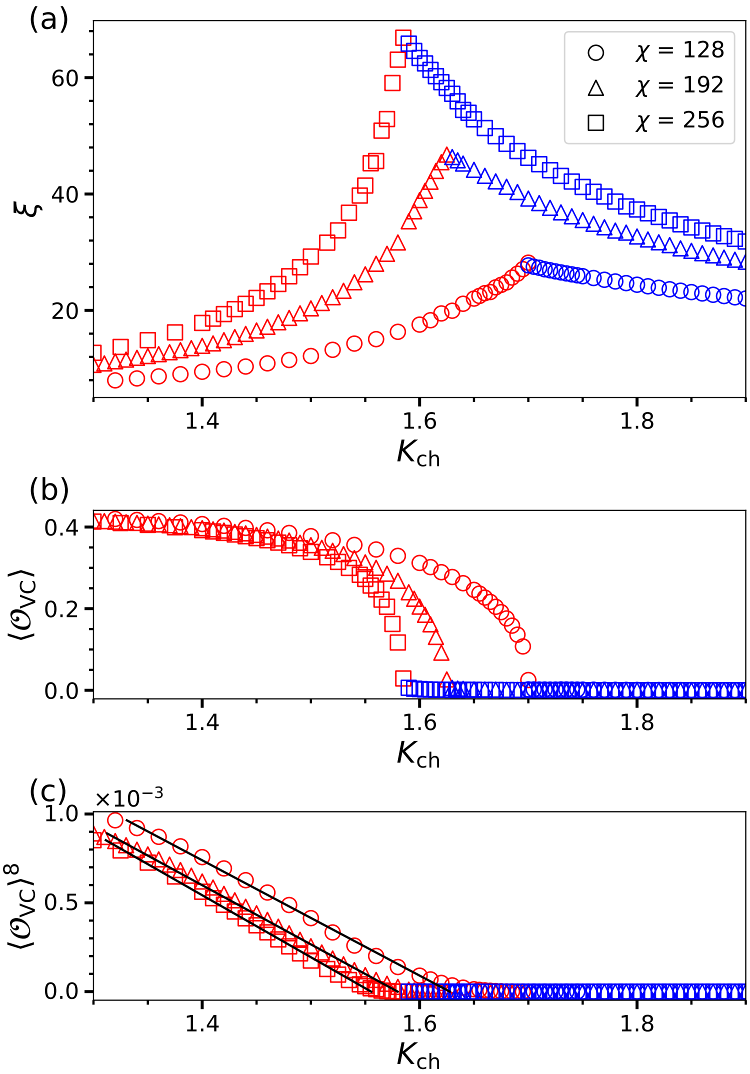

FIGURE 5.13: (a) Correlation length ξ in Eq. (2.81), (b) the VC order parameter $\langle \mathcal{O}_{\rm VC} \rangle$ in Eq. (3.52), and (c) $\langle \mathcal{O}_{\rm VC} \rangle^8$, calculated by iDMRG across the VC-RS transition at $\Delta = 1.05$ in Fig. 5.9. Red (blue) symbols indicate data points calculated using an initial point in the VC (RS) phase. In (a), a maximum of ξ occurs at $K_{\rm ch,c} \approx 1.70$, 1.63, and 1.59 for $\chi = 128$, 192, and 256, respectively. In (c), black solid lines are linear fittings done for each χ in regions not too close to the transition. The intercept with the horizontal axis gives $K_{\rm ch,c} \approx 1.63$, 1.58, and 1.55 for $\chi = 128$, 192, and 256, respectively. The difference between the two estimates of the transition point becomes smaller with an increase in χ. Reproduced from Fig. 12 of Ref. [56]. Copyright 2024 by the American Physical Society.

maximum occurs at a lower value of K_{ch} with increasing χ, and without a systematic extrapolation method, the precise determination of the transition point in the infinite-χ limit is difficult. Accordingly, the transition point estimated using $\chi = 192$ will be used while plotting the phase diagram in Fig. 5.9. The scaling in Eq. (2.82) of the EE S as a function of the maxima of the correlation length ξ in Fig. 5.14(a) gives the value $c = 0.57(1)$, which agrees reasonably with the Ising universality class with $c = 1/2$.

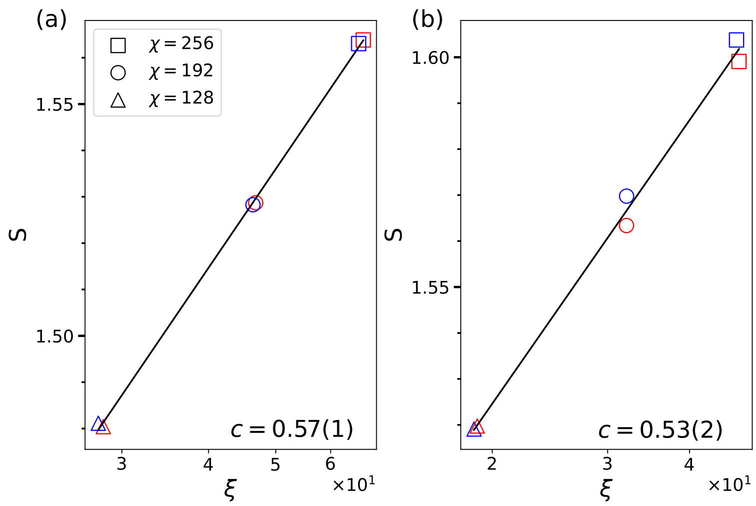

FIGURE 5.14: Half-chain EE S in Eq. (2.53) versus the correlation length ξ in Eq. (2.81), calculated by iDMRG at (a) the VC-RS transition at $\Delta = 1.05$ in Fig. 5.13 and (b) SC-c-Haldane* transition at $\Delta = 0.95$ in Fig. 5.15. For each bond dimension χ, the point with the highest correlation length in each phase is plotted. The same symbols and colors as in Figs. 5.13 and 5.15 are used. A logarithmic scale is used for the horizontal axis. Solid lines show the fitting with Eq. (2.82); the estimated central charge c shown in each panel agrees reasonably with the Ising universality class with $c = 1/2$. Reproduced from Fig. 13 of Ref. [56]. Copyright 2024 by the American Physical Society.

In Fig. 5.13(c), $\langle \mathcal{O}_{\mathrm{VC}} \rangle^8$ is plotted as a function of K_{ch}. In the region where the order parameter is almost insensitive to the bond dimension χ, $\langle \mathcal{O}_{\mathrm{VC}} \rangle^8$ is well fitted by a linear function, giving additional support for the Ising transition. Using the intercept of the linear regression with the K_{ch} axis, one can obtain an alternative estimate for the transition points, which are indicated in the caption of Fig. 5.13. As other transitions near the Ising transition influence the behavior of the order parameter. It is difficult to observe the order parameter growth according to Eq. (5.1) on a sufficiently large range to obtain a trustworthy fit. Thus, we preferred to use the simpler estimate using the maximum of ξ to determine the phase diagram in Fig. 5.9.

SC-c-Haldane* transition

In Secs. 3.3.1 and 3.3.2, we predicted the SC-c-Haldane* transition. This is the $\mathcal{U}$-dual to the SD-Haldane* transition and thus it is expected to belong to the Ising universality class. This transition will be analyzed at the representative point $\Delta = 0.95$ with the same method used for the VC-RS transition. The correlation length, the SC order parameter (Eq. (1.16)) and its 8th power are

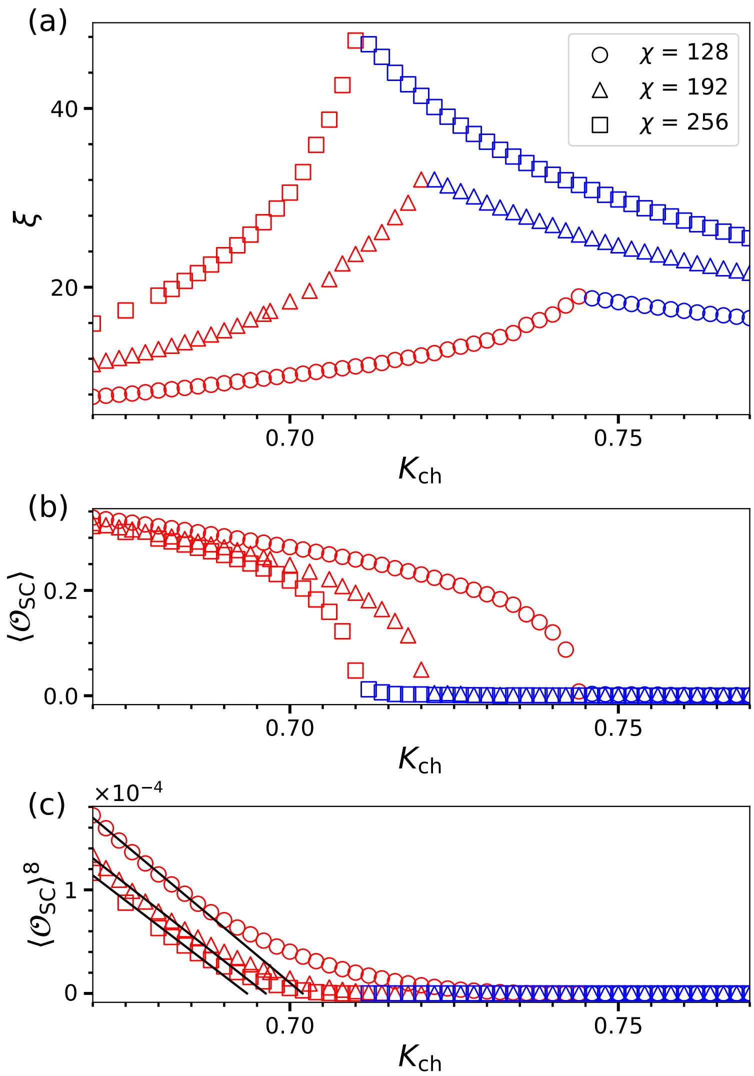

FIGURE 5.15: (a) Correlation length ξ in Eq. (2.81), (b) the SC order parameter $\langle \mathcal{O}_{SC} \rangle$ in Eq. (1.16), and (c) $\langle \mathcal{O}_{SC} \rangle^8$, calculated by iDMRG across the SC-c-Haldane* transition at $\Delta = 0.95$ in Fig. 5.9. Red (blue) symbols indicate data points calculated using an initial point in the SC (c-Haldane*) phase. In (a), a maximum of ξ occurs at $K_{ch} \approx 0.75$, 0.72, and 0.71 for $\chi = 128$, 192, and 256, respectively. In (c), a linear fitting is done for each χ, as shown by solid lines. The intercept with the horizontal axis gives $K_{ch} \approx 0.701$, 0.696, and 0.693 for $\chi = 128$, 192, and 256, respectively. Reproduced from Fig. 14 of Ref. [56]. Copyright 2024 by the American Physical Society.

plotted as a function of K_{ch} in Fig. 5.15(a,b,c). The increase in the maximum of ξ with χ indicates a continuous transition. The onset of the growth of the $\langle \mathcal{O}_{\mathrm{SC}} \rangle$ coincides with the maximum of the correlation length, indicating a continuous transition. The presence of a phase transition on the self-dual line at $K_{\mathrm{ch}} = 1/2$ tends to obscure the behavior of the order parameter away from the transition point; still, it can be accurately fitted by a power function giving support for a Ising transition. In the caption of Fig. 5.15, transition points determined from the fitting of $\langle \mathcal{O}_{\mathrm{SC}} \rangle^8$ are indicated just for information. Similar to the VC-RS transition, the maxima of ξ depend on the bond dimension, thus results obtained with $\chi = 196$ were used to draw the phase diagram in Fig. 5.9. Finally, the calculation of the central charge from the fitting of the EE with the maxima of correlation length in Fig. 5.14 gives $c = 0.53(2)$ in good agreement with the theoretical value of the central charge for the Ising transition.

5.2.4 Topological transitions between featureless phases

The RS, Haldane*, and c-Haldane* phases cannot be characterized by local order parameters. However, it is clear from the discussion in Sec. 4.2.2 that those phases are different. Therefore, topological phase transitions, which are associated with changes in topological indices, should occur between them. Topological indices defined in Eq. (2.86) are calculated using the generalized transfer matrix method presented in Sec. 2.8.4. The RS-Haldane* transition at $\Delta = 0.95$, the Haldane*-c-Haldane* transition at $\Delta = 0.70$, and c-Haldane-RS transition at $\Delta = 0.95$ are reported in Fig. 5.16. Inside each phase, each topological index takes a constant value equal to ± 1 in agreement with the theoretical value predicted from Table 4.1 and Eq. (2.86). All topological indices in both RS phases for high- and low-K_{ch} values take the value $+1$, confirming that this phase is topologically trivial. Topological indices related to the $D_2 \times \sigma$ symmetry take the value -1 in both the Haldane* and c-Haldane* phases. These phases are therefore non-trivial SPT phases protected by $D_2 \times \sigma$ symmetry. The index associated with time-reversal symmetry $\mathbb{Z}_2^T$, however, takes the value -1 exclusively in the Haldane* phase while being trivial in the c-Haldane* phase, indicating that they are two distinct SPT phases.

5.2.5 Criticality on the self-dual line

Finally, transitions on the self-dual line $K_{\mathrm{ch}} = 1/2$ will be characterized by calculating their central charges. Depending on Δ, different transitions should occur on the self-dual line. As already argued by the hard-core bosons approach in Sec. 4.1 for the anisotropic case, or by the field theory around the SU(4)-symmetric critical point [137, 138] for the isotropic case, these transitions should belong to the Gaussian universality class, and their central charges should be $c = 1$. In Fig. 5.17(a,b,c), S-ξ relations are shown for three representative values of Δ corresponding, respectively, to the strong easy-axis case, the isotropic case, and the strong easy-plane case. The calculated central charge for the easy-axis and easy-plane cases are $c = 1.02(2)$ and

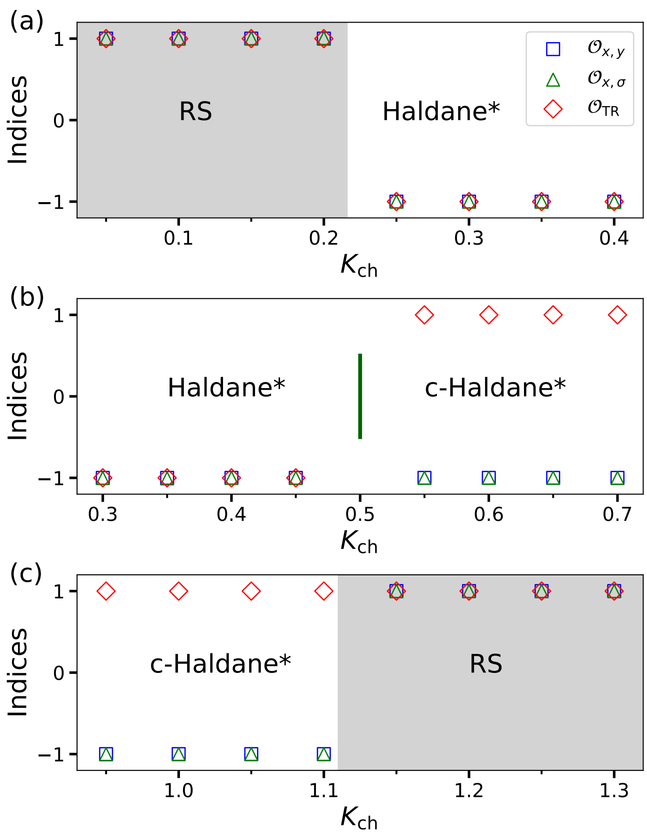

FIGURE 5.16: Topological indices (2.86) calculated by iDMRG across (a) the RS-Haldane* transition at $\Delta = 0.95$ (b) the Haldane*-c-Haldane* transition at $\Delta = 0.7$, and (c) the c-Haldane*-Haldane transition at $\Delta = 0.95$. The green vertical line in (b) indicates the self-dual point $K_{\mathrm{ch}} = 1/2$. The boundaries between the shaded and unshaded regions in (a,c) correspond to the phase boundaries obtained from the maximum of ξ; see, e.g., Fig. 5.12. Reproduced from Fig. 16 of Ref. [56]. Copyright 2024 by the American Physical Society.

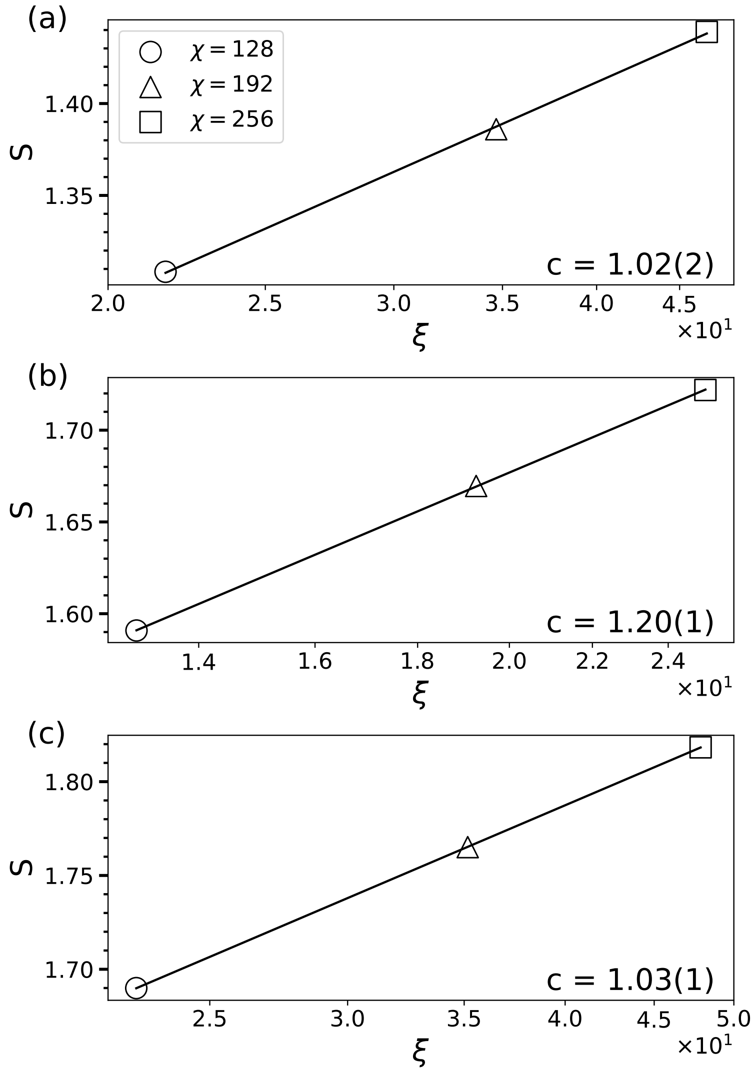

FIGURE 5.17: Half-chain EE S in Eq. (2.53) versus the correlation length ξ in Eq. (2.81), calculated by iDMRG on the self-dual line $K_{\mathrm{ch}} = 1/2$ in Fig. 5.9. (a) The Néel-VC transition at $\Delta = 1.8$. (b) The SD-SC transition at $\Delta = 1.0$. (c) The Haldane*-c-Haldane* transition at $\Delta = 0.6$. A logarithmic scale is used for the horizontal axis. Solid lines show the fitting with Eq. (2.82), and the estimated central charge c is shown in each panel. Reproduced from Fig. 17 of Ref. [56]. Copyright 2024 by the American Physical Society.

$c = 1.03(1)$, respectively, which agree well with the predicted value. In contrast, the central charge for the isotropic case $c = 1.20(1)$, is slightly different from the expected value. Given the relatively small correlation length $\xi \approx 25$, more precise calculations with larger χ might be necessary to accurately estimate c.

5.3 Conclusions

In this chapter, the ground-state phase diagrams of the XXZ-CCI ladder (1.18) in the K_{ch}-$J_\perp$ (Fig. 5.1) and K_{ch}-Δ (Fig. 5.9) planes have been investigated with numerical simulations based on the iDMRG and exact diagonalization algorithms. Both phase diagrams agree generally well with our predictions based on the effective field theory, presented in Figs. 3.3 and 3.5.

Among the discrepancies between theoretical prediction and numerical results, the following was the most concerning: In the iDMRG calculation for isotropic models, some finite bond dimension effect caused the splitting of the $c = 3/2$ transition line and the emergence of unphysical symmetry-broken phases as observed in Fig. 5.9. As the extent of these unphysical regions diminishes with an increase in the bond dimension, a careful extrapolation of the transition line with the bond dimension might help mitigate this error. Near the isotropic line, we chose to use ED calculation and the twist operator to determine the $c = 3/2$ transition. Another possibility could be to use other DMRG algorithms that can take into account the $\mathrm{SU}(2)$ symmetry directly during the calculation.

Using iDMRG, through the calculation of the central charge as in Figs. 5.3, 5.11, 5.14 and 5.17, or the analysis of the behavior of the order parameter as in Figs. 5.2, 5.4, 5.10, 5.13 and 5.15 the natures of Ising and Gaussian transitions have been confirmed. Inside the featureless RS and Haldane phases, the crossover between regions dominated by different correlations has been confirmed via the examination of the structure factors as in Fig. 5.6 and the correlation functions as in Fig. 5.7. All numerical results are qualitatively consistent with the prediction made in Sec. 3.2.2.

Finally, the calculation of the topological indices associated with $D_2 \times \sigma \times \mathbb{Z}_2^T$ symmetry presented in Fig. 5.16 confirms the nature of the featureless phases. While the RS phase is trivial, both Haldane* and c-Haldane* phases are SPT phases that can be mutually differentiated by the topological index associated with the time-reversal symmetry.

Chapter 6

Conclusions

6.1 Summary

In this dissertation, the ground-state phase diagram of the XXZ-CCI ladder (1.18) has been studied using Abelian bosonization, spin-chirality duality, the spinor hard-core bosons approach, iDMRG, and exact diagonalization, both to deepen our understanding of the ring-exchange model (1.11) and to explore the possibility of new SPT phases in spin-$\frac{1}{2}$ ladder models.

Main results

The phase diagram of the isotropic model in the K_{ch}-$J_\perp$ plane consists of a featureless RS phase, the Haldane phase, and three non-magnetic ordered phases (SD, SC, and plaquette), as shown in Figs. 3.3 and 5.1. These phases are separated by an Ising transition, a $c = 3/2$ transition, and the $\mathcal{U}$ self-dual line; the last is also a Gaussian transition. The featureless phases can be further divided into regions distinguished by their dominant correlations in terms of spin, dimer, or chirality. In particular, the regions in the RS phase with dominant SVC and UVC correlations for large K_{ch} can be seen respectively as $\mathcal{U}$- and $\mathcal{U}_{\mathrm{s}}$-dual counterparts of the region with dominant Néel correlation.

The introduction of XXZ anisotropy in the rung interaction immediately splits the $c = 3/2$ transition line into Gaussian and Ising transitions. In the phase diagram in the K_{ch}-Δ plane (for $J_\perp = J/2$), eight distinct gapped phases emerge, separated by two crossing of transitions on each side of the self-dual line. Easy-axis anisotropy stabilizes either the Néel or VC order, while easy-plane anisotropy stabilizes two non-trivial SPT phases: the Haldane* and c-Haldane* phases, as shown in Figs. 3.4 and 5.9. Phases on different sides of the self-dual line are related by the $\mathcal{U}$ spin-chirality duality.

The transitions between the different phases and crossovers between dominant correlations were confirmed numerically.

Comparison with previous studies

In the isotropic case, the phase diagram in Fig. 5.1 is qualitatively equivalent to the phase diagrams of the ring-exchange model reported in both theoretical studies [25, 76, 157, 173, 253] and numerical studies [25, 90, 91, 95, 132, 173]. In particular, our results shown in Fig. 5.1 align with previous findings in the weak interchain couplings regime (shown in Fig. 1.5(a)) and for

$K_{\text{ch}} > 0$ at constant $J_{\perp} = J/2$ (shown in Fig. 1.6), suggesting that the CCI model effectively captures the physics of ring exchange in ladder systems.

The crossing of transitions observed on the $K_{\text{ch}} < J/2$ side of the self-dual line under anisotropy closely resembles the transition crossings found in models with inter-leg DDI [192, 194] (as shown in Fig. 1.5(a)). Indeed, both models have essentially the same effective field theory in the weak interchain couplings regime.

Main contributions

Our approach, which leverages spin-chirality dualities, has extended the theoretical understanding of the ground-state phase diagram beyond the perturbative regimes around the weak interchain couplings regime or around the SU(4)-symmetric point. The regimes of strong positive and strong negative CCI are interpreted as dual counterparts of the weak interchain coupling regime.

In particular, the transition crossings observed at large K_{ch} in the presence of anisotropy, along with the identification of the c-Haldane* phase, i.e., a twisted variant of the Haldane phase, are unique contributions of this work. Unique characteristics of the c-Haldane* state, particularly in relation to time-reversal symmetry, distinguish this phase from other Haldane phases. We demonstrated that the RS, Haldane*, and c-Haldane* phases are differentiated by the topological indices (2.86) associated with the $D_2 \times \sigma$ symmetry and time-reversal symmetry $\mathbb{Z}_2^T$, as shown in Fig. 5.16.

Additionally, by developing a mapping of the system to a spin-1 hardcore bosons model, strongly anisotropic regimes have been investigated. In particular, we predict a direct transition between the Néel and VC phases, or between the Haldane* and c-Haldane* phases, in the presence of strong anisotropy. These transitions occur along the self-dual line and belong to the Gaussian universality class. This prediction is supported by estimating the central charge c from the plot of the half-chain entanglement entropy S versus the correlation length ξ (see Fig. 5.17(a, c)). This analysis extends previous studies of the self-dual line's criticality beyond the vicinity of the SU(4)-symmetric point to the entire self-dual line.

6.2 Outlook

6.2.1 Implications for an XXZ ladder with four-spin ring exchange

In this dissertation, the CCI model (1.18) has been introduced as a simplified version of the ring-exchange model (1.11). An important direction for future research will be to expand our understanding of the phase diagram of the full ring-exchange model.

While the values of the ring-exchange term K are relatively small in cuprate ladders [22, 151], falling within the weak interchain couplings regime, possible effects of large K have garnered significant attention in the context of solid ^{3}He [65, 161, 222] and Wigner crystals [122, 240]. Therefore an understanding the strong-coupling regime is essential.

Additionally, the effects of anisotropy on the phase diagram have remained largely unexplored in previous studies [90, 91, 95, 132, 173, 253]. The numerous similarities between the CCI and ring-exchange models, as highlighted in this dissertation, suggest strongly that anisotropy could also induce SPT phases in the ring-exchange model.

The difference between the XXZ-CCI and XXZ-K model becomes clearer by rewriting the XXZ-K model as

$$\begin{aligned} H_{\text{XXZ-}K} = &\left(\frac{J}{2} + K\right) H_1 + \frac{J}{2} H_2 + K H_{\text{ch}} + 4K H_{\text{RR}} \\ &+ J_\perp \sum_j \left(S_{1,j} \cdot S_{2,j}\right)_\Delta + 2K \sum_j S_{1,j} \cdot S_{2,j} + \text{const.} \end{aligned} \tag{6.1}$$

The term H_{RR} is given by

$$H_{\text{RR}} = \sum_j \left(S_{1,j} \cdot S_{2,j}\right)\left(S_{1,j+1} \cdot S_{2,j+1}\right), \tag{6.2}$$

and is absent in the XXZ-CCI ladder model.

In the Abelian bosonization analysis for weak interchain couplings $J_\perp, 2K \ll J$, a precise cancellation of relevant terms occurs between the H_{RR} and H_{DD} terms [157, 173]. As a result, the effect of the H_{RR} term is simply to remove the "$3d'^2$" term in Eq. (3.33a). Relevant terms from the two-spin interactions and the H_{LL} term remain, reducing the model to an effective XXZ-DDI model. Consequently, we expect a phase structure similar to Fig. 3.1(a).

Under the spin-chirality duality transformation, the H_2 and H_{ch} terms in (6.1) are exchanged, while the other terms remain invariant. Therefore, the XXZ-K model is self-dual at $K = J/2$. While the spin-chirality duality transformation enabled a mapping between the regimes of weak and strong interchain couplings in the XXZ-CCI model, the presence of the H_{RR} term disrupts the duality between these two regimes in the XXZ-K model. In particular, the H_{RR} term might have highly non-perturbative effects on the phase structure for large $4K$, making a theoretical analysis challenging.

In our preliminary numerical investigation of the XXZ-K model using iDMRG calculations[1], the presence of the H_{RR} term hindered convergence to chirality-related phases[2], necessitating more careful investigation; possibly using iDMRG algorithms capable of explicitly taking SU(2) symmetry into account.

Another intriguing open issue is to study the combined effects of XXZ anisotropy, frustration, and ring exchange, potentially extending the work of Metavitsiadis *et al.* [157]. While our model allowed for diagonal Heisenberg interactions, only weak interactions were considered within the scope of this dissertation. In the regime where $J \approx J_\perp \approx J_\times$, strong competition among the different interactions may induce a rich phase structure.

[1] Not published nor included in this dissertation.

[2] The position of the phase transition became highly dependent on χ.

6.2.2 Dominant correlation in extended ladder model

In this dissertation, the dominant correlations within the “featureless” phases were analyzed for the isotropic case using bosonization and fermionization in Sec. 3.2.2. An interesting topic would be to examine the dominant correlations in the anisotropic case or in extended ladder systems [62, 63, 145, 148, 192–194] following a similar approach.

Figure 6.1 presents an analysis of the masses of the Majorana fields under easy-plane anisotropy for both $J_\perp > 0$ (a) and $J_\perp < 0$ (b). Here, the masses depend on the coupling constants as

$$\begin{aligned} m_{\mathrm{t}}^{12} &\approx \frac{\pi}{2}\left[\bar{a}^2(J_\perp - 2J_\times + J_\perp\delta) - 24\bar{d}^2 K_{\mathrm{ch}}\right] \\ &= 12\pi\bar{d}^2[\gamma(J_\perp - 2J_\times) + \gamma J_\perp \delta - K_{\mathrm{ch}}], \end{aligned} \tag{6.3a}$$

$$\begin{aligned} m_{\mathrm{t}}^{3} &\approx \frac{\pi}{2}\left[\bar{a}^2(J_\perp - 2J_\times - J_\perp\delta) - 24\bar{d}^2 K_{\mathrm{ch}}\right] \\ &= 12\pi\bar{d}^2[\gamma(J_\perp - 2J_\times) - \gamma J_\perp \delta - K_{\mathrm{ch}}], \end{aligned} \tag{6.3b}$$

$$\begin{aligned} m_{\mathrm{s}} &\approx -\frac{\pi}{2}\left[3\bar{a}^2(J_\perp - 2J_\times) + \bar{a}^2 J_\perp\delta + 24\bar{d}^2 K_{\mathrm{ch}}\right] \\ &= -12\pi\bar{d}^2[3\gamma(J_\perp - 2J_\times) + \gamma J_\perp \delta + K_{\mathrm{ch}}]. \end{aligned} \tag{6.3c}$$

Lines with a negative slope represent positive masses, while those with a positive slope represent negative masses. Changes in the sign of the mass are associated with phase transitions, while crossings of the two smallest masses correspond to crossovers in the dominant correlation. The value of the dominant correlation function is determined by the mass with the smallest absolute value, and the associated operator can be identified using Eq. (3.45). By performing a similar analysis in the easy-axis regime, we can predict the phase diagram in Fig. 6.2. Using the duality transformations $\mathcal{U}$ and $\mathcal{U}_{\mathrm{s}}$, this current analysis can be extended to regimes of strong positive and negative CCIs. It would be interesting to numerically confirm the different dominant correlations in the variety of regimes as predicted here.

6.2.3 Extending duality transformations for the discovery of exotic phases

Finally, it would also be interesting to search for other examples of SPT phases in extended ladder systems with $D_2 \times \sigma \times \mathbb{Z}_2^T$ symmetry, whose classification is described by the second group cohomology $\mathcal{H}^2(\mathbb{Z}_2^3 \times \mathbb{Z}_2^T, U(1)) = \mathbb{Z}_2^7$ [30, 31, 200, 225, 276]. Duality transformations could be a powerful tool in the search for such new phases.

In the present work, the spin-chirality duality has played a key role in identifying a rich variety of featureless and ordered phases. This approach naturally places transitions between mutually dual phases on the self-dual surface. In particular, we have identified an example of a continuous topological transition between the Haldane* and c-Haldane* phases, a transition protected by time-reversal symmetry.

While the duality transformation $\mathcal{U}$ in Eq. (4.7) considered here is a local unitary transformation, nonlocal duality transformations have also proven

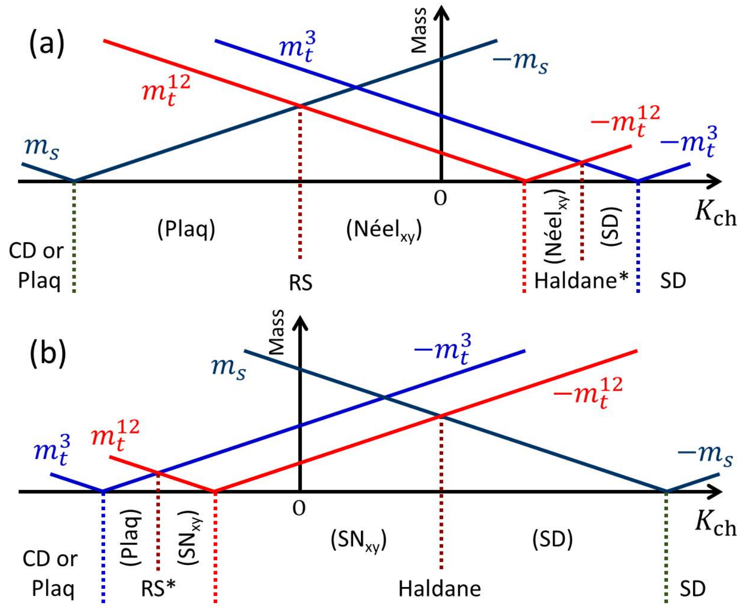

FIGURE 6.1: Schematic representation of the masses of the Majorana fields and the dominant correlation as a function of K_{ch}. (a) Weak interchain coupling regime of the XXZ-CCI model with easy-plane anisotropy for $J_\perp > 0$. (b) Same for $J_\perp < 0$. Solid lines represent the values of different masses (lines with negative slopes indicate positive masses, and vice versa). Brown dashed vertical lines represent crossovers, while other dashed lines represent phase transitions. Phase names are indicated without parentheses, while dominant correlations within featureless phases are given in parentheses.

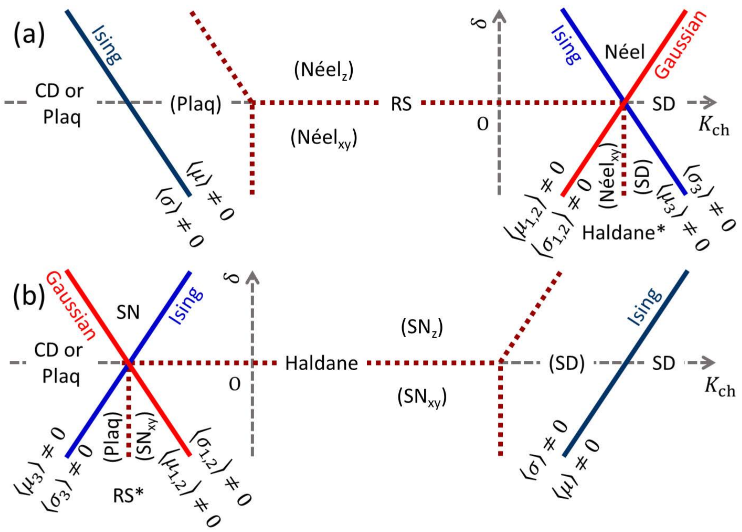

FIGURE 6.2: Ground-state phase diagram of the XXZ-CCI model and its dominant correlations in the K_{ch}-δ plane, based on the analysis of signs and relative magnitudes of masses in the weak interchain couplings regime, as shown in Fig. 6.1. Solid lines indicate transitions, while dashed lines represent crossovers.

useful in studies of SPT phases and their transitions [36, 258, 275]. Extending the use of duality transformations may thus provide a promising guide for exploring novel phases and transitions.

Appendix A

Microscopic origins of spin interactions

A.1 Hubbard model and Heisenberg exchange couplings

One of the simplest models where magnetic interaction emerges is the half-filled Hubbard model [38, 57]. The half-filled Hubbard model effectively describes an ensemble of N electrons loaded on a lattice of N sites. Each electron can hop to a neighboring site with an amplitude t. If two electrons are present simultaneously at the same site, they interact through Coulomb interaction with an energy given by $U > 0$. The Hamiltonian is given by

$$H_{\mathrm{Hub}} = -t \sum_{\{i,j\}} \sum_{\alpha=\uparrow,\downarrow} \left(c^{\dagger}_{i,\alpha} c_{j,\alpha} + h.c. \right) + U \sum_{j} n_{j,\uparrow} n_{j,\downarrow}. \tag{A.1}$$

Here, $n_{j,\alpha} = c^{\dagger}_{j,\alpha} c_{j,\alpha}$ is the occupation number operator, whose eigenvalues are in $\{0, 1\}$, and $\{i, j\}$ represents neighboring sites. The first term tends to favor situations where electrons are delocalized and can hop freely. In contrast, the second term gives some penalty to configurations where two electrons are present on the same site, thereby limiting the mobility of the electrons. In the regime of strong U, for a half-filled system, the system will favor configurations with one electron per site to minimize the Coulomb energy. In this regime, each electron is localized on a single site, and the material becomes a Mott insulator. In a Mott insulator, the virtual hopping process creates some correlation between the electrons, mediating some antiferromagnetic interaction. By applying perturbation theory up to the second order and treating the hopping term of the Hamiltonian as the perturbation, the effective Hamiltonian (restricted to the Hilbert space with precisely one electron at each site) can be obtained as

$$H = \frac{2t^2}{U} \sum_{\{i,j\}} \boldsymbol{S}_i \cdot \boldsymbol{S}_j. \tag{A.2}$$

This is a quantum Heisenberg antiferromagnet with an exchange coupling $J = \frac{2t^2}{U}$. Here the local spin-$\frac{1}{2}$ operator is defined on the site j as

$$S^{a}_{j} = \frac{1}{2} \sum_{\alpha,\beta} c^{\dagger}_{j,\alpha} \sigma^{a}_{\alpha,\beta} c_{j,\beta}, \tag{A.3}$$

where σ^a ($a \in \{x, y, z\}$) are the standard Pauli matrices. Other mechanisms can lead to ferromagnetic Heisenberg interaction.

A.2 Origins of dimer-dimer interaction

The DDI introduced in Sec. 1.3.2 can have multiple origins. In this section, we will provide two different mechanisms.

The DDI can, for example, be mediated by phonons. Their role in the emergence of the DDI can be understood via a simple toy model [204]. The following Hamiltonian represents a spin-$\frac{1}{2}$ Heisenberg ladder, where the strength of the interaction along the legs depends on the lattice displacement ρ_j:

$$H = \sum_{n=1}^{2} \sum_j J(1 - \alpha\rho_j) \boldsymbol{S}_{n,j} \cdot \boldsymbol{S}_{n,j+1} + \sum_j \frac{k}{2}\rho_j^2. \tag{A.4}$$

The last term describes the potential energy associated with elastic deformation. Upon integrating over the lattice displacement, the Hamiltonian with DDIs emerges as an effective model for the spin degrees of freedom:[1]

$$H = \sum_{n=1}^{2} \sum_j J(1 + \frac{J\alpha^2}{4k}) \boldsymbol{S}_{n,j} \cdot \boldsymbol{S}_{n,j+1} - \frac{J^2\alpha^2}{k}\left(H_{\text{LL}} + \sum_j \frac{3}{16}\right) + E_{\text{Pho}}. \tag{A.5}$$

The last term is the contribution from the phonon to the total energy.

In a spin-orbital system [106, 141, 203], the DDI can appear as a low-energy effective model of a two-band Hubbard model represented by the Hamiltonian

$$H_{\text{Hub}} = \sum_j \sum_{\alpha=\uparrow,\downarrow} \sum_{a=1,2} \left[-t\left(c^\dagger_{j,\alpha,a} c_{j+1,\alpha,a} + h.c.\right) + U\left(c^\dagger_{j,\alpha,a} c_{j,\alpha,a} - 1\right)^2 \right]. \tag{A.6}$$

Here, a represents the band index. As in the single-band Hamiltonian, for $\frac{1}{4}$-filling (one electron per site), the charge excitations (doubly occupied sites) are gapped, and the low-energy effective Hamiltonian for spin and orbital degrees of freedom is obtained as

$$H = J \sum_j \left(\frac{1}{2} + 2\boldsymbol{S}_j \cdot \boldsymbol{S}_{j+1}\right)\left(\frac{1}{2} + 2\boldsymbol{T}_j \cdot \boldsymbol{T}_{j+1}\right). \tag{A.7}$$

Here, $\boldsymbol{S}$ and $\boldsymbol{T}$ represent the spin and orbital operators. In terms of the fermionic operators, they are given by

$$S_j^\beta = \frac{1}{2} \sum_{a,\alpha,\alpha'} c^\dagger_{j,\alpha,a} \sigma^\beta_{\alpha,\alpha'} c_{j,\alpha',a}\,, \tag{A.8a}$$

$$T_j^b = \frac{1}{2} \sum_{a,a',\alpha} c^\dagger_{j,\alpha,a} \sigma^b_{a,a'} c_{j,\alpha,a'}. \tag{A.8b}$$

[1] We use the fact that $(\boldsymbol{S}_i \cdot \boldsymbol{S}_j)^2 = \frac{3}{16} - \frac{1}{2}\boldsymbol{S}_i \cdot \boldsymbol{S}_j$.

This model is equivalent to a spin ladder upon identifying $\boldsymbol{S}_j$ with $\boldsymbol{S}_{1,j}$ and $\boldsymbol{T}_j$ with $\boldsymbol{S}_{2,j}$.

A.3 Origins of chirality-chirality interaction

The role of phonons in the emergence of the CCI can be understood similarly to the emergence of DDI. The antisymmetric exchange, also known as the Dzyaloshinskii–Moriya interaction (DMI) [45, 170], is a magnetic interaction between two electrons with spins $\boldsymbol{S}_i$ and $\boldsymbol{S}_j$, localized around two ions at $\boldsymbol{r}_i$ and $\boldsymbol{r}_j$, respectively, mediated by a third ion at $\boldsymbol{r}_k$, called the ligand. The DMI is caused by the superexchange mechanism when spin-orbit coupling is taken into account. The DMI can be represented by the following Hamiltonian:

$$H_{\mathrm{DMI}}(i,j,k) := \boldsymbol{D}_{i,j,k} \cdot \left(\boldsymbol{S}_i \times \boldsymbol{S}_j\right). \tag{A.9}$$

Here, $\boldsymbol{D}_{i,j,k}$ is a vector whose direction is given by $\left(\boldsymbol{r}_i - \boldsymbol{r}_k\right) \times \left(\boldsymbol{r}_j - \boldsymbol{r}_k\right)$. The DMI is nonzero when the ligand is not aligned with the two other ions.

To see how CCI can be generated by interaction with phonons [195], one can consider a toy model consisting of a spin-$\frac{1}{2}$ ladder where the DMI along the rung is mediated by ligands localized at the center of both adjacent plaquettes. For simplicity, we consider the situation where the variation in the position of the ligand is much larger than the variation in the position of the two other ions, such that for all j, $\boldsymbol{r}_{1,j} - \boldsymbol{r}_{2,j} = \boldsymbol{v}$ and $\boldsymbol{r}_k - \left(\boldsymbol{r}_{1,j} + \boldsymbol{r}_{1,j}\right)/2 = \boldsymbol{V} + \boldsymbol{\rho}_j$. Here, $\boldsymbol{v}$ and $\boldsymbol{V}$ are constant vectors aligned along the rung or the leg, respectively, and $\boldsymbol{\rho}_j$ represents the variation of the position of the ligand on plaquette j. In this situation, the DMI can be linearized and approximated by

$$\boldsymbol{D}_{i,j,k} = d\boldsymbol{v} \times \boldsymbol{\rho}_j, \tag{A.10a}$$

with d being some coefficient. The following Hamiltonian can describe such a ladder:[2]

$$\begin{aligned} H := \sum_{n=1}^{2} \sum_j J \boldsymbol{S}_{n,j} \cdot \boldsymbol{S}_{n,j+1} + \sum_j \frac{k}{2} \left(\boldsymbol{v} \times \boldsymbol{\rho}_j\right)^2 \\ + \sum_j \boldsymbol{D}_{(1,j),(2,j),j} \cdot \left(\boldsymbol{S}_{1,j} \times \boldsymbol{S}_{2,j}\right) + \sum_j \boldsymbol{D}_{(1,j+1),(2,j+1),j} \cdot \left(\boldsymbol{S}_{1,j+1} \times \boldsymbol{S}_{2,j+1}\right). \end{aligned} \tag{A.11}$$

Here, the second term represents the potential energy of the ligand. The two last terms represent DMI mediated by the ligand on plaquette j. Using Eq.

[2]The elastic term is slightly different from the one in Eq. (A.4) for convenience. Since $\left(\boldsymbol{v} \times \boldsymbol{\rho}_j\right) = \left(\boldsymbol{v}^2 \boldsymbol{\rho}_j^2\right) - \left(\boldsymbol{v} \cdot \boldsymbol{\rho}_j\right)^2$, one sees that $\frac{k}{2}\left(\boldsymbol{v} \times \boldsymbol{\rho}_j\right)^2$ is an anisotropic elastic term.

(A.10), we can rewrite Eq. (A.11) as

$$\begin{aligned} H = \sum_{n=1}^{2} \sum_{j} J \boldsymbol{S}_{n,j} \cdot \boldsymbol{S}_{n,j+1} + \sum_{j} \frac{k}{2} \left(\boldsymbol{v} \times \boldsymbol{\rho}_j \right)^2 \\ + \sum_{j} d \left(\boldsymbol{v} \times \boldsymbol{\rho}_j \right) \cdot \left(\boldsymbol{S}_{1,j} \times \boldsymbol{S}_{2,j} + \boldsymbol{S}_{1,j+1} \times \boldsymbol{S}_{2,j+1} \right). \end{aligned} \tag{A.12}$$

Upon integrating over $\boldsymbol{v} \times \boldsymbol{\rho}_j$, one derives an effective Hamiltonian for the spins which takes the form of the CCI with an extra rung interaction:[3]

$$H = \sum_{n=1}^{2} \sum_{j} J \boldsymbol{S}_{n,j} \cdot \boldsymbol{S}_{n,j+1} + \frac{d^2}{4k} \left(-H_{\mathrm{ch}} + \sum_{j} (2 \boldsymbol{S}_{1,j} \cdot \boldsymbol{S}_{2,j} - \frac{3}{2}) \right) + E_{\mathrm{Pho}}. \tag{A.13}$$

[3]In the calculation, the relation $(\boldsymbol{S}_a \times \boldsymbol{S}_b) \cdot (\boldsymbol{S}_a \times \boldsymbol{S}_b) = \frac{3}{8} - \frac{1}{2}(\boldsymbol{S}_a \cdot \boldsymbol{S}_b)$ has been used extensively.

Appendix B

Some details of the bosonization analysis

B.1 Bosonization of four-spin interactions

Here we provide field-theoretical expressions of the four-spin interactions H_{LL} and H_{DD} in Eq. (1.20). It is convenient to express these interactions first by the non-Abelian bosonization [73], which manifestly respects the SU(2) symmetry of the system. Here we closely follow the convention of Ref. [157], where similar calculations have been done (see also Ref. [25]). In the non-Abelian bosonization, the spin operator is decomposed into uniform and staggered components as

$$\boldsymbol{S}_{n,j} = a\Big[\boldsymbol{J}_n(x) + (-1)^j \Omega \boldsymbol{n}_n(x)\Big], \tag{B.1}$$

where Ω corresponds to $\bar{a}/a$ in our convention. The uniform component is given by the sum of the chiral SU(2) currents as $\boldsymbol{J}(x) = \boldsymbol{J}_{\mathrm{R}}(x) + \boldsymbol{J}_{\mathrm{L}}(x)$. By applying operator product expansions, the four-spin interactions are expressed as [157]

$$\begin{aligned} H_{\mathrm{LL}} = \int dx [&36\gamma^2 a\Omega^2 O_\epsilon(x) \\ &+ 3\gamma^2 a^2\Omega^2(1 + a\Omega^2) O_a(x) + \dots], \end{aligned} \tag{B.2a}$$

$$\begin{aligned} H_{\mathrm{DD}} = \int dx [&12\gamma^2 a\Omega^2 O_\epsilon \\ &+ 2\gamma^2 a(1 + a\Omega^2)^2 (O_b(x) - O(x)) + \dots], \end{aligned} \tag{B.2b}$$

where $\gamma = 1/(2\pi)$,

$$O_\epsilon(x) = \epsilon_1(x)\epsilon_2(x), \tag{B.3a}$$

$$O_a(x) = \boldsymbol{J}_{1,L}(x)\cdot\boldsymbol{J}_{1,R}(x) + \boldsymbol{J}_{2,L}(x)\cdot\boldsymbol{J}_{2,R}(x), \tag{B.3b}$$

$$O_b(x) = \boldsymbol{J}_{1,L}(x)\cdot\boldsymbol{J}_{2,R}(x) + \boldsymbol{J}_{1,R}(x)\cdot\boldsymbol{J}_{2,L}(x), \tag{B.3c}$$

$$O(x) = \boldsymbol{J}_{1,L}(x)\cdot\boldsymbol{J}_{2,L}(x) + \boldsymbol{J}_{1,R}(x)\cdot\boldsymbol{J}_{2,R}(x), \tag{B.3d}$$

and the dimer operator $\epsilon_n(x)$ corresponds to $\sin(2\sqrt{\pi}\phi_n)$ in our convention. Henceforth, we neglect $O(x)$, which is decoupled from the other perturbations in the renormalization group flow. We find that both H_{LL} and H_{DD} have the strongly relevant perturbation $O_\epsilon(x)$, which gives the contributions $\mp 24(2\gamma a\Omega)^2 K_{\mathrm{ch}}/(2a)$ to $g_\pm$ in Eq. (3.33a). Differences between H_{LL} and H_{DD}

can be found in the marginal perturbations. In particular, the inter-chain current-current interaction $O_b(x)$ appears only in H_{DD}, and this interaction is expected to be responsible for the difference between the ladder models of the present study and Refs. [27, 28, 89, 92, 180, 192, 194, 215, 220, 246], as discussed at the end of Sec. 3.2.4. In the Abelian bosonization, this interaction can be expressed as [68]

$$\begin{aligned} O_b = & -\frac{b_1^2}{2a^2}\cos\left(2\sqrt{2\pi}\phi_+\right)\cos\left(\sqrt{2\pi}\theta_-\right) \\ & + \frac{1}{8\pi}\sum_{\nu=\pm}\nu\left[2(\partial_x\phi_\nu)^2 - \frac{1}{2}(\partial_x\theta_\nu)^2\right]. \end{aligned} \tag{B.4}$$

We therefore find the contribution of the CCI to γ_1 in Eq. (3.33c) with $C = 8\gamma^2(1 + a\Omega^2)^2$.

B.2 Link between the Haldane and Haldane* phases

In this section, we examine the connection between the Haldane and Haldane* phases. The phase diagram in Fig. 1.3 can be recovered using our bosonization approach, as done by Ogino *et al.* in Appendix A of Ref. [194]. In terms of λ_z and λ_{xy}, the coupling constants of the most relevant terms in the effective field theory (3.31) of the XXZ-CCI ladder are expressed as

$$g_\pm = \frac{1}{2a}\left[a_1^2\lambda_z \mp 4K_{\mathrm{ch}}(9d^2 - 3d'^2)\right], \tag{B.5a}$$

$$\tilde{g}_- = \frac{b_0^2}{a}\lambda_{xy}. \tag{B.5b}$$

Setting $K_{\mathrm{ch}} = 0$, the phase diagram in the λ_z-λ_{xy} plane is obtained as in Fig. B.1, which is similar to Fig. 1.3. The symmetry around the λ_z-axis present in Fig. 1.3 is recovered. Indeed, the transformation $U_1^z(\pi)$ given in Eq. (1.6) is equivalent to a shift of the θ_- field by $\sqrt{\frac{\pi}{2}}$ and appears in the change of the pinning position inside the RS, RS*, Haldane, and Haldane* phases.

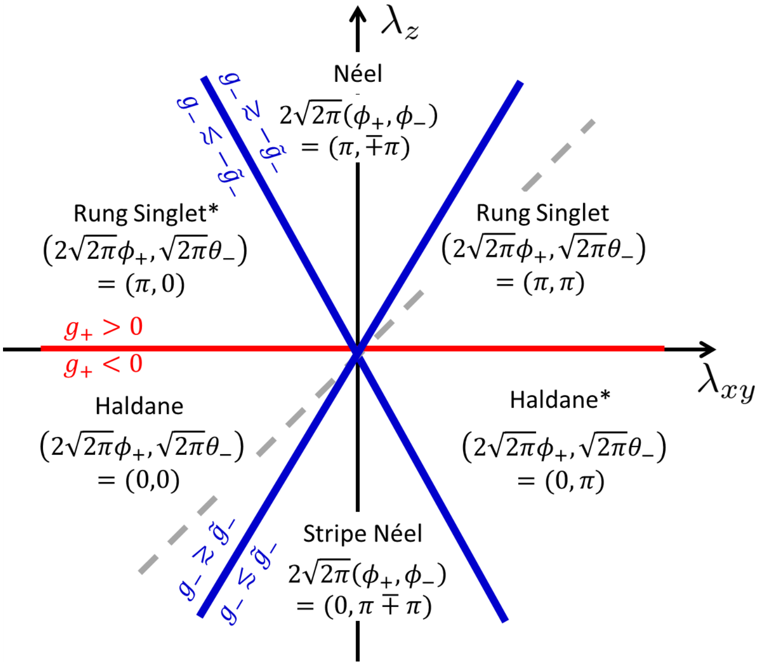

FIGURE B.1: Schematic ground-state phase diagram of the XXZ-ladder in Eq. (1.4), obtained by a field-theoretical analysis for weak interchain couplings [194]. The red and blue lines represent the Gaussian and Ising transitions, respectively. The phase diagram is qualitatively equivalent to the phase diagram obtained by numerical methods by Liu *et al.* given in Fig. 1.3. Redrawn from Fig. 18 in Ref. [194].

Bibliography

[1] I. Affleck. “The quantum Hall effects, σ-models at $\Theta = \pi$ and quantum spin chains”. In: *Nuclear Physics B* 257 (1985), pp. 397–406. DOI: 10.1016/0550-3213(85)90383-0.

[2] Ian Affleck. “Critical behaviour of SU(n) quantum chains and topological non-linear σ-models”. In: *Nuclear Physics B* 305.4 (1988), pp. 582–596.

[3] Ian Affleck. “Exact critical exponents for quantum spin chains, non-linear σ-models at $\theta = \pi$ and the quantum Hall effect”. In: *Nuclear Physics B* 265.3 (1986), pp. 409–447.

[4] Ian Affleck. “Fields, Strings and Critical Phenomena, Les Houches,” in: North-Holland, Amsterdam, 1988.

[5] Ian Affleck. “Quantum spin chains and the Haldane gap”. In: *Journal of Physics: Condensed Matter* 1.19 (1989), pp. 3047–3072. DOI: 10.1088/0953-8984/1/19/001. URL: https://doi.org/10.1088/0953-8984/1/19/001.

[6] Ian Affleck and Elliott H. Lieb. “A proof of part of Haldane’s conjecture on spin chains”. In: *Letters in Mathematical Physics* 12 (1986), pp. 57–69. DOI: 10.1007/BF00400304.

[7] Ian Affleck et al. “Rigorous results on valence-bond ground states in antiferromagnets”. In: *Phys. Rev. Lett.* 59 (7 1987), pp. 799–802. DOI: 10.1103/PhysRevLett.59.799. URL: https://link.aps.org/doi/10.1103/PhysRevLett.59.799.

[8] Ian Affleck et al. “Valence bond ground states in isotropic quantum antiferromagnets”. In: *Communications in Mathematical Physics* 115.3 (1988), pp. 477–528. ISSN: 1432-0916. DOI: 10.1007/BF01218021. URL: https://doi.org/10.1007/BF01218021.

[9] Cliò Efthimia Agrapidis, Jeroen van den Brink, and Satoshi Nishimoto. “Ground state and low-energy excitations of the Kitaev-Heisenberg two-leg ladder”. In: *Phys. Rev. B* 99 (22 2019), p. 224418. DOI: 10.1103/PhysRevB.99.224418. URL: https://link.aps.org/doi/10.1103/PhysRevB.99.224418.

[10] A. A. Aligia and G. Ortiz. “Quantum Mechanical Position Operator and Localization in Extended Systems”. In: *Phys. Rev. Lett.* 82 (12 1999), pp. 2560–2563. DOI: 10.1103/PhysRevLett.82.2560. URL: https://link.aps.org/doi/10.1103/PhysRevLett.82.2560.

[11] A. A. Aligia et al. “Phase diagrams from topological transitions: The Hubbard chain with correlated hopping”. In: *Phys. Rev. B* 61 (12 2000), pp. 7883–7886. DOI: 10.1103/PhysRevB.61.7883. URL: https://link.aps.org/doi/10.1103/PhysRevB.61.7883.

[12] Philip W Anderson. "An approximate quantum theory of the antiferromagnetic ground state". In: *Physical Review* 86.5 (1952), p. 694.

[13] Philip W Anderson. *Basic notions of condensed matter physics*. CRC press, 2018.

[14] Daniel Arovas, J. R. Schrieffer, and Frank Wilczek. "Fractional Statistics and the Quantum Hall Effect". In: *Phys. Rev. Lett.* 53 (7 1984), pp. 722–723. DOI: 10.1103/PhysRevLett.53.722. URL: https://link.aps.org/doi/10.1103/PhysRevLett.53.722.

[15] Sebastien J Avakian and Erik S Sørensen. "Eleven competing phases in the Heisenberg-Gamma ($J\Gamma$) ladder". In: *New Journal of Physics* 26.1 (2024), p. 013036. DOI: 10.1088/1367-2630/ad1d0f. URL: https://dx.doi.org/10.1088/1367-2630/ad1d0f.

[16] P. Azaria, E. Boulat, and P. Lecheminant. "Effect of symmetry-breaking perturbations in the one-dimensional SU(4) spin-orbital model". In: *Phys. Rev. B* 61 (18 2000), pp. 12112–12125. DOI: 10.1103/PhysRevB.61.12112. URL: https://link.aps.org/doi/10.1103/PhysRevB.61.12112.

[17] T. Barnes et al. "Excitation spectrum of Heisenberg spin ladders". In: *Phys. Rev. B* 47 (6 1993), pp. 3196–3203. DOI: 10.1103/PhysRevB.47.3196. URL: https://link.aps.org/doi/10.1103/PhysRevB.47.3196.

[18] Eytan Barouch and Barry M. McCoy. "Statistical Mechanics of the XY Model. II. Spin-Correlation Functions". In: *Phys. Rev. A* 3 (2 1971), pp. 786–804. DOI: 10.1103/PhysRevA.3.786. URL: https://link.aps.org/doi/10.1103/PhysRevA.3.786.

[19] B. Andrei Bernevig and Shou-Cheng Zhang. "Quantum Spin Hall Effect". In: *Phys. Rev. Lett.* 96 (10 2006), p. 106802. DOI: 10.1103/PhysRevLett.96.106802. URL: https://link.aps.org/doi/10.1103/PhysRevLett.96.106802.

[20] H. Bethe. "Zur Theorie der Metalle I: Eigenwerte und Eigenfunktionen der linearen Atomkette". In: *Zeitschrift für Physik* 71 (1931), pp. 205–226. DOI: 10.1007/BF01341708.

[21] R. Botet, R. Jullien, and M. Kolb. "Finite-size-scaling study of the spin-1 Heisenberg-Ising chain with uniaxial anisotropy". In: *Phys. Rev. B* 28 (1983), p. 3914.

[22] S. Brehmer et al. "Effects of biquadratic exchange on the spectrum of elementary excitations in spin ladders". In: *Phys. Rev. B* 60 (1 1999), pp. 329–334. DOI: 10.1103/PhysRevB.60.329. URL: https://link.aps.org/doi/10.1103/PhysRevB.60.329.

[23] W. J. L. Buyers et al. "Experimental evidence for the Haldane gap in a spin-1 nearly isotropic, antiferromagnetic chain". In: *Phys. Rev. Lett.* 56 (1986), p. 371.

[24] Pasquale Calabrese and John Cardy. "Entanglement entropy and quantum field theory". In: *Journal of Statistical Mechanics: Theory and Experiment* 2004.06 (2004), P06002. DOI: 10.1088/1742-5468/2004/06/p06002. URL: https://doi.org/10.1088%2F1742-5468%2F2004%2F06%2Fp06002.

[25] S. Capponi, P. Lecheminant, and M. Moliner. "Quantum phase transitions in multileg spin ladders with ring exchange". In: *Phys. Rev. B* 88 (7 2013), p. 075132. DOI: 10.1103/PhysRevB.88.075132. URL: https://link.aps.org/doi/10.1103/PhysRevB.88.075132.

[26] Andrei Catuneanu, Erik S. Sørensen, and Hae-Young Kee. "Nonlocal string order parameter in the $S = \frac{1}{2}$ Kitaev-Heisenberg ladder". In: *Phys. Rev. B* 99 (19 2019), p. 195112. DOI: 10.1103/PhysRevB.99.195112. URL: https://link.aps.org/doi/10.1103/PhysRevB.99.195112.

[27] Jyong-Hao Chen et al. "Model of chiral spin liquids with Abelian and non-Abelian topological phases". In: *Phys. Rev. B* 96 (22 2017), p. 224420. DOI: 10.1103/PhysRevB.96.224420. URL: https://link.aps.org/doi/10.1103/PhysRevB.96.224420.

[28] Jyong-Hao Chen et al. "Model of spin liquids with and without time-reversal symmetry". In: *Phys. Rev. B* 99 (18 2019), p. 184445. DOI: 10.1103/PhysRevB.99.184445. URL: https://link.aps.org/doi/10.1103/PhysRevB.99.184445.

[29] Wei Chen, Kazuo Hida, and B. C. Sanctuary. "Ground-state phase diagram of $S = 1$ XXZ chains with uniaxial single-ion-type anisotropy". In: *Phys. Rev. B* 67 (10 2003), p. 104401. DOI: 10.1103/PhysRevB.67.104401. URL: https://link.aps.org/doi/10.1103/PhysRevB.67.104401.

[30] Xie Chen, Zheng-Cheng Gu, and Xiao-Gang Wen. "Classification of gapped symmetric phases in one-dimensional spin systems". In: *Phys. Rev. B* 83 (3 2011), p. 035107. DOI: 10.1103/PhysRevB.83.035107. URL: https://link.aps.org/doi/10.1103/PhysRevB.83.035107.

[31] Xie Chen, Zheng-Cheng Gu, and Xiao-Gang Wen. "Complete classification of one-dimensional gapped quantum phases in interacting spin systems". In: *Phys. Rev. B* 84 (23 2011), p. 235128. DOI: 10.1103/PhysRevB.84.235128. URL: https://link.aps.org/doi/10.1103/PhysRevB.84.235128.

[32] Xie Chen, Zheng-Cheng Gu, and Xiao-Gang Wen. "Local unitary transformation, long-range quantum entanglement, wave function renormalization, and topological order". In: *Phys. Rev. B* 82 (15 2010), p. 155138. DOI: 10.1103/PhysRevB.82.155138. URL: https://link.aps.org/doi/10.1103/PhysRevB.82.155138.

[33] Xie Chen et al. "Symmetry protected topological orders and the group cohomology of their symmetry group". In: *Phys. Rev. B* 87 (15 2013), p. 155114. DOI: 10.1103/PhysRevB.87.155114. URL: https://link.aps.org/doi/10.1103/PhysRevB.87.155114.

[34] Xie Chen et al. "Symmetry-Protected Topological Orders in Interacting Bosonic Systems". In: *Science* 338.6114 (2012), pp. 1604–1606. ISSN: 0036-8075. DOI: 10.1126/science.1227224.

[35] Andrey Chubukov, Eduardo Gagliano, and Carlos Balseiro. “Phase diagram of the frustrated spin-1/2 Heisenberg antiferromagnet with cyclic-exchange interaction”. In: *Phys. Rev. B* 45 (14 1992), pp. 7889–7898. DOI: 10.1103/PhysRevB.45.7889. URL: https://link.aps.org/doi/10.1103/PhysRevB.45.7889.

[36] Sreejith Chulliparambil, Hua-Chen Zhang, and Hong-Hao Tu. “Symmetry-protected topological phases, conformal criticalities, and duality in exactly solvable SO(n) spin chains”. In: *Phys. Rev. B* 108 (9 2023), p. 094411. DOI: 10.1103/PhysRevB.108.094411. URL: https://link.aps.org/doi/10.1103/PhysRevB.108.094411.

[37] R. Coldea et al. “Spin Waves and Electronic Interactions in La_2CuO_4”. In: *Phys. Rev. Lett.* 86 (23 2001), pp. 5377–5380. DOI: 10.1103/PhysRevLett.86.5377. URL: https://link.aps.org/doi/10.1103/PhysRevLett.86.5377.

[38] Piers Coleman. *Introduction to Many-Body Physics*. 1st. This is a comprehensive textbook that provides an in-depth exploration of many-body physics, covering models and concepts essential to the field. It is considered an invaluable resource for students and researchers alike. Cambridge: Cambridge University Press, 2015. ISBN: 9780521864886. DOI: 10.1017/CBO9781139015509. URL: https://doi.org/10.1017/CBO9781139015509.

[39] Tessa Cookmeyer, Johannes Motruk, and Joel E. Moore. “Four-Spin Terms and the Origin of the Chiral Spin Liquid in Mott Insulators on the Triangular Lattice”. In: *Phys. Rev. Lett.* 127 (8 2021), p. 087201. DOI: 10.1103/PhysRevLett.127.087201. URL: https://link.aps.org/doi/10.1103/PhysRevLett.127.087201.

[40] Elbio Dagotto. “Experiments on ladders reveal a complex interplay between a spin-gapped normal state and superconductivity”. In: *Reports on Progress in Physics* 62.11 (1999), p. 1525. DOI: 10.1088/0034-4885/62/11/202. URL: https://dx.doi.org/10.1088/0034-4885/62/11/202.

[41] Elbio Dagotto and T.M. Rice. “Surprises on the Way from One- to Two-Dimensional Quantum Magnets: The Ladder Materials”. In: *Science* 271 (1996), pp. 618–623. DOI: 10.1126/science.271.5249.618.

[42] Eugene Demler and Fei Zhou. “Spinor Bosonic Atoms in Optical Lattices: Symmetry Breaking and Fractionalization”. In: *Phys. Rev. Lett.* 88 (16 2002), p. 163001. DOI: 10.1103/PhysRevLett.88.163001. URL: https://link.aps.org/doi/10.1103/PhysRevLett.88.163001.

[43] Amit Dutta et al. *Quantum Phase Transitions in Transverse Field Spin Models: From Statistical Physics to Quantum Information*. Delhi: Cambridge University Press, 2015. DOI: 10.1017/CBO9781107706057.

[44] Freeman J Dyson, Elliott H Lieb, and Barry Simon. “Phase transitions in quantum spin systems with isotropic and nonisotropic interactions”. In: *Statistical Mechanics: Selecta of Elliott H. Lieb* (2004), pp. 163–211.

[45] I. Dzyaloshinsky. “A thermodynamic theory of “weak” ferromagnetism of antiferromagnetics”. In: *Journal of Physics and Chemistry of Solids* 4.4 (1958), pp. 241–255. ISSN: 0022-3697. DOI: https://doi.org/10.1016/0022-3697(58)90076-3. URL: https://www.sciencedirect.com/science/article/pii/0022369758900763.

[46] D. V. Else and C. Nayak. “Classifying symmetry-protected topological phases through the anomalous action of the symmetry on the edge”. In: *Physical Review B* 90.24 (2014), p. 235137. DOI: 10.1103/PhysRevB.90.235137. arXiv: arXiv:1409.5436 [cond-mat.str-el].

[47] M. Fannes, B. Nachtergaele, and R. F. Werner. “Exact antiferromagnetic ground states of quantum spin chains”. In: *Europhysics Letters* 10 (1989), pp. 633–637. DOI: 10.1209/0295-5075/10/7/005.

[48] M. Fannes, B. Nachtergaele, and R. F. Werner. “Finitely correlated pure states”. In: *Journal of Functional Analysis* 120 (1994). Available at: ftp://ace2.ma.utexas.edu/pub/mp_arc/converted/92/92-132.ps.gz, pp. 511–534. DOI: 10.1006/jfan.1994.1066.

[49] M. Fannes, B. Nachtergaele, and R. F. Werner. “Finitely correlated states on quantum spin chains”. In: *Communications in Mathematical Physics* 144 (1992), pp. 443–490. URL: https://projecteuclid.org/euclid.cmp/1104249404.

[50] M. Fannes, B. Nachtergaele, and R. F. Werner. “Valence bond states on quantum spin chains as ground states with spectral gap”. In: *Journal of Physics A: Mathematical and General* 24 (1991), pp. L185–L190. DOI: 10.1088/0305-4470/24/4/009.

[51] R. Fernández, J. Fröhlich, and A. D. Sokal. *Random Walks, Critical Phenomena, and Triviality in Quantum Field Theory*. Berlin: Springer, 1992.

[52] L. Fidkowski and A. Kitaev. “Topological phases of fermions in one dimension”. In: *Physical Review B* 83.29 (2011), p. 075103. DOI: 10.1103/PhysRevB.83.075103. arXiv: arXiv:1008.4138 [cond-mat.str-el].

[53] Matthew Fishman, Steven R. White, and E. Miles Stoudenmire. “Codebase release 0.3 for ITensor”. In: *SciPost Phys. Codebases 4-r0.3* (2022). DOI: 10.21468/SciPostPhysCodeb.4-r0.3. URL: https://scipost.org/10.21468/SciPostPhysCodeb.4-r0.3.

[54] Matthew Fishman, Steven R. White, and E. Miles Stoudenmire. “The ITensor Software Library for Tensor Network Calculations”. In: *SciPost Phys. Codebases* 4 (2022). DOI: 10.21468/SciPostPhysCodeb.4. URL: https://scipost.org/10.21468/SciPostPhysCodeb.4.

[55] Matéo Fontaine and Shunsuke Furukawa. “Phase Diagram of a Spin-$\frac{1}{2}$ Heisenberg Ladder with a Chirality–Chirality Interaction”. In: *Journal of the Physical Society of Japan* 93.12 (2024), p. 124710. DOI: 10.7566/JPSJ.93.124710. eprint: https://doi.org/10.7566/JPSJ.93.124710. URL: https://doi.org/10.7566/JPSJ.93.124710.

[56] Matéo Fontaine, Koudai Sugimoto, and Shunsuke Furukawa. "Symmetry, topology, duality, chirality, and criticality in a spin-$\frac{1}{2}$ XXZ ladder with a four-spin interaction". In: *Phys. Rev. B* 109 (13 2024), p. 134413. DOI: 10.1103/PhysRevB.109.134413. URL: https://link.aps.org/doi/10.1103/PhysRevB.109.134413.

[57] Eduardo Fradkin. *Field Theories of Condensed Matter Physics*. 2nd. Cambridge: Cambridge University Press, 2013. DOI: 10.1017/CBO9781139015509.

[58] Holger Frahm and V. E. Korepin. "Critical exponents for the one-dimensional Hubbard model". In: *Phys. Rev. B* 42 (16 1990), pp. 10553–10565. DOI: 10.1103/PhysRevB.42.10553. URL: https://link.aps.org/doi/10.1103/PhysRevB.42.10553.

[59] Michael Freedman et al. "Topological quantum computation". In: *Bulletin of the American Mathematical Society* 40.1 (2003), pp. 31–38.

[60] S. Friedli and Y. Velenik. *Statistical Mechanics of Lattice Systems: A Concrete Mathematical Introduction*. Cambridge: Cambridge University Press, 2017.

[61] Liang Fu, C. L. Kane, and E. J. Mele. "Topological Insulators in Three Dimensions". In: *Phys. Rev. Lett.* 98 (10 2007), p. 106803. DOI: 10.1103/PhysRevLett.98.106803. URL: https://link.aps.org/doi/10.1103/PhysRevLett.98.106803.

[62] Yohei Fuji. "Effective field theory for one-dimensional valence-bond-solid phases and their symmetry protection". In: *Phys. Rev. B* 93 (10 2016), p. 104425. DOI: 10.1103/PhysRevB.93.104425. URL: https://link.aps.org/doi/10.1103/PhysRevB.93.104425.

[63] Yohei Fuji. "Symmetries and quantum phases in one-dimensional spin systems". PhD thesis. University of Tokyo, 2015. URL: https://repository.dl.itc.u-tokyo.ac.jp/?action=pages_view_main&active_action=repository_view_main_item_detail&item_id=8089&item_no=1&page_id=41&block_id=85.

[64] Keisuke Fujii. *Quantum Computation with Topological Codes: from Qubit to Topological Fault-Tolerance*. Vol. 8. SpringerBriefs in Mathematical Physics. Berlin: Springer, 2015. DOI: 10.1007/978-3-319-17145-8. arXiv: arXiv:1504.01444 [quant-ph].

[65] Hiroshi Fukuyama. "Nuclear Magnetism in Two-Dimensional Solid Helium Three on Graphite". In: *Journal of the Physical Society of Japan* 77.11 (2008), p. 111013. DOI: 10.1143/JPSJ.77.111013. URL: https://doi.org/10.1143/JPSJ.77.111013.

[66] Shunsuke Furukawa. "Characterization of Exotic Orders in Quantum Spin Systems". PhD thesis. Tokyo Institute of Technology, 2007.

[67] Shunsuke Furukawa, Grégoire Misguich, and Masaki Oshikawa. "Systematic Derivation of Order Parameters through Reduced Density Matrices". In: *Phys. Rev. Lett.* 96 (4 2006), p. 047211. DOI: 10.1103/PhysRevLett.96.047211. URL: https://link.aps.org/doi/10.1103/PhysRevLett.96.047211.

[68] Shunsuke Furukawa et al. "Ground-state phase diagram of a spin-$\frac{1}{2}$ frustrated ferromagnetic XXZ chain: Haldane dimer phase and gapped/gapless chiral phases". In: *Phys. Rev. B* 86 (9 2012), p. 094417. DOI: 10.1103/PhysRevB.86.094417. URL: https://link.aps.org/doi/10.1103/PhysRevB.86.094417.

[69] Shunsuke Furukawa et al. "Quantum Fluctuations of Chirality in One-Dimensional Spin-1/2 Multiferroics: Gapless Dielectric Response from Phasons and Chiral Solitons". In: *Journal of the Physical Society of Japan* 77.12 (2008), p. 123712. DOI: 10.1143/JPSJ.77.123712. URL: https://doi.org/10.1143/JPSJ.77.123712.

[70] Shunsuke C. Furuya and Masahiro Sato. "Quantized edge magnetizations and their symmetry protection in one-dimensional quantum spin systems". In: *Phys. Rev. B* 104 (18 2021), p. 184401. DOI: 10.1103/PhysRevB.104.184401. URL: https://link.aps.org/doi/10.1103/PhysRevB.104.184401.

[71] T. Giamarchi. *Quantum Physics in One Dimension*. International Series of Monographs on Physics. Oxford University Press, New York, 2004. ISBN: 9780198525004.

[72] V. L. Ginzburg and L. D. Landau. "On the Theory of Superconductivity". In: *Zh. Eksp. Teor. Fiz.* 20 (1950), p. 1064.

[73] A.O. Gogolin, A.A. Nersesyan, and A.M. Tsvelik. *Bosonization and Strongly Correlated Systems*. Cambridge University Press, New York, 2004. ISBN: 9780521617192.

[74] J. Goldstone. "Field Theories with Superconductor Solutions". In: *Il Nuovo Cimento* 19 (1961), pp. 154–164. DOI: 10.1007/BF02812722.

[75] O. Golinelli, Th. Jolicoeur, and R. Lacaze. "Finite-lattice extrapolations for a Haldane-gap antiferromagnet". In: *Phys. Rev. B* 50 (1994), p. 3037.

[76] V. Gritsev, B. Normand, and D. Baeriswyl. "Phase diagram of the Heisenberg spin ladder with ring exchange". In: *Phys. Rev. B* 69 (9 2004), p. 094431. DOI: 10.1103/PhysRevB.69.094431. URL: https://link.aps.org/doi/10.1103/PhysRevB.69.094431.

[77] Zheng-Cheng Gu and Xiao-Gang Wen. "Tensor-entanglement-filtering renormalization approach and symmetry-protected topological order". In: *Phys. Rev. B* 80 (15 2009), p. 155131. DOI: 10.1103/PhysRevB.80.155131. URL: https://link.aps.org/doi/10.1103/PhysRevB.80.155131.

[78] V. Gurarie and L. Radzihovsky. "Zero modes of two-dimensional chiral p-wave superconductors". In: *Phys. Rev. B* 75 (21 2007), p. 212509. DOI: 10.1103/PhysRevB.75.212509. URL: https://link.aps.org/doi/10.1103/PhysRevB.75.212509.

[79] J. Haegeman et al. "An order parameter for symmetry-protected phases in one dimension". In: *Physical Review Letters* 109.32 (2012), p. 050402. DOI: 10.1103/PhysRevLett.109.050402. arXiv: arXiv:1201.4174 [cond-mat.str-el].

[80] M. Hagiwara et al. “Observation of S = 1/2 degrees of freedom in an S = 1 linear-chain Heisenberg antiferromagnet”. In: *Physical Review Letters* 65.33 (1990), p. 3181. DOI: 10.1103/PhysRevLett.65.3181.

[81] Tigran Hakobyan. “Antiferromagnetic ordering of energy levels for a spin ladder with four-spin cyclic exchange: Generalization of the Lieb-Mattis theorem”. In: *Phys. Rev. B* 78 (1 2008), p. 012407. DOI: 10.1103/PhysRevB.78.012407. URL: https://link.aps.org/doi/10.1103/PhysRevB.78.012407.

[82] F. D. M. Haldane. “Continuum dynamics of the 1-D Heisenberg antiferromagnet: Identification with the O(3) nonlinear sigma model”. In: *Physics Letters A* 93.9 (1983), pp. 464 –468. ISSN: 0375-9601. DOI: https://doi.org/10.1016/0375-9601(83)90631-X. URL: http://www.sciencedirect.com/science/article/pii/037596018390631X.

[83] F. D. M. Haldane. “Nonlinear Field Theory of Large-Spin Heisenberg Antiferromagnets: Semiclassically Quantized Solitons of the One-Dimensional Easy-Axis Néel State”. In: *Phys. Rev. Lett.* 50 (15 1983), pp. 1153–1156. DOI: 10.1103/PhysRevLett.50.1153. URL: https://link.aps.org/doi/10.1103/PhysRevLett.50.1153.

[84] F. D. M. Haldane. “"Θ physics" and quantum spin chains (abstract)”. In: *Journal of Applied Physics* 57 (1985), p. 3359. DOI: 10.1063/1.335096.

[85] T. Hara and H. Tasaki. *Mathematics and Physics of Phase Transitions and Critical Phenomena (in Japanese)*. Tokyo: Kyoritsu, 2015.

[86] M. Hastings. “An area law for one-dimensional quantum systems”. In: *Journal of Statistical Mechanics: Theory and Experiment* 34 (2007), P08024. DOI: 10.1088/1742-5468/2007/08/P08024. arXiv: arXiv:0705.2024 [quant-ph].

[87] Y. Hatsugai. “Quantized Berry phases as a local order parameter of a quantum liquid”. In: *Journal of the Physical Society of Japan* 75.36 (2006), p. 123601. DOI: 10.1143/JPSJ.75.123601. arXiv: arXiv:cond-mat/0603230 [cond-mat].

[88] Yasuhiro Hatsugai. “Quantized Berry phases for a local characterization of spin liquids in frustrated spin systems”. In: *Journal of Physics: Condensed Matter* 19 (2007), p. 145209. DOI: 10.1088/0953-8984/19/14/145209. arXiv: arXiv:cond-mat/0607024 [cond-mat].

[89] Keigo Hijii and Kiyohide Nomura. “Phase transition of $S = \frac{1}{2}$ two-leg Heisenberg spin ladder systems with a four-spin interaction”. In: *Phys. Rev. B* 80 (1 2009), p. 014426. DOI: 10.1103/PhysRevB.80.014426. URL: https://link.aps.org/doi/10.1103/PhysRevB.80.014426.

[90] Keigo Hijii and Kiyohide Nomura. “Universality class of an $S = \frac{1}{2}$ quantum spin ladder system with four-spin exchange”. In: *Phys. Rev. B* 65 (10 2002), p. 104413. DOI: 10.1103/PhysRevB.65.104413. URL: https://link.aps.org/doi/10.1103/PhysRevB.65.104413.

[91] Keigo Hijii, Shaojin Qin, and Kiyohide Nomura. "Staggered dimer order and criticality in an $S = \frac{1}{2}$ quantum spin ladder system with four-spin exchange". In: *Phys. Rev. B* 68 (13 2003), p. 134403. DOI: 10.1103/PhysRevB.68.134403. URL: https://link.aps.org/doi/10.1103/PhysRevB.68.134403.

[92] Keigo Hijii and Tôru Sakai. "Ground state phase diagram of an $S = \frac{1}{2}$ two-leg Heisenberg spin ladder system with negative four-spin interaction". In: *Phys. Rev. B* 88 (10 2013), p. 104403. DOI: 10.1103/PhysRevB.88.104403. URL: https://link.aps.org/doi/10.1103/PhysRevB.88.104403.

[93] T. Hikihara and A. Furusaki. "Correlation amplitude for the S = 1/2 XXZ spin chain in the critical region: Numerical renormalization-group study of an open chain". In: *Phys. Rev. B* 58 (2 1998), R583–R586. DOI: 10.1103/PhysRevB.58.R583. URL: https://link.aps.org/doi/10.1103/PhysRevB.58.R583.

[94] Toshiya Hikihara, Akira Furusaki, and Sergei Lukyanov. "Dimer correlation amplitudes and dimer excitation gap in spin-1/2 XXZ and Heisenberg chains". In: *Phys. Rev. B* 96 (13 2017), p. 134429. DOI: 10.1103/PhysRevB.96.134429. URL: https://link.aps.org/doi/10.1103/PhysRevB.96.134429.

[95] Toshiya Hikihara, Tsutomu Momoi, and Xiao Hu. "Spin-Chirality Duality in a Spin Ladder with Four-Spin Cyclic Exchange". In: *Phys. Rev. Lett.* 90 (8 2003), p. 087204. DOI: 10.1103/PhysRevLett.90.087204. URL: https://link.aps.org/doi/10.1103/PhysRevLett.90.087204.

[96] Toshiya Hikihara and Oleg A. Starykh. "Phase diagram of the frustrated spin ladder". In: *Phys. Rev. B* 81 (6 2010), p. 064432. DOI: 10.1103/PhysRevB.81.064432. URL: https://link.aps.org/doi/10.1103/PhysRevB.81.064432.

[97] Toshiya Hikihara and Shoji Yamamoto. "Magnetic Phase Diagram of Spin-1/2 Two-Leg Ladder with Four-Spin Ring Exchanges". In: *Journal of the Physical Society of Japan* 77.1 (2008), p. 014709. DOI: 10.1143/JPSJ.77.014709. URL: https://doi.org/10.1143/JPSJ.77.014709.

[98] T. Hirano, H. Katsura, and Y. Hatsugai. "Degeneracy and consistency condition for Berry phases: gap closing under a local gauge twist". In: *Physical Review B* 78.40 (2008), p. 054431. DOI: 10.1103/PhysRevB.78.054431. arXiv: arXiv:0803.3185 [cond-mat.str-el].

[99] T. Hirano, H. Katsura, and Y. Hatsugai. "Topological classification of gapped spin chains: quantized Berry phase as a local order parameter". In: *Physical Review B* 77.39 (2008), p. 094431. DOI: 10.1103/PhysRevB.77.094431. arXiv: arXiv:0710.4198 [cond-mat.str-el].

[100] Z Hiroi and M Takano. "Absence of superconductivity in the doped antiferromagnetic spin-ladder compound (La, Sr) CuO2. 5". In: *Nature* 377.6544 (1995), pp. 41–43.

[101] Z. Hiroi et al. “A new homologous series $Sr_{n-1}Cu_{n+1}O_{2n}$ found in the SrOCuO system treated under high pressure”. In: *Journal of Solid State Chemistry* 95.1 (1991), pp. 230–238. ISSN: 0022-4596. DOI: https://doi.org/10.1016/0022-4596(91)90394-W. URL: https://www.sciencedirect.com/science/article/pii/002245969190394W.

[102] P Horsch and W Von der Linden. “Spin-correlations and low lying excited states of the spin-1/2 Heisenberg antiferromagnet on a square lattice”. In: *Zeitschrift für Physik B Condensed Matter* 72.2 (1988), pp. 181–193.

[103] E. M. McCarron III et al. “The incommensurate structure of (Sr14-xCax)Cu24O41 (0 < x < 8), a superconductor byproduct”. In: *Materials Research Bulletin* 23.9 (1988), pp. 1355–1365. DOI: 10.1016/0025-5408(88)90019-1. URL: https://doi.org/10.1016/0025-5408(88)90019-1.

[104] Adilet Imambekov, Mikhail Lukin, and Eugene Demler. “Spin-exchange interactions of spin-one bosons in optical lattices: Singlet, nematic, and dimerized phases”. In: *Phys. Rev. A* 68 (6 2003), p. 063602. DOI: 10.1103/PhysRevA.68.063602. URL: https://link.aps.org/doi/10.1103/PhysRevA.68.063602.

[105] K. Ishida et al. “Low Temperature Heat-Capacity Anomalies in Two-Dimensional Solid ^3He”. In: *Phys. Rev. Lett.* 79 (18 1997), pp. 3451–3454. DOI: 10.1103/PhysRevLett.79.3451. URL: https://link.aps.org/doi/10.1103/PhysRevLett.79.3451.

[106] Chigak Itoi, Shaojin Qin, and Ian Affleck. “Phase diagram of a one-dimensional spin-orbital model”. In: *Phys. Rev. B* 61 (10 2000), pp. 6747–6756. DOI: 10.1103/PhysRevB.61.6747. URL: https://link.aps.org/doi/10.1103/PhysRevB.61.6747.

[107] Shenghan Jiang and Olexei Motrunich. “Ising ferromagnet to valence bond solid transition in a one-dimensional spin chain: Analogies to deconfined quantum critical points”. In: *Phys. Rev. B* 99 (7 2019), p. 075103. DOI: 10.1103/PhysRevB.99.075103. URL: https://link.aps.org/doi/10.1103/PhysRevB.99.075103.

[108] V. Kalmeyer and R. B. Laughlin. “Equivalence of the resonating-valence-bond and fractional quantum Hall states”. In: *Phys. Rev. Lett.* 59 (18 1987), pp. 2095–2098. DOI: 10.1103/PhysRevLett.59.2095. URL: https://link.aps.org/doi/10.1103/PhysRevLett.59.2095.

[109] C. L. Kane and E. J. Mele. “Quantum Spin Hall Effect in Graphene”. In: *Phys. Rev. Lett.* 95 (22 2005), p. 226801. DOI: 10.1103/PhysRevLett.95.226801. URL: https://link.aps.org/doi/10.1103/PhysRevLett.95.226801.

[110] C. L. Kane and E. J. Mele. “Z_2 Topological Order and the Quantum Spin Hall Effect”. In: *Phys. Rev. Lett.* 95 (14 2005), p. 146802. DOI: 10.1103/PhysRevLett.95.146802. URL: https://link.aps.org/doi/10.1103/PhysRevLett.95.146802.

[111] Yuki Kawaguchi and Masahito Ueda. "Spinor Bose–Einstein condensates". In: *Physics Reports* 520.5 (2012), pp. 253–381. ISSN: 0370-1573. DOI: https://doi.org/10.1016/j.physrep.2012.07.005. URL: https://www.sciencedirect.com/science/article/pii/S0370157312002098.

[112] Norio Kawakami and Sung-Kil Yang. "Correlation functions in the one-dimensional t-J model". In: *Phys. Rev. Lett.* 65 (18 1990), pp. 2309–2311. DOI: 10.1103/PhysRevLett.65.2309. URL: https://link.aps.org/doi/10.1103/PhysRevLett.65.2309.

[113] T. Kennedy. "Exact diagonalisations of open spin-1 chains". In: *Journal of Physics: Condensed Matter* 2.26 (1990), pp. 5737–5745. DOI: 10.1088/0953-8984/2/26/010. URL: https://doi.org/10.1088/0953-8984/2/26/010.

[114] T. Kennedy and H. Tasaki. "Hidden symmetry breaking and the Haldane phase in S = 1 quantum spin chains". In: *Communications in Mathematical Physics* 147.49 (1992), pp. 431–484. URL: https://projecteuclid.org/euclid.cmp/1104250747.

[115] Tom Kennedy, Elliott H Lieb, and B Sriram Shastry. "Existence of Néel order in some spin-1/2 Heisenberg antiferromagnets". In: *Journal of statistical physics* 53 (1988), pp. 1019–1030.

[116] Tom Kennedy and Hal Tasaki. "Hidden $Z_2 \times Z_2$ symmetry breaking in Haldane-gap antiferromagnets". In: *Phys. Rev. B* 45 (1 1992), pp. 304–307. DOI: 10.1103/PhysRevB.45.304. URL: https://link.aps.org/doi/10.1103/PhysRevB.45.304.

[117] Eugene H. Kim, Ö. Legeza, and J. Sólyom. "Topological order, dimerization, and spinon deconfinement in frustrated spin ladders". In: *Phys. Rev. B* 77 (20 2008), p. 205121. DOI: 10.1103/PhysRevB.77.205121. URL: https://link.aps.org/doi/10.1103/PhysRevB.77.205121.

[118] Eugene H. Kim et al. "Phase transitions between topologically distinct gapped phases in isotropic spin ladders". In: *Phys. Rev. B* 62 (22 2000), pp. 14965–14974. DOI: 10.1103/PhysRevB.62.14965. URL: https://link.aps.org/doi/10.1103/PhysRevB.62.14965.

[119] Alexei Kitaev. "Anyons in an exactly solved model and beyond". In: *Annals of Physics* 321.1 (2006). January Special Issue, pp. 2–111. ISSN: 0003-4916. DOI: https://doi.org/10.1016/j.aop.2005.10.005. URL: https://www.sciencedirect.com/science/article/pii/S0003491605002381.

[120] Alexei Kitaev and John Preskill. "Topological Entanglement Entropy". In: *Phys. Rev. Lett.* 96 (11 2006), p. 110404. DOI: 10.1103/PhysRevLett.96.110404. URL: https://link.aps.org/doi/10.1103/PhysRevLett.96.110404.

[121] A.Yu. Kitaev. "Fault-tolerant quantum computation by anyons". In: *Annals of Physics* 303.1 (2003), pp. 2–30. ISSN: 0003-4916. DOI: https://doi.org/10.1016/S0003-4916(02)00018-0. URL: https://www.sciencedirect.com/science/article/pii/S0003491602000180.

[122] A. D. Klironomos et al. "Spin coupling in zigzag Wigner crystals". In: *Phys. Rev. B* 76 (7 2007), p. 075302. DOI: 10.1103/PhysRevB.76.075302. URL: https://link.aps.org/doi/10.1103/PhysRevB.76.075302.

[123] A. Klümper, A. Schadschneider, and J. Zittartz. "Matrix Product Ground States for One-Dimensional Spin-1 Quantum Antiferromagnets". In: *Europhysics Letters* 24.4 (1993), p. 293. DOI: 10.1209/0295-5075/24/4/010. URL: https://dx.doi.org/10.1209/0295-5075/24/4/010.

[124] S. Knabe. "Energy gaps and elementary excitations for certain VBS-quantum antiferromagnets". In: *Journal of Statistical Physics* 52 (1988), pp. 627–638. DOI: 10.1007/BF01019711.

[125] A. K. Kolezhuk and H.-J. Mikeska. "Biquadratic exchange in spin-1 chains". In: *International Journal of Modern Physics B* 12 (1998), pp. 2325–2405. DOI: 10.1142/S0217979298001467.

[126] A. K. Kolezhuk and H.-J. Mikeska. "Finitely Correlated Generalized Spin Ladders". In: *International Journal of Modern Physics B* 12.23 (1998), pp. 2325–2348. DOI: 10.1142/S0217979298001356. URL: https://doi.org/10.1142/S0217979298001356.

[127] Tohru Koma and Hal Tasaki. "Decay of superconducting and magnetic correlations in one-and two-dimensional Hubbard models". In: *Physical review letters* 68.21 (1992), p. 3248.

[128] Tohru Koma and Hal Tasaki. "Symmetry breaking in Heisenberg antiferromagnets". In: *Communications in mathematical physics* 158 (1993), pp. 191–214.

[129] V. E. Korepin, N. M. Bogoliubov, and A. G. Izergin. *Quantum Inverse Scattering Method and Correlation Functions*. Cambridge: Cambridge University Press, 2010. ISBN: 9780521385309. DOI: 10.1017/CBO9780511628832.

[130] H. A. Kramers. "Théorie générale de la rotation paramagnétique dans les cristaux". In: *Proceedings of the Royal Netherlands Academy of Arts and Sciences* 33 (1930), pp. 959–972.

[131] L. D. Landau. "On the Theory of Phase Transitions". In: *Phys. Z. Sowjetunion* 11 (1937), p. 26.

[132] A. Läuchli, G. Schmid, and M. Troyer. "Phase diagram of a spin ladder with cyclic four-spin exchange". In: *Phys. Rev. B* 67 (10 2003), p. 100409. DOI: 10.1103/PhysRevB.67.100409. URL: https://link.aps.org/doi/10.1103/PhysRevB.67.100409.

[133] A. Läuchli et al. "Two-Step Restoration of SU(2) Symmetry in a Frustrated Ring-Exchange Magnet". In: *Phys. Rev. Lett.* 95 (13 2005), p. 137206. DOI: 10.1103/PhysRevLett.95.137206. URL: https://link.aps.org/doi/10.1103/PhysRevLett.95.137206.

[134] R. B. Laughlin. "Anomalous Quantum Hall Effect: An Incompressible Quantum Fluid with Fractionally Charged Excitations". In: *Phys. Rev. Lett.* 50 (18 1983), pp. 1395–1398. DOI: 10.1103/PhysRevLett.50.1395. URL: https://link.aps.org/doi/10.1103/PhysRevLett.50.1395.

[135] P. Lecheminant. "ONE-DIMENSIONAL QUANTUM SPIN LIQUIDS". In: *Frustrated Spin Systems*. Ed. by H T Diep. 3rd. Singapore: WORLD SCIENTIFIC, 2020. Chap. 6, pp. 333–395. DOI: 10.1142/9789811214141_0006. URL: https://www.worldscientific.com/doi/abs/10.1142/9789811214141_0006.

[136] P. Lecheminant, Alexander O. Gogolin, and Alexander A. Nersesyan. "Criticality in self-dual sine-Gordon models". In: *Nuclear Physics B* 639.3 (2002), pp. 502 –523. ISSN: 0550-3213. DOI: https://doi.org/10.1016/S0550-3213(02)00474-1. URL: http://www.sciencedirect.com/science/article/pii/S0550321302004741.

[137] P. Lecheminant and K. Totsuka. "Competing orders and hidden duality symmetries in two-leg spin ladder systems". In: *Phys. Rev. B* 74 (22 2006), p. 224426. DOI: 10.1103/PhysRevB.74.224426. URL: https://link.aps.org/doi/10.1103/PhysRevB.74.224426.

[138] P. Lecheminant and K. Totsuka. "Phases of the generalized two-leg spin ladder: A view from the SU(4) symmetry". In: *Phys. Rev. B* 71 (2 2005), p. 020407. DOI: 10.1103/PhysRevB.71.020407. URL: https://link.aps.org/doi/10.1103/PhysRevB.71.020407.

[139] Michael Levin and Xiao-Gang Wen. "Detecting Topological Order in a Ground State Wave Function". In: *Phys. Rev. Lett.* 96 (11 2006), p. 110405. DOI: 10.1103/PhysRevLett.96.110405. URL: https://link.aps.org/doi/10.1103/PhysRevLett.96.110405.

[140] Michael A. Levin and Xiao-Gang Wen. "String-net condensation: A physical mechanism for topological phases". In: *Phys. Rev. B* 71 (4 2005), p. 045110. DOI: 10.1103/PhysRevB.71.045110. URL: https://link.aps.org/doi/10.1103/PhysRevB.71.045110.

[141] Y. Q. Li et al. "SU(4) Theory for Spin Systems with Orbital Degeneracy". In: *Phys. Rev. Lett.* 81 (16 1998), pp. 3527–3530. DOI: 10.1103/PhysRevLett.81.3527. URL: https://link.aps.org/doi/10.1103/PhysRevLett.81.3527.

[142] Elliott Lieb and Daniel Mattis. "Ordering energy levels of interacting spin systems". In: *Journal of Mathematical Physics* 3.4 (1962), pp. 749–751.

[143] Elliott Lieb, Theodore Schultz, and Daniel Mattis. "Two soluble models of an antiferromagnetic chain". In: *Annals of Physics* 16.3 (1961), pp. 407–466. ISSN: 0003-4916. DOI: https://doi.org/10.1016/0003-4916(61)90115-4. URL: https://www.sciencedirect.com/science/article/pii/0003491661901154.

[144] W. LiMing et al. "From Néel long-range order to spin liquids in the multiple-spin exchange model". In: *Phys. Rev. B* 62 (10 2000), pp. 6372–6377. DOI: 10.1103/PhysRevB.62.6372. URL: https://link.aps.org/doi/10.1103/PhysRevB.62.6372.

[145] Zheng-Xin Liu et al. "Symmetry-protected topological phases in spin ladders with two-body interactions". In: *Phys. Rev. B* 86 (19 2012), p. 195122. DOI: 10.1103/PhysRevB.86.195122. URL: https://link.aps.org/doi/10.1103/PhysRevB.86.195122.

[146] Sergei Lukyanov and Alexander Zamolodchikov. "Exact expectation values of local fields in the quantum sine-Gordon model". In: *Nuclear Physics B* 493.3 (1997), pp. 571 –587. ISSN: 0550-3213. DOI: https://doi.org/10.1016/S0550-3213(97)00123-5. URL: http://www.sciencedirect.com/science/article/pii/S0550321397001235.

[147] A. H. MacDonald, S. M. Girvin, and D. Yoshioka. "Reply to "Comment on 't/U expansion for the Hubbard model"'". In: *Phys. Rev. B* 41 (4 1990), pp. 2565–2568. DOI: 10.1103/PhysRevB.41.2565. URL: https://link.aps.org/doi/10.1103/PhysRevB.41.2565.

[148] Salvatore R. Manmana et al. "Topological phases in ultracold polar-molecule quantum magnets". In: *Phys. Rev. B* 87 (8 2013), p. 081106. DOI: 10.1103/PhysRevB.87.081106. URL: https://link.aps.org/doi/10.1103/PhysRevB.87.081106.

[149] W Marshall. "Antiferromagnetism". In: *Proceedings of the Royal Society of London. Series A. Mathematical and Physical Sciences* 232.1188 (1955), pp. 48–68.

[150] Ryuichi Masutomi, Yoshitomo Karaki, and Hidehiko Ishimoto. "Gapless Spin Liquid Behavior in Two-Dimensional Solid ^{3}He". In: *Phys. Rev. Lett.* 92 (2 2004), p. 025301. DOI: 10.1103/PhysRevLett.92.025301. URL: https://link.aps.org/doi/10.1103/PhysRevLett.92.025301.

[151] M. Matsuda et al. "Magnetic excitations and exchange interactions in the spin-$\frac{1}{2}$ two-leg ladder compound $La_6Ca_8Cu_{24}O_{41}$". In: *Phys. Rev. B* 62 (13 2000), pp. 8903–8908. DOI: 10.1103/PhysRevB.62.8903. URL: https://link.aps.org/doi/10.1103/PhysRevB.62.8903.

[152] T. Matsui. "The split property and the symmetry breaking of the quantum spin chain". In: *Communications in Mathematical Physics* 218.63 (2001), pp. 393–416.

[153] Daniel C Mattis. "Ground-state symmetry in XY model of magnetism". In: *Physical Review Letters* 42.23 (1979), p. 1503.

[154] I. P. McCulloch. *Infinite size density matrix renormalization group, revisited*. 2008. eprint: arXiv:0804.2509.

[155] Ian P McCulloch. "From density-matrix renormalization group to matrix product states". In: *Journal of Statistical Mechanics: Theory and Experiment* 2007.10 (2007), P10014–P10014. DOI: 10.1088/1742-5468/2007/10/p10014. URL: https://doi.org/10.1088/1742-5468/2007/10/p10014.

[156] N. D. Mermin and H. Wagner. "Absence of Ferromagnetism or Antiferromagnetism in One- or Two-Dimensional Isotropic Heisenberg Models". In: *Phys. Rev. Lett.* 17 (22 1966), pp. 1133–1136. DOI: 10.1103/PhysRevLett.17.1133. URL: https://link.aps.org/doi/10.1103/PhysRevLett.17.1133.

[157] Alexandros Metavitsiadis and Sebastian Eggert. "Competing phases in spin ladders with ring exchange and frustration". In: *Phys. Rev. B* 95 (14 2017), p. 144415. DOI: 10.1103/PhysRevB.95.144415. URL: https://link.aps.org/doi/10.1103/PhysRevB.95.144415.

[158] Spyridon Michalakis and Justyna P. Zwolak. "Stability of frustration-free Hamiltonians". In: *Communications in Mathematical Physics* 322 (2013), pp. 277–302. DOI: 10.1007/s00220-013-1770-1. arXiv: arXiv:1109.1588 [math-ph].

[159] J. Miller and A. Miyake. "Hierarchy of universal entanglement in 2D measurement-based quantum computation". In: *npj Quantum Information* 2.66 (2016), p. 16036. DOI: 10.1038/npjqi.2016.36. URL: https://www.nature.com/articles/npjqi201636.

[160] G. Misguich et al. "Spin Liquid in the Multiple-Spin Exchange Model on the Triangular Lattice: ^{3}He on Graphite". In: *Phys. Rev. Lett.* 81 (5 1998), pp. 1098–1101. DOI: 10.1103/PhysRevLett.81.1098. URL: https://link.aps.org/doi/10.1103/PhysRevLett.81.1098.

[161] G. Misguich et al. "Spin-liquid phase of the multiple-spin exchange Hamiltonian on the triangular lattice". In: *Phys. Rev. B* 60 (2 1999), pp. 1064–1074. DOI: 10.1103/PhysRevB.60.1064. URL: https://link.aps.org/doi/10.1103/PhysRevB.60.1064.

[162] S. Miyashita and S. Yamamoto. "Effects of edges in S = 1 Heisenberg antiferromagnetic chains". In: *Physical Review B* 48.67 (1993), pp. 913–919. DOI: 10.1103/PhysRevB.48.913.

[163] Y. Mizuno, T. Tohyama, and S. Maekawa. "Electronic States of Doped Spin Ladders (Sr,Ca)14Cu24O41". In: *Journal of the Physical Society of Japan* 66.4 (1997), pp. 937–940. DOI: 10.1143/JPSJ.66.937. URL: https://journals.jps.jp/doi/10.1143/JPSJ.66.937.

[164] Yoshiaki Mizuno, Takami Tohyama, and Sadamichi Maekawa. "Magnetic Interaction in Insulating Cuprates". In: *Journal of Low Temperature Physics* 117.3-4 (1999), pp. 389–393. DOI: 10.1023/A:1022577918657.

[165] R. Moessner and S. L. Sondhi. "Resonating Valence Bond Phase in the Triangular Lattice Quantum Dimer Model". In: *Phys. Rev. Lett.* 86 (9 2001), pp. 1881–1884. DOI: 10.1103/PhysRevLett.86.1881. URL: https://link.aps.org/doi/10.1103/PhysRevLett.86.1881.

[166] A. Molnar et al. "A generalization of the injectivity condition for projected entangled pair states". In: *preprint* 68 (2017). arXiv: arXiv:1706.07329 [quant-ph].

[167] Tsutomu Momoi. "Quantum fluctuations in quantum lattice systems with continuous symmetry". In: *Journal of Statistical Physics* 85 (1 1996), pp. 193–210. DOI: 10.1007/BF02175562.

[168] Tsutomu Momoi et al. "Scalar chiral ground states of spin ladders with four-spin exchanges". In: *Phys. Rev. B* 67 (17 2003), p. 174410. DOI: 10.1103/PhysRevB.67.174410. URL: https://link.aps.org/doi/10.1103/PhysRevB.67.174410.

[169] J. E. Moore and L. Balents. "Topological invariants of time-reversal-invariant band structures". In: *Phys. Rev. B* 75 (12 2007), p. 121306. DOI: 10.1103/PhysRevB.75.121306. URL: https://link.aps.org/doi/10.1103/PhysRevB.75.121306.

[170] Tôru Moriya. "Anisotropic Superexchange Interaction and Weak Ferromagnetism". In: *Phys. Rev.* 120 (1 1960), pp. 91–98. DOI: 10.1103/PhysRev.120.91. URL: https://link.aps.org/doi/10.1103/PhysRev.120.91.

[171] Olexei I. Motrunich. "Variational study of triangular lattice spin-1/2 model with ring exchanges and spin liquid state in $\kappa-(\mathrm{ET})_2\mathrm{Cu}_2(\mathrm{CN})_3$". In: *Phys. Rev. B* 72 (4 2005), p. 045105. DOI: 10.1103/PhysRevB.72.045105. URL: https://link.aps.org/doi/10.1103/PhysRevB.72.045105.

[172] Christopher Mudry et al. "Quantum phase transitions beyond Landau-Ginzburg theory in one-dimensional space revisited". In: *Phys. Rev. B* 99 (20 2019), p. 205153. DOI: 10.1103/PhysRevB.99.205153. URL: https://link.aps.org/doi/10.1103/PhysRevB.99.205153.

[173] M. Müller, T. Vekua, and H.-J. Mikeska. "Perturbation theories for the $S = \frac{1}{2}$ spin ladder with a four-spin ring exchange". In: *Phys. Rev. B* 66 (13 2002), p. 134423. DOI: 10.1103/PhysRevB.66.134423. URL: https://link.aps.org/doi/10.1103/PhysRevB.66.134423.

[174] B. Nachtergaele. "The spectral gap for some spin chains with discrete symmetry breaking". In: *Communications in Mathematical Physics* 175 (1996), pp. 565–606. URL: https://projecteuclid.org/euclid.cmp/1104276093.

[175] Masaaki Nakamura. "Identification of topologically different valence bond states in spin ladders". In: *Physica B: Condensed Matter* 329-333 (2003). Proceedings of the 23rd International Conference on Low Temperature Physics, pp. 1000 –1001. ISSN: 0921-4526. DOI: https://doi.org/10.1016/S0921-4526(02)02180-4. URL: http://www.sciencedirect.com/science/article/pii/S0921452602021804.

[176] Masaaki Nakamura and Synge Todo. "Order Parameter to Characterize Valence-Bond-Solid States in Quantum Spin Chains". In: *Phys. Rev. Lett.* 89 (7 2002), p. 077204. DOI: 10.1103/PhysRevLett.89.077204. URL: https://link.aps.org/doi/10.1103/PhysRevLett.89.077204.

[177] Masaaki Nakamura and Johannes Voit. "Lattice twist operators and vertex operators in sine-Gordon theory in one dimension". In: *Phys. Rev. B* 65 (15 2002), p. 153110. DOI: 10.1103/PhysRevB.65.153110. URL: https://link.aps.org/doi/10.1103/PhysRevB.65.153110.

[178] Y. Nambu. "Axial Vector Current Conservation in Weak Interactions". In: *Physical Review Letters* 4 (1960), pp. 380–382. DOI: 10.1103/PhysRevLett.4.380.

[179] Chetan Nayak et al. "Non-Abelian anyons and topological quantum computation". In: *Reviews of Modern Physics* 80 (2008), pp. 1083–1159.

[180] A. A. Nersesyan and A. M. Tsvelik. "One-Dimensional Spin-Liquid without Magnon Excitations". In: *Phys. Rev. Lett.* 78 (20 1997), pp. 3939–3942. DOI: 10.1103/PhysRevLett.78.3939. URL: https://link.aps.org/doi/10.1103/PhysRevLett.78.3939.

[181] E Jordao Neves and J Fernando Perez. "Long range order in the ground state of two-dimensional antiferromagnets". In: *Physics Letters A* 114.6 (1986), pp. 331–333.

[182] M. P. Nightingale and H. W. J. Blöte. "Gap of the linear spin-1 Heisenberg antiferromagnet: a Monte Carlo calculation". In: *Phys. Rev. B* 33 (1986), p. 659.

[183] Marcel den Nijs and Koos Rommelse. "Preroughening transitions in crystal surfaces and valence-bond phases in quantum spin chains". In: *Phys. Rev. B* 40 (7 1989), pp. 4709–4734. DOI: 10.1103/PhysRevB.40.4709. URL: https://link.aps.org/doi/10.1103/PhysRevB.40.4709.

[184] Hidetoshi Nishimori. "Spin quantum number in the ground state of the Mattis-Heisenberg model". In: *Journal of Statistical Physics* 26 (1981), pp. 839–845.

[185] Yoshihiro Nishiyama, Naomichi Hatano, and Masuo Suzuki. "Phase Transition and Hidden Orders of the Heisenberg Ladder Model in the Ground State". In: *Journal of the Physical Society of Japan* 64.6 (1995), pp. 1967–1979. DOI: 10.1143/JPSJ.64.1967. URL: https://doi.org/10.1143/JPSJ.64.1967.

[186] K. Nomura. "Onset of incommensurability in quantum spin chains". In: *Journal of the Physical Society of Japan* 72 (2003), pp. 476–478. DOI: 10.1143/JPSJ.72.476. eprint: arXiv:cond-mat/0210143.

[187] Y. Ogata. "A class of asymmetric gapped Hamiltonians on quantum spin chains and its characterization I". In: *Communications in Mathematical Physics* 348.72 (2016), pp. 847–895. DOI: 10.1007/s00220-016-2724-0. arXiv: arXiv:1510.07753 [math-ph].

[188] Y. Ogata. "A class of asymmetric gapped Hamiltonians on quantum spin chains and its characterization II". In: *Communications in Mathematical Physics* 348.73 (2016), pp. 897–957. DOI: 10.1007/s00220-016-2725-z. arXiv: arXiv:1510.07751 [math-ph].

[189] Y. Ogata. "A class of asymmetric gapped Hamiltonians on quantum spin chains and its characterization III". In: *Communications in Mathematical Physics* 352 (2017). This paper provides a thorough examination of asymmetric gapped Hamiltonians on quantum spin chains, adding substantial theoretical insights into their structure and classification., pp. 1205–1263. DOI: 10.1007/s00220-017-2905-1. arXiv: arXiv:1606.05508 [math-ph]. URL: https://doi.org/10.1007/s00220-017-2905-1.

[190] Y. Ogata. "A $\mathbb{Z}_2$-index of symmetry protected topological phases with reflection symmetry for quantum spin chains". In: (2019). preprint (2019). arXiv: arXiv:1904.01669 [cond-mat.str-el].

[191] Yoshiko Ogata. "A Z_2-Index of Symmetry Protected Topological Phases with Time Reversal Symmetry for Quantum Spin Chains". In: *Communications in Mathematical Physics* 374.2 (2020), pp. 705–734. ISSN: 1432-0916. DOI: 10.1007/s00220-019-03521-5. URL: https://doi.org/10.1007/s00220-019-03521-5.

[192] Takuhiro Ogino et al. “Continuous phase transition between Néel and valence bond solid phases in a $J-Q$-like spin ladder system”. In: *Phys. Rev. B* 103 (8 2021), p. 085117. DOI: 10.1103/PhysRevB.103.085117. URL: https://link.aps.org/doi/10.1103/PhysRevB.103.085117.

[193] Takuhiro Ogino et al. “Ground-state phase diagram of a spin-$\frac{1}{2}$ frustrated XXZ ladder”. In: *Phys. Rev. B* 106 (15 2022), p. 155106. DOI: 10.1103/PhysRevB.106.155106. URL: https://link.aps.org/doi/10.1103/PhysRevB.106.155106.

[194] Takuhiro Ogino et al. “Symmetry-protected topological phases and competing orders in a spin-$\frac{1}{2}$ XXZ ladder with a four-spin interaction”. In: *Phys. Rev. B* 104 (7 2021), p. 075135. DOI: 10.1103/PhysRevB.104.075135. URL: https://link.aps.org/doi/10.1103/PhysRevB.104.075135.

[195] Shigeki Onoda and Naoto Nagaosa. “Chiral Spin Pairing in Helical Magnets”. In: *Phys. Rev. Lett.* 99 (2 2007), p. 027206. DOI: 10.1103/PhysRevLett.99.027206. URL: https://link.aps.org/doi/10.1103/PhysRevLett.99.027206.

[196] R. Orús and G. Vidal. “Infinite time-evolving block decimation algorithm beyond unitary evolution”. In: *Phys. Rev. B* 78 (15 2008), p. 155117. DOI: 10.1103/PhysRevB.78.155117. URL: https://link.aps.org/doi/10.1103/PhysRevB.78.155117.

[197] T. Osafune et al. “Optical Study of the Charge Dynamics in (Sr,Ca,La)14Cu24O41: Observation of Hole Doping into the Cu2O3 Ladders”. In: *Physical Review Letters* 78.10 (1997), pp. 1980–1983. DOI: 10.1103/PhysRevLett.78.1980. URL: https://doi.org/10.1103/PhysRevLett.78.1980.

[198] Masaki Oshikawa. “Hidden Z_2*Z_2 symmetry in quantum spin chains with arbitrary integer spin”. In: *Journal of Physics: Condensed Matter* 4.36 (1992), pp. 7469–7488. DOI: 10.1088/0953-8984/4/36/019. URL: https://doi.org/10.1088/0953-8984/4/36/019.

[199] Masaki Oshikawa, Masanori Yamanaka, and Ian Affleck. “Magnetization Plateaus in Spin Chains: “Haldane Gap” for Half-Integer Spins”. In: *Phys. Rev. Lett.* 78 (10 1997), pp. 1984–1987. DOI: 10.1103/PhysRevLett.78.1984. URL: https://link.aps.org/doi/10.1103/PhysRevLett.78.1984.

[200] Yunqing Ouyang et al. “Computing Classification of Interacting Fermionic Symmetry-Protected Topological Phases Using Topological Invariants”. In: *Chinese Physics Letters* 38.12 (2021), p. 127101. DOI: 10.1088/0256-307X/38/12/127101. URL: https://dx.doi.org/10.1088/0256-307X/38/12/127101.

[201] Toplal Pandey and Gennady Y. Chitov. “Brane order and quantum magnetism in modulated anisotropic ladders”. In: *Phys. Rev. B* 106 (9 2022), p. 094413. DOI: 10.1103/PhysRevB.106.094413. URL: https://link.aps.org/doi/10.1103/PhysRevB.106.094413.

[202] J. B. Parkinson and J. C. Bonner. “Spin chains in a field: crossover from quantum to classical behavior”. In: *Phys. Rev. B* 32 (1985), p. 4703.

[203] Swapan K. Pati, Rajiv R. P. Singh, and Daniel I. Khomskii. "Alternating Spin and Orbital Dimerization and Spin-Gap Formation in Coupled Spin-Orbital Systems". In: *Phys. Rev. Lett.* 81 (24 1998), pp. 5406–5409. DOI: 10.1103/PhysRevLett.81.5406. URL: https://link.aps.org/doi/10.1103/PhysRevLett.81.5406.

[204] Karlo Penc, Nic Shannon, and Hiroyuki Shiba. "Half-Magnetization Plateau Stabilized by Structural Distortion in the Antiferromagnetic Heisenberg Model on a Pyrochlore Lattice". In: *Phys. Rev. Lett.* 93 (19 2004), p. 197203. DOI: 10.1103/PhysRevLett.93.197203. URL: https://link.aps.org/doi/10.1103/PhysRevLett.93.197203.

[205] D. Pérez-García et al. "String Order and Symmetries in Quantum Spin Lattices". In: *Phys. Rev. Lett.* 100 (16 2008), p. 167202. DOI: 10.1103/PhysRevLett.100.167202. URL: https://link.aps.org/doi/10.1103/PhysRevLett.100.167202.

[206] Lev Pitaevskii and Sandro Stringari. "Uncertainty principle, quantum fluctuations, and broken symmetries". In: *Journal of low temperature physics* 85 (1991), pp. 377–388.

[207] Frank Pollmann and Ari M. Turner. "Detection of symmetry-protected topological phases in one dimension". In: *Phys. Rev. B* 86 (12 2012), p. 125441. DOI: 10.1103/PhysRevB.86.125441. URL: https://link.aps.org/doi/10.1103/PhysRevB.86.125441.

[208] Frank Pollmann et al. "Entanglement spectrum of a topological phase in one dimension". In: *Phys. Rev. B* 81 (6 2010), p. 064439. DOI: 10.1103/PhysRevB.81.064439. URL: https://link.aps.org/doi/10.1103/PhysRevB.81.064439.

[209] Frank Pollmann et al. "Symmetry protection of topological phases in one-dimensional quantum spin systems". In: *Phys. Rev. B* 85 (7 2012), p. 075125. DOI: 10.1103/PhysRevB.85.075125. URL: https://link.aps.org/doi/10.1103/PhysRevB.85.075125.

[210] Frank Pollmann et al. "Theory of Finite-Entanglement Scaling at One-Dimensional Quantum Critical Points". In: *Phys. Rev. Lett.* 102 (25 2009), p. 255701. DOI: 10.1103/PhysRevLett.102.255701. URL: https://link.aps.org/doi/10.1103/PhysRevLett.102.255701.

[211] Hendrik Poulsen-Nautrup and Tzu-Chieh Wei. "Symmetry-protected topologically ordered states for universal quantum computation". In: *Physical Review A* 92 (2015), p. 052309. DOI: 10.1103/PhysRevA.92.052309. arXiv: arXiv:1509.02947 [quant-ph].

[212] Xiao-Liang Qi, Taylor L. Hughes, and Shou-Cheng Zhang. "Topological field theory of time-reversal invariant insulators". In: *Phys. Rev. B* 78 (19 2008), p. 195424. DOI: 10.1103/PhysRevB.78.195424. URL: https://link.aps.org/doi/10.1103/PhysRevB.78.195424.

[213] N. Read and Dmitry Green. "Paired states of fermions in two dimensions with breaking of parity and time-reversal symmetries and the fractional quantum Hall effect". In: *Phys. Rev. B* 61 (15 2000), pp. 10267–10297. DOI: 10.1103/PhysRevB.61.10267. URL: https://link.aps.org/doi/10.1103/PhysRevB.61.10267.

[214] N. Read and Subir Sachdev. "Large-N expansion for frustrated quantum antiferromagnets". In: *Phys. Rev. Lett.* 66 (13 1991), pp. 1773–1776. DOI: 10.1103/PhysRevLett.66.1773. URL: https://link.aps.org/doi/10.1103/PhysRevLett.66.1773.

[215] Tianhao Ren and Robert M. Konik. *Ultrafast Control of Magnetic Correlations in a Heisenberg Spin Ladder*. 2023. eprint: arXiv:2307.13914.

[216] Raffaele Resta. "Quantum-Mechanical Position Operator in Extended Systems". In: *Phys. Rev. Lett.* 80 (9 1998), pp. 1800–1803. DOI: 10.1103/PhysRevLett.80.1800. URL: https://link.aps.org/doi/10.1103/PhysRevLett.80.1800.

[217] Raffaele Resta and Sandro Sorella. "Electron Localization in the Insulating State". In: *Phys. Rev. Lett.* 82 (2 1999), pp. 370–373. DOI: 10.1103/PhysRevLett.82.370. URL: https://link.aps.org/doi/10.1103/PhysRevLett.82.370.

[218] T. M. Rice. "t-J ladders and cuprate ladder compounds". In: *Zeitschrift für Physik B Condensed Matter* 103.2 (1996), pp. 165–172. ISSN: 1431-584X. DOI: 10.1007/s002570050353. URL: https://doi.org/10.1007/s002570050353.

[219] Brenden Roberts, Shenghan Jiang, and Olexei I. Motrunich. "Deconfined quantum critical point in one dimension". In: *Phys. Rev. B* 99 (16 2019), p. 165143. DOI: 10.1103/PhysRevB.99.165143. URL: https://link.aps.org/doi/10.1103/PhysRevB.99.165143.

[220] Neil J. Robinson et al. "Nontopological Majorana Zero Modes in Inhomogeneous Spin Ladders". In: *Phys. Rev. Lett.* 122 (2 2019), p. 027201. DOI: 10.1103/PhysRevLett.122.027201. URL: https://link.aps.org/doi/10.1103/PhysRevLett.122.027201.

[221] M. Roger and J. M. Delrieu. "Cyclic four-spin exchange on a two-dimensional square lattice: Possible applications in high-T_c superconductors". In: *Phys. Rev. B* 39 (4 1989), pp. 2299–2303. DOI: 10.1103/PhysRevB.39.2299. URL: https://link.aps.org/doi/10.1103/PhysRevB.39.2299.

[222] M. Roger, J. H. Hetherington, and J. M. Delrieu. "Magnetism in solid ^{3}He". In: *Rev. Mod. Phys.* 55 (1 1983), pp. 1–64. DOI: 10.1103/RevModPhys.55.1. URL: https://link.aps.org/doi/10.1103/RevModPhys.55.1.

[223] S. Sachdev. *Quantum Phase Transitions*. Cambridge: Cambridge University Press, 2011.

[224] Anders W Sandvik. "Finite-size scaling of the ground-state parameters of the two-dimensional Heisenberg model". In: *Physical Review B* 56.18 (1997), p. 11678.

[225] Norbert Schuch, David Pérez-García, and Ignacio Cirac. "Classifying quantum phases using matrix product states and projected entangled pair states". In: *Phys. Rev. B* 84 (16 2011), p. 165139. DOI: 10.1103/PhysRevB.84.165139. URL: https://link.aps.org/doi/10.1103/PhysRevB.84.165139.

[226] H. J. Schulz. "Phase diagrams and correlation exponents for quantum spin chains of arbitrary spin quantum number". In: *Phys. Rev. B* 34 (9 1986), pp. 6372–6385. DOI: 10.1103/PhysRevB.34.6372. URL: https://link.aps.org/doi/10.1103/PhysRevB.34.6372.

[227] T. Senthil. "Symmetry-Protected Topological Phases of Quantum Matter". In: *Annual Review of Condensed Matter Physics* 6.1 (2015), pp. 299–324. DOI: 10.1146/annurev-conmatphys-031214-014740. URL: https://doi.org/10.1146/annurev-conmatphys-031214-014740.

[228] T. Senthil et al. "Deconfined Quantum Critical Points". In: *Science* 303.5663 (2004), pp. 1490–1494. ISSN: 0036-8075. DOI: 10.1126/science.1091806. URL: https://science.sciencemag.org/content/303/5663/1490.

[229] B Sriram Shastry. "Bounds for correlation functions of the Heisenberg antiferromagnet". In: *Journal of Physics A: Mathematical and General* 25.5 (1992), p. L249.

[230] D. G. Shelton, A. A. Nersesyan, and A. M. Tsvelik. "Antiferromagnetic spin ladders: Crossover between spin S=1/2 and S=1 chains". In: *Phys. Rev. B* 53 (13 1996), pp. 8521–8532. DOI: 10.1103/PhysRevB.53.8521. URL: https://link.aps.org/doi/10.1103/PhysRevB.53.8521.

[231] Ken Shiozaki and Shinsei Ryu. "Matrix product states and equivariant topological field theories for bosonic symmetry-protected topological phases in (1+1) dimensions". In: *Journal of High Energy Physics* 2017 (2017), p. 100. DOI: 10.1007/JHEP04(2017)100.

[232] T Siegrist, LF Schneemeyer, and SA Sunshine. "JV Waszc zak and RS Roth: Mat". In: *Res. Bull* 23 (1988), p. 1429.

[233] T. Siegrist et al. "A new layered cuprate structure-type, (A1-xA'x)14Cu24O41". In: *Materials Research Bulletin* 23.10 (1988), pp. 1429–1438. DOI: 10.1016/0025-5408(88)90019-1. URL: https://doi.org/10.1016/0025-5408(88)90019-1.

[234] Pimonpan Sompet et al. "Realizing the symmetry-protected Haldane phase in Fermi-Hubbard ladders". In: *Nature* 606.7914 (2022), pp. 484–488. ISSN: 1476-4687. DOI: 10.1038/s41586-022-04688-z. URL: https://doi.org/10.1038/s41586-022-04688-z.

[235] Erik S. Sørensen and Hae-Young Kee. "Twice hidden string order and competing phases in the spin-1/2 Kitaev-Gamma ladder". In: *npj Quantum Materials* 9.1 (2024), p. 10. ISSN: 2397-4648. DOI: 10.1038/s41535-024-00621-x. URL: https://doi.org/10.1038/s41535-024-00621-x.

[236] Dan M. Stamper-Kurn and Masahito Ueda. "Spinor Bose gases: Symmetries, magnetism, and quantum dynamics". In: *Rev. Mod. Phys.* 85 (3 2013), pp. 1191–1244. DOI: 10.1103/RevModPhys.85.1191. URL: https://link.aps.org/doi/10.1103/RevModPhys.85.1191.

[237] M. Steiner et al. "Inelastic neutron scattering studies on 1D near Heisenberg antiferromagnets: a test of the Haldane conjecture". In: *J. Appl. Phys.* 61 (1987), p. 3953.

[238] S. P. Strong and A. J. Millis. "Competition between singlet formation and magnetic ordering in one-dimensional spin systems". In: *Phys. Rev. Lett.* 69 (16 1992), pp. 2419–2422. DOI: 10.1103/PhysRevLett.69.2419. URL: https://link.aps.org/doi/10.1103/PhysRevLett.69.2419.

[239] S. P. Strong and A. J. Millis. "Competition between singlet formation and magnetic ordering in one-dimensional spin systems". In: *Phys. Rev. B* 50 (14 1994), pp. 9911–9923. DOI: 10.1103/PhysRevB.50.9911. URL: https://link.aps.org/doi/10.1103/PhysRevB.50.9911.

[240] Cheta Nayak Sudip Chakravarty Steven Kivelson and Klaus Voelker. "Wigner glass, spin liquids and the metal-insulator transition". In: *Philosophical Magazine B* 79.6 (1999), pp. 859–868. DOI: 10.1080/13642819908214845. URL: https://doi.org/10.1080/13642819908214845.

[241] B. Sutherland. *Beautiful Models—70 Years of Exactly Solved Quantum Many-Body Problems*. Singapore: World Scientific, 2004. ISBN: 9789812388485. DOI: 10.1142/5602.

[242] Kaplan TA, P Horsch, and W Von der Linden. "Order parameter in quantum antiferromagnets". In: *Journal of the Physical Society of Japan* 58.11 (1989), pp. 3894–3898.

[243] M Takahashi. "Half-filled Hubbard model at low temperature". In: *Journal of Physics C: Solid State Physics* 10.8 (1977), p. 1289. DOI: 10.1088/0022-3719/10/8/031. URL: https://dx.doi.org/10.1088/0022-3719/10/8/031.

[244] M. Takahashi. *Thermodynamics of One-Dimensional Solvable Models*. Cambridge: Cambridge University Press, 2009. ISBN: 9780521895549. DOI: 10.1017/CBO9780511524332.

[245] Mikio TAKANO et al. "Application of High Pressure and High Oxygen : Pressure to Copper Oxides : I-A New Materials and Material Design : I. Oxide Superconductors, Experiments I : Material Syntheses and Crystal Structures". In: *JJAP series* 7 (Feb. 1992), pp. 3–13. URL: https://cir.nii.ac.jp/crid/1540854195284291328.

[246] Shintaro Takayoshi and Masahiro Sato. "Coefficients of bosonized dimer operators in spin-$\frac{1}{2}$ XXZ chains and their applications". In: *Phys. Rev. B* 82 (21 2010), p. 214420. DOI: 10.1103/PhysRevB.82.214420. URL: https://link.aps.org/doi/10.1103/PhysRevB.82.214420.

[247] Shintaro Takayoshi, Masahiro Sato, and Shunsuke Furukawa. "Spontaneous population imbalance in two-component Bose and Fermi gases". In: *Phys. Rev. A* 81 (5 2010), p. 053606. DOI: 10.1103/PhysRevA.81.053606. URL: https://link.aps.org/doi/10.1103/PhysRevA.81.053606.

[248] Sanyee Tang and JE Hirsch. "Long-range order without broken symmetry: Two-dimensional Heisenberg antiferromagnet at zero temperature". In: *Physical Review B* 39.7 (1989), p. 4548.

[249] Hal Tasaki. "Long-range order,"tower" of states, and symmetry breaking in lattice quantum systems". In: *Journal of Statistical Physics* 174 (2019), pp. 735–761.

[250] Hal Tasaki. *Physics and mathematics of quantum many-body systems*. Graduate texts in physics. Berlin: Springer, 2020. DOI: 10.1007/978-3-030-41265-4. URL: https://link.springer.com/book/10.1007%2F978-3-030-41265-4.

[251] Hal Tasaki. "Quantum liquid in antiferromagnetic chains: a stochastic geometric approach to the Haldane gap". In: *Physical Review Letters* 66 (1991). Erratum: Phys. Rev. Lett. 75, 354 (1995), pp. 798–801. DOI: 10.1103/PhysRevLett.66.798.

[252] Hal Tasaki. "Topological Phase Transition and $\mathbb{Z}_2$ Index for $S = 1$ Quantum Spin Chains". In: *Phys. Rev. Lett.* 121 (14 2018), p. 140604. DOI: 10.1103/PhysRevLett.121.140604. URL: https://link.aps.org/doi/10.1103/PhysRevLett.121.140604.

[253] K. Totsuka, P. Lecheminant, and S. Capponi. "Semiclassical approach to competing orders in a two-leg spin ladder with ring exchange". In: *Phys. Rev. B* 86 (1 2012), p. 014435. DOI: 10.1103/PhysRevB.86.014435. URL: https://link.aps.org/doi/10.1103/PhysRevB.86.014435.

[254] Alexander A. Tsirlin et al. "Spin ladder compound $Pb_{0.55}Cd_{0.45}V_2O_5$: Synthesis and investigation". In: *Phys. Rev. B* 76 (10 2007), p. 104429. DOI: 10.1103/PhysRevB.76.104429. URL: https://link.aps.org/doi/10.1103/PhysRevB.76.104429.

[255] M. Tsuchiizu and A. Furusaki. "Generalized two-leg Hubbard ladder at half filling: Phase diagram and quantum criticalities". In: *Phys. Rev. B* 66 (24 2002), p. 245106. DOI: 10.1103/PhysRevB.66.245106. URL: https://link.aps.org/doi/10.1103/PhysRevB.66.245106.

[256] D. C. Tsui, H. L. Stormer, and A. C. Gossard. "Two-Dimensional Magnetotransport in the Extreme Quantum Limit". In: *Phys. Rev. Lett.* 48 (22 1982), pp. 1559–1562. DOI: 10.1103/PhysRevLett.48.1559. URL: https://link.aps.org/doi/10.1103/PhysRevLett.48.1559.

[257] Temo Vekua and Andreas Honecker. "Quantum dimer phases in a frustrated spin ladder: Effective field theory approach and exact diagonalization". In: *Phys. Rev. B* 73 (21 2006), p. 214427. DOI: 10.1103/PhysRevB.73.214427. URL: https://link.aps.org/doi/10.1103/PhysRevB.73.214427.

[258] Ruben Verresen, Roderich Moessner, and Frank Pollmann. "One-dimensional symmetry protected topological phases and their transitions". In: *Phys. Rev. B* 96 (16 2017), p. 165124. DOI: 10.1103/PhysRevB.96.165124. URL: https://link.aps.org/doi/10.1103/PhysRevB.96.165124.

[259] Guifré Vidal. "Efficient Simulation of One-Dimensional Quantum Many-Body Systems". In: *Phys. Rev. Lett.* 93 (4 2004), p. 040502. DOI: 10.1103/PhysRevLett.93.040502. URL: https://link.aps.org/doi/10.1103/PhysRevLett.93.040502.

[260] Chao Wang et al. "Simulation of ring-exchange models with projected entangled pair states". In: *Phys. Rev. B* 105 (2 2022), p. 024417. DOI: 10.1103/PhysRevB.105.024417. URL: https://link.aps.org/doi/10.1103/PhysRevB.105.024417.

[261] H. Watanabe and H. Murayama. "Unified Description of Nambu-Goldstone Bosons without Lorentz Invariance". In: *Physical Review Letters* 108 (2012), p. 251602. DOI: 10.1103/PhysRevLett.108.251602.

[262] Hiroshi Watanabe, Kiyohide Nomura, and Satoshi Takada. "S=1/2 Quantum Heisenberg Ladder and S=1 Haldane Phase". In: *Journal of the Physical Society of Japan* 62.8 (1993), pp. 2845–2860. DOI: 10.1143/JPSJ.62.2845. URL: https://doi.org/10.1143/JPSJ.62.2845.

[263] Tzu-Chieh Wei. "Quantum spin models for measurement-based quantum computation". In: *Advances in Physics: X* 3.1 (2018), p. 1461026. DOI: 10.1080/23746149.2018.1461026.

[264] Phillip Weinberg and Marin Bukov. "QuSpin: a Python Package for Dynamics and Exact Diagonalisation of Quantum Many Body Systems part I: spin chains". In: *SciPost Phys.* 2 (1 2017), p. 003. DOI: 10.21468/SciPostPhys.2.1.003. URL: https://scipost.org/10.21468/SciPostPhys.2.1.003.

[265] Phillip Weinberg and Marin Bukov. "QuSpin: a Python Package for Dynamics and Exact Diagonalisation of Quantum Many Body Systems. Part II: bosons, fermions and higher spins". In: *SciPost Phys.* 7 (2 2019), p. 20. DOI: 10.21468/SciPostPhys.7.2.020. URL: https://scipost.org/10.21468/SciPostPhys.7.2.020.

[266] X. G. Wen. "Chiral Luttinger liquid and the edge excitations in the fractional quantum Hall states". In: *Phys. Rev. B* 41 (18 1990), pp. 12838–12844. DOI: 10.1103/PhysRevB.41.12838. URL: https://link.aps.org/doi/10.1103/PhysRevB.41.12838.

[267] X. G. Wen. "Gapless boundary excitations in the quantum Hall states and in the chiral spin states". In: *Phys. Rev. B* 43 (13 1991), pp. 11025–11036. DOI: 10.1103/PhysRevB.43.11025. URL: https://link.aps.org/doi/10.1103/PhysRevB.43.11025.

[268] X. G. Wen. "Mean-field theory of spin-liquid states with finite energy gap and topological orders". In: *Phys. Rev. B* 44 (6 1991), pp. 2664–2672. DOI: 10.1103/PhysRevB.44.2664. URL: https://link.aps.org/doi/10.1103/PhysRevB.44.2664.

[269] X. G. Wen. "Vacuum degeneracy of chiral spin states in compactified space". In: *Phys. Rev. B* 40 (10 1989), pp. 7387–7390. DOI: 10.1103/PhysRevB.40.7387. URL: https://link.aps.org/doi/10.1103/PhysRevB.40.7387.

[270] X. G. Wen and Q. Niu. "Ground-state degeneracy of the fractional quantum Hall states in the presence of a random potential and on high-genus Riemann surfaces". In: *Phys. Rev. B* 41 (13 1990), pp. 9377–9396. DOI: 10.1103/PhysRevB.41.9377. URL: https://link.aps.org/doi/10.1103/PhysRevB.41.9377.

[271] X. G. Wen, Frank Wilczek, and A. Zee. "Chiral spin states and superconductivity". In: *Phys. Rev. B* 39 (16 1989), pp. 11413–11423. DOI: 10.1103/PhysRevB.39.11413. URL: https://link.aps.org/doi/10.1103/PhysRevB.39.11413.

[272] Xiao-Gang Wen. "Choreographed entanglement dances: Topological states of quantum matter". In: *Science* 363.6429 (2019), eaal3099. ISSN: 0036-8075. DOI: 10.1126/science.aal3099. URL: https://science.sciencemag.org/content/363/6429/eaal3099.

[273] S. R. White and D. A. Huse. "Numerical renormalization-group study of low-lying eigenstates of the antiferromagnetic S=1 Heisenberg chain". In: *Physical Review B* 48 (1993), p. 3844. DOI: 10.1103/PhysRevB.48.3844.

[274] S. R. White, R. M. Noack, and D. J. Scalapino. "Resonating Valence Bond Theory of Coupled Heisenberg Chains". In: *Phys. Rev. Lett.* 73 (6 1994), pp. 886–889. DOI: 10.1103/PhysRevLett.73.886. URL: https://link.aps.org/doi/10.1103/PhysRevLett.73.886.

[275] Hong Yang et al. "Duality, criticality, anomaly, and topology in quantum spin-1 chains". In: *Phys. Rev. B* 107 (12 2023), p. 125158. DOI: 10.1103/PhysRevB.107.125158. URL: https://link.aps.org/doi/10.1103/PhysRevB.107.125158.

[276] Jian Yang, Chen Fang, and Zheng-Xin Liu. "Symmetry-protected nodal points and nodal lines in magnetic materials". In: *Phys. Rev. B* 103 (24 2021), p. 245141. DOI: 10.1103/PhysRevB.103.245141. URL: https://link.aps.org/doi/10.1103/PhysRevB.103.245141.

[277] Dmitri A. Yarotsky. "Ground states in relatively bounded quantum perturbations of classical lattice systems". In: *Communications in Mathematical Physics* 261 (2006), pp. 799–819. DOI: 10.1007/s00220-005-1430-1. arXiv: arXiv:math-ph/0412040 [math-ph].

[278] Beni Yoshida. "Topological phases with generalized global symmetries". In: *Physical Review B* 93 (2016), p. 155131. DOI: 10.1103/PhysRevB.93.155131. arXiv: arXiv:1508.03468 [cond-mat.str-el].

[279] Bei Zeng et al. *Quantum information meets quantum matter: from quantum entanglement to topological phases of many-body systems*. Quantum science and technology. New York, NY: Springer, 2019. DOI: 10.1007/978-1-4939-9084-9. URL: https://link.springer.com/book/10.1007%2F978-1-4939-9084-9.